NANOSTRUCTURED POLYANION-BASED CATHODE MATERIALS FOR RECHARGEABLE LITHIUM-ION BATTERY

VISHWANATHAN RAMAR

(B.E., ANNA UNIVERSITY, INDIA)

A THESIS SUBMITTED

FOR THE DEGREE OF DOCTOR OF PHILOSOPHY

DEPARTMENT OF MECHANICAL ENGINEERING

NATIONAL UNIVERSITY OF SINGAPORE

2014

DECLARATION

I hereby declare that the thesis is my original work and it has been written by me in its entirety.

I have duly acknowledged all the sources of information which have been used in this thesis.

This thesis has not been submitted for any degree in any university previously.

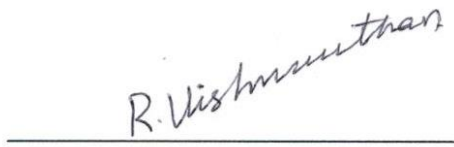

VISHWANATHAN RAMAR

6th JANUARY 2014

Acknowledgments

First and foremost, I would like to express my heartfelt gratitude to my supervisor Dr. Palani Balaya for providing me this valuable opportunity of permitting me to perform research under his supervision. The complete freedom and motivation that he provided me during the course of my research in his laboratory helped me immensely. Without his constant support, guidance and patience this thesis would have never been possible. My heartfelt gratitude goes to the Department of Mechanical Engineering for offering me with NUS research scholarship throughout the course of my PhD study.

I would like to thank Dr. Kuppan Saravanan, Dr. Srirama Hariharan, Dr. Satyanarayana Reddy Gajjela, Dr. Sappani Devaraj, Dr. Mirjana Kuzma and Dr. Sunil Kumar for sharing their knowledge on experimental techniques. My gratitude also goes to group members Mr. Girish Salian Dayanand, Mr. Markas Law Lee Lam and Mr. Ashish Rudola and for making the laboratory a vibrant and lively workplace. Special thanks to Dr. Srirama Hariharan, Dr. Sunil Kumar, Dr. Krishnamoorthy Ananthanarayanan, Dr. Satyanarayana Reddy Gajjela and Mr. Selva Surendhiran for spending their valuable time in reading and commenting on this thesis. Special thanks to Mr. Vasanth Natarajan for immensely helping me in documenting the thesis. My appreciation also goes to my lab alumni Dr. Wong Kim Hai, Dr. Hwang Sheng Lee and Mrs. Kannaiyan Ganga for their support. Special gratitude goes to TPL-1 lab officers Mr. Yeo Khee Ho, Mrs. Hung-Ang Yan Leng, ESP Lab officer Mr. Chew Yew Lin and the technical staff at Department office whose support in various capacities ensured and the completion of my thesis in a

timely manner. I would also like to thank Ms. Teo Lay Tin Sharen and Ms. Thong Siew Fah for their help on the administrative matters.

I would like to thank officers of materials and science division Mr. Thomas (PXRD) and Mr. Hong Wei (FESEM) for their kind assistance. I wish to express my utmost gratitude to Ms. Toh Soh Lian (PXRD and FTIR), Dr. Zhang Jixuan (TEM), Mr. Lee Ka Yau (FESEM and EDXS), Dr. Yuan Ze Liang (XPS) and Ms. Geok Kheng (High temperature XRD) for their kind assistance.

I am grateful to Dr. Ruhul Amin for his valuable suggestions during the 223rd ECS meeting- 2013 conference, Toronto, Canada. I would also wish to extend my sincere gratitude to Prof. Hong Li, Prof. Atsuo Yamada and Prof Saiful Islam for their valuable suggestions during the LIBD 2013 conference, Arcachon, France.

I am sincerely grateful to Mr. Velmurugan, Mrs. Rajalakshmi, Mr. Sivasubramanian, Mr. Sethumadhan, Mr. Hariharan, Dr. Chinnadurai, Dr. Karthikeyan, Dr. Ramakrishnan, Mrs. Latha, Mr. Thinagaran, Mrs. Banumathi, and Mrs. Ganabadhiyammal who have inspired and encouraged me. Special thanks to my dearest friends Dr. Srirama, Mr. Siva Prasad and Mr. Venkatesh who has been alongside me during my college days. I thank my dearest friends Mr. Vasanth Natarajan and Mrs. Madhuvika Murugan for making my stay in Singapore a memorable experience.

Special thanks to my brother Mr. Kasirajan Ramar who has supported me right from the childhood, until now. Words are not enough to express my love and gratitude to my father, S. Ramar and my mother, S. Chandra Ramar who have gifted me this life and their precious love. Special thanks to my

father-in-law, Mr. Allaman and mother-in-law, Mrs. Sathyabama Allaman for their continuous support. Last but not least, I would like to acknowledge my dearest wife Mrs. Nikila Gowri Vishwanathan and my little angel Ms. Swagatha Vishwanathan without whom I would have never been what I am today.

Vishwanathan Ramar

6th January 2014

Table of Contents

Summary

Increasing levels of greenhouse gas emissions from conventional transportation sector has become a serious challenge in recent years. The development of on-board energy storage systems capable of storing electrical energy from sustainable energy sources namely solar and wind is a key solution to this problem. Among the various energy storage systems proposed for electric vehicle (EV) applications, lithium-ion batteries (LIBs) have been considered to be promising candidates owing to their high specific energy, long cycle life and wide operating temperature. However, the cost and vulnerable safety of battery materials hinder the widespread penetration of batteries in the EV market. A mobile phone battery needs a few grams of cathode material while an EV battery-pack might need up to a hundred kilo-grams of cathode material per pack. Hence, lithium-ion battery for EV applications will be forced to explore cheaper and safer cathode materials, as the cost of the cathode is nearly one-third of the total cost of lithium-ion battery-packs. In this regard, the nucleus of the current investigation will focus on the ways and means of tailoring the properties of earth abundant Mn and Fe -based cathode materials.

In **chapter 1,** the need for energy storage systems mainly batteries and their use in EV application is discussed. A concise literature review of the various cathode materials, anode materials and electrolytes for lithium-ion batteries is provided. Finally, the scope of this thesis is outlined.

In **chapter 2,** experimental techniques and procedures employed for the electrode material preparation and its characterization are provided.

Appropriate details relating to half-cell and full cell assembly along with their electrochemical characterization is outlined.

In **chapter 3,** lithium storage in $LiMnPO_4$/C cathode material was prepared with an architecture featuring carbon coated, interconnected nano-grains constructed with mesopores using a soft template synthesis method followed by high energy ball milling process. This architecture facilitates enhanced lithium ionic and electronic transports; favors improved lithium storage performance. Mesoporous $LiMnPO_4$/C electrode delivers discharge capacity of 140 mAh g^{-1} at 0.05C using galvanostatic cycling mode. The electrochemical response of $LiMnPO_4$/C at constant current mode is complemented by diffusion studies using cyclic voltammetry and impedance spectroscopy. The interdependence of lithium storage performance on carbon content, milling time, grain size and porous characteristics (surface area, pore size and pore volume) is also discussed. Finally, the feasibility of $LiMnPO_4$/C cathode is evaluated against $Li_4Ti_5O_{12}$/C anode in a full cell.

In **chapter 4,** we discuss the effect of Fe^{2+} and/or Mg^{2+} doping in high potential $LiMnPO_4$ cathode material. The lithium storage capacity of 159 mAh g^{-1} is obtained at 0.1C for isovalent co-doped $LiMn_{0.9}Fe_{0.05}Mg_{0.05}PO_4$/C material with relatively less polarization of ~139 mV. This capacity is much better than $LiMn_{0.9}Fe_{0.1}PO_4$/C and $LiMn_{0.95}Mg_{0.05}PO_4$/C which deliver only 136.8 and 128.4 mAh g^{-1} at 0.1C with polarization of ~222 and 334 mV respectively. $LiMn_{0.9}Fe_{0.05}Mg_{0.05}PO_4$/C electrode material delivers a capacity of 116 mAh g^{-1} at 1C after 200 cycles, which is 96% of its initial capacity. The improved cycling stability of $LiMn_{0.9}Fe_{0.05}Mg_{0.05}PO_4$/C is attributed to the suppressed Mn dissolution in the electrolyte compared to the other samples.

The enhanced storage performance of co-doped $LiMnPO_4$ is thus explained in terms of (i) favorable extraction and insertion reactions and (ii) enhanced transport properties.

In **chapter 5,** $LiMn_{1-x}Fe_xPO_4/C$ (x = 0, 0.2, 0.5 and 0.8) Mn-Fe mixed transition metal phosphate was synthesized with the similar morphology, particles size and carbon content by a soft template synthesis method followed by high energy ball milling process to enhance the manganese utilization. $LiMn_{1-x}Fe_xPO_4$ (x = 0.2, 0.5 and 0.8) showed two distinct charge and discharge profiles, resulting in lithium storage performance of 160, 159, 158 mAh g^{-1} at 0.1C compared to $LiMnPO_4/C$ that exhibits capacity of only 120 mAh g^{-1}. The voltage polarization for Mn-Fe mixed phosphate electrodes was found to be ~85 mV: 20 mV in the Mn:Fe redox potential region unlike $LiMnPO_4/C$ (340 mV) at 0.1C. Most importantly, Mn-rich $LiMn_{0.8}Fe_{0.2}PO_4/C$ showed enhanced electrochemical kinetics, rate performance, cycling stability, thermal stability, structural stability and reduced voltage polarization. The capacity retention of 86% is obtained for $LiMn_{0.8}Fe_{0.2}PO_4/C$ after 700 cycles at 1C. $LiMn_{0.8}Fe_{0.2}PO_4/C$ electrode exhibits stable discharge capacity of ~155 mAh g^{-1} when cycled between room temperature (RT) - 60°C. The enhanced electrochemical kinetics of Mn-rich $LiMn_{0.8}Fe_{0.2}PO_4/C$ is demonstrated in terms of (i) redox combination which in turn provides favourable environment for the lithiation and delithiation processes owing to difference in the equilibrium potential of Fe^{2+}/Fe^{3+} and Mn^{2+}/Mn^{3+} unlike $LiMnPO_4$, (ii) partial suppression of Jahn-Teller distortion, (iii) reasonably good structural and thermal stability of delithiated phase and (iv) enhanced transport properties. Finally, the full cell performance of Mn-rich $LiMn_{0.8}Fe_{0.2}PO_4/C$ is

demonstrated with an insertion anode $Li_4Ti_5O_{12}$/C and conversion anode Fe_2O_3/C.

In **chapter 6,** $LiMn_{0.8}Fe_{0.15}Mg_{0.05}PO_4$/C was synthesized with particles size in the range of 30-50 nm by a soft template synthesis method followed by high energy ball milling process to enhance the manganese utilization. The presence of Mg^{2+} in Mn-Fe mixed transition metal phospho-olivine showed better electrochemical kinetics, manganese utilization, rate performance, cycling stability, thermal stability, structural stability, reduced voltage polarization and reduced volume change during the electrochemical delithiation. The voltage polarization at 10C for $LiMn_{0.8}Fe_{0.15}Mg_{0.05}PO_4$/C is 550 and 850 mV for Mn^{3+}/Mn^{2+} and Fe^{3+}/Fe^{2+} redox couples compared to $LiMn_{0.8}Fe_{0.2}PO_4$/C sample that shows voltage polarization of 1010 and 1210 mV for Mn^{3+}/Mn^{2+} and Fe^{3+}/Fe^{2+} redox couples respectively. $LiMn_{0.8}Fe_{0.15}Mg_{0.05}PO_4$/C electrode retains 82% of its initial capacity at 1C after 1000 cycles. $LiMn_{0.8}Fe_{0.15}Mg_{0.05}PO_4$/C sample also delivers extremely stable capacity of ~157 mAh g^{-1} when cycled in the temperature range RT - 60°C. The possible reasons for enhanced manganese utilization of $LiMn_{0.8}Fe_{0.15}Mg_{0.05}PO_4$/C was demonstrated in terms of (i) redox combination which provides favorable environment for the lithiation and delithiation processes owing to low equilibrium potential of Fe^{2+}/Fe^{3+} and electrochemically inactive Mg^{2+}, (ii) partial suppression of Jahn-Teller distortion, (iii) structural and thermal stability of delithiated phase and (iv) enhanced transport properties.

In **chapter 7,** the synthesis and electrochemical characterization of low and high temperature polymorphs of Li_2MnSiO_4/C cathode material was

investigated. These materials were synthesized with carbon coating using two-step synthesis method followed by high energy ball milling process. Two polymorphs were isolated by controlling the synthesis temperature which was *Pmn*2_1 (low temperature) and *P*2_1/*n* (high temperature) polymorphs. Among these, the electrochemical performance of low temperature (*Pmn*2_1) polymorph was better than high temperature polymorph (*P*2_1/*n*). The lithium storage of *Pmn*2_1 polymorph is 262 mAh g^{-1} at 0.1C; in contrast *P*2_1/*n* polymorph that shows only 164 mAh g^{-1}. The lithium storage performance of Pmn2_1 is almost two times higher than *P*2_1/*n* at all current rates. This is explained by the simplest migration pathway of Li^+ ions in *Pmn*2_1 polymorph as compared to *P*2_1/*n* polymorph. *Ex-situ* XRD patterns of carbon coated sample reveals that the structure is stable upon first charging up to 4.6 V and after 30 galvanostatic cycles. It can be suggested that apart from the type of polymorphs, the structural stability and carbon coating are also very important to achieve enhanced lithium storage performance in Li_2MnSiO_4.

In **chapter 8**, conclusions and suggestions for future research are provided.

Key words: lithium-ion battery, cathode, electrochemical performance, olivine, Jahn-Teller distortion, lithium metal phosphate, lithium manganese phosphate, solid solution, doping, substitution, lithium metal silicate, lithium manganese silicate.

Significant findings from the current studies

- A novel synthesis process for the preparation of olivine phosphate based cathode materials was developed.
- Lithium storage performance of $LiMnPO_4/C$ was found to be highly interdependent on the carbon content, ball-milling time, grain size, surface area, pore size and pore volume.
- Co-substitution of Fe^{2+} and Mg^{2+} ($LiMn_{0.9}Fe_{0.05}Mg_{0.05}PO_4$) resulted in enhanced lithium storage capacity, cyclability and lesser manganese dissolution and voltage polarization compared to $LiMnPO_4/C$.
- Mn rich transition metal phosphate ($LiMn_{0.8}Fe_{0.2}PO_4$) delivered superior electrochemical performance compared to $LiMn_{0.9}Fe_{0.05}Mg_{0.05}PO_4$ and $LiMnPO_4/C$. The enhanced electrochemical kinetics of Mn-rich Mn-Fe mixed phosphates are attributable to (i) redox combination which in turn provides favorable environment for the lithiation and delithiation processes owing to difference in the equilibrium potential of Fe^{2+}/Fe^{3+} and Mn^{2+}/Mn^{3+} redox couples, (ii) partial suppression of Jahn-Teller distortion, (iii) reasonably good structural and thermal stability of delithiated phase and (iv) enhanced transport properties.
- Substitution of Mg^{2+} in Mn-Fe mixed transition metal phosphate ($LiMn_{0.8}Fe_{0.15}Mg_{0.05}PO_4$) resulted in suppressed Jahn-Teller distortion, better structural and thermal stability of delithiated phases compared to $LiMn_{0.8}Fe_{0.2}PO_4$. Ultimately, the storage performance in the high voltage Mn redox was much better in $LiMn_{0.8}Fe_{0.15}Mg_{0.05}PO_4$. This electrode retained 82% of its initial capacity at 1C after 1000 cycles. No significant

capacity fading was observed when the cells were cycled in the temperature range RT - 60°C.

- Two different polymorphs of Li_2MnSiO_4 were isolated by controlling the synthesis temperature. The low temperature *Pmn2₁* polymorph of Li_2MnSiO_4/C showed the better electrochemical performance and cycling stability compared to $P2_1/n$ polymorph. The cycling stability of $Pmn2_1$ polymorph is the highest among the reports in literature. $Pmn2_1$ polymorph offers a simpler migration pathway for Li^+ ion compared to $P2_1/n$ polymorph. Besides, the structural stability of $Pmn2_1$ during cycling and carbon coating are critical in achieving high storage performance.

List of Tables

List of Figures

List of Abbreviations

LIBs	Lithium-ion Batteries
LIB	Lithium-ion Battery
EVs	Electric Vehicles
ES	Energy Storage
Ni-Cd	Nickel Cadmium
Ni-MH	Nickel Metal Hydride
$LiPF_6$	Lithium hexafluro phosphate
EC	Ethylene Carbonate
DEC	Diethyl Carbonate
CCP	Cubic Closed-Packed
CNTs	Carbon Nanotubes
SEI	Solid Electrolyte Interface
PC	Propylene Carbonate
DMC	Dimethylene Carbonate
EMC	Ethyl Methyl Carbonate
CTAB	Cetyl Trimethyl Ammonium Bromide
HEBM	High Energy Ball Milling
PXRD	Powder X-Ray Diffraction
FESEM	Field Emission Scanning Electron Microscopy
EDXS	Energy Dispersive X-ray Spectroscopy
TEM	Transmission Electron Microscopy
HRTEM	High Resolution Transmission Electron Microscopy

SAED	Selected Area Electron Diffraction
BET	Brunauer Emmett Teller
BJH	Barrett-Joyner-Halenda
EA	Elemental Analysis
ICP-OES	Inductively Coupled Plasma Optical Emission Spectroscopy
XPS	X-ray Photoelectron Spectroscopy
FTIR	Fourier Transform Infrared Spectroscopy
GC	Galvanostatic Cycling
CV	Cyclic Voltammetry
EIS	Electrochemical Impedance Spectroscopy
OCV	Open Circuit Voltage
NMP	N-methyl pyrrolidone
PVDF	Polyvinylidene fluoride
RT	Room Temperature

List of Publications

Patent

1. An Approach for Manufacturing Efficient Mesoporous Nano-Composite Positive Electrode $LiMn_{1-x}Fe_xPO_4$ Materials.
   P. Balaya and **V. Ramar, Patent Application No: WO 2013/002730, Jan 2013 (entered into national phase).**

Publications

1. Enhancing the electrochemical kinetics of high voltage olivine $LiMnPO_4$ by isovalent co-doping.
   V.Ramar and P.Balaya, ***Phys. Chem. Chem. Phys***., 2013, 15, 17240-17249, DOI:10.1039/C3CP52311J.

2. The effect of synthesis parameters on the lithium storage performance of $LiMnPO_4$/C
   V. Ramar, K. Saravanan, S.R Gajjela, S. Hariharan and P. Balaya. **Electrochim Acta**., 2013, 105, 496-505, DOI:10.1016/j.electacta.2013.05.025.

3. Developing a rusty, light weight lithium-ion battery - An effective material and electrode design for high performance conversion anodes.
   S. Hariharan, **V. Ramar**, S. P. Joshi and P. Balaya.
   RSC Advances, 2013, 3, 6386-6394, DOI:10.1039/C3RA23244A.

4. A Rationally Designed Dual Role Anode Material for Lithium-ion and Sodium-ion Batteries-Case Study of Eco-Friendly Fe_3O_4.
   S. Hariharan, K. Saravanan, **V. Ramar** and P. Balaya.
   Phys. Chem. Chem. Phys., 2013, 15, 2945-2953, DOI:10.1039/C2CP44572G.

5. Influence of nanosize and thermodynamics on lithium storage in insertion and conversion reactions.
   S. Hariharan, **V. Ramar** and P. Balaya.
   Proc. SPIE 8377, Energy Harvesting and Storage: Materials, Devices, and Applications III, 837703, 2012, DOI:10.1117/12.921157.

6. $Li(Mn_xFe_{1-x})PO_4$/C (x = 0.5, 0.75 and 1) nanoplates for lithium storage application.
   K. Saravanan, **V. Ramar**, P. Balaya and J. J. Vittal.
   J. Mater. Chem., 2011, 21, 14925-14935, DOI:10.1039/C1JM11541C.

7. Nanostructured mesoporous materials for lithium-ion battery applications.
   K. Saravanan**,** S. Hariharan, **V. Ramar**, H. S. Lee, M. Kuezma, S. Devaraj, D. H. Nagaraju, K. Ananthanarayanan and C. W. Mason.
   Proc. SPIE 8035, Energy Harvesting and Storage: Materials, Devices, and Applications II, 803503, 2011, DOI:10.1117/12.884460.

Manuscripts to be communicated

1. Understanding the electrochemical kinetics and redox potential shift of olivine cathode materials $Li(Mn_{1-x}Fe_x)PO_4/C$ (x = 0, 0.2, 0.5 and 0.8).
   V.Ramar, S. Girish and P.Balaya (**2014**, in preparation).

2. The effect of polymorphism on the lithium storage performance of Li_2MnSiO_4.
   V.Ramar and P.Balaya (**2014**, in preparation).

3. Influence of Mg^{2+} substitution on the manganese utilization of olivine based cathode material $Li(Mn_{0.8}Fe_{0.15}Mg_{0.05})PO_4/C$ for rechargeable Li-ion battery.
   V.Ramar and P.Balaya (**2014**, in preparation).

Oral Presentations

1. High capacity cathode material for Li ion battery applications: Li_2MnSiO_4.
   V. Ramar and P. Balaya, **7th-ICMAT,** Singapore, 30th June -5th July **2013**.

2. Li_2MnSiO_4: High storage capacity cathode material for Li ion battery applications.
   V. Ramar and P. Balaya, **223rd ECS Meeting,** Toronto, Canada, 12th – 16th May **2013**.

3. Mesoporous nano-composite $LiMn_{1-x}Fe_xPO_4/C$ (x = 0, 0.2, 0.5. 0.8 and 1.0) as potential cathode for Lithium-ion battery application.
   V. Ramar, H. S. Lee, K. Saravanan and P. Balaya, **6th-ACEPS,** India, 5th - 8th January **2012**.

Poster Presentations

1. Mesoporous $Li(Mn_{0.8}Fe_{0.15}Mg_{0.05})PO_4/C$ cathode material for energy storage application.
   V. Ramar and P. Balaya, **7th-ICMAT,** Singapore, 30th June -5th July **2013**.

2. $Li(Mn_{0.8}Fe_{0.2-x}Mg_x)PO_4/C$ (x = 0, 0.05) : A potential cathode material for Li-ion battery application.
   V. Ramar, S. Hariharan and P. Balaya, **LiBD-6,** Arcachon, France, 16nd - 21th June **2013**.

3. Li $(Mn_{1-x}Fe_x)$ PO_4/C: High Rate Mesoporous Cathode Materials for Li-ion Battery Application.

V. Ramar, K. Saravanan and P. Balaya, **ICYRAM,** Singapore, 2nd -5th July **2012**.

4. Optimized Porous Nano-composite $LiMnPO_4/C$ as an Advanced Cathode Material for Li-Ion Battery Applications.
   V. Ramar, K. Saravanan and P. Balaya, **6th-ICMAT,** Singapore, 27th June -1st July **2011**.

Chapter 1

1. Introduction and literature survey

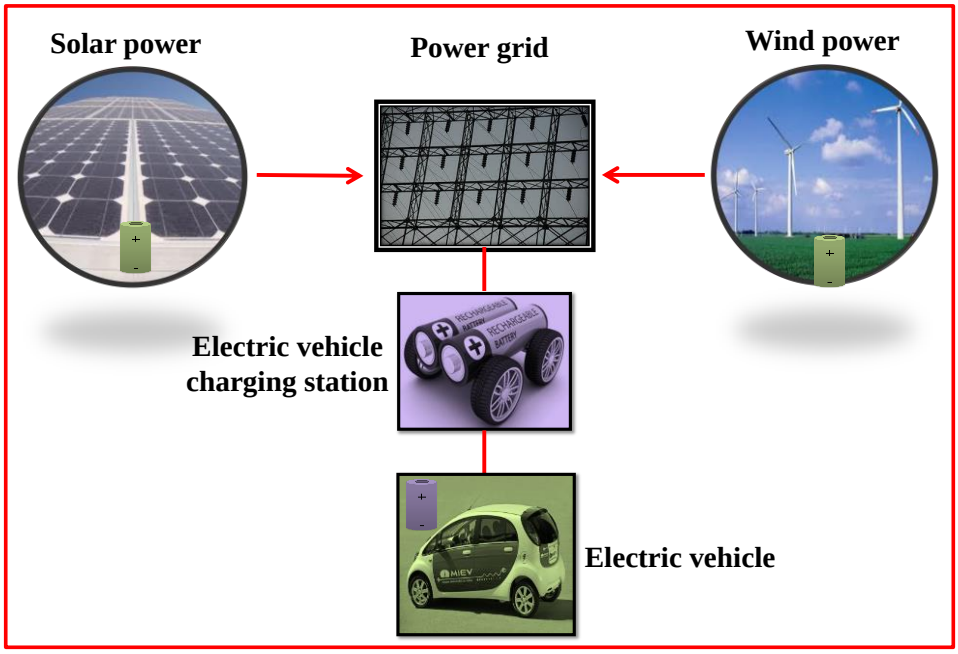

1.1 Preface to Chapter 1

This chapter emphasizes the importance of energy storage systems particularly lithium-ion batteries (LIBs) for its use in electric vehicle application. A brief literature survey of various components of LIBs namely cathode materials, anode materials and electrolytes are provided. Finally, the scope of the present thesis work is presented at the end of this chapter.

1.2 Importance of energy storage systems

In recent years, electricity is the most dominant form of energy and this demand is expected to be triple by the end of the present decade.[1] The total global energy generation is estimated to be ~20 x 10^{12} watts, out of which approximately 68% of the electricity comes from fossil fuels.[2] For every kWh energy obtained from fossil fuels, ~1 kg of CO_2 is produced raising concerns on global warming.[1] Further, increasing cost of fossil fuels coupled with their limited availability has triggered research interests in generating electricity from alternative clean energy sources. Among the various forms of alternate energy, solar and wind energy are clean, abundant and readily available.[3, 4] However, they are intermittent in time and geography. Hence, there is a pressing need to design sustainable energy storage systems (ES) which could store clean energy so that it could be used up later on demand.

1.3 Choice of energy storage systems

Based on the type of energy storage, ES systems could be classified into mechanical, thermal, electrical and electrochemical energy storage systems as described below in **Figure 1.1**. Amongst them, electrochemical energy storage in which electrical energy is stored in the form of chemical energy and vice-versa are believed to be highly promising[5] due to the following virtues:

- Smoke free operation
- Absence of moving parts
- Quick response time
- High round trip efficiency

- Long cycle life

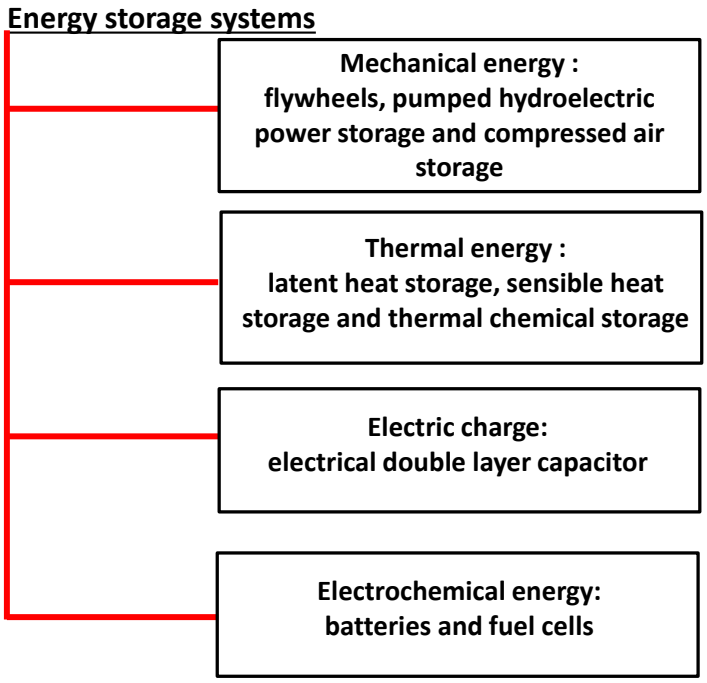

Figure 1.1 Classification of the energy storage systems.

1.3.1 Electrochemical energy storage systems

Electrochemical energy storage systems could further be classified into fuel cells, electrochemical capacitors and batteries. ***Fuel cells*** are electrochemical device which converts the chemical energy into electrical energy through the chemical reaction with the fuel. ***Electrochemical capacitors*** are device in which the ions present in the electrode-electrolyte interface results in the development of the electrical double layers leading to the flow of electricity through the outer circuit. ***Batteries*** are electrochemical devices consisting of electrochemical cells that are made of cathode electrode, anode electrode, separator and an electrolyte. An electrochemical cell is a transducer device that converts the stored chemical energy into electrical energy by means of redox process. Generally, batteries are classified into two types, based on their working principles and usage, namely primary and

secondary batteries. Primary batteries are non-rechargeable that are designed to be used once; while secondary batteries are rechargeable that are designed to be used multiple numbering times.

1.3.1.1 Choice of batteries

As seen from **Figure 1.2**, capacitors have high power density but low energy density while fuel cells have high energy density and low power density. Most importantly, batteries are promising as their energy and power densities are moderately high, making them an attractive candidate for electric vehicle (EV) applications. For many years, Ni-Cd (Nickel Cadmium) batteries were used to power the portable electronics until the development of Ni-MH (Nickel metal hydride) and LIBs. Though both these rechargeable storage devices were progressing around at the same time (1990) LIBs outperformed Ni-MH as well as all the other existing storage technologies **Figure 1.3**, because of their salient features such as (i) high energy density, lightweight and design flexibility, (ii) no memory effect, (iii) low maintenance, (iv) prolong cycle life, (v) less self-discharge, (vi) less toxic and (vii) wide range of applications and operating temperature. The wide range of applicability of LIBs surpasses the worldwide values and sales of other batteries. For example, LIBs are used for 63% of the portable rechargeable batteries whereas Ni-Cd and Ni-MH batteries are only 23 and 14 % respectively. The above mentioned prominent features also explain why LIBs receive much more interest at both the research level and practical level applications. Adding to this, the choice of lithium-ion for rechargeable batteries is mainly attributed to its high electropositive behavior (-3.04 V vs. standard hydrogen electrode) and its

lightweight (6.94 g mol^{-1}) which gives rise to high energy density of the battery **Figure 1.3.**[6, 7]

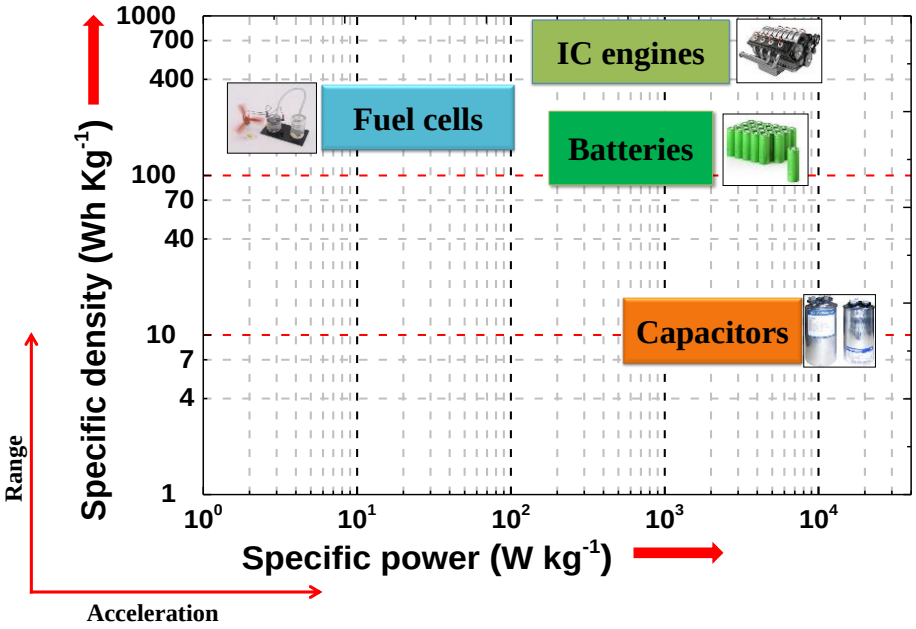

Figure 1.2 Ragone plot for electrochemical systems in comparison with conventional IC engines.[6]

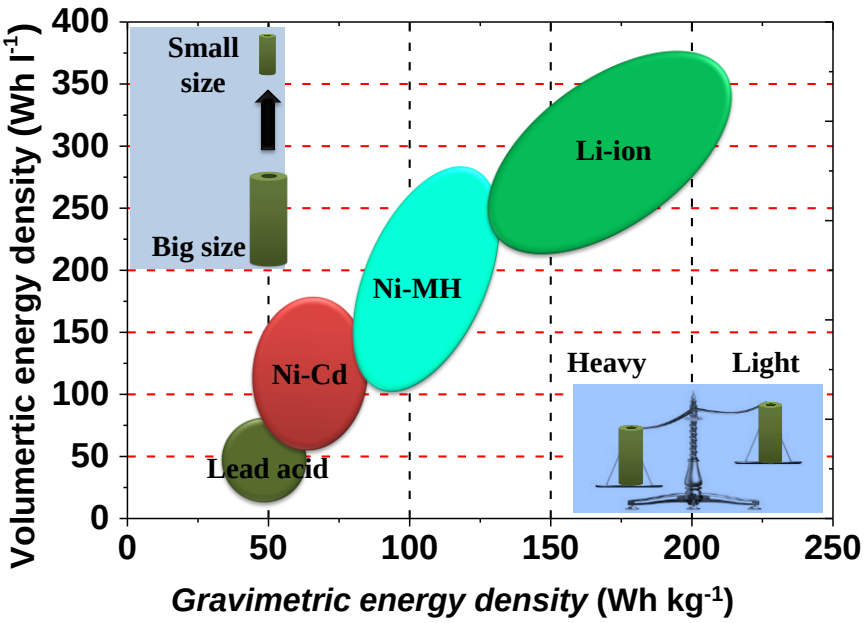

Figure 1.3 Comparison of the various rechargeable battery technologies in terms of gravimetric energy density and volumetric energy density.[7]

Having discussed the importance of LIB systems, the following section will focus on the role of LIBs in EV applications, operating principle of LIBs and followed by latest related research trends in electrode materials and electrolytes.

1.4 Lithium-ion batteries for electric vehicles

Among various applications of LIBs, the most important application in recent times has been its use in electric vehicles.

1.4.1 Electric vehicles

Electric vehicles (EVs) are zero emission vehicles in which the required energy is supplied by an on-board energy storage system for vehicular motion. The weight and volume of LIBs play crucial role for EV applications. Besides the weight and volume, LIBs must also fulfill the energy and power density[8] requirements for EV applications **(Figure 1.4)**. Energy density (Wh kg^{-1}) is the amount of energy stored per unit mass or volume while power density (W kg^{-1}) is defined as the maximum power that can be supplied per unit mass or volume. The range of electric vehicular motion is determined by the energy density while the acceleration of the vehicles is determined by its power density of the LIB systems. A successful on-board energy storage system for EV should satisfy the following requirements:

- Safety.
- Low cost.
- Durability.
- High energy density and power density.

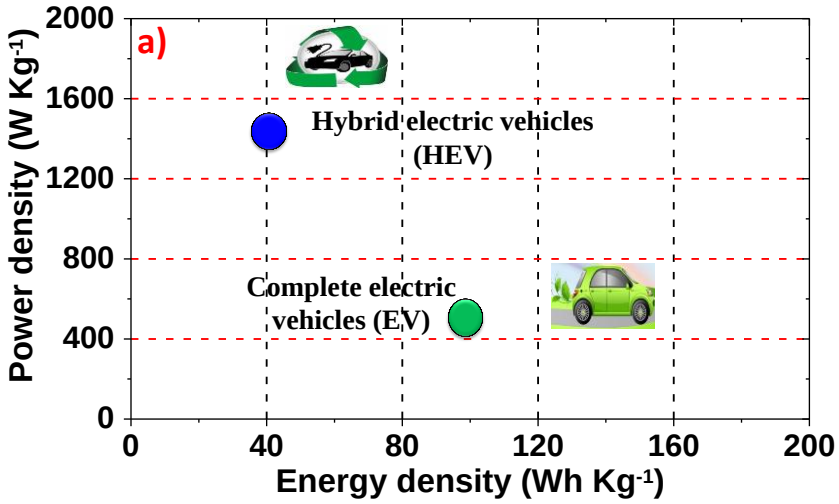

b)

Vehicles	Capacity of battery (in kWh)	Weight of battery (in kg)	Distance per charge (in km)	Speed (in km h^{-1})
Plug-in hybrid electric vehicles (HEV)	**5.6 - 18**	**60-200**	**10-60**	**>100**
Pure electric vehicles (EV)	**25-54**	**450**	**150-200**	**>100**

Figure 1.4 (a) Ragone plot for plug-in hybrid electric and complete electric vehicles in terms of energy density and power density of the lithium-ion battery and (b) Characterization of lithium-ion battery for plug-in hybrid electric and electric vehicles in terms of capacity of battery, weight of battery, distance per charge and optimum speed of the vehicle.[8, 9]

1.4.2 Lithium-ion battery

1.4.2.1 Operating principle

Rechargeable LIBs operate on the principle of intercalation/deintercalation in which the Li^+-ion are inserted/ extracted into/from the electrode material accompanied by the addition/removal of electrons. Typically, LIB is comprised of two electrochemically active materials namely cathode and anode electrodes soaked in liquid electrolyte which is an ionic conductor and an electronic insulator. Two electrodes are kept apart by a separator membrane to prevent electrical shorting. The

electrode at which redox reactions take place at higher potential is known as cathodes while the electrode at which the redox reactions occur at lower potential is known as anodes.

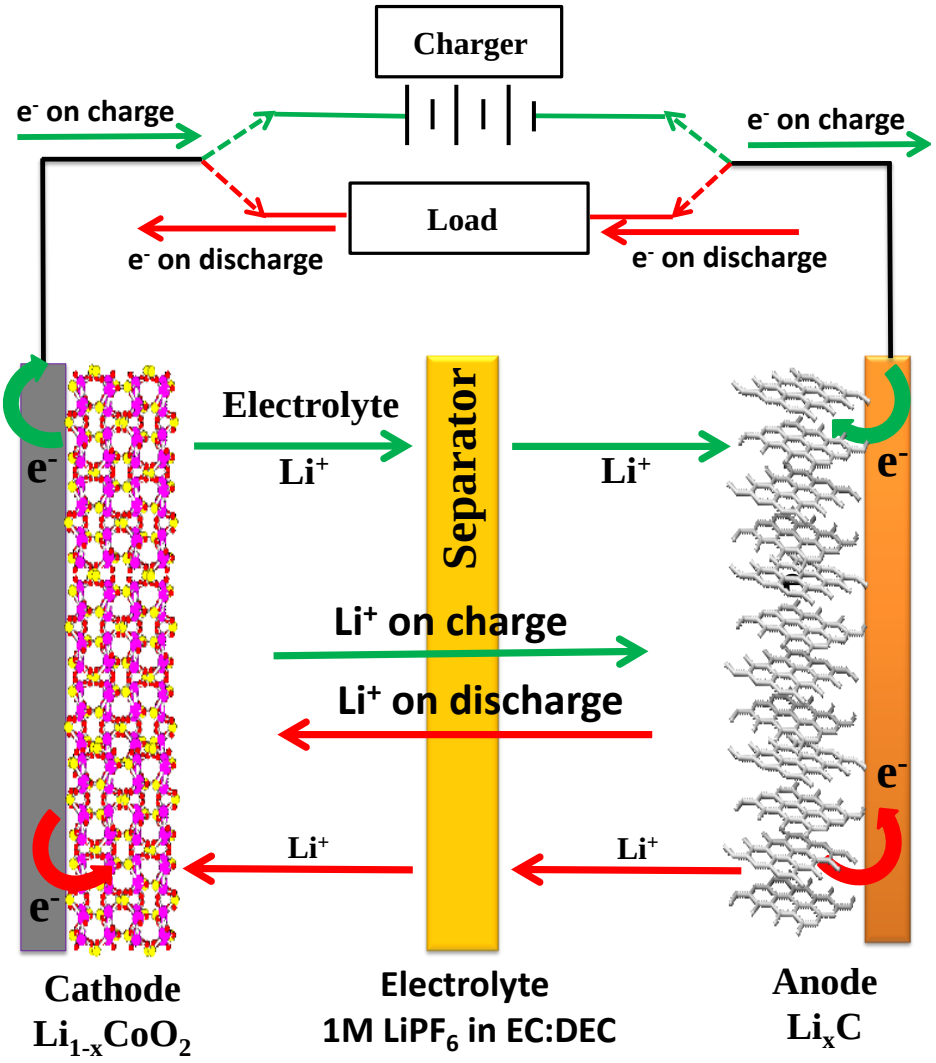

Figure 1.5 Schematic illustration of the operation of a lithium-ion battery.[7]

A battery's performance depends on the nature of the active material, operating temperature and the current drain.[10, 11] The electrical energy of a battery expressed either per unit of weight (Wh kg^{-1}) which is a product of specific capacity (Ah kg^{-1}), and voltage (V) of the battery or per unit of volume (Wh l^{-1}), both of which are completely dependent on the internal chemistry of a particular battery system.[10-13] The principle of operation of

LIBs is shown in **Figure 1.5**. For this pictorial representation, lithium cobalt oxide ($LiCoO_2$) and graphite (C_6) are chosen as cathode and an anode material respectively while lithium hexaflurophosphate ($LiPF_6$) in ethylene carbonate (EC) and diethyl carbonate (DEC) is chosen as the electrolyte. During charging, Li^+ ions extracted from the cathode travel through the electrolyte and get inserted into the anode. This is accompanied by the movement of electrons through external circuit to preserve the charge neutrality. The entire process is reversed during the discharge operation. Such shuttling of Li^+ ions between the cathode and anode is generally referred to as the *rocking chair concept* of the LIB. The redox reactions that occur at the cathode and anode side are summarized in the **Equations (1.1-1.3)**

At the cathode side: $$\boldsymbol{LiCoO_2 \rightleftharpoons Li_{1-x}CoO_2 + xLi^+ + xe^-} \quad \textbf{(1.1)}$$

At the anode side: $$\boldsymbol{C + xLi^+ + xe^- \rightleftharpoons Li_xC} \quad \textbf{(1.2)}$$

Overall reaction: $$\boldsymbol{LiCoO_2 + C \rightleftharpoons Li_xC + Li_{1-x}CoO_2 \ (x = 0.5)} \quad \textbf{(1.3)}$$

In **Equation 1.3**, the value of x is limited to 0.5 in $LiCoO_2$ and the reason behind this limitation will be discussed in section 1.6.1.1. The open circuit voltage (OCV) of the electrochemical cell is the difference in the electrochemical potentials of the cathode and anode material during the redox reaction and is given by the **Equation (1.4).**

$$\boldsymbol{E = -\frac{\Delta G^0}{nF} = \frac{\bar{\mu}_{Li_{Cathode}} - \bar{\mu}_{Li_{anode}}}{nF}} \quad \textbf{(1.4)}$$

where $\boldsymbol{E}$ is the open circuit voltage, $\boldsymbol{\Delta G^0}$ is the free energy associated with the redox reaction, $\boldsymbol{F}$ is the Faraday's constant (96485 C mol^{-1}), $\boldsymbol{n}$ is the number of electrons that are involved during the redox reaction and

μ $Li_{Cathode}$ and μ Li_{anode} are the electrochemical potentials of the cathode and anode material respectively.

Since the research work undertaken in this thesis mainly focuses on the cathode materials for LIBs, more emphasis on the literature survey is given to the cathode materials. However, relevant research works in anode materials and electrolytes are also discussed briefly. Some of the family of cathode materials investigated for LIBs is listed in **Table 1.1**. Adding to this, characteristics data for some the cathode materials are listed in **Table 1.2.**

Table 1.1 Families of cathode materials for lithium-ion batteries.

Lithium metal oxides	
Layered oxides	**Spinel oxides**
$LiCoO_2$ **$LiNiO_2$** **$Li(Ni_{1/3}Mn_{1/3}Co_{1/3})O_2$** **$Li(Ni_{1/2}Mn_{1/2})O_2$**	**$LiMn_2O_4$**
Polyanion-based materials	
Olivine phosphate	**Silicates**
$LiMPO_4$ (M=Fe, Mn, Co and Ni)	**Li_2MSiO_4 (M=Fe, Mn, Co and Ni)**
Pyrophosphates	**Borates**
$Li_2MP_2O_7$ (M=Fe and Mn)	**$LiMBO_3$ (M=Fe and Mn)**

Table 1.2 Characteristics of various cathode materials for lithium-ion battery.[14]

Structure	Cathode	Potential ~(V)	Practical capacity ~(mAh g^{-1})	Environmental concern	Cost	Structural stability	Safety
Layered	$LiCoO_2$	4	130-150	Acceptable	High	Stable up to 0.5 mole of lithium extraction	Acceptable
	$LiNiO_2$	4	220	Acceptable	High	Unstable	Acceptable
	$LiNi_{1/3}Mn_{1/3}Co_{1/3}O_2$	4	180-220	Acceptable	High	Stable	Acceptable
	$LiNi_{1/2}Mn_{1/2}O_2$	4	160-200	Acceptable	High	Stable	Acceptable
Spinel	$LiMn_2O_4$	4	130-145	Acceptable	Acceptable	Stable	Good
Olivine	$LiFePO_4$	3.45	150	Friendly	Low	Stable	Excellent
	$LiMnPO_4$	4.1	150	Acceptable	Acceptable	Stable	Excellent

1.5 Requirements of an ideal cathode material

- Li extraction/insertion must be highly reversible.
- High specific capacity.
- High redox potential.
- Stable operating voltage window.
- Should not react with the electrolyte.
- Low cost.
- Environmentally friendly.
- Preferably a high mixed conductor (both ionic and electronic).
- More than one mole of Li per formula unit.
- Stable handling in atmosphere (not hygroscopic, not air-sensitive).
- Simple and reproducible synthesis.

1.6 Research trend in cathode materials

1.6.1 Layered oxides

1.6.1.1 Lithium cobalt oxide ($LiCoO_2$)

Layered $LiCoO_2$ has been introduced by Goodenough *et al*.[15] as a potential cathode material for LIBs in late 1980's . $LiCoO_2$ has similar structure of α-$NaFeO_2$ with the lithium ions present in the octahedral sites of cubic closed-packed (CCP) lattices.[15] The crystal structure of $LiCoO_2$ is

shown in **Figure 1.6.** On complete extraction of Li^+ ions, a hexagonal close-packed (hcp) framework is formed owing to the rearrangement of oxygen layers in CoO_2.[16] The theoretical capacity of $LiCoO_2$ is ~274 mAh g^{-1} assuming complete removal of Li^+ ions from layered structure.[17] However, only 0.5 moles of Li^+ could be removed due to structural changes in the $LiCoO_2$, resulting in a low practicable capacity of ~130 mAh g^{-1} at 4.2 V *vs.* Li/Li^+.[17, 18, 19] The electrochemical reaction of layered $LiCoO_2$ with lithium in the half cell is described in **Equation 1.5. Figure 1.7** shows a typical voltage profile of commercial layered $LiCoO_2$ cycled between the voltage windows of 3.0-4.3 V at room temperature. It exhibits an average redox potential of approximately 3.9 V with the discharge capacity of 124 mAh g^{-1}. $LiCoO_2$ shows a high Li^+ ion diffusion of 5 x 10^{-9} cm^2 s^{-1} and such high diffusivity helps to achieving good cyclic performance.[16] The electronic conductivity of $LiCoO_2$ varies significantly with Li^+-ion extraction which turns it into a semiconductor at x = 1, and also it behaves like a metal at x = 0.6 (x is the number of mole of Li^+ ion). Extraction of Li^+ ions, from $LiCoO_2$ changes the layered structure to hexagonal closed-packed CoO_2.[16] Several structural changes exist between lithiated $LiCoO_2$ and delithiated CoO_2 phases during charging above 4.5 V which limits the high current rate applications of this material. The CCP oxygen layers move from ABCA to ABA stacking arrangement, thus causing a structural change. Owing to these limitations, one could not attain capacities above 170 mAh g^{-1}.[20] A significant increment in the capacity about 170 mAh g^{-1} when cycled between 2.75 - 4.4 V has been achieved by doping (Al^{3+}, Mg^{2+} and Fe^{2+}) and coating a metal oxide or phosphate on the surface of the particles.[21-25] Several other research groups

have also investigated extensively on enhancing safety, cyclability and energy density.[26-28] SONY corporation commercialized its first LIB which contains $LiCoO_2$ as a cathode and carbon as an anode.[29, 30] Though $LiCoO_2$ has been successfully commercialized, its toxicity, high cost, limited availability and safety concerns have paved way for developing alternate cathode materials.

$$\boldsymbol{LiCoO_2 \leftrightharpoons Li_{1-x}CoO_2 + xLi^+ + xe^-} \qquad \textbf{(1.5)}$$

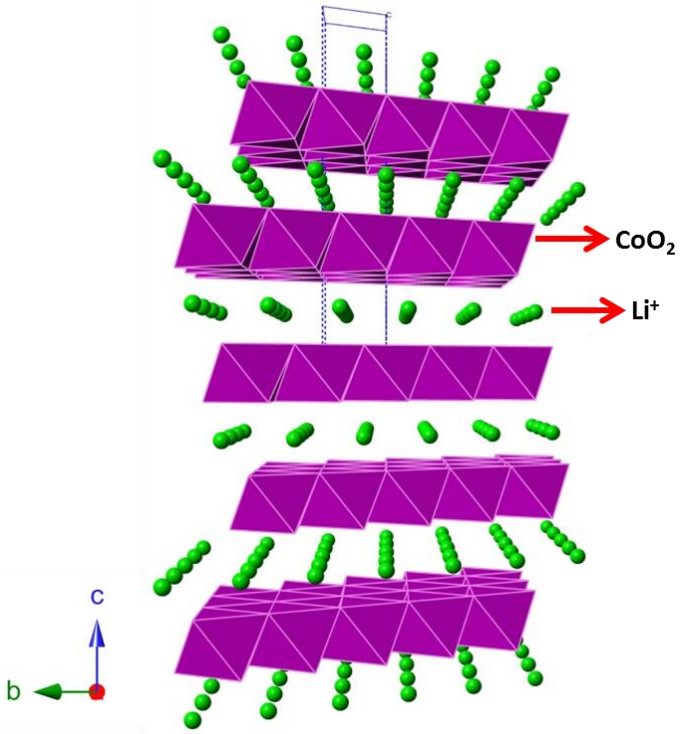

Figure 1.6 Crystal structure of $LiCoO_2$ with space group $R\bar{3}m$.[31]

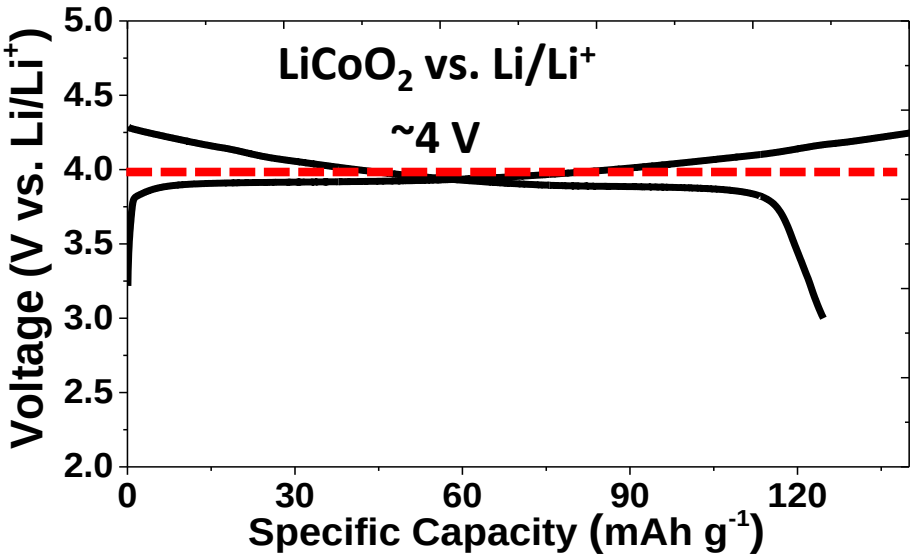

Figure 1.7 A typical voltage profile of commercial layered $LiCoO_2$ *vs.* Li/Li^+.

1.6.1.2 Lithium nickel oxide ($LiNiO_2$)

The structure of $LiNiO_2$[28, 32] is similar to $LiCoO_2$ which has the theoretical capacity of 274 mAh g^{-1} assuming complete removal of lithium ions from the crystal structure. Adding to this, Ni is quite abundant compared to Co.[32-34] The electrochemical reaction of $LiNiO_2$ with lithium in the half cell is shown in **Equation 1.6.** The diffusion of Li^+ ions in $LiNiO_2$ ($6x10^{-6}$ cm^2 s^{-1}) is much higher compared to $LiCoO_2$ (5×10^{-9} cm^2 s^{-1}) which favors high current rate operation.[35] However, the practical capacities are in the range 150-160 mAh g^{-1} in the voltage window 2.5 V- 4.1 V.[17] Most importantly, using pure $LiNiO_2$ as a cathode in batteries has been challenging as excess stoichiometry of Ni in the structure is generally observed after synthesis of this compound.[36] Excess of Ni^{2+} ions in the lithium layer clips the NiO_2 layers together resulting in a blockage for the Li^+-ion mobility and suppresses the rate capability of the material.[37] Further, after extraction, Ni^{3+} ions in the lithium ion layer exhibit a strong repulsive force during insertion which stops the deintercalation of Li^+-ion in the lattices.[33] Pure $LiNiO_2$ shows poor thermal

stability with strong exothermic peaks observed at 200 ºC.[38] Several groups have attempted to surmount the drawbacks of $LiNiO_2$ by doping experiments using elements namely Al^{3+}, Ga^{2+}, Ca^{2+}, Mg^{2+}, Ti^{4+}, Mn^{2+}, Fe^{2+}, Nb^{5+} and Co^{2+} respectively. Amongst them, Co^{2+} and Al^{3+} doped $LiNiO_2$ showed significant improvement in the thermal stability and in stabilizing the structure of $LiNiO_2$.[39, 40]

$$\boldsymbol{LiNiO_2 \rightleftharpoons Li_{1-x}NiO_2 + xLi^+ + xe^-} \quad \textbf{(1.6)}$$

1.6.1.3 Mixed transition metal layered oxides ($LiNi_{1/2}Mn_{1/2}O_2$ and $LiNi_{1/3}Mn_{1/3}Co_{1/3}O_2$)

Mixed transition metal layered oxide has received much interest in the past decade as potential cathode materials. Layered $LiNi_{1/2}Mn_{1/2}O_2$ was first reported by Dahn *et al*.[41,42] The theoretical capacity of this layered compound is ~280 mAh g^{-1} based on one electron transfer per formula unit.[43] Further, this layered oxide delivers capacities of only ~200 mAh g^{-1} in the voltage window 2.5 - 4.5 V with much better rate capability.[44-49] Layered $LiNi_{1/3}Mn_{1/3}Co_{1/3}O_2$ was first reported by Ozhuku *et al*.[50] The theoretical capacity of $LiNi_{1/3}Mn_{1/3}Co_{1/3}O_2$ is 278 mAh g^{-1}. This mixed layered oxide delivers capacity of ~200 mAh g^{-1} with better rate capability in the voltage window 2.5 - 4.6 V compared to other layered oxide compounds discussed.[51-57] The overall electrochemical reactions of $LiNi_{1/2}Mn_{1/2}O_2$ and $LiNi_{1/3}Mn_{1/3}Co_{1/3}O_2$ with lithium in the half cell are shown in **Equation 1.7-1.8** respectively**.**

$$\boldsymbol{LiNi_{0.5}Mn_{0.5}O_2 \rightleftharpoons Li_{1-x}Ni_{0.5}Mn_{0.5}O_2 + xLi^+ + xe^-} \quad \textbf{(1.7)}$$

$$\boldsymbol{LiNi_{1/3}Mn_{1/3}Co_{1/3}O_2 \rightleftharpoons Li_{1-x}Ni_{1/3}Mn_{1/3}Co_{1/3}O_2 + xLi^+ + xe^-} \quad \textbf{(1.8)}$$

1.6.2 Spinel oxides

1.6.2.1 Lithium manganese oxide ($LiMn_2O_4$)

Unlike two dimensional layered lithium hosts namely $LiCoO_2$ and $LiNiO_2$, manganese based compound does not form layered $LiMnO_2$, it forms three dimensional spinel structure $LiMn_2O_4$. Spinel $LiMn_2O_4$ have been strongly pursued as cathodes primarily because of the high operating potential and high storage capacity.[40, 58, 59] The original work was first proposed by Thackeray *et al*.[60] and then later established by Bellcore Labs.[61]

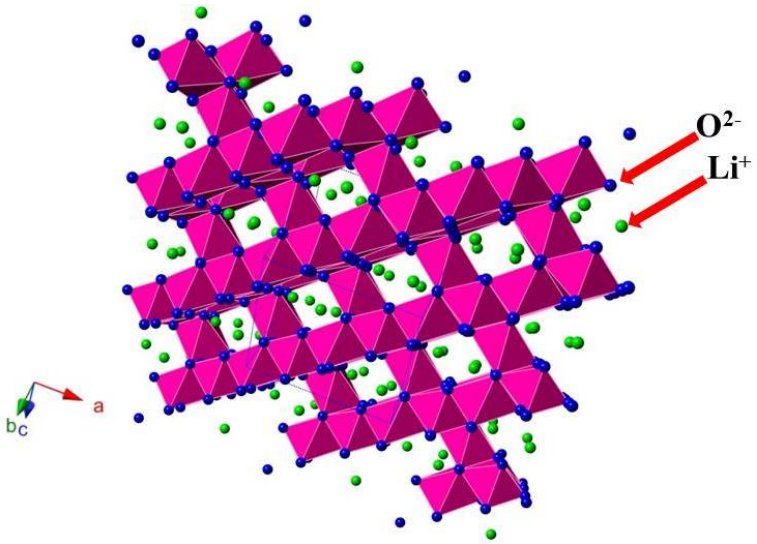

Figure 1.8 Crystal structure of $LiMn_2O_4$ with the space group.[60]

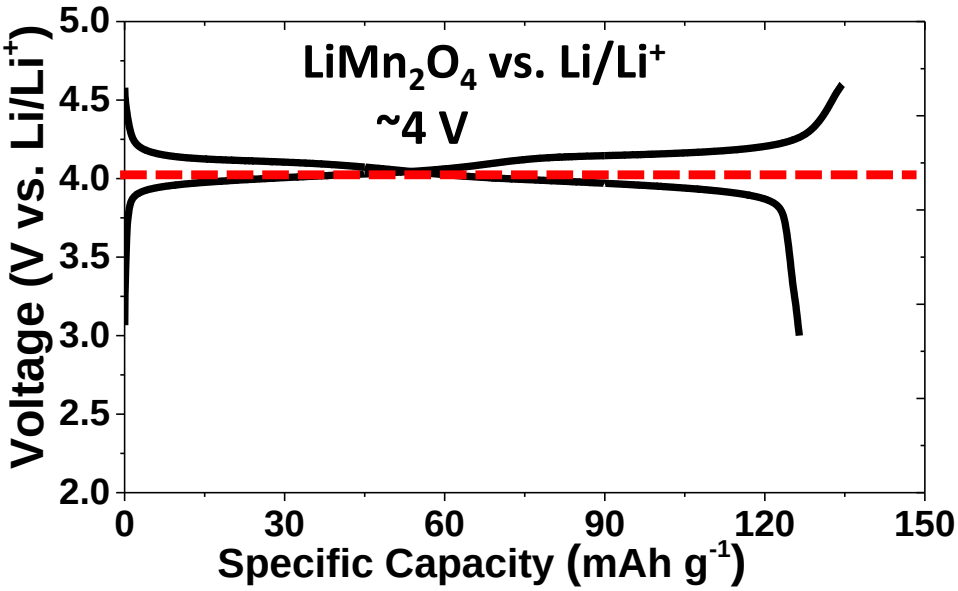

Figure 1.9 A typical voltage profile of commercial spinel $LiMn_2O_4$ *vs.* Li/Li^+.

The general molecular formula of spinel oxides are $A[B_2]X_4$ in which A is the occupancy of cations in the tetrahedral sites while B is the occupancy of cations in the octahedral sites and X represents the anions in the tetrahedral sites.[62, 63] The crystal structure of spinel $LiMn_2O_4$ is shown in **Figure 1.8**. This can be described as face-centered cubic close-packed oxygen in which lithium and manganese occupy 8a tetrahedral sites and 16a octahedral sites. Lithium ions in tetrahedral sites could be reversibly extracted and inserted which transforms cubic $LiMn_2O_4$ to cubic λ-MnO_2. On the other hand, when more lithium ions extracted and inserted into 16c octahedral sites at redox potential ~2.8 V reversibly, cubic $LiMn_2O_4$ transforms to lithium rich tetragonal structure. The overall electrochemical redox reaction is given below in **Equation 1.9**,[64, 65]

$$\underset{Tetragonal}{Li_2Mn_2O_4} - Li^+ - e^- \rightleftharpoons \underset{Cubic}{LiMn_2O_4} \rightleftharpoons \underset{Cubic}{\lambda MnO_2} + Li^+ + e^- \quad \textbf{(1.9)}$$

The extraction of Li^+ ions at 4.0 V is escorted by the phase formation of delithiated $Li_{1-x}Mn_2O_4$ due to the ordering of Li^+ ions in the tetrahedral sites while at 2.8 V remaining Li^+ ions are inserted into the empty octahedral sites resulting in an asymmetric lattice distortion. This lattice distortion is caused by the Jahn-Teller distortions of the Mn^{3+} ions which results in the phase transition from cubic phase to tetragonal phase.[66]

Spinel $LiMn_2O_4$ has the following limitations

- Mn dissolution in the electrolyte owing to disproportionation of Mn^{3+} ions and then Mn^{2+} ions get reduced on the surface of anode.[67, 68]
- Jahn-Teller distortion of Mn^{3+} ions.[69, 70]
- Instability of cubic $Li_xMn_2O_4$ ($x<0.1$) transforming to λ-MnO_2 due to complete extraction of lithium ions.[71, 72]

Further, at high temperature operation (>50 °C), it exhibits the capacity fading.[73] Considerable effects have been made to enhance the cyclability of $LiMn_2O_4$ by doping (Li^+, Ni^{2+}, Mg^{2+}, Co^{2+}, Zn^{2+} and Al^{3+}), surface coating ($AlPO_4$), changing the $LiPF_6$ electrolyte to LiBOB (lithium bis(oxalato)borate) and electrolyte additives.[33, 73-82] Spinel $LiMn_2O_4$ has been considered to be a promising next generation cathode material owing to the fact that it is cheap and environmental friendly compared to layered $LiCoO_2$ and $LiNiO_2$ and offers a higher nominal potential of 4.0 V with the theoretical capacity of 148 mAh g^{-1}.[83, 84] However, it delivers a capacity of ~130 mAh g^{-1} only. **Figure 1.9** shows the charge and discharge profile of spinel cycled between the voltage windows of 3.0-4.6 V at room temperature. It exhibits a redox potential of ~4.0 V with the discharge capacity of ~126 mAh g^{-1}.

1.6.3 Olivine phosphates

1.6.3.1 Lithium iron phosphate ($LiFePO_4$)

The intrinsic toxicity, high cost and chemical instability along with the safety issues of layered $LiCoO_2$ has triggered serious research towards alternative cathode materials which contains iron and manganese transition metals polyanion-based compounds. The major breakthrough in this aspect was the by Padhi *et al.*[13, 85] olivine structured $LiFePO_4$.[13, 86] This material satisfies all the above mentioned demands of a potential cathode material for high energy density LIBs.[86] Its strong covalent P-O bonds which ensures intrinsic structural stability and limit the release of oxygen during the cycling unlike layered oxide cathodes.[87 88] This Fe-containing polyanion offers lower redox potential for the redox couples by an inductive effect.[13] Furthermore, the relative abundance of Fe and P on the earth's crust has favored the commercialization of this battery material.[88] However, it suffers from low electronic conductivity (~10^{-9} S cm^{-1} at room temperature).[89-91] The crystal structure of olivine $LiFePO_4$ is shown in **Figure 1.10**. In $LiFePO_4$, the O^{2-} ions are connected to the P^{5-} ions by strong covalent bond. The olivine structure contains a distorted hexagonal close-packing of oxygen anions with three cations occupying the interstitial sites namely corner-sharing FeO_6 octahedra perpendicular to the *a* axis, edge-sharing LiO_6 octahedra aligned in parallel along the *b* axis and tetrahedral PO_4 groups connecting neighboring planes.[92, 93] $LiFePO_4$ exhibits a theoretical capacity of 170 mAh g^{-1} with a flat voltage profile at ~3.45 V vs. Li/Li^+ resulting in a specific energy of 586 Wh kg^{-1} (170 mAh g^{-1} x 3.45 V) which is as good as conventional layered $LiCoO_2$.[94] **Figure 1.11** shows the typical voltage profile of in-house synthesized olivine $LiFePO_4$

cycled between the voltage windows of 2.3 - 4.3 V at room temperature. In phospho-olivine, there is co-existence of two phases,[95-97] resulting in a flat voltage profile with the discharge capacity of ~165 mAh g^{-1} (**Figure 1.11**), and this property feature is the unique of this cathode material. The overall electrochemical redox reaction of $LiFePO_4$ is given below in **Equation 1.10.** Initially, high capacity at high current rate was thought to be almost impossible due to the sluggish kinetics.[98-100] Considerable improvements in the lithium storage performance of $LiFePO_4$ have been realized by carbon coating,[101-107] reducing the particle in nano-meter scale,[94, 102, 106, 108-111] reducing b-axis thickness,[102, 106, 112] substitution of cations in Li^+ sites,[110, 113] cations substitution in transition metal sites,[92, 93, 114-117] carbothermal reduction of $LiFePO_4$ with carbon on the surface,[118] and off-stoichiometry of active material with conductive phase on the surface of the particles.[119]

$$\boldsymbol{LiFePO_4 \rightleftharpoons Li_{1-x}FePO_4 + xLi^+ + xe^-} \qquad \textbf{(1.10)}$$

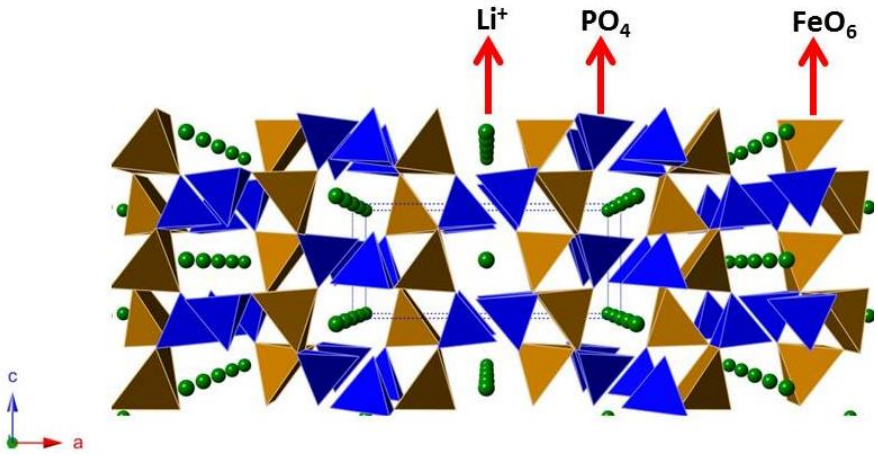

Figure 1.10 Crystal structure of olivine-phosphate $LiFePO_4$.[88]

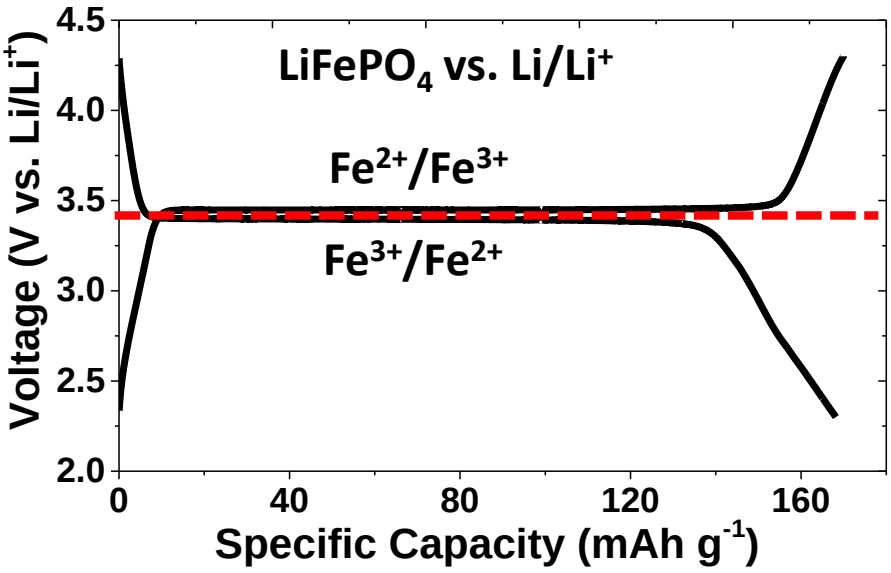

Figure 1.11 A typical voltage profile of in-house synthesized $LiFePO_4$ *vs.* Li/Li^+.

1.6.3.2 Lithium manganese phosphate ($LiMnPO_4$)

Olivine $LiMnPO_4$ offers a competitive gain in specific energy of 701 Wh kg^{-1} (171 mAh g^{-1} x 4.1 V) owing to its Mn^{2+}/Mn^{3+} redox couple potential around 4.1 V vs. Li/Li^+, which is ~0.65 V higher than that of $LiFePO_4$ and importantly compatible with the commercial electrolytes unlike high potential cathodes such as $LiCoPO_4$ and $LiNiPO_4$.[13, 90, 108, 120-125] The crystal structure of olivine $LiMnPO_4$ is shown in **Figure 1.12**. The O^{2-} ions are connected to the P^{5-} ions by strong covalent bond. The olivine structure contains a distorted hexagonal close-packing of oxygen anions with three cations occupying the interstitial sites namely corner-sharing MnO_6 octahedra, edge-sharing LiO_6 octahedra and tetrahedral PO_4 groups connecting neighboring planes.[13, 85] The overall electrochemical redox reaction of $LiMnPO_4$ is given below in **Equation 1.11**. Despite high OCV, the current durability in $LiMnPO_4$ is orders of magnitude lower to that in $LiFePO_4$, thus the effective energy density of $LiMnPO_4$ is smaller than that of $LiFePO_4$.[89, 90, 126] Futher, deploying

$LiMnPO_4$ as cathode material in lithium-ion batteries pose many serious challenges such as (i) poor electronic conductivity (~$3x10^{-9}$ S cm^{-1} at 300 °C) and ionic diffusivity,[89, 91, 127, 128] (ii) strong polarons,[127] (iii) Jahn-Teller distortion in charged state[129] and (iv) interfacial strain between the $LiMnPO_4$ and $MnPO_4$ phases.[130] Previous reports in the literature [13, 94, 131, 132] have also suggested that a complete extraction of Li^+-ion from $LiMnPO_4$ is not possible. All these factors lead to poor lithium storage performance in $LiMnPO_4$. This has led to the research to focus on improving the performance $LiFePO_4$ rather than using higher potential $LiMnPO_4$. More than thausands of papers have been published on $LiFePO_4$ in the past 10 years. On the other hand, literature for promising $LiMnPO_4$ cathode is limited. To improve the storage performance, various groups have devised different synthetic approaches such as sol-gel method,[108, 133] polyol method,[121] soft template method,[134, 135] solvothermal,[136] spray pyrolysis with wet ball milling,[137-139] ultrasonic spray pyrolysis,[140] direct precipitation,[141] solid state reactions in molten hydrocarbon,[142] hydrothermal,[143-146] microwave-hydrothermal[147] and off-stoichiometry methods.[148] Despite these efforts, only few groups have attained storage capacity of more than 120 mAh g^{-1} in $LiMnPO_4$ [108, 121, 133, 137, 140-145, 147, 149-154] by employing Constant Current-Constant Voltage (CCCV) mode of charging in which the cells are fully charged and held at the upper cut-off voltage for a long time. **Figure 1.13** represents the voltage profile of in-house synthesized $LiMnPO_4$ *vs.* Li/Li^+ cycled between the voltage windows of 2.3 - 4.6 V at room temperature, the redox potential is ~4.0 V higher than that of $LiFePO_4$ (~3.45 V).[134, 135 13, 90] Though, the theoretical capacity of $LiMnPO_4$ is

170 mAh g^{-1}, in practice achieving maximum capacity of pure $LiMnPO_4$ is yet challenging.[134]

$$LiMnPO_4 \rightleftharpoons Li_{1-x}MnPO_4 + xLi^+ + xe^- \quad (1.11)$$

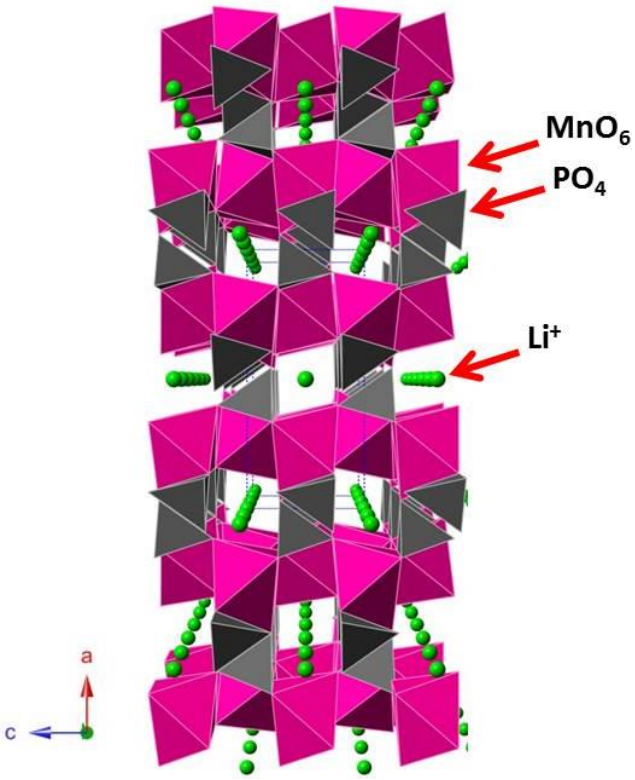

Figure 1.12 Crystal structure of olivine-phosphate $LiMnPO_4$.[155]

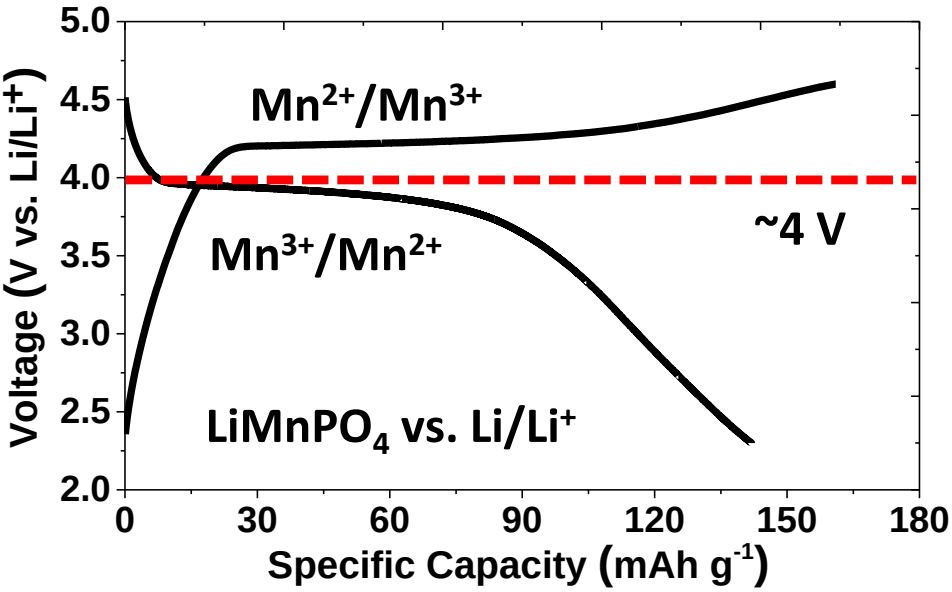

Figure 1.13 A typical voltage profile of in-house synthesized $LiMnPO_4$ *vs.* Li/Li^+.[134]

1.6.3.3 Multicomponent olivine phosphate

(a) $LiMn_{1-x}Fe_xPO_4$ solid solution

Nano-structuring, carbon coatings, and synthesizing the material in favorable morphology have helped in enhancing the electrochemical performance of $LiMnPO_4$.[134, 156-159] Besides this, the electrochemical performances of $LiMnPO_4$ have also been enhanced by forming solid solutions containing various transition metals especially Fe^{2+} substitution.[136, 160-162] The mixed transition metal phospho-olivine $LiMn_xFe_{1-x}PO_4$ has drawn considerable attention as it exhibits improved bulk conductivity.[163-167] Several reports on the electrochemical performance of $LiMn_xFe_{1-x}PO_4$ (x = 0.25, 0.50 and 0.75) solid solution have reported that the manganese rich [$LiMn_xFe_{1-x}PO_4$ (x > 0.75)] component are not appropriate cathode material for LIBs owing to its sluggish manganese activity and huge anisotropic distortion of Mn^{3+} in the charge state.[13, 120, 131, 160, 168, 169] In contrast, the latest report by Martha *et al.*[161] and Wang *et al.*[170] have demonstrated that the Mn rich component [$LiMn_xFe_{1-x}PO_4$ (x = 0.8 or 0.75)] can be an excellent advanced cathode material for LIBs. Further, a study on $LiMn_xFe_{1-x}PO_4$ by Molenda *et al.*[164, 171] evidently shows manganese is more electrochemically active and better utilization of Mn rich mixed Mn-Fe transition metal phospho-olivine than $LiMnPO_4$ owing to its lower activation energy and enhanced bulk conductivity.[124, 171, 164] The theoretical work by Seo *et al.*[172] revealed that the substitution of transition metal ions in $LiMnPO_4$ could suppress the Jahn-Teller distortion and enable faster mobility of electrons which is localized in Mn^{3+} ions. Furthermore, the ratios of Fe and Mn in the solid solution have been to have shown positive influence on the rate performance.[161, 166] Adding to this, $LiFe_{1-x}Co_xPO_4$,

$LiMn_{1-x}Co_xPO_4$ and $LiCo_{1/3}Mn_{1/3}Fe_{1/3}PO_4$ solid solutions are also promising owing to the higher redox potential of Co^{2+}/Co^{3+} redox couple (~ 4.8 V), thus increasing the energy density.[160, 173]

(b) Redox shift in $LiMn_xFe_{1-x}PO_4$ solid solution

The changes in the overall cell potential and energy density of multicomponent $LiMn_{1-x}Fe_xPO_4$/C solid solution could be demonstrated by schematic **Figure 1.14**. The amount of Mn^{2+}/Mn^{3+} redox in the electrode composition decides the energy density and the overall cell voltage.[160]

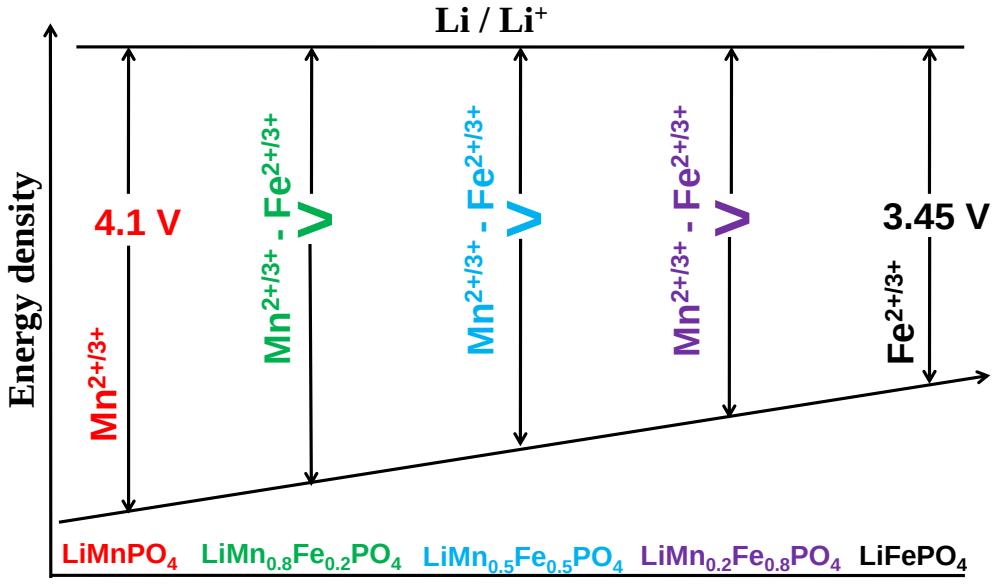

Figure 1.14 Positions of the Mn^{2+}/Mn^{3+} and Fe^{2+}/Fe^{3+} redox couples with respect to that of Li/Li^+.[160]

Figure1.15 shows the typical voltage profile of $LiMn_xFe_{1-x}PO_4$ (x = 0, 0.2, 0.50 and 0.8) *vs.* Li/Li^+ in which distinct plateaus corresponding to the Mn^{2+}/Mn^{3+} and Fe^{2+}/Fe^{3+} redox couples are seen. The huge reduction in the voltage polarization compared to $LiMnPO_4$, especially at Mn^{2+}/Mn^{3+} redox region and improved electrochemical performance could be attributed to Fe-O-Mn superexchange interaction, lower activation energy and electronic

configuration of Mn^{2+} ($3d^5$) and Fe^{2+} ($3d^6$) of solid solution phospho-olivines.[13, 120, 134, 164, 171, 174]

The overall electrochemical redox reaction of mixed-transition metal $LiMn_xFe_{1-x}PO_4$ is given below in **Equation 1.12**.

$$LiMn_xFe_{1-x}PO_4 \rightleftharpoons Li_{1-y}Mn_xFe_{1-x}PO_4 + yLi^+ + ye^- \qquad (1.12)$$

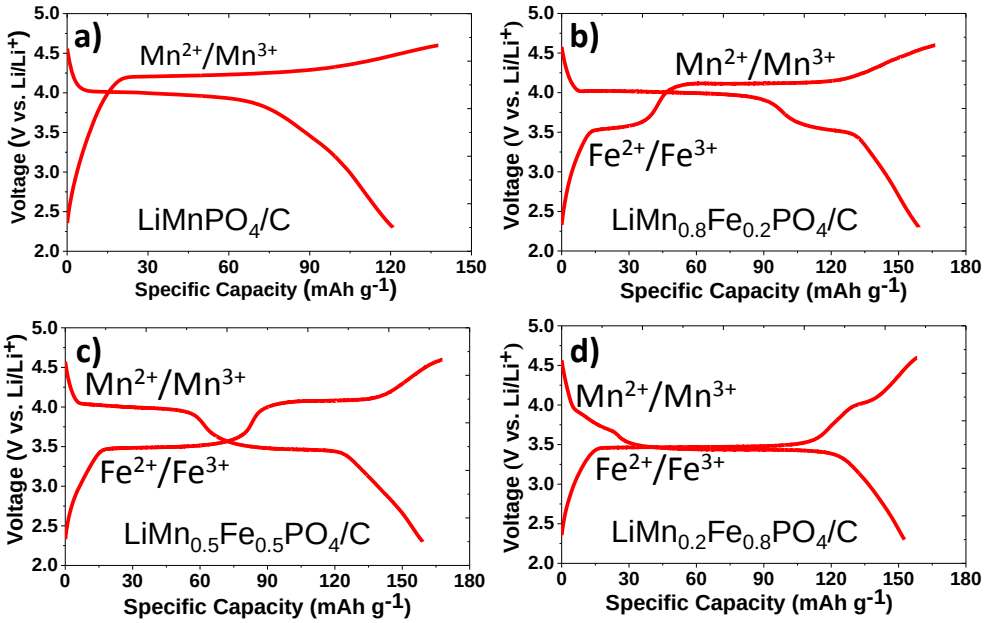

Figure1.15 A typical voltage profiles of in-house synthesized $LiMn_xFe_{1-x}PO_4$ (x = 0, 0.2, 0.50 and 0.8) *vs.* Li/Li^+.[175]

(c) $LiMn_{1-x}M_xPO_4$ (M = Cation doping)

Partial substitution of cations enables to enhance the storage performance of $LiMnPO_4$ without compromising on the energy density significantly as the presence of dopant is much smaller and is not reflected in the voltage profiles.[135, 137, 150, 151, 176-182] Kim *et al.*[180] demonstrated the nucleation enhancer concept in enhancing the lithium storage performance of $LiMnPO_4$ cathode by co-doping with Fe^{2+} and Mg^{2+}. Chen *et al.*[176, 178] showed that the presence of cations in the $LiMnPO_4$ improved the conversion of delithiated phase. Further, Mg^{2+} doping improved the structural stability of the

delithiated phase. Lee *et al.*[177], Yang *et al.*[183] , Yi *et al.*[181] and Shiratsuchi *et al.*[151] demonstrated the effect of various cation substitution (M=Mg^{2+}, Ca^{2+}, V^{3+}, Fe^{2+}, Co^{2+}, Gd^{3+}, Ti^{3+} and Zr^{4+}) in enhancing the electrochemical performance of $LiMnPO_4$.

1.6.3.4 Lithium cobalt and nickel phosphate ($LiCoPO_4$ and $LiNiPO_4$)

In general, the redox potential of M^{2+}/M^{3+} (M= Ni > Co > Mn > Fe) redox couple varies based on the inductive effect between transition metals and P-O bonding in olivine phosphate.[13, 90, 184, 185] Further, the redox potential of various polyanion based intercalation compound was predicted using ab-initio calculation.[186, 187] Potential limitation of $LiFePO_4$ paved way to investigate high voltage olivine cathode such as $LiCoPO_4$ and $LiNiPO_4$. The redox potential of $LiCoPO_4$ and $LiNiPO_4$ are 4.8 and 5.1 V *vs.* Li/Li^+ respectively.[185, 188-190] Despite this merits, the redox potential of $LiCoPO_4$ and $LiNiPO_4$ cathode material are too high for oxidation potentials of existing electrolytes.[184] The theoretical energy density of $LiCoPO_4$ is 800 Wh g^{-1} by the virtue of capacity 167 mAh g^{-1} and Co^{2+}/Co^{3+} redox couple ~4.8 V *vs.* Li/Li^+.[185, 189-194] Amine *et al.*[185] showed a lithium storage perforamance of 70 mAh g^{-1} with the redox potential of ~4.8 V. This poor discharge capacity is attributed to the low intrinsic electronic and ionic conductivity and also due to the low oxidation potential of exiting electrolyte. Yang *et al.*[193] demonstrated that the enhancement in the electronic conductivity by carbon coating is difficult in $LiCoPO_4$ unlike $LiFePO_4$ and $LiMnPO_4$. Rabanal *et al.*[195] showed the improvement in the ionic diffusivity of $LiCoPO_4$ by ball milling approach. Han *et al.*[196] simplified the synthesis process by ball mill assited microwave heating. Lloris *et al.*[190] demonstrated an enhanced discharge capacity of 125

mAh g^{-1} using excess lithium sources during the synthesis. Further, the lithium storage performance of $LiCoPO_4$ is improved by partial substitution of Fe or V.[173, 196] Bramnik *et al.*[197] showed that the completely delithiated phase appears to be unstable and undergoes amorphization. The phase transitions are reversible, but the slow kinetics accompanied with the electrolyte decomposition contributed to the capacity loss upon cycling. Markevich *et al.*[198] demonstrated the reason for capacity fading of $LiCoPO_4$ in 1M $LiPF_6$ EC: DMC electrolyte solution by spectroscopy studies. The poor lithium storage perofromance of $LiCoPO_4$ is due to the nucleophillic attack of F^- on the P atoms, resulting in deformation of P-O bonds. Considerable research needs to be done to find out a higher oxidation potential electrolyte for high voltage $LiNiPO_4$ (5.1 V) material.[184, 192, 199] Hence, high voltage olivine phosphates could be used for relevant applications only if right electrolytes are developed in the future.The overall electrochemical redox reaction of high potential $LiCoPO_4$ and $LiNiPO_4$ is given below in **Equation 1.13**.

$$\boldsymbol{LiMPO_4 \rightleftharpoons Li_{1-x}MPO_4 + xLi^+ + xe^- (M = Co\ and\ Ni)} \qquad \textbf{(1.13)}$$

1.6.4 Lithium metal silicates

Polyanion-based transition metal compound have been considered as an alternative to the existing toxic and expensive intercalation layered cathode material, due to their thermal stability and also their inherent safety which arises from the strong oxygen bonding (covalent bond) within the polyanion. Besides this, the possibility of high redox potential due to inductive effect is also an attractive feature of polyanion cathode materials.[13] Among various polyanion-based compounds, $LiFePO_4$ is the most studied cathode material. However, the lithium storage capacity is limited to 170 mAh g^{-1} and redox

potential about 3.45 V.[13, 106] Recently, silicate-based cathode materials, Li_2MSiO_4 (M = Fe, Mn, Co and Ni) have been proposed as an attractive cathode material.[200-203] These compounds are related to the orthorhombic Li_3PO_4 structure and belong to the large family of tetrahedral structure which exhibits rich polymorphism.[186, 201-206] Adding to this, being highly abundant, cost effective, environmental friendly, safe and thermally stable, the possibility of exchanging two moles of lithium ions in Li_2MSiO_4 with theoretical capacity of 333 mAh g^{-1} (assuming 2 moles Li^+ ions extraction) has attracted much research within the battery community.[207-212] Among the silicate cathodes, Li_2FeSiO_4 and Li_2MnSiO_4 are more attractive than other cathode members.[201, 204, 210, 213-216] Most commonly, $Si(OC_2H_5)_4$ (TEOS), $Li(CH_3COO)$, and transition metal acetates/oxalates were used as precursors to synthesize these compounds.

1.6.4.1 Lithium iron silicate (Li_2FeSiO_4)

Lithium iron silicate is relatively cheap compared to lithium iron phosphate owing to cheap elements such as Fe and Si in the compound and it has very stable structure owing to covalently bonded Si-O.[201, 203, 204, 210] However, realistic oxidation state of Fe will be between Fe^{2+} and Fe^{3+},[203, 217] the theoretical capacity of Li_2FeSiO_4 is limited to ~170 mAh g^{-1} and its relatively low practical potential (2.8 V after the first cycle), leading to the energy density of ~480 Wh kg^{-1}.[216, 218-222] The overall electrochemical redox reaction of Li_2FeSiO_4 is given below in **Equation 1.14**. Further, the synthesis of pure Li_2FeSiO_4 is not facile owing to rich polymorphs.[206, 216, 219, 223-225] Hence, rapid synthesis of pure lithium iron silicates with good electrochemical performances still remains a challenge. The substitution of other transition

metal which can undergo transition from $M^{2+}/M^{3+}/M^{4+}$ is required to facilitate the removal of two moles of Li^{+} ions and accompanied by $2e^{-}$ transfer.[220, 223, 226] On the other hand, manganese has three realistic oxidation states $Mn^{2+}/Mn^{3+}/Mn^{4+}$ and results in extraction of 2 moles of lithium ions. Most of the experimental studies have shown that though the manganese has $Mn^{2+}/Mn^{3+}/Mn^{4+}$ transitions, they appear to occur only on charging. The potential curve observed on the subsequent reduction cycle has a capacity fading, suggesting that the structural change during charging cycle.[200, 203]

$$\boldsymbol{Li_2FeSiO_4 \leftrightharpoons Li_{2-x}FeSiO_4 + xLi^{+} + xe^{-}} \qquad \textbf{(1.14)}$$

Solid state reaction is the most commonly used method for synthesizing these materials which includes grinding and calcining the starting materials at high temperature. Orthosilicate such as Li_2FeSiO_4,[201] Li_2MnSiO_4,[212] $Li_2Mn_xFe_{1-x}SiO_4$[226, 227] and Li_2CoSiO_4[205, 228] were also synthesized by this method. Gong *et al.*[220] demonstrated a hydrothermal-assisted sol-gel method to synthesize carbon coated nano-structured Li_2FeSiO_4/C and synthesized mixed transition metal $Li_2Mn_xFe_{1-x}SiO_4$ successfully. Li_2FeSiO_4 cathode material was also synthesized using Pechini method[211] and modified sol-gel method.[218] Dominko *et al.*[203] showed that Li_2FeSiO_4 could be prepared by hydrothermal method. Muraliganth *et al.*[229] demonstrated that Li_2FeSiO_4 could be synthesized by microwave-assisted solvothermal method. Dongping *et al.*[230] showed that more than one mole of lithium ion could be extracted/inserted into Li_2FeSiO_4 structure, delivers an enhanced discharge capacity of ~220 mA h g^{-1}, when it is cycled between 1.5–4.8 V. Recently, Chen *et al.*[231] reported highest lithium storage performance of 254 mAh g^{-1} corresponding to 77.5% utilization of its theoretical capacity at

room temperature with excellent cycling stability (500 cycles) and rate capability (up to 40C). Nadherna *et al*.[232] demonstrated the electrochemical performance of Li_2FeSiO_4 at elevated temperature using ionic liquids. Armand *et al*.[233] performed first principles calculations to investigate the effect of N for O substitution on the electrochemical properties of Li_2FeSiO_4. They found that the lithium ions insertion potential associated to the $Fe^{3+/}Fe^{4+}$ redox couple could be decreased by N substitution.

1.6.4.2 Lithium manganese silicate (Li_2MnSiO_4)

Li_2MnSiO_4 material is most attractive than Li_2FeSiO_4 due to the possibility of investigating $Mn^{2+}/Mn^{3+}/Mn^{4+}$ redox chemistry and thus achieving a higher capacity.[204, 234] The overall electrochemical redox reaction of Li_2MnSiO_4 is given below in **Equation 1.15**. However, the complete reversible extraction/insertion of lithium is yet a challenge due to structural instability caused by Jahn-Teller distortion during cycling and amorphization upon cycling.[200, 235, 236] As mentioned, lithium manganese silicates are known to exhibit rich polymorphs owing to a range of crystal chemistry.[200-204, 211, 217, 223, 237] However, synthesis of single phase without impurity has been challenging until now[200, 203, 211, 223, 229, 235, 237-240] and so far only four polymorphs have been isolated. However, it is not straight forward to isolate these polymorphs owing to small difference in the formation energy between the polymorphs.[211] Different polymorphs could be achieved during the synthesis of Li_2MnSiO_4 materials by controlling the temperature, pressure, temperature ramp up rate and ramp down rate of the synthesis and post-treatment of the materials.[211] For example, two low temperature polymorphs *Pmn*2_1 and *Pmnb* with an orthorhombic structure,[200, 203] a high temperature

$P2_1/n$ polymorph with a monoclinic structure[212] and a meta-stable monoclinic *Pn* polymorph[241] have been reported earlier. For instance, the crystal structure of low temperature $Pmn2_1$ and high temperature $P2_1/n$ polymorphs are shown in **Figure 1.16**. All crystal structures are based on distorted hexagonal close-packed oxygen ions with cations in distorted corner sharing tetrahedra, however they differ in the tetrahedral cations orientation (MnO_4-SiO_4 chains).[242] $Pmn2_1$ polymorph has their MnO_4 and SiO_4 tetrahedra all pointing in the same direction. In $P2_1/n$ polymorph, half of the MnO_4 and SiO_4 tetrahedra point towards in one direction while the other half in the opposite.[242] The structural investigation using ^{6}Li MAS NMR spectroscopy with first-principle calculation offers better understanding on the structural differences among various polymorphs of Li_2MnSiO_4.[237] In literature, more than one mole of lithium extraction and insertion reaction was reported for low temperature polymorphs $Pmn2_1$ at room temperature[226, 236, 239, 243, 244] and for high temperature polymorphs ($P2_1/n$) at elevated temperature.[239, 240, 245] Further, Fisher *et al*.[242] showed that the $Pmn2_1$ polymorph has simplest Li-ion migration pathway and lower energy barrier due to high symmetry of Li sites in the unit cells. This is in contrast; $P2_1/n$ which has two symmetrically distinct Li sites in the unit cells, whose formation energies are slightly different resulting in complex migration pathway for Li^+-ions.

$$\boldsymbol{Li_2MnSiO_4 \rightleftharpoons Li_{2-x}MnSiO_4 + xLi^+ + xe^-} \qquad \textbf{(1.15)}$$

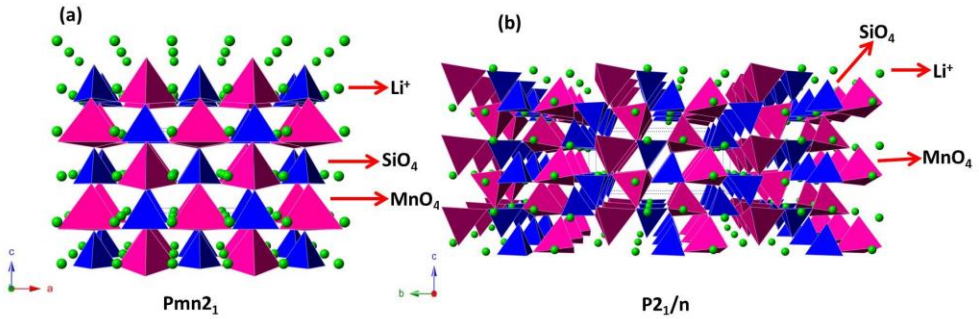

Figure 1.16 Crystal structure of Li_2MnSiO_4, (a) *Pmn2₁* orthorhombic structure and (b) *P2₁/n* monoclinic structure.

Adding to this, lithium metal silicates also suffer from low intrinsic conductivity (10^{-14} to 10^{-16} S cm^{-1}).[235] Initial studies on Li_2MnSiO_4 reported the extraction/insertion of less than one mole Li^+ ions per formula unit owing to its poor conductivity.[200, 203, 246] There are reports which showed the extraction/insertion of more than one mole Li^+-ions per formula unit with lithium storage capacity exceeding 200 mAh g^{-1}. For instance, (a) the extraction/insertion of 1.25 lithium ions per formula unit with a discharge capacity of 209 mAh g^{-1} demonstrated for carbon coated nano-composite Li_2MnSiO_4,[236] (ii) a storage capacity of 293 and 313 mAh g^{-1} reported for PEDOT/Li_2MnSiO_4 nano-composite at room temperature and elevated temperature (40 ^oC) respectively.[244] and (iii) a storage capacity of 210 and 250 mAh g^{-1} reported for Li_2MnSiO_4 at room temperature and elevated temperature (55 ^oC) respectively.[229] The extraction/insertion of Li^+ ion per formula unit in the above reports was accomplished at wide voltage window 1.5-4.5 V or at elevated temperature. They also proved that such a high discharge capacity is related to the redox chemistry of manganese ($Mn^{2+}/Mn^{3+}/Mn^{4+}$). Kuezma *et al.*[240] reported a flat extraction/insertion plateau for high temperature *P*2_1*/n* polymorph of Li_2MnSiO_4 attained by microwave

assisted solvothermal method. Though high temperature $P2_1/n$ polymorph of Li_2MnSiO_4 exhibited high capacity with flat voltage profile at elevated temperature, it suffers from severe capacity fade. Devaraj *et al.*[239] showed flat charge/discharge plateau for low temperature $Pmn2_1$ polymorph Li_2MnSiO_4/C with extraction/insertion of 1.5 Li^+-ions per formula unit at room temperature in a narrow potential window 2.0–4.5 V. *Ex-situ* XPS study confirms that the extraction and insertion plateaus are associated with redox chemistry of $Mn^{4+}/Mn^{3+}Mn^{2+}$. Li *et al.*[236] showed a sol-gel method to prepare Li_2MnSiO_4/C nano-composite, which exhibits first discharge capacity of ~203 mAh g^{-1}.

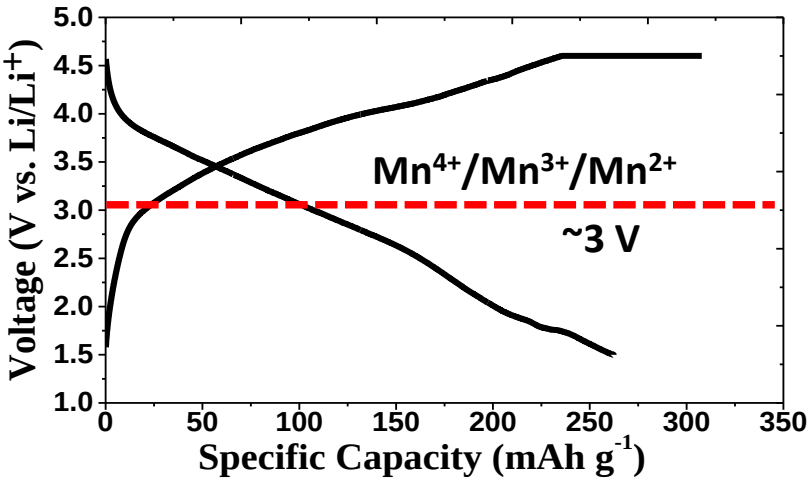

Figure 1.17 A typical voltage profile of in-house synthesized Li_2MnSiO_4 *vs.* Li/Li^+.[175]

A typical voltage profile of an in-house synthesized low temperature $Pmn2_1$ polymorph of Li_2MnSiO_4 is shown in **Figure 1.17** in which discharge capacity much higher than the transition metal phosphate was achieved.[209]

1.6.5 Lithium iron and manganese pyrophosphates ($Li_2FeP_2O_7$ and $Li_2MnP_2O_7$)

After intense research on lithium metal phosphates, recently attention has been shifted to a novel polyanion-based lithium metal pyrophosphates cathode with the general molecular formula $Li_2MP_2O_7$ (M= Fe, Mn, Co and

Ni).[247-252] Pyrophosphates have two dimensional diffusional channels for lithium ions in sharp contrast to $LiFePO_4$.[13, 253] Most interestingly, pyrophosphates offer the possibility of a two electron redox reaction.[250] The overall electrochemical redox reaction of $Li_2MP_2O_7$ (M= Fe, Mn, Co and Ni) is given below in **Equation 1.16**. Lee *et al.*[249] have showed that from migration energy calculation, it was found that the $Li_2MP_2O_7$ without partial occupation have a two dimensional Li^+-ions pathway while the condition of partial occupancies of Li^+-ions and transition metal ions, the diffusion pathway of Li^+ ions is a three dimensional. Ye *et al.*[254] reported the observation of an unusually high Fe^{3+}/Fe^{2+} redox potential at ~4.0 V vs. Li/Li^+ in mixed transition metal $Li_2M_xFe_{1-x}P_2O_7$ (M = Mn, Co and Mg) phases with a monoclinic $P2_1/c$ structure. Such a high potential operation of Fe^{3+}/Fe^{2+} above 3.5 V is believed to be possible by the existence of more electronegative and it was stabilized by doping. Nishimura *et al.*[250] reported high discharge capacity around 110 mAh g^{-1} at 0.05C without any carbon coating and nano-sizing. Saito *et al.*[255] reported high discharge capacities of 97 and 104 mAh g^{-1} at 0.1C respectively for carbon coated $Li_2FeP_2O_7$ and Mg-doped $Li_2FeP_2O_7$. Tamaru et al. demonstrated high potential $Li_2MnP_2O_7$ which displays Mn^{3+}/Mn^{2+} redox potential at 4.45 V *vs*. Li/Li^+. This is the highest potential cathode ever obtained for the Mn^{3+}/Mn^{2+} redox couple. Nishimura *et al.*[256] synthesized a new polymorph of $Li_2MnP_2O_7$ (β-$Li_2MnP_2O_7$) which exhibits reversible electrochemical activity at 4.0 V *vs.* Li/Li^+.

$$\boldsymbol{Li_2MP_2O_7 \rightleftharpoons Li_{2-x}MP_2O_7 + xLi^+ + xe^-(M = Fe, Mn, Co \,\&\, Ni)} \quad \textbf{(1.16)}$$

1.6.6 Lithium iron and manganese borates ($LiFeBO_3$ and $LiMnBO_3$)

Another new class of cathode materials is lithium metal borates with the general formula $LiMBO_3$ (M = Fe and Mn). This material was first introduced by Legagneur *et al.*[257] Borates have the following advantages over phosphates, (i) it has a lower molecular weight (58.8 g mol^{-1}) as compared to the phosphate polyanion (95.0 g mol^{-1}),[258] (ii) theoretical capacity of $LiFeBO_3$ is 220 mAh g^{-1} as against 170 mAh g^{-1} for $LiFePO_4$,[258] (iii) true density of borates (3.46 g cm^{-3}) and phosphates (3.45 g cm^{-3}) are almost the same, (iv) smaller triangle anion of borates only occupies lower volume resulting in higher volumetric energy density,[258] and (v) electronic conductivity of $LiFeBO_3$ ($3.9x10^{-7}$ S cm^{-1}) is higher than $LiFePO_4$ (10^{-9} S cm^{-1}).[258] Though lithium metal borates are promising from an energy density viewpoint, they are prone to surface poisoning upon exposure to air and thus synthesizing these cathode materials requires special procedures.[258] Apart from $LiFeBO_3$,[258, 259] $LiMnBO_3$[260, 261] and mixed-metal compounds $LiMn_xFe_{1-x}BO_3$ have also been reported.[262] The overall electrochemical redox reaction of $LiMBO_3$ (M= Fe and Mn) is given below in **Equation 1.17**.

$$\boldsymbol{LiMBO_3 \rightleftharpoons Li_{1-x}MBO_3 + xLi^+ + xe^-\ (M = Fe\ \&\ Mn)} \qquad \textbf{(1.17)}$$

Having discussed the prominent families of cathode materials and the research trends in the context of LIBs, the following section deals with the literature review on the anode materials for LIBs. Based on the mechanism of lithium storage, the anode materials are generally classified into three types namely insertion material, alloying material and conversion material.

1.7 Requirements of an ideal anode material

- High lithium storage performance.
- Fast extraction/insertion kinetics.
- Low structural changes during insertion/extraction.
- Most favorable low potential.

1.8 Research trend in anode materials

Some of the family of anode materials investigated for LIBs is listed in **Table 1.3.**

Table 1.3 Families of anode materials for Lithium-ion batteries.

Insertion hosts
Carbonaceous materials **Lithium titanate** **Titanium dioxide**
Conversion hosts
Manganese oxides **Iron oxides** **Cobalt oxides**
Alloying hosts

1.9 Insertion hosts

1.9.1 Carbonaceous materials

1.9.1.1 Graphite

Among the various anode materials that have been studied for LIBs, graphite anode is the successful material that has entered into consumer market. The lithium intercalation mechanism in graphite happens by a staging

reaction in which the lithium ions first intercalates into particular layers before reaching the neighboring layers.[263] Lithium insertion between the layers of graphite results in an increase in interlayer spacing without disturbing the prearrangement of carbon atoms within the layers.[264] The end product after complete lithium insertion is LiC_6 and the theoretical capacity is 372 mAh g^{-1}.[265-267] Despite all advantages such as abundance and excellent storage performance, employing graphite as anode in LIBs threatens the overall safety of the storage system especially while charging at high current rates. This is owing to the low insertion potential of graphite being close to 0 V. At high current rates, lithium plating occurs on the anode surface due to polarization, leading to dendritic formation which penetrates the separator resulting in electrical shorting and thermal runaway.

1.9.1.2 Carbon nanotubes

Carbon nanotubes (CNTs) have been investigated as anode materials for LIBs.[268-271] In CNTs, lithium intercalation occurs by means of effective diffusion of lithium ions into the sites in the nanotube surface via side walls. The theoretical capacities of single wall carbon nanotubes is ~1116 mAh g^{-1} (LiC_2) which is much higher than graphite.[263, 272] The lithium storage performance of CNTs purely depends on the morphology and method of synthesis. CNTs with bamboo like morphology [273] delivers capacity of ~135 mAh g^{-1} while arc like morphology[274] exhibits the capacity of ~200 mAh g^{-1}. Wu *et al*.[275] demonstrated excellent lithium storage capacity of ~1400 mAh g^{-1}. Chen *et al*.[276] showed that the ball milled sample could storage huge amount of lithium due to faster lithium ion diffusion and defects that has been created during milling. Though the storage capacity of carbon nanotubes is huge, the

mechanism of intercalation into the sites of CNTs is not documented clearly in literature. It is assumed that the interspace/space between the tubes could be the intercalation sites for lithium ions.[263] Although carbon nanotubes offers several advantages namely mechanical strength, robustness and durability, their laborious preparation process and low yield hampers its commercialization in LIBs.

1.9.1.3 Graphene

Graphene consists of free standing sheet of sp^2 carbon. Graphene was first invented by Novoselov *et al*.[277] in 2004. The honeycomb network forms the basis of several allotropes such as 3D stacked graphene, rolled graphene (1D nanotubes) and wrapped grapheme (0D nanotubes).[263, 278] The chemical and structural understanding is rudimentary.[279] The lithium storage capacity of graphene has expected to be higher than that of graphite owing to lithium ions adsorption which occuring on both sides of the graphene sheets.[280-284] Density calculation showed that the 0.7 nm graphene sheets could possibly deliver highest storage capacity (Li_4C_6).[285] Lian *et al*.[286] demonstrated the capacity of 1264 mAh g^{-1} at high current rates and it also showed a good cycling performance.

1.9.2 Lithium titanate

A solution to overcome the safety issues related to the low potential graphite is the use of slightly high redox potential anode materials (>1 V), where thermodynamically the lithium dendrite formation is not feasible. The original works on spinel $Li_4Ti_5O_{12}$ anode material was initiated by Thackeray *et al*, Ozhuku *et al*, and Dahn *et al*[287-289] which satisfies the criteria where the redox couple Ti^{4+}/Ti^{3+} operates at 1.55 V vs. Li/Li^+. $Li_4Ti_5O_{12}$ is categorized

by a defect spinel structure $\left(\mathbf{Fd\bar{3}m}\right)$ in which the lithium ions occupy 8(a) sites, titanium ions occupy octahedral 16(d) sites and oxygen ions occupy 32(e) sites with an oxygen positional factor ~0.26.[287] During Li^+ ions insertion, Ti^{4+} is reduced to Ti^{3+} within the octahedral sites, leading to a topotactic transition between $Li_4Ti_5O_{12}$ and $Li_7Ti_5O_{12}$. Colbow *et al*.[290] reported that both the $LiTi_2O_4$ and $Li_4Ti_5O_{12}$ showed the intercalation potential of 1.36 V and 1.55 V respectively.[291] The specific capacity of $Li_4Ti_5O_{12}$ is limited by the available octahedral sites for lithium ion insertion which is 175 mAh g^{-1} corresponding to insertion of 3 moles of lithium ion. Spinel $Li_4Ti_5O_{12}$ has 3D network channels to intercalate into the empty octahedral sites and it shows zero expansion.[292, 293] Hence, it makes them a good candidate for LIBs as anode. However, the electronic conductivity of this anode material is poor due to empty 3d orbital.[294] Hence, to achieve good electrochemical performance at high current rates it is important to improve the electronic conductivity. Significant contribution has been made by several research groups to enhance the electronic conductivity of spinel $Li_4Ti_5O_{12.}$ The lithium storage performance of spinel was improved by (i) preparing the material in nano-size by various synthesis method, (ii) cations (Mg^{2+}, Al^{3+}, Ni^{3+}, Fe^{3+}, Mn^{3+}, Co^{3+}, Cr^{3+}, Ga^{3+}, Zr^{4+}, Mo^{4+}, V^{5+} and Ta^{5+}) or anions (F^- and Br^-) doping in Li, Ti and O sites.[295] Further, surface modification by carbon, Ag, CNT and TiN (nitridation) has been made to improve the electronic conductivity.[295] Borghols *et al*. reported the storage behavior in $Li_4Ti_5O_{12}$ particles of various sizes namely 12 nm and 31 nm.[296] Feckl *et al.* showed excellent high rate performance up to 800C using nano $Li_4Ti_5O_{12}$.[297] **Figure 1.18** shows the

voltage profile of in-house synthesized spinel $Li_4Ti_5O_{12}$ with the average redox potential of 1.55 V *vs.* Li/Li^+.

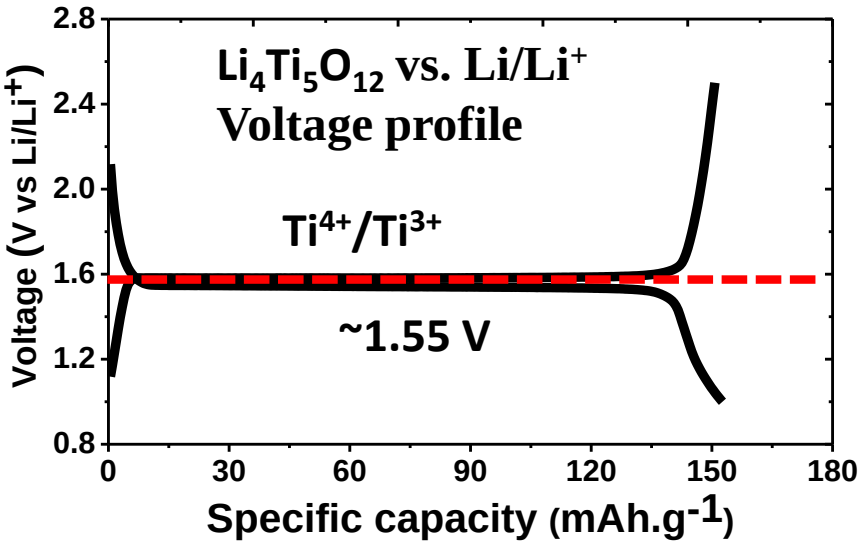

Figure 1.18 A typical voltage profile of in-house synthesized spinel $Li_4Ti_5O_{12}$ *vs.* Li/Li^+.[298]

Spinel $Li_4Ti_5O_{12}$ has gained significant attention due to the following advantages[287, 288] namely slightly high redox potential,[84, 287] absence of SEI,[299] zero strain,[300] state of charge indication.[301] **Figure 1.19** illustrates the overall potential of a battery which consists of spinel $Li_4Ti_5O_{12}$ and various cathode materials.

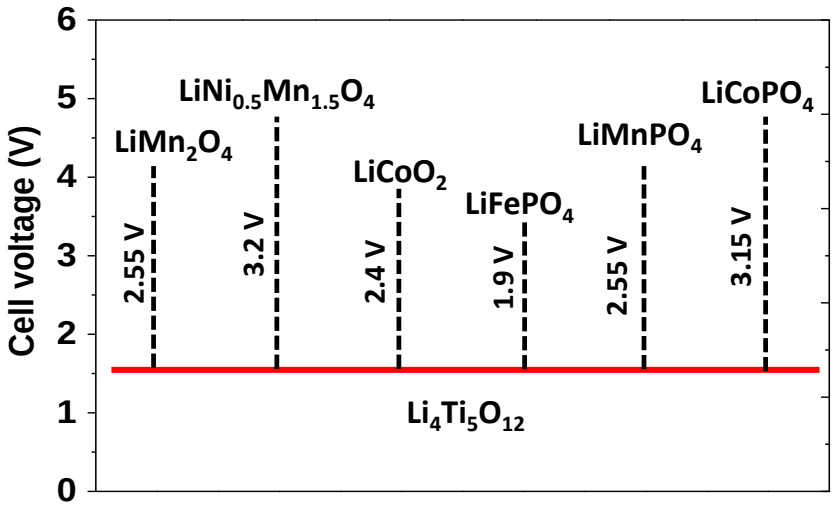

Figure 1.19 Potential of full cells combining different cathode materials with spinel $Li_4Ti_5O_{12}$ anode.[295]

For example, the electrochemical performance of full cell consisting of $LiMn_2O_4$ with $Li_4Ti_5O_{12}$ showed excellent retention about 82% upon 5000 cycles at 4C[302] while the full cell with $LiNi_{0.5}Mn_{1.5}O_4$ vs. $Li_4Ti_5O_{12}$ retains 83% of its initial capacity after 1000 cycles.[303] Reale *et al.*[304] demonstrated full cell performance by combining $LiFePO_4$ vs.$Li_4Ti_5O_{12.}$ Despite all the advantages, the high redox potential and low storage capacity limits its applications.

1.9.3 Titanium dioxide

In search of exploring potential anode materials with safety, TiO_2 have been a subject of research as an anode material for LIBs for a long time. Similar to spinel $Li_4Ti_5O_{12}$, the redox potential of Li^+ ions in TiO_2 occurs at ~1.75 V vs. Li/Li^+ and hence eliminating the possibility of dendrites and SEI formation. Adding to this, the theoretical storage capacity is 335 mAh g^{-1} higher than the theoretical capacity of $Li_4Ti_5O_{12}$ (175 mAh g^{-1}).[305-307] Now, 8 different polymorphs of TiO_2 are identified among them anatase[308, 309], rutile[310] and bronze[174, 311, 312] are well studied polymorph for LIBs. **Figure 1.20** shows a typical voltage profile of an in-house synthesized TiO_2 (anatase) in which Li^+ insertion and extraction plateaus are at 1.75 and 1.91 V respectively.

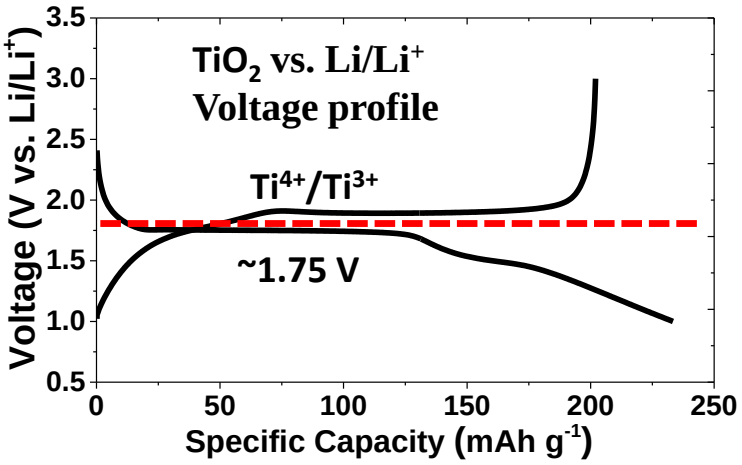

Figure 1.20 A typical voltage profile of in-house synthesized TiO_2 *vs*. Li/Li^+.[313]

1.10 Mechanism of conversion reaction

Owing to capacity limitation in insertion host, new mechanisms and materials that could allow higher Li^+ uptake were actively studied. On this line, lithium storage by conversion reaction[314] has attracted much attention as it allows more than one mole of lithium storage per formula unit.

Poizot *et al.*[314] reported lithium storage by conversion reaction in various transition metal oxides (TMOs). The reversible lithium storage was shown to occur at low potential up to 0.01 V. The mechanism of conversion reaction is summarized in **Equation 1.18**

$$\boldsymbol{A_aB_b + (b.n)Li \rightleftharpoons aA + bLi_nB} \qquad \textbf{(1.18)}$$

where A = transition metal, B = anion (O, S, F, N and P), n = oxidation state of B. During discharge (lithium uptake), transition metal oxides are reduced into nano-composites of transition metal embedded in an amorphous Li_2O matrix. The reverse reaction (lithium extraction) results in the formation of the nano-size transition metal oxide.[315, 316] The reversible lithium storage is attributed to the nanometric size of the transition metal particles which easily converted into Li_nB matrix upon lithium removal.[317] Mechanism of conversion

reactions has been demonstrated for oxides, fluorides, nitrides, phosphides and sulphides.[315, 316]

1.10.1 Conversion reaction on selected transition metal oxides

Transition metal oxides are well-studied materials for lithium storage by conversion reaction for LIBs owing to its availability and ease of synthesis. The advantages of conversion mechanism over graphite anodes are (i) high storage capacity, atleast 2-3 times more than graphite and (ii) higher operating potential *vs.* Li/Li^+ unlike graphite. Despite these advantages, the process of Li^+ uptake and extraction by conversion reaction in the host is accompanied by the huge volume change ~100%,[318] resulting in electrical disconnections between the particles and current collector. Such large volume change causes poor electrochemical performance, hampering its practical applications. Conversion reaction on selected transition metal oxides is summarized below.

1.10.1.1 Iron oxides

Iron oxides have more advantages when compared to other transition metal oxides as they are cheap, easily available and environmentally friendly. Iron oxides namely α-Fe_2O_3,[319-321] γ-Fe_2O_3,[322] and Fe_3O_4[323-326] have been well-studied for lithium storage. The theoretical storage capacity of α-Fe_2O_3, γ-Fe_2O_3 and Fe_3O_4 are 1007, 1007 and 926 mAh g^{-1} respectively. The average lithium ion uptake voltage is in the range ~0.7-0.9 V. The lithium uptake by conversion mechanism in all type of iron oxides is summarized in **Equations 1.19-1.20**. Despite several attempts, the first cycle reversibility and cyclability achieved in Fe_2O_3 material have been disappointingly low. Hariharan *et al.*[324] demonstrated a high first cycle reversibility of 90% for the first time in Fe_2O_3 conversion anode by incorporating the effective active material-electrode

design. This material consists of following features namely well-connected active particles, adequate surface area, storage particle-current collector adhesion and higher degree of electrode drying.[319, 324] **Figure 1.21** shows the voltage profile of in-house synthesized α-Fe_2O_3 in which a long flat plateau at ~0.80 V is seen corresponding to conversion reaction.

$$Fe_2O_3 + 6Li \rightleftharpoons 2Fe + 3Li_2O \quad (1.19)$$

$$Fe_3O_4 + 8Li \rightleftharpoons 3Fe + 4Li_2O \quad (1.20)$$

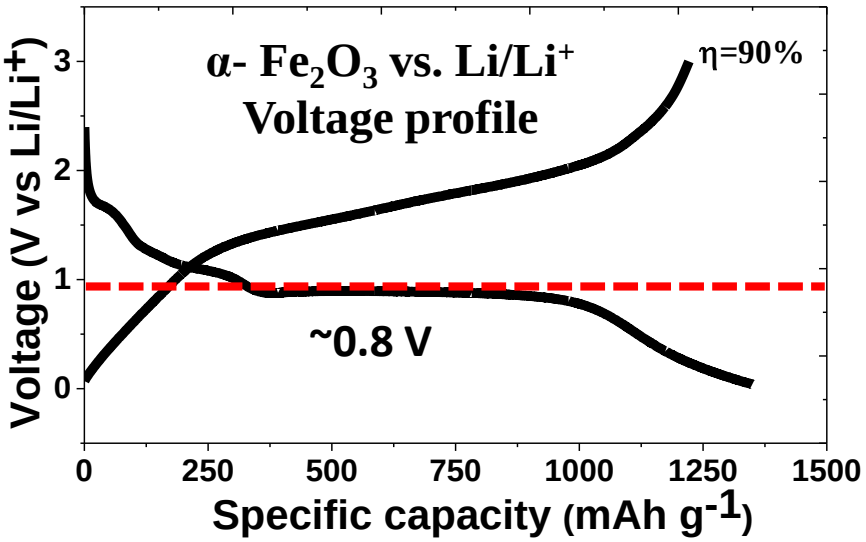

Figure 1.21 A voltage profile of in-house synthesized α-Fe_2O_3 *vs.* Li/Li^+.[324]

1.10.1.2 Manganese oxides

MnO_2 has a high theoretical storage capacity of 1233 mAh g^{-1} compared to other metal oxides that undergo conversion reaction. Other manganese oxides such as Mn_2O_3,[327] Mn_3O_4,[328] and MnO[329] have also been studied for lithium storage for LIBs. The theoretical storage capacities of Mn_2O_3, Mn_3O_4 and MnO are 1018, 934 and 755 mAh g^{-1} respectively. The conversion reaction in all type of manganese oxides is summarized in **Equations 1.21 - 1.24**.

$$MnO_2 + 4Li \rightleftharpoons Mn + 2Li_2O \quad (1.21)$$

$$Mn_2O_3 + 6Li \rightleftharpoons 2Mn + 3Li_2O \quad (1.22)$$

$$Mn_3O_4 + 8Li \rightleftharpoons 3Fe + 4Li_2O \quad (1.23)$$

$$MnO + 2Li \rightleftharpoons Mn + Li_2O \quad (1.24)$$

The lithium ions uptake in all type of manganese oxides results in a plateau at 0.4 V.[330-332] Most of the reports on lithium storage by conversion reaction in manganese oxides have shown capacities above 1000 mAh g^{-1}.[327, 329, 333-335]

1.10.1.3 Cobalt oxides

Co_3O_4 and CoO have been known to store lithium ions by conversion reaction.[336, 337] The theoretical storage capacities of Co_3O_4 and CoO are 890 and 715 mAh g^{-1} respectively. The conversion reaction in two forms of cobalt oxides are summarized in **Equations 1.25 - 1.26**.

$$Co_2O_3 + 8Li \rightleftharpoons 3Co + 4Li_2O \quad (1.25)$$

$$CoO + 2Li \rightleftharpoons Co + Li_2O \quad (1.26)$$

Various research groups have reported lithium storage capacities in excess of 800 mAh g^{-1}.[338-343] Although cobalt oxides exhibit favorable storage performance, their toxicity and high cost discourage its application in LIBs.

1.11 Alloying hosts

The ability of lithium to alloy with metals in the presence of electrolyte has triggered research interests on exploring alloying hosts for lithium storage.[344] The alloying reaction is presented in **Equation 1.27**.

$$xLi + M \rightleftharpoons Li_xM \quad (1.27)$$

Among the various metals, tin, antimony and silicon are the well-studied materials for lithium storage by alloying reaction. The storage capacities achieved by alloying reaction are higher than insertion materials

such as graphite. For instance, silicon has the highest lithium storage capacity of 4000 mAh g^{-1} while tin has a capacity of 990 mAh g^{-1}.[345-347] As the lithium storage capacities of alloying materials are high, they improve the energy density and reduce the weight of the batteries. Despite high capacities, alloying materials suffer from huge volume changes during alloying and de-alloying reactions.[346, 348] Volume changes in turn induce stresses in the electrode which lead to cracking and disconnections between the electrode materials and the current collector. Such degradation, results in storage capacity loss with cycles leading to poor cycle life. Several groups are trying to overcome these drawbacks by adopting the following techniques namely nano-structuring to accommodate the strain,[349] preparing active material with buffer matrix to hold volume expansion,[350] carbon coating,[349, 351] and selecting suitable binders that holds together the active material and the current collector.[352, 353]

1.12 Electrolytes

Electrolytes are essential component in LIBs, as they act as a medium for the lithium ions to transfer between the electrodes.[354] It consists of a lithium salt dissolved in the suitable non-aqueous organic solvents. Electrolytes for LIBs should have the following characteristics,[123, 354]

- Good ionic conductivity and electronically insulating.
- High chemical and electrochemical stability is needed to avoid the decomposition of electrolyte during redox reaction.
- Low melting point to facilitate sufficient conductivity at low temperature cycling.

- High boiling point is desirable which prevents evaporation and pressure build up in the batteries.
- Preferably, environmentally friendly and low cost.

Electrolyte is mainly classified into three types based on their nature such as liquid, polymer and ceramic/glass electrolyte.

1.12.1 Liquid electrolytes

Generally, an electrolyte consists of inorganic lithium salts ($LiPF_6$, $LiClO_4$, $LiBF_4$, $LiAsF_6$ and $LiCF_3SO_3$ etc.,) and organic carbonates as solvents.[355] Among these lithium salts, $LiPF_6$ displays several advantages compared to other lithium salts namely less toxic, excellent passivation with aluminum current collector and good thermal stability.[123, 356] Propylene carbonate (PC), ethylene carbonate (EC), Diethylene carbonate (DEC), Dimethylene carbonate (DMC) and Ethyl methyl carbonate (EMC) are most studied as solvents for LIBs.[123, 354, 356] $LiPF_6$ dissolved in EC: DEC solvent (volume ratio, 1:1) has less resistivity (ionic conductivity ~10^{-2} S cm^{-1}) and broad range of working temperature and potential. Besides these advantages, HF generated in the cell owing to poor drying of electrodes leads to increase in internal resistance of the electrolyte.[357-359] Further, liquid electrolytes also possess certain disadvantages such as non-flexibility of design, leakage due to improper sealing and pressure buildup in the cell when operating at high temperature (>50 °C).

1.13 Scope of the present study

The objective of this thesis is to investigate lithium storage properties of high redox potential and/or high storage capacity cathode materials and to enhance the specific energy of lithium-ion batteries **(Figure 1.22)**. The

specific energy can be increased by careful selection of cathode material as it is the product of redox potential and specific storage capacity. On these lines, the nucleus of the current investigation will focus on ways and means of tailoring the properties of cathode materials to improve the lithium storage performance, energy density and thereby lowering the weight of the batteries. The redox potential of battery can be improved by identifying materials which has high potential redox couple and also be compatible with existing electrolyte while specific capacity can be improved by identifying materials which could exchange more than one mole of lithium-ions from/into the structure. In this context, two classes of cathode materials namely $LiMnPO_4$ and Li_2MnSiO_4 are identified as subjects of this thesis work **Figure 1.22**. Adding to this, these materials are extremely safe, low cost and offer high energy density.

$LiMnPO_4$ poses many concerns such as poor electrochemical performance, rate performance, cycling stability, polarization owing to sluggish kinetics, strong polarons, Jahn-Teller distortion, volume mismatch between lithiated and delithiated phase and metastable nature of delithiated phase. In chapter 1, we aim to address these issues by developing an architecture featuring carbon coated, interconnected nano-grains constructed with mesopores. In chapter 2, the electrochemical performance is further enhanced especially at low current rates by combining this architecture (chapter 1) with isovalent co-doping (Fe^{2+} and Mg^{2+}). In chapter 3, further enhancement in electrochemical performance at high current rates is demonstrated by making Mn-Fe mixed transition metal composition with high Mn content. In chapter 4, the manganese utilization is improved especially at

high current rates by Mg^{2+} substitution in Mn rich Mn-Fe mixed olivine-phosphate. In chapter 5, besides olivine-phosphate, lithium storage properties of low temperature $Pmn2_1$ polymorph and high temperature $P2_1/n$ polymorph of Li_2MnSiO_4 are investigated.

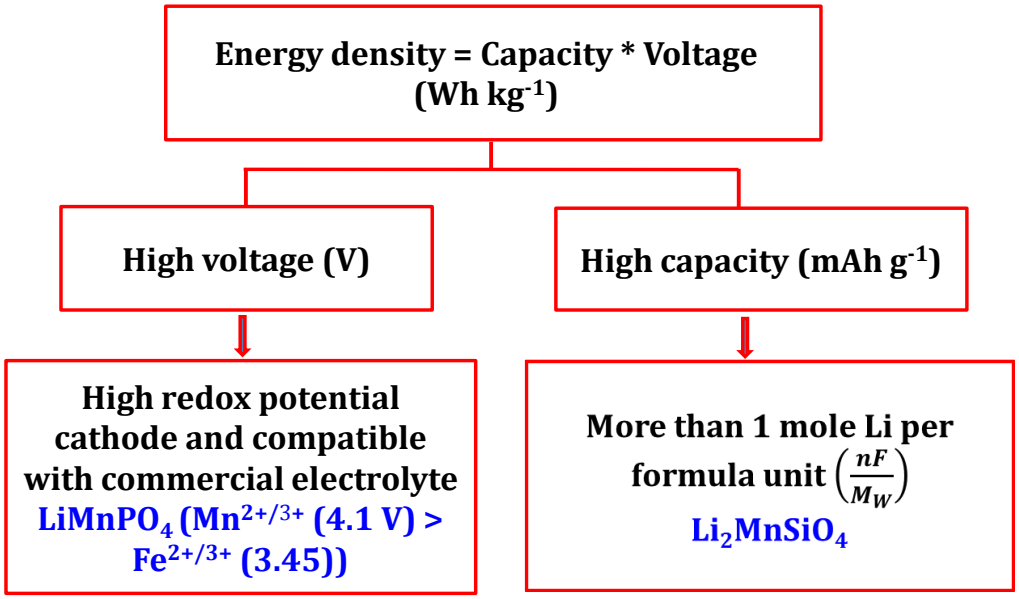

Figure 1.22 Schematic illustration of strategies employed in this thesis to enhance the energy density.

Chapter 2

2. Experimental Techniques

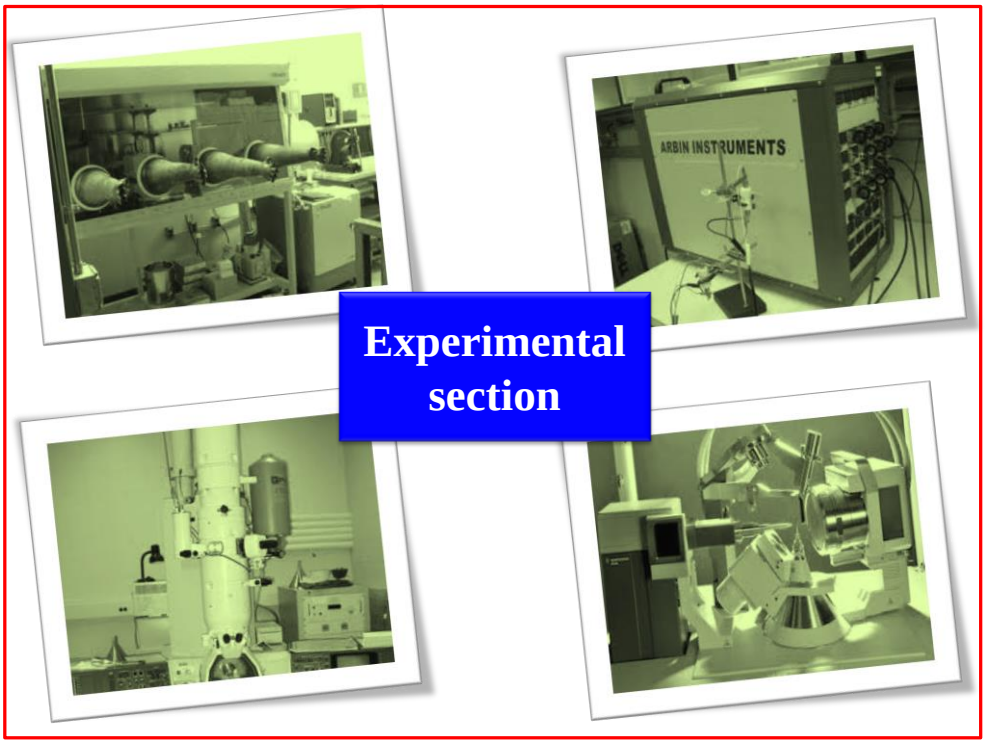

2.1 Preface to Chapter 2

This chapter highlights the various experimental techniques performed in active electrode material preparation, characterization, cell assembly and cell testing **(Figure 2.1)**.

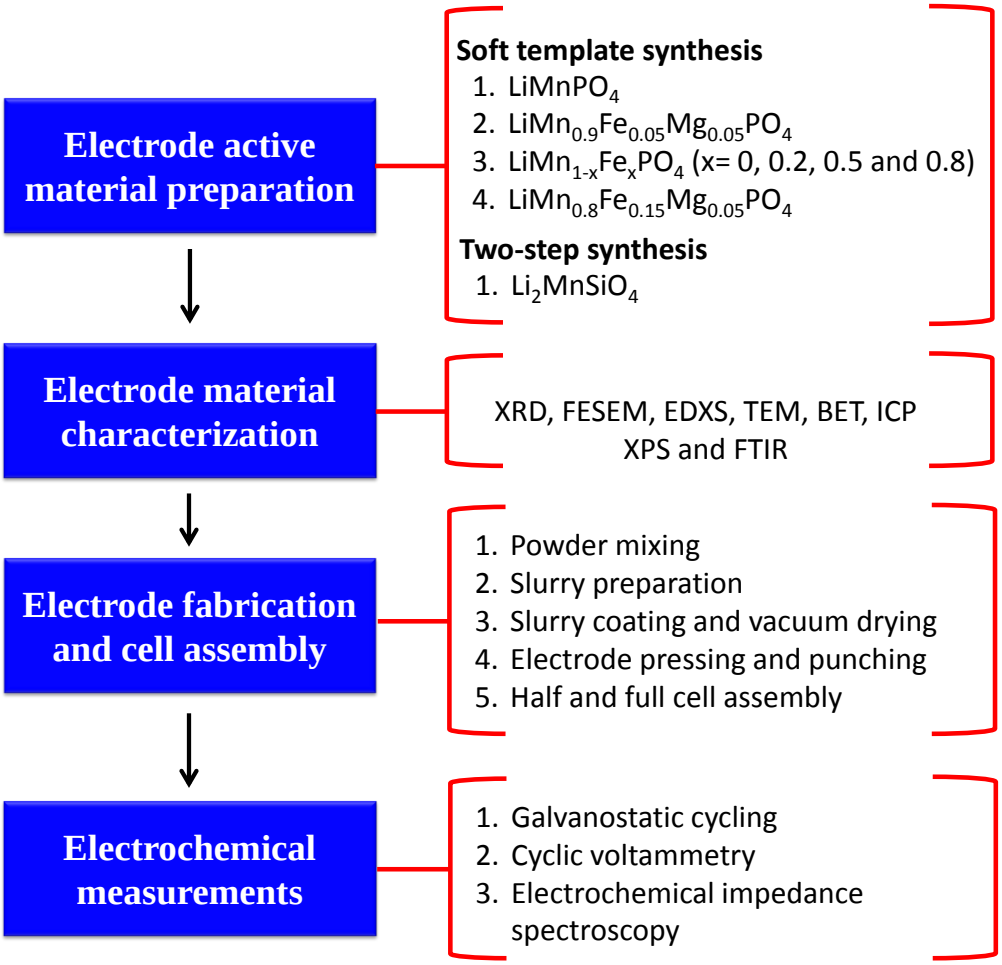

Figure 2.1 Flowchart of experimental methodologies.

2.2 Electrode active material preparation

In this thesis, the active electrode materials were prepared using either of the following synthesis methods: **soft template method** and **two-step method**. $LiMnPO_4$, $LiMn_{0.9}Fe_{0.05}Mg_{0.05}PO_4$, $LiMn_{1-x}Fe_xPO_4$ (x= 0, 0.2, 0.5 and 0.8) and $LiMn_{0.8}Fe_{0.15}Mg_{0.05}PO_4$ were synthesized using a soft template method, while Li_2MnSiO_4 was synthesized using a two-step approach. Details

of synthesis for above materials are presented in respective chapters. All the solvents and chemicals were commercially available and were used as received, unless otherwise stated.

2.2.1 Soft template method

In a typical soft template synthesis procedure, a cationic surfactant, cetyl trimethyl ammonium bromide (CTAB) was dissolved in a solution of ethanol and water and to this solution; the precursors of the active electrode material are added. Finally, the resulting precipitates are calcined in inert atmosphere to obtain the desired product. A template is defined as a structure-directing agent that enables the assembly of reactants.[360] The template forms a micelle, when it is dissolved in a solution this restricts the growth of the reactants.[360] The removal of templates by heat treatment results in a porous structure which is a replica of the particle aggregation.

2.2.2 Two-step method

In a typical two-step synthesis route, the precursors of transition metal and polyanion were dissolved in a round bottom flask with a mixture of millQ water and absolute ethanol. The resulting precipitates are calcined in an inert atmosphere to obtain the desired product. The calcined product was then ground with lithium precursor and calcined them in desired temperature in inert atmosphere to obtain the final product.

2.3 Electrode material characterization

The prepared electrode active materials were characterized by Powder X-Ray Diffraction (PXRD), Rietveld refinement, Field Emission Scanning Electron Microscopy (FESEM), Energy Dispersive X-ray Spectroscopy (EDXS), Transmission Electron Microscopy (TEM), Brunauer Emmett Teller

(BET) surface area measurement, Elemental analyses (viz. Carbon Hydrogen Nitrogen and heteroatoms analysis (CHNX analysis) and Inductively Coupled Plasma Optical Emission Spectroscopy (ICP-OES)), X-ray Photoelectron Spectroscopy (XPS) and Fourier Transform Infrared Spectroscopy (FTIR)**.** Finally, the electrochemical characterization was done on active electrode materials using techniques such as Galvanostatic Cycling (GC), Cyclic Voltammetry (CV) and Electrochemical Impedance Spectroscopy (EIS).

2.3.1 Powder X-ray diffraction

(a) Principle

PXRD technique is an analytical method that provides details on the atomic and molecular structure present in the crystalline material. The crystalline material diffracts the incident X-ray beams in a specific directions **Figure 2.2**. Then, the intensities and angles of diffracted beam are measured to identify the crystal structure. PXRD technique works on the principle of Bragg's law of diffraction **(Equation 2.1)**.[361-364]

$$2d \times Sin\theta = n\lambda \qquad \textbf{(2.1)}$$

In **Equation 2.1**, λ is the wavelength of the incident X-ray beam, θ represents the angle of incidence between the incident beam and the scattering plane, and d represents the interplanar spacing between the neighboring planes. As per Bragg's law, constructive interference would occur when the path difference is an integral multiple **(n)** of the wavelength **(Equation 2.1).** For destructive interference, the X-rays will be out of phase which then will not satisfy Bragg's law.

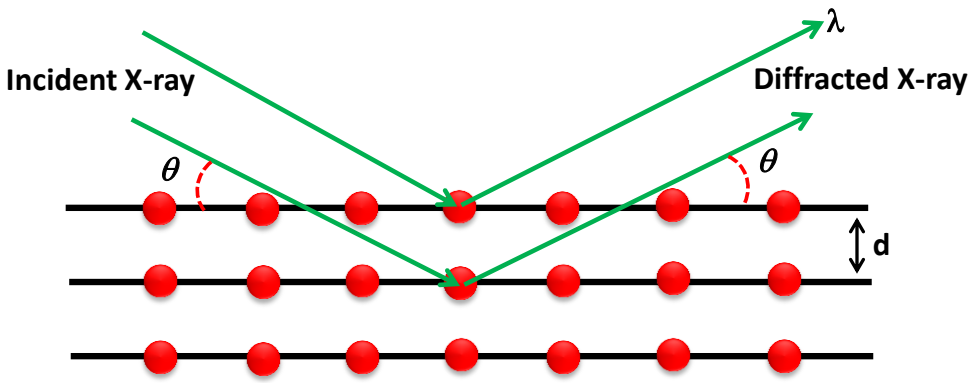

Figure 2.2 Schematic depiction of X-ray diffraction by crystals.

(b) Procedure

In this thesis, powder X-ray diffraction patterns were recorded using a Shimadzu 6000 diffractometer and **Cu-Kα** with a wavelength of 1.5418 Å was used as X-ray source. The powder was spread uniformly above an amorphous glass slide which was then loaded into the diffractometer. X-ray diffraction patterns were collected over 2θ in the range of 10 - 60°. A representative X-ray diffraction pattern consists of diffraction angle plotted along the X-axis and the intensity along the Y-axis **Figure 2.3**.

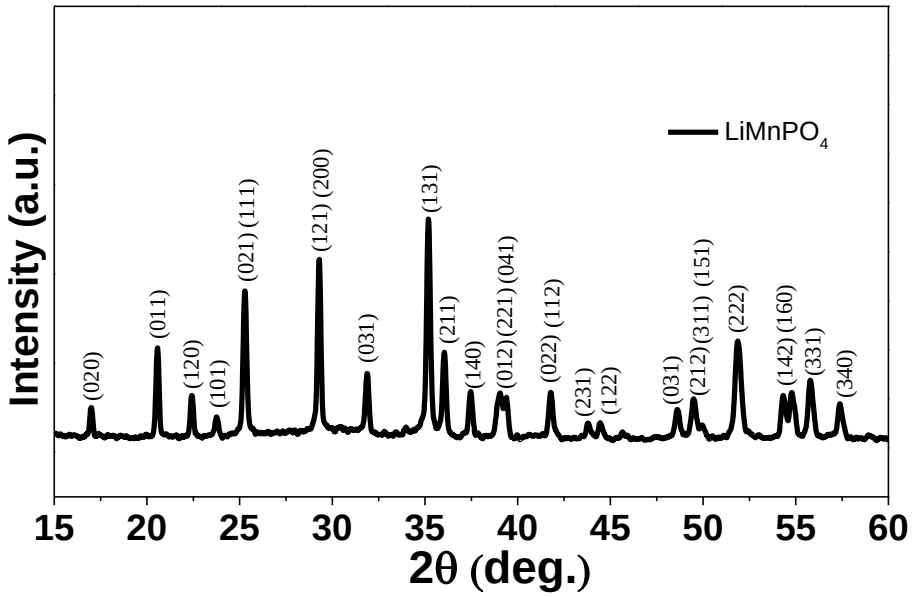

Figure 2.3 A typical XRD pattern recorded on $LiMnPO_4$ powder for 2θ in the range 10-60°.

All peaks in the illustrated diffraction pattern could be indexed to the pure phase of $LiMnPO_4$ belonging to the *Pmnb* space group (JCPDS card no. 33-0803) with an orthorhombic structure.

Standard X-ray diffraction patterns provided by International Centre for Diffraction Data (ICDD) were used for comparison and to fit the experimental XRD data with the standard patterns, Rietveld refinement was done using TOPAS 3.0 software.

2.3.2 Field emission scanning electron microscopy and energy dispersive X-ray spectroscopy

(a) Principle

FESEM is an analytical technique that provides an electronically magnified image of the sample under study.[365-368] Electron beam, ranging from few hundred eV to keV, are focused onto the sample surface under a high vacuum. Then a stream of electrons is narrowed by the electromagnetic lens to form a monochromatic electron beam. High-energy electrons are emitted by reflection while secondary electrons are emitted by inelastic scattering. The emitted electrons are received and are amplified to then produce an image of the sample.

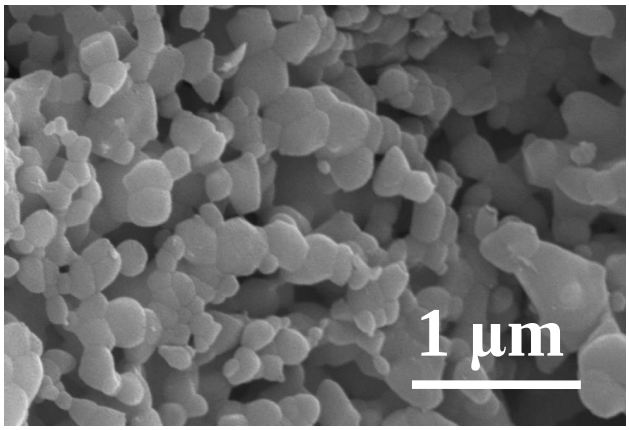

Figure 2.4 FESEM image of $LiMnPO_4$

(b) Procedure

Morphological aspects were studied using a Hitachi S4300 field emission scanning electron microscope. The sample was positioned on a carbon tape and placed on the sample holder and atomic layers of gold or platinum were then deposited on the sample using a DC sputtering instrument. The microscope was operated at an accelerating voltage of 5 kV and current 10 mA. A representative FESEM image recorded under the above conditions is shown in **Figure 2.4**.

In selected cases, EDXS were recorded using a JEOL JSM-6701F field emission scanning electron microscope equipped with EDXS (JED-2300) instrument which was rated at 15 kV with probe current of 2.56 nA. EDXS is an analytical technique that provides details on the elemental composition and distribution of the sample under study. During element analysis, electrons strike the surface of the sample resulting in emission of X-rays from inner shell electrons. This emitted X-rays are then analyzed and the elemental composition is determined. A representative elemental mapping images and energy dispersive spectra of $LiMn_{0.8}Fe_{0.15}Mg_{0.05}PO_4/C$ is shown in **Figure 2.5.**

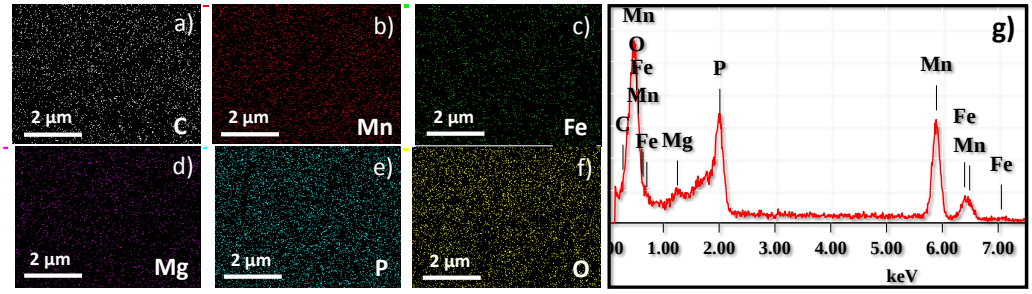

Figure 2.5 (a-f) Elemental mapping images and (g) energy dispersive spectrum of $LiMn_{0.8}Fe_{0.15}Mg_{0.05}PO_4/C$.

2.3.3 Transmission electron microscopy

(a) Principle

TEM is a technique in which electron beam transmitted through a thin sample interacts with the sample[365-368] and the image is produced by analyzing the interacted electron beams. The magnified image is then captured and focused on charge coupled device (CCD) camera and depicted on a fluorescent screen. This technique could offer a resolution of nearly 0.5 Å and magnification >50 million times. It provides details on the morphology, crystalline size and crystallanity. Further, SAED pattern can be obtained by changing the back focal plane of objective lens. Based on interplanar spacing, the crystal structure and lattice parameters are determined.

(b) Procedure

TEM images were obtained using JEOL TEM 2010 microscope. Prior to the experiments, the sample was dispersed in ethanol by sonication; a drop was loaded on Cu-grid and dried. Finally, the specimen was taken into the TEM chamber.

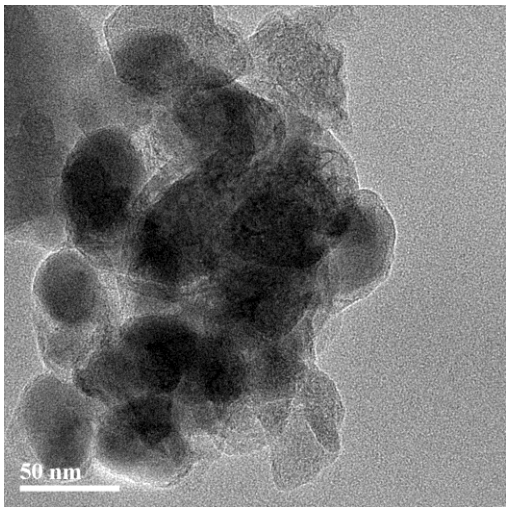

Figure 2.6 TEM image recorded on $LiMn_{0.8}Fe_{0.2}PO_4/C$.

Figure 2.6 illustrates a representative TEM image of $LiMn_{0.8}Fe_{0.2}PO_4/C$ recorded using JEOL TEM 2010 microscope. Besides TEM images, High Resolution Transmission Electron Microscopy Images (HRTEM) (at 200 kV) and Selected Area Electron Diffraction patterns (SAED) were also recorded using JEOL TEM 2010 microscope.

2.3.4 BET Surface area measurement

(a) Principle

BET method is a technique used to calculate the surface area, pore size distribution, porosity and pore volume of the sample. This method relies on the adsorption and desorption of the N_2 gas on the sample surface which forms thin monolayers. By measuring the volume of the gases adsorbed, the characteristics of the sample are calculated.[369-371]

(b) Procedure

In this thesis, Nitrogen adsorption and desorption isotherms were measured at 77K on Nova 2200e surface area and pore analyzer (Quantachrome, USA). Prior to the measurement all the samples were degassed at 130^o C overnight. The nitrogen adsorption and desorption data were analyzed by the Nova 2200e software and the BET specific surface area was calculated from nitrogen adsorption isotherms in the relative pressure range of 0.05 - 0.3. The total pore volume was estimated from the amount of N_2 adsorbed at a relative pressure of ~0.99. The pore size distribution was calculated from desorption isotherm using BJH (Barret-Joyner-Halenda method) method. **Figure 2.7** displays the isotherm and pore size distribution of $LiMn_{0.9}Fe_{0.05}Mg_{0.05}PO_4$ as a representative sample.

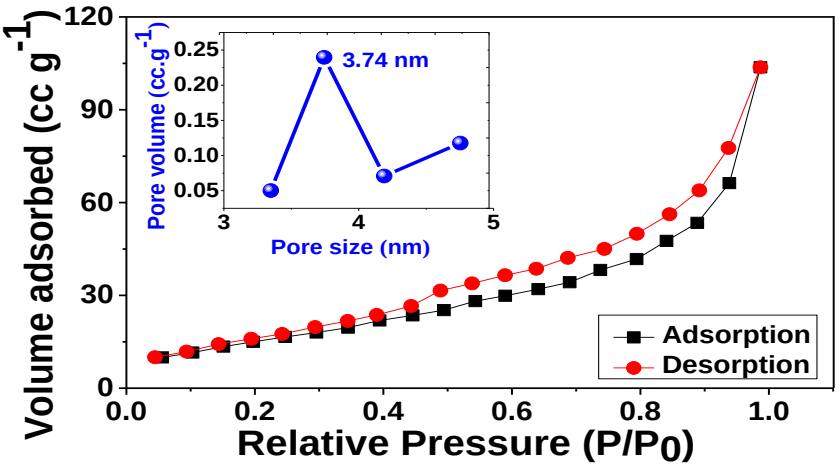

Figure 2.7 Nitrogen adsorption and desorption isotherm with pore size distribution (inset) of $LiMn_{0.9}Fe_{0.05}Mg_{0.05}PO_4$.

2.3.5 Elemental Analysis

(a) Principle

Elemental analysis (EA) is an analytical technique, where the elemental constituents and composition is estimated.[372, 373] CHNX analysis is used to determine the carbon, nitrogen and hydrogen and heteroatoms (halogens and sulfur) in the compound by burning the sample in the oxygen atmosphere and trapping the combustion products in CO_2/H_2O/nitric oxide. Finally, trapped product is analysed to calculate the composition of elements present in the sample. The metals present in the materials were estimated by ICP-OES.[372, 373] During this measurement, the excited ions are captured by means of electromagnetic radiation. The intensity of this radiation is directly proportional to the amount of elements presents in the sample.

(b) Procedure

In this thesis, CHNX elemental analyzer (Elementar Vario MICRO CUBE) is used for analysing the carbon in the electrode material. Dual-view Optima 5300 DV ICP-OES analyzer is used for ICP-OES analysis. In ICP-

OES, the sample was digested with HNO_3/HCL/HF and topped up to 10 ml with H_2O.

2.3.6 X-ray Photoelectron Spectroscopy

(a) Principle

XPS is a surface technique used to measure the chemical and oxidation state of the elements present in the sample.[374] When X-ray of known energy is incident in the surface of sample, photoelectrons are excited from the surface of the sample (~1-10 nm). The total energy of photoelectrons outflowed from the surface of the material is given in **Equation (2.2),**[374]

$$E_k = h\upsilon - E_B - \varphi \qquad (2.2)$$

where, $h\upsilon$ represents the total photon energy at excitation source, E_k and E_B represents the kinetic and binding energy of the photoelectrons respectively and φ represents the work function-the potential difference between the Fermi and vacuum level of the solids.

(b) Procedure

XPS studies were performed with a Kratos AXIS Ultra DVD (Kratos Analytical Ltd) at a base pressure of 1×10^{-9} Torr and a working pressure of 5×10^{-9} Torr using a mono Al-Kα radiation. Analysis of XPS spectra was done using XPS Peak-fit software. A Shirley-type background was subtracted from the recorded spectra. The derived binding energies (BE) were accurate to ± 0.1 eV.

2.3.7 Fourier Transform Infrared Spectroscopy

(a) Principle

FTIR provides valuable details on the bonding and molecular structure of the sample.[375] When infra-red (IR) radiations are strike on the surface of the

sample, some of the radiation is absorbed while the remaining is transmitted. The absorbed radiation frequency is equivalent to the frequency of molecules that vibrates. The transmitted radiation discloses absorbed energy at each frequency. Each frequency refers to particular molecular vibrations in the material. The frequency at which the radiations are absorbed is detected by the spectrometer. Since the absorbed frequencies are unique, the resulting FTIR spectra are a finger print of the particular sample under study.

(b) Procedure

In this thesis, a Nicolet 510 spectrometer was used to obtain the FTIR data. Prior to the measurements, the pellet was made using spectroscopic grade KBr. The pressed pellet was then loaded into station to obtain the FTIR spectrum.

2.4 Electrode fabrication and cell assembly

(1) Powder mixing

Electrodes were fabricated by mixing the cathode active material with acetylene black carbon additive and polyvinylidene fluoride (PVDF - Kynar 2801) in a particular weight ratio. **Table 2.1** summarizes the electrode weight ratios of active electrode material, carbon additive and binder of various nano-composite electrodes studied in this thesis. Here, the active material is the Li^+-ions host material, acetylene black is the conductive carbon additive and the binder holds the nano-composite material with the current collector, maintaining an intimate contact.

(2) Slurry preparation

The premixed electrode powders by means high energy ball milling, consisting of electrode active material and carbon additives, was added to a

glass container comprising of PVDF binder to prepare slurry using N-methyl pyrrolidone (NMP). The viscosity of the slurry was adjusted by adding NMP and the slurry was stirred for 8 h to deliver uniform blending of the electrode active material, carbon additive and PVDF binder.

Table 2.1 Weight ratio of active electrode material, carbon additive and binder used in this thesis.

Materials	Chapter	Active material: Carbon: Binder
$LiMnPO_4/C$	**Chapter 3**	**65:25:10**
$LiMn_{0.9}Fe_{0.05}Mg_{0.05}PO_4/C$	**Chapter 4**	**65:25:10**
$LiMn_{1-x}Fe_xPO_4/C$ (x = 0, 0.2, 0.5 and 0.8)	**Chapter 5**	**64:26:10**
$LiMn_{0.8}Fe_{0.15}Mg_{0.05}PO_4/C$	**Chapter 6**	**64:26:10**
Li_2MnSiO_4/C	**Chapter 7**	**65:25:10**

(3) Slurry coating and drying

The stirred slurry was then coated (~15 - 20µm thickness) uniformly on an aluminium foil (~10µm thickness) using a doctor blade technique. The solvent was then evaporated by drying the fabricated electrodes overnight at 110 °C in vacuum oven. The dried electrodes were pressed using a twin roller (Hohsen Corporation) at 37 psi to ensure the close contact between the grains and the current collector. The pressed electrodes were cut into circular discs of 16 mm diameter (area of electrode 2.01 cm^2) and consequently dried again overnight at 110°C in a vacuum chamber. Typically, the active material loading is ~1.25 - 3 mg cm^{-2} in the electrode (total loading being 2.5 - 6 mg).

(4) Half-cell assembly

Subsequently, the coin cell assembly was done in a glove box (MBraun Germany) which maintains <5 ppm of O_2 and <1 ppm of H_2O. **Figure 2.8**

illustrates an exploded view the coin-cell assembly in which Li metal (Kyokuto Metal Co., Japan) was used as the counter and reference electrode against cathode electrodes namely, $LiMnPO_4/C$, $LiMn_{0.9}Fe_{0.05}Mg_{0.05}PO_4/C$, $LiMn_{1-x}Fe_xPO_4/C$ (x = 0, 0.2, 0.5 and 0.8), $LiMn_{0.8}Fe_{0.15}Mg_{0.05}PO_4/C$ and Li_2MnSiO_4/C. 1M $LiPF_6$ in mixture of ethylene carbonate (EC) and diethyl carbonate (DEC) (1:1 volume ratio) was used as the electrolyte while (GF/C) glass microfiber filters was used as the separator.

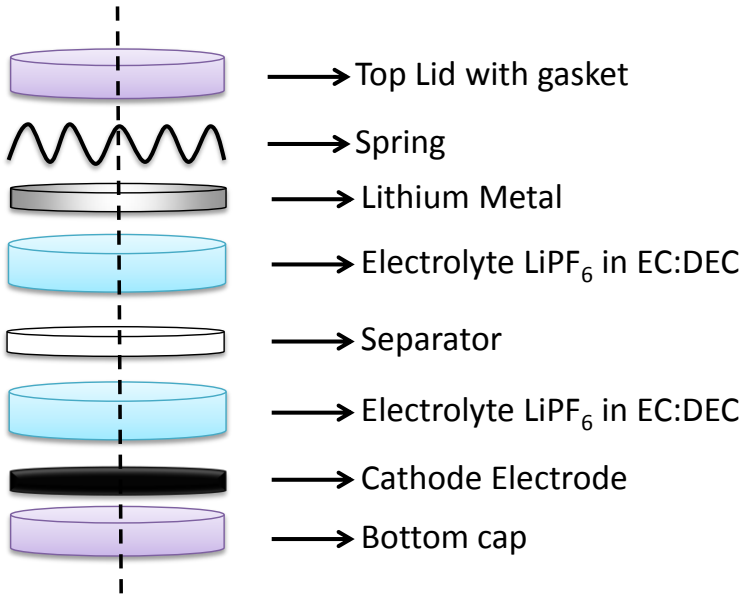

Figure 2.8 Schematic illustrates an exploded view of the half cell showing the essential parts.

The nano-composite cathode electrode was placed on the bottom cap and 100 µL of electrolyte was added while separator membrane was placed on the surface of the electrode. Circular metallic lithium discs of size 12 mm diameter and ~0.59 mm thick was then placed on top of the separator. The spring was placed on the surface of the metallic lithium while the top lid with gasket was then placed on the spring. Finally, the sealing was done using a crimping machine (Hoshen Corporation, Japan). The assembled half-cells

were then brought out from the glove box and aged for 24 h at room temperature before performing any electrochemical measurements.

(5) Full cell assembly

Instead of metallic lithium in full cell, in-house low potential materials were used as anodes **Figure 2.9**. $LiPF_6$ in EC: DEC was used as electrolyte for full-cells. **Table 2.2** summarizes the various full cells that have been studied in this thesis. The assembled full-cells were then brought out from the glove box and aged for 6 h at room temperature before performing galvanostatic cycling.

Table 2.2 List of full cells studied in this thesis.

Full cell combination	Chapter
$LiMnPO_4$ vs. $Li_4Ti_5O_{12}$	**Chapter 3**
$LiMn_{0.8}Fe_{0.2}PO_4$ vs. α-Fe_2O_3 **$LiMn_{0.8}Fe_{0.2}PO_4$ vs. $Li_4Ti_5O_{12}$**	**Chapter 5**

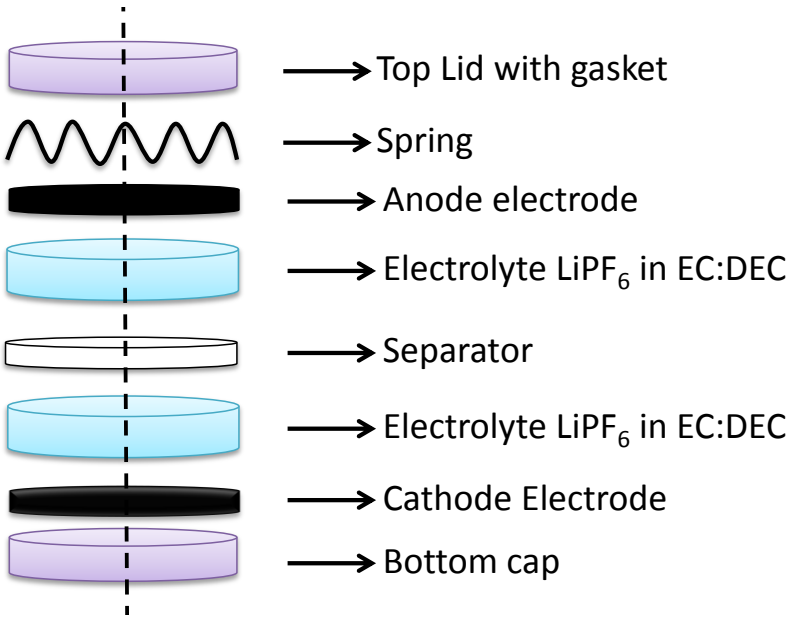

Figure 2.9 Schematic illustrates an exploded view of the full cell showing the essential parts.

2.5 Electrochemical measurements

2.5.1 Galvanostatic cycling

Electrochemical performance of the synthesized electrode materials were performed using galvanostatic cycling (Constant Current (CC mode) or Constant Current-Constant Voltage (CC-CV-mode only at charged state, not at discharged state)). In galvanostatic cycling, a fixed current pulse is applied while the variation in voltage is measured. In constant current-constant voltage cycling, a fixed current pulse is supplied while the variation in voltage is read until it reaches to higher potential (up to 4.6 V) and then voltage is maintained constant for a fixed time with the voltage window of 2.3-4.6 V/1.5-4.6 V. The electrochemical performance cycling stated in this thesis was performed with CC/CC-CV mode of cycling **Table 2.3** at room temperature or high temperature using Arbin battery tester (Model-BT2000, USA). Voltage profile is measured by galvanostatic method where a constant current was applied to battery to obtain voltage values at different SOC. The electrochemical performance cycling is showed by plotting the variation in potential as a function of capacity. The capacity values were calculated based on active material weight in the electrode (excluding in-situ and ex-situ carbon content).

Table 2.3 Mode of cycling employed in this thesis work.

Materials	Chapter	Voltage window (V)	Mode of cycling
$LiMnPO_4/C$	**Chapter 3**	**2.3-4.6**	**CC**
$LiMn_{0.9}Fe_{0.05}Mg_{0.05}PO_4/C$	**Chapter 4**	**2.3-4.6**	**CC-CV**
$LiMn_{1-x}Fe_xPO_4/C$ (x = 0, 0.2, 0.5 and 0.8)	**Chapter 5**	**2.3-4.6**	**CC**
$LiMn_{0.8}Fe_{0.15}Mg_{0.05}PO_4/C$	**Chapter 6**	**2.3-4.6**	**CC**
Li_2MnSiO_4/C	**Chapter 7**	**1.5-4.6**	**CC-CV**

The rate performance study was conducted by applying the same current while charging /discharging the cells.

Equation 2.3 shown below was used to calculate the observed capacity

$$\boldsymbol{Observed\ capacity}\ (\boldsymbol{mAh\ g^{-1}}) = \frac{\boldsymbol{Step\ time\ (h) * i\ (mA)}}{\boldsymbol{W_{act}(g)}} \qquad \textbf{(2.3)}$$

In **Equation 2.3,** the $\boldsymbol{step\ time}$ is the time taken to accomplish a complete charge or discharge (**in hours**). $\boldsymbol{W_{act}}$ is the weight of electrode active material loaded in the electrode (**in grams**). $\boldsymbol{i}$ is the

current applied to charge or discharge the cells (**in mA**).

The total active electrode material weight ($\boldsymbol{W_{act}}$) in **Equation 2.3** was determined as follows:

$$\boldsymbol{W_{act}} =$$

$$\left(\boldsymbol{W_{electrode} - W_{bare\ aluminum\ foil}}\right) * \boldsymbol{Fraction\ of\ active\ material} \textbf{ (2.4)}$$

In **Equation 2.4,** $\boldsymbol{W_{electrode}}$ is the weight of the electrode including the weight of the aluminum foil and $\boldsymbol{W_{bare\ aluminum\ foil}}$ is the weight of the bare aluminum foil. The fraction of active electrode material is the percentage of active material present in the nano-composite electrode. For instance, in case of active electrode material: carbon: binder composition of **65:25:10**, the fraction of active electrode material is **0.65**.

In **Equation 2.3,** $\boldsymbol{i}$ is the current applied for a particular current rate is estimated as follow

$$\boldsymbol{i = theoretical\ capacity}\ (\boldsymbol{mAh\ g^{-1}}) * \boldsymbol{C\ rate} * \boldsymbol{W_{act}(g)} \qquad \textbf{(2.5)}$$

In **Equation 2.5,** the $\boldsymbol{theoretical\ capacity}$ is the capacity theoretically expected for the active electrode material **(in mAh g^{-1})**. **1C rate**

is defined as the charge or discharge in 1 hour. The $\boldsymbol{theoretical\ capacity}$ in **Equation 2.5** is calculated as follows,

$$\boldsymbol{theoretical\ capacity}\ (\boldsymbol{mAh\ g^{-1}}) = \left(\frac{\boldsymbol{Faraday\ constant * n}}{\boldsymbol{M * 3600}}\right) * \mathbf{1000} \quad \textbf{(2.6)}$$

In **Equation 2.6**, $\boldsymbol{Faraday\ constant}$ value is 96485 C mol^{-1}. $\boldsymbol{n}$ is the number of electrons per formula unit and $\boldsymbol{M}$ is the molecular weight of the active electrode material. For instance, the theoretical capacity of $LiMnPO_4$ is calculated as follows. The electrochemical reaction of $\boldsymbol{LiMnPO_4}$ is shown in **Equation 2.7** in which theoretically 1 mole of Li^+-ion could be extracted from/inserted into the structure.

$$\boldsymbol{LiMnPO_4 \rightleftharpoons Li_{1-x}MnPO_4 + xLi^+ + xe^-} \quad \textbf{(2.7)}$$

The theoretical capacity of $\boldsymbol{LiMnPO_4}$ is calculated by using the **Equation 2.6** with $\boldsymbol{n}$ = 1 and $\boldsymbol{M}$ = 156.85 for $LiMnPO_4$.

$$\boldsymbol{theoretical\ capacity}\ (\boldsymbol{mAh\ g^{-1}}) = \left(\frac{\boldsymbol{96485 * 1}}{\boldsymbol{156.85 * 3600}}\right) * \mathbf{1000} \quad \textbf{(2.8)}$$

Hence, from **Equation 2.8,** the $\boldsymbol{theoretical\ capacity}$ of $LiMnPO_4$ is calculated to be 171 mAh g^{-1}. From the theoretical capacity values and active electrode material weight ($\boldsymbol{W_{act}}$), value of applied current $\boldsymbol{i}$ at a particular current rate was calculated using **Equation 2.5**. From the calculated values of the applied current ***i,*** weight of active electrode material ($\boldsymbol{W_{act}}$) and step time, the actual capacities were calculated from **Equation 2.3**.

2.5.2 Cyclic voltammetry

CV is a potentiodynamic electrochemical study technique that gives details on the redox potential, electron transfer kinetics and phase transition that happen during the electrochemical reaction.[376, 377] During CV

measurements, the voltage applied on the electrode is ramped in both forward direction (oxidation) and reverse direction (reduction) at a certain scan rate. Scan rate is the rate of change of voltage as a function of scanning time. During this experiment, the electrolytic current is plotted (y-axis) as a function of the applied voltage (x-axis). In a typical cyclic voltammogram, the peak position corresponds to the redox reactions that happen during the oxidation and reduction reaction of redox couple. During oxidation and reduction process, the current response was measured from the CV curve which is denoted as i_{ap} and i_{cp}. Here, i_{ap} and i_{cp} refers to anodic peak current (during oxidation) and cathodic peak current (during reduction) in the CV curve. In this thesis, CVs were recorded at various scan rates such as 0.058, 0.1, 0.2, 0.3, 0.4 and 0.5 mV s^{-1} using VMP3 Biologic potentiostat (Biologic science instruments, France) at room temperature.

2.5.3 Electrochemical impedance spectroscopy

EIS is a non-destructive tool useful for evaluating the kinetic properties of the electrode materials. In EIS experiments, small amplitude of AC signal is applied to an electrochemical cell and the current in the cell is read. The response of the cell is calculated in terms of phase and magnitude of the current measured. The EIS spectra are typically presented as Nyquist plots in which the real part is plotted on the X-axis while the imaginary part of impedance is plotted along the Y axis. Generally, the impedance spectrum of electrochemical cell has three essential regions. The first part, R_s is the solution resistance associated with the electrolyte and electrical contacts. The second region associates with the complex charge transfer process while the third region indicates the Warburg element associated with solid state Li^+-ions

diffusion in the bulk electrode. The fitting of experimental data is done using an equivalent circuit model. In this thesis, the EIS experiments were performed using VMP3 Biologic science instrument and the experimental data were analyzed using EC –Lab V10.19 software. AC signal of magnitude of 5 mV was used to measure the impedance with the frequency in the range of 1 MHz to 10 mHz.

Chapter 3

3. The effect of synthesis parameters on the lithium storage performance of $LiMnPO_4/C$

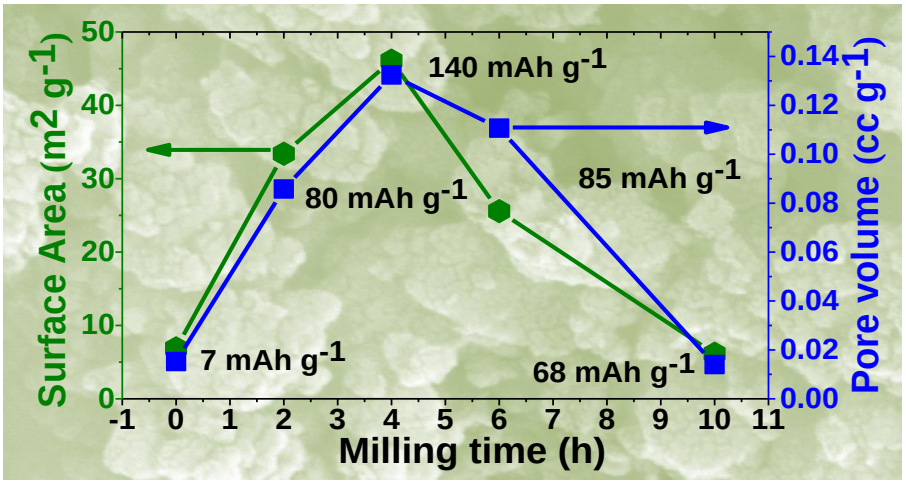

3.1 Preface to Chapter 3

An architecture featuring carbon coated, interconnected nano-grains constructed with mesopores were developed for $LiMnPO_4$/C cathode material. This architecture facilitates enhanced lithium ionic and electronic transports; favours improved lithium storage performance. Mesoporous $LiMnPO_4$/C electrode delivers discharge capacity of 140 mAh g^{-1} at 0.05C using galvanostatic cycling mode. This observed best electrochemical response of $LiMnPO_4$/C at constant current mode is complemented by diffusion studies using cyclic voltammetry and impedance spectroscopy. Further, the interdependence of lithium storage performance on carbon content, milling time (2, 4, 6 and 10 h), grain size and porous characteristics (surface area, pore size and pore volume) is also discussed in detail. Finally, the feasibility of $LiMnPO_4$/C cathode is evaluated against $Li_4Ti_5O_{12}$/C anode in a full cell configuration.

3.2 Introduction

Energy storage systems are essential to power the enormously growing global energy demands of the electric automotive and smart grid applications. LIBs have been considered to be promising energy storage system because of their high energy density, wide range of applications and long cycle life. However, the safety and cost of commercial electrode materials like $LiCoO_2$ are a matter of concern. Hence, the development of low cost cathode material with better safety is highly relevant. An orthorhombic structure phospho-olivine $LiMPO_4$ (M = Fe, Mn, Co and Ni) was recognized to be attractive positive electrode material owing to its salient features such as low cost and environmental friendliness.[13, 113] The olivine structure is stabilized by the strong P-O covalent bonding which prevents oxygen evolution.[127] Such an inherent structural robustness makes them safe candidates for LIBs compared to layered transition metal oxide such as $LiCoO_2$. However, olivine cathode materials suffer from poor electronic conductivity and ionic diffusivity.[92, 131, 378, 379] Among the phospho-olivines, $LiFePO_4$ stands out to be the most studied material owing to its attractive features such as safety, good cycle life and environmentally benign. $LiFePO_4$ exhibits a theoretical capacity of 170 mAh g^{-1} with a flat voltage profile at ~ 3.45 V vs. Li/Li^+ resulting in a specific energy of 586 Wh kg^{-1} (170 mAh g^{-1} x 3.45 V). On the other hand, the relatively less studied $LiMnPO_4$ offers a competitive gain in specific energy of 701 Wh kg^{-1} (171 mAh g^{-1} x 4.1 V) owing to its Mn^{2+}/ Mn^{3+} redox couple potential around 4.1 V vs. Li/Li^+, which is ~0.65 V higher than that of $LiFePO_4$ and importantly compatible with the commercial electrolytes unlike high potential cathodes such as $LiCoPO_4$ and $LiNiPO_4$.[108, 120-122] The high

open-circuit voltage with suitable and stable voltage window could make this material an attractive cathode for LIBs. However, deploying $LiMnPO_4$ as a cathode material in lithium ion batteries pose many challenges such as (i) poor electronic conductivity (~$3x10^{-9}$ S cm^{-1} at 300 °C) and ionic diffusivity,[89, 91, 127, 128] (ii) strong polarons,[127] (iii) Jahn-Teller distortion in charged state,[129] (iv) interfacial strain between the $LiMnPO_4$ and $Li_{1-x}MnPO_4$ phases,[130] and (v) metastable nature of the delithiated $Li_{1-x}MnPO_4$ phase.[189] All these factors lead to poor lithium storage performance in $LiMnPO_4$. Previous reports in the literature[13, 94, 131, 132] have also suggested that a complete extraction of Li^+-ions from $LiMnPO_4$ is not possible. To improve the storage performance, various groups have devised various novel synthetic approaches such as sol-gel method,[108, 133] polyol method,[121] soft template method,[135] solvothermal,[136] spray pyrolysis with wet ball milling,[137-139] ultrasonic spray pyrolysis,[140] direct precipitation,[141] solid state reactions in molten hydrocarbon,[142] hydrothermal,[143-146] microwave-hydrothermal[147] and off-stoichiometry methods.[148] Despite these efforts, only few groups have attained storage capacity more than 120 mAh g^{-1} in $LiMnPO_4$ [108, 121, 133, 137, 140-145, 147, 149-154] by employing Constant Current-Constant Voltage (CCCV) mode of charging in which the cells are fully charged and held at the upper cut-off voltage for a long time.

The lithium storage performance of $LiMnPO_4$ can be improved if the material is prepared with a favourable architecture. For this purpose, mesoporous $LiMnPO_4$ particles comprising of interconnected nano-grains and pores of comparable size with a thin layer of carbon coating **(Scheme 1)** was prepared and discussed in this chapter. A high energy ball mill (HEBM)

assisted soft template method followed by a post heat treatment was used for this purpose.

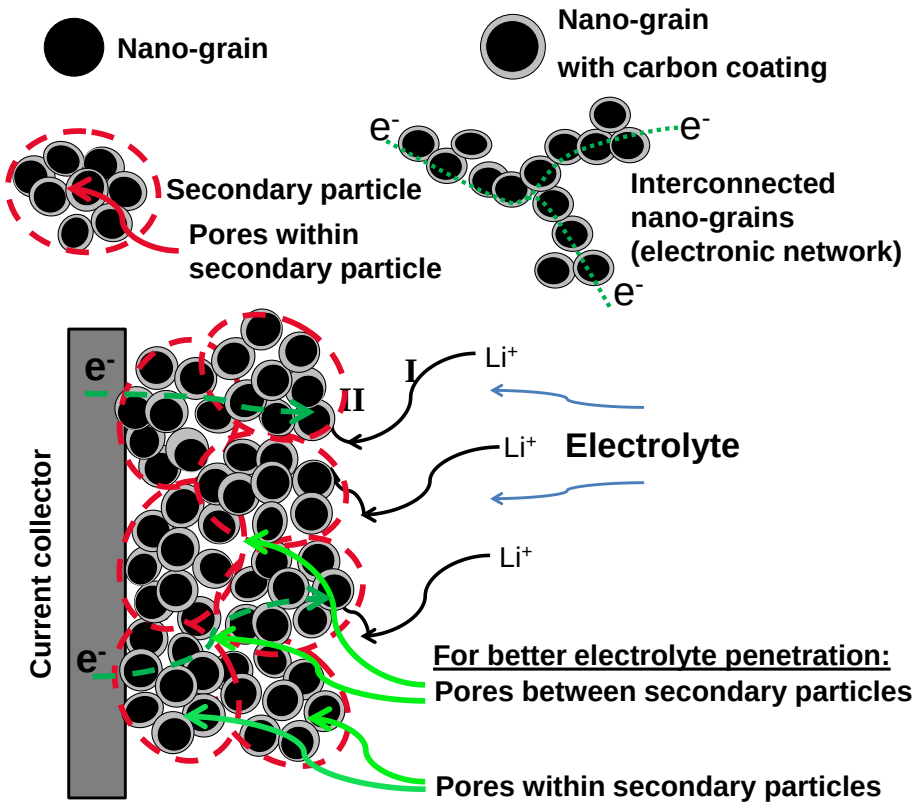

Scheme 1 Schematic illustration of strategies employed in this work to enhance the electrochemical kinetics of $LiMnPO_4$/C.

The above mentioned an architecture offers the following advantages **(Scheme 1)**: (a) nano-structuring that provides short transport length for lithium ions, (b) improved electronic conductivity owing to a homogenous coating of carbon around the active surfaces, (c) interconnectivity of primary (grain-grain) and secondary particles improving the electronic network, (d) mesopores within or between secondary particles providing better penetration of the liquid electrolyte into the core of the grains which allows facile extraction of Li^+ ions from the bulk of the electrode, and e) post heat treatment

to relieve the lattice strain induced during milling.[380, 381] Such tailored electrodes incorporating this architecture deliver lithium storage performance of 140, 120, 98, 94, 61, 41 and 20 mAh g^{-1} at 0.05, 0.1, 0.2, 0.5, 1, 2 and 5C rate respectively. The interdependence of lithium storage performance on carbon content, milling time (2, 4, 6 and 10 h HEBM), grain size and porous characteristics (surface area, pore size and pore volume) of $LiMnPO_4$/C is highlighted. Finally, the feasible operation of this cathode along with $Li_4Ti_5O_{12}$ /C anode in a full cell is demonstrated.

3.3 Experimental Section

3.3.1 Synthesis of $LiMnPO_4$/C

$LiMnPO_4$/C sample was synthesized using soft template method followed by high energy ball milling process (HEBM) **(Scheme 2)**. Typically, 0.01 M of cationic surfactant CTAB ($(C_{16}H_{33})N(CH_3)_3Br$, Sigma Aldrich) was dissolved in a round bottom flask with a mixture of millQ water and absolute ethanol in the volume ratio of 1:5 and the solution was stirred for 90 min. to initiate micellar formation, followed by the addition of lithium dihydrogen phosphate (LiH_2PO_4, Sigma Aldrich) and manganese acetate tetrahydrate ($Mn(CH_3CO_2)_2.4H_2O$, Sigma Aldrich) in stoichiometric proportions. The solution was further stirred for 24 h and the solvents were evaporated using an IKA RV10 roto-evaporator. The product was calcined in a tubular furnace at 650 $^{\circ}$C for 4 h in an Argon (Ar) atmosphere. The calcined product was then ball-milled using FRITSCH premium line – pulverisette 7 instrument at 500 rpm for 2, 4, 6 and 10 h with 25 wt% of acetylene black, the weight ratio of sample: balls being 1:40. Further, the post ball milled samples were heat treated at 450 $^{\circ}$C for 2 h in an Ar atmosphere.[134]

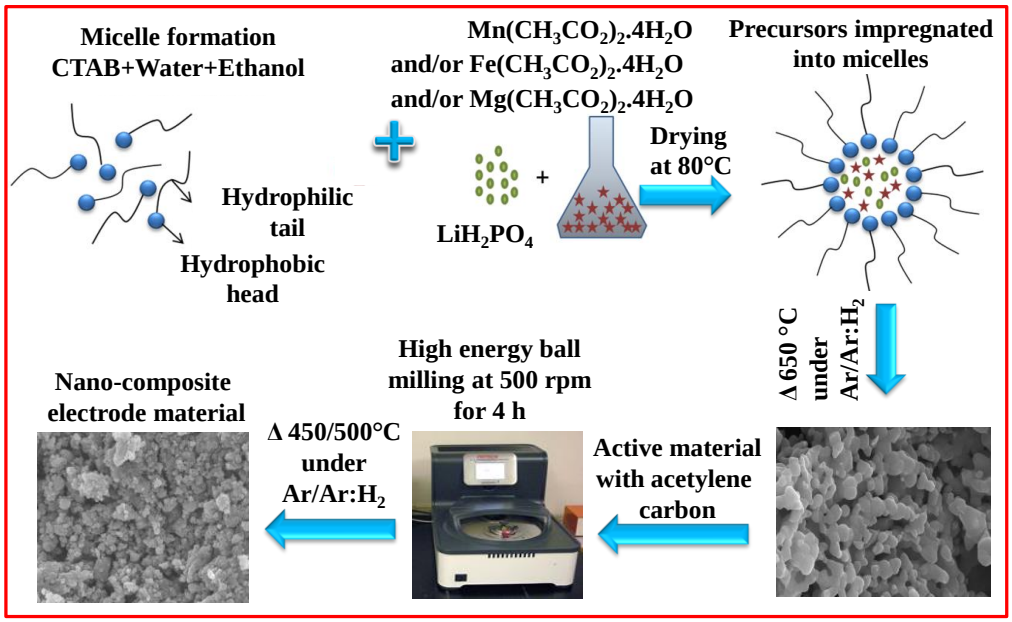

Scheme 2 Schematic illustrations of high energy ball mill assisted soft template synthesis.

3.3.2 Material and electrochemical characterization

$LiMnPO_4$/C samples were characterized using PXRD, Rietveld refinement, FESEM, EDXS, TEM, BET, galvanostatic cycling, cyclic voltammetry and electrochemical impedance spectroscopy. The details are given in chapter 2, section 2.2.1 2.3 , section 2.4 and section 2.5 .

3.4 Results and Discussion

3.4.1 Effect of milling time, grain size and carbon content on lithium storage performance

The initial experiments were performed for understanding the effect of milling time, grain size and carbon content on lithium storage performance of $LiMnPO_4$. As mentioned, $LiMnPO_4$ is known to be a poor mixed conductor (electronic and ionic conductivity) as compared to $LiFePO_4$. Hence, enhancing both the ionic and electronic conductivities is equally important for achieving good storage performance. The pristine $LiMnPO_4$ was ball milled systematically with varying amount of carbon and subjected to a mild post

heat treatment to improve the electrochemical kinetics of the electrode materials.

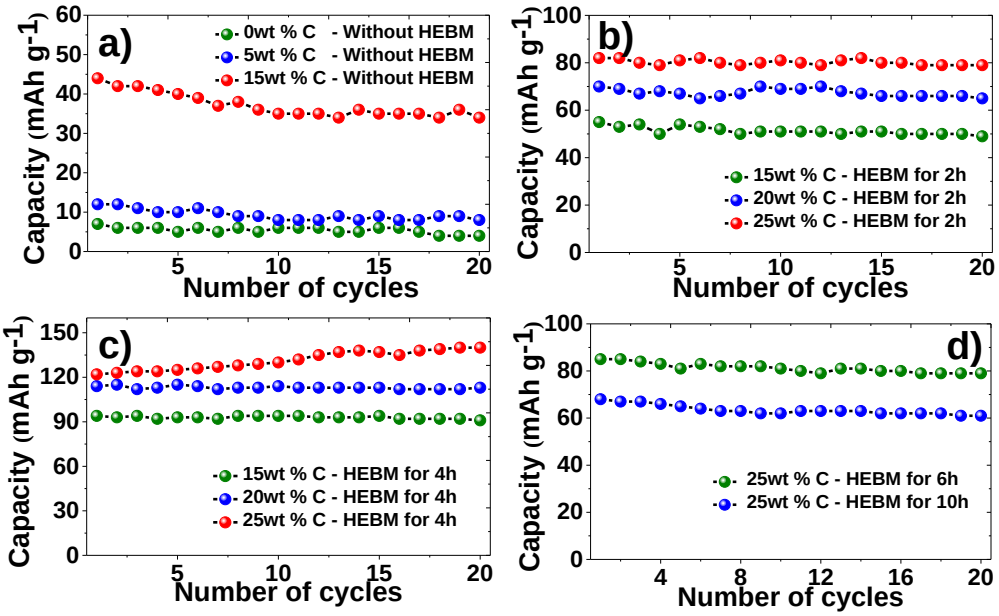

Figure 3.1 Specific discharge capacity *vs*. cycle number of pristine and ball milled $LiMnPO_4$/C with various amount of carbon content at 0.05C rate, (a) pristine, (b) 2 h HEBM, (c) 4 h HEBM, (d) 6 h HEBM, and (e) 10 h HEBM.

Initially, $LiMnPO_4$ was hand mixed with carbon (0, 5, 15 wt%) (Note no ball milling was employed). The samples with 0, 5 and 15 wt% carbon resulted in discharge capacities of 7, 12 and 44 mAh g^{-1} at 0.05C respectively (**Figure 3.1a)**. The reversible capacity obtained is much lower than the theoretical value. In the next series of experiments, $LiMnPO_4$ was ball milled with varying amount of carbon (15, 20 and 25 wt%) for 2 h instead of hand mixing. These samples showed considerable improvement in their storage performance with discharge capacities of 55, 70 and 82 mAh g^{-1} at 0.05C respectively (**Figure 3.1b).** To verify the influence of milling time on storage, further experiments were conducted in which the milling time was increased to 4 h, keeping the carbon content at 15, 20 and 25 wt%. These samples demonstrated improved discharge capacities of 95, 115 and 140 mAh g^{-1} at

0.05C respectively (**Figure 3.1c).** It is interesting to note that the discharge capacity increased remarkably just by increasing the ball milling time by 2 h (25 wt% carbon, 4 h HEBM vs. 25 wt% carbon, 2 h HEBM). Any further increase in milling time resulted only in poor electrochemical performance with discharge capacities of 85 and 68 mAh g^{-1} for 6 and 10 h of ball milling with 25 wt% respectively (**Figure 3.1d)**. Factors responsible for these changes in the lithium storage performance during milling will be discussed later. For further discussions, we restrict our studies to pristine (without carbon) and ball milled samples with 25 wt% conductive carbon.

Figure 3.2 illustrates the PXRD patterns of the pristine (with no carbon) and ball milled samples ($LiMnPO_4$/C with 25% carbon) at various milling times (2, 4, 6 and 10 h).

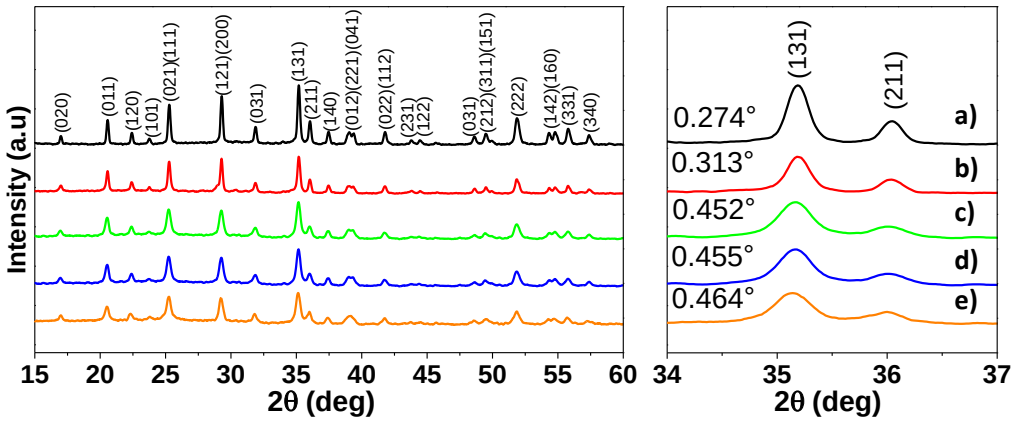

Figure 3.2 PXRD patterns (JCPDS card no. 33-0803) for pristine $LiMnPO_4$ and $LiMnPO_4$/C samples with 25 wt% carbon at various milling times with the expanded 2θ region on the right showing the peak broadening, (angle expressed in degrees refers to the full width at half maximum of (131) peak for these materials): (a) pristine (with no carbon/no ball milling), (b) 2 h, (c) 4 h, (d) 6 h, and (e) 10 h.

All peaks in the diffraction pattern could be indexed to the pure phase of $LiMnPO_4$ belonging to the *Pmnb* space group (JCPDS card no. 33-0803) with an orthorhombic structure. The expanded 2θ region on the right side of the **Figure 3.2** shows that peak broadening increases with the milling time

indicating the grain size reduction. No significant changes are observed in the lattice parameters and cell volume **(Table 3.1 and Figure 3.2)**. The lattice parameters obtained for these $LiMnPO_4$/C samples are comparable with the literature.[152]

Table 3.1 The influence of HEBM time on grain size, lattice parameters and cell volume of the $LiMnPO_4$ samples obtained by Rietveld refinement.

Milling time (h)	a (Å)	b (Å)	c (Å)	V (Å^3)	Crystallite Size (nm)
0	6.107(5)	10.446(5)	4.746(6)	302.85	110 ± 3
2	6.127(4)	10.467(4)	4.755(7)	305.58	60 ± 3
4	6.109(2)	10.462(3)	4.759(10)	304.22	40 ± 3
6	6.109(6)	10.456(5)	4.754(6)	303.74	36 ± 3
10	6.110(5)	10.453(5)	4.750(8)	303.46	33 ± 3

The good fit as indicated by the low reliability factors (R_{exp}:10.48%, R_{wp}:8.80%, R_p:7.22%) **(Figure 3.3)** and atomic positions (**Table 3.2**) obtained from Rietveld refinement of measured PXRD pattern of the 4 h ball milled sample also confirms the orthorhombic structure of $LiMnPO_4$.

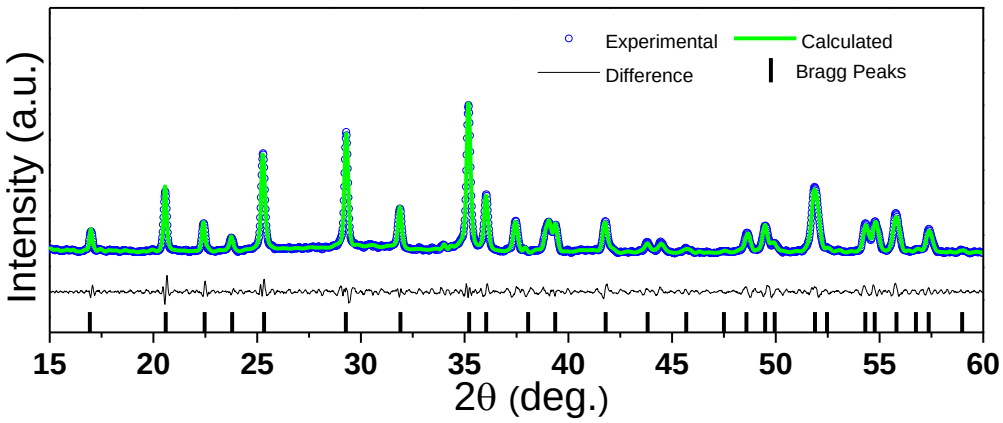

Figure 3.3 Rietveld refinement of 4 h HBEM mesoporous $LiMnPO_4$ (R_{exp}:10.48%, R_{wp}:8.80% and R_p:7.22%).

Table 3.2 Atomic positions of $LiMnPO_4$/C.

$LiMnPO_4$ (R_{exp}:10.48 R_{wp}:8.80 R_p:7.22)				
Atom	Site	x	y	z
Li1 (Li^{+1})	4a	0.0	0.0	0.0
Mn1(Mn^{+2})	4c	0.2500	0.2817	0.0281
P1(P^{+5})	4c	0.2500	0.0923	0.4081
O1(O^{-2})	4c	0.2500	0.0968	0.2664
O2(O^{-2})	4c	0.2500	0.4561	0.2073
O3(O^{-2})	8d	0.0492	0.1609	0.2781

In addition, a mild re-heat treatment was done to relieve the strain that has been created during ball mill processes.[381] It is important to note that no significant changes have been observed in the PXRD pattern, lattice parameters, cell volume and crystallite size owing to the mild heat treatment **(Figure 3.4 and Table 3.).**

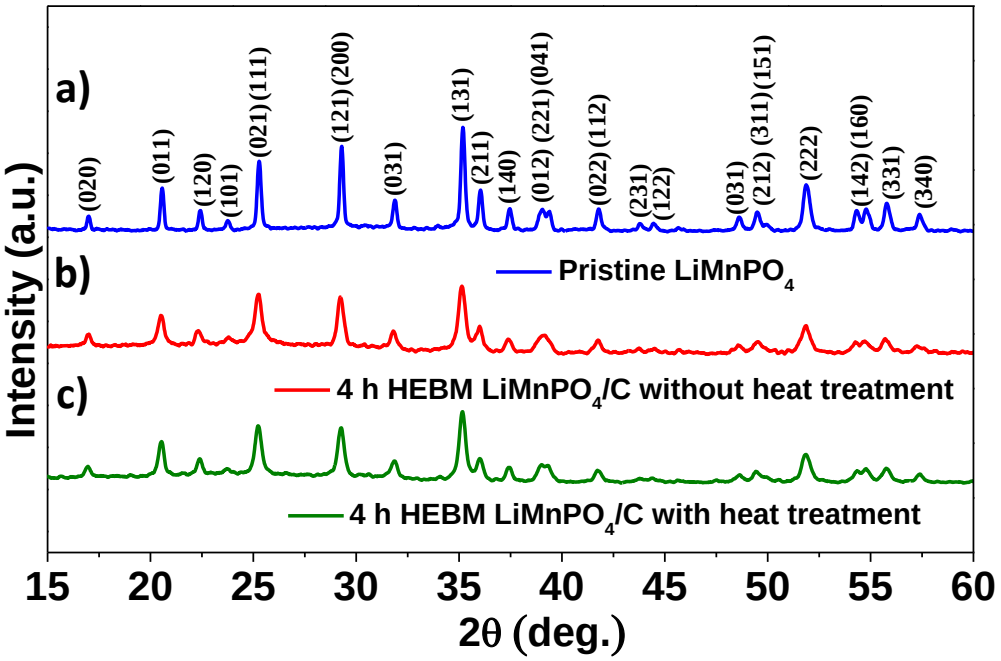

Figure 3.4 PXRD patterns of, (a) pristine, (b) 4 h HEBM $LiMnPO_4$/C without reheat treatment, (c) 4 h HEBM with a mild re-heat treatment.

Table 3.3 The influence of re-heat treatment on grain size, lattice parameters and cell volume of the 4 h HEBM $LiMnPO_4$/C samples obtained by Rietveld refinement.

Unit cell parameters	a (Å)	b (Å)	c (Å)	V (Å^3)	Crystallite Size (nm)
4 h HEBM before heat treatment	6.109(4)	10.462(5)	4.762(10)	304.42	40 ± 3
4 h HEBM after heat treatment	6.109(2)	10.459(3)	4.759(10)	304.07	40 ± 3

FESEM images presented in **Figure 3.5** illustrate the morphology of the pristine and the various ball milled $LiMnPO_4$/C samples. The crystallite size of the ball milled samples gradually decreases with increase in the milling time **(refer Table 3.1, Table 3. and Figure 3.5)**. However, prolonged ball milling beyond 4 h leads to noticeable agglomeration of the grains **(Figure 3.5d-3.5e)** which is also confirmed by a detrimental effect on the surface area and pore volume (discussed later in section 3.4.3).

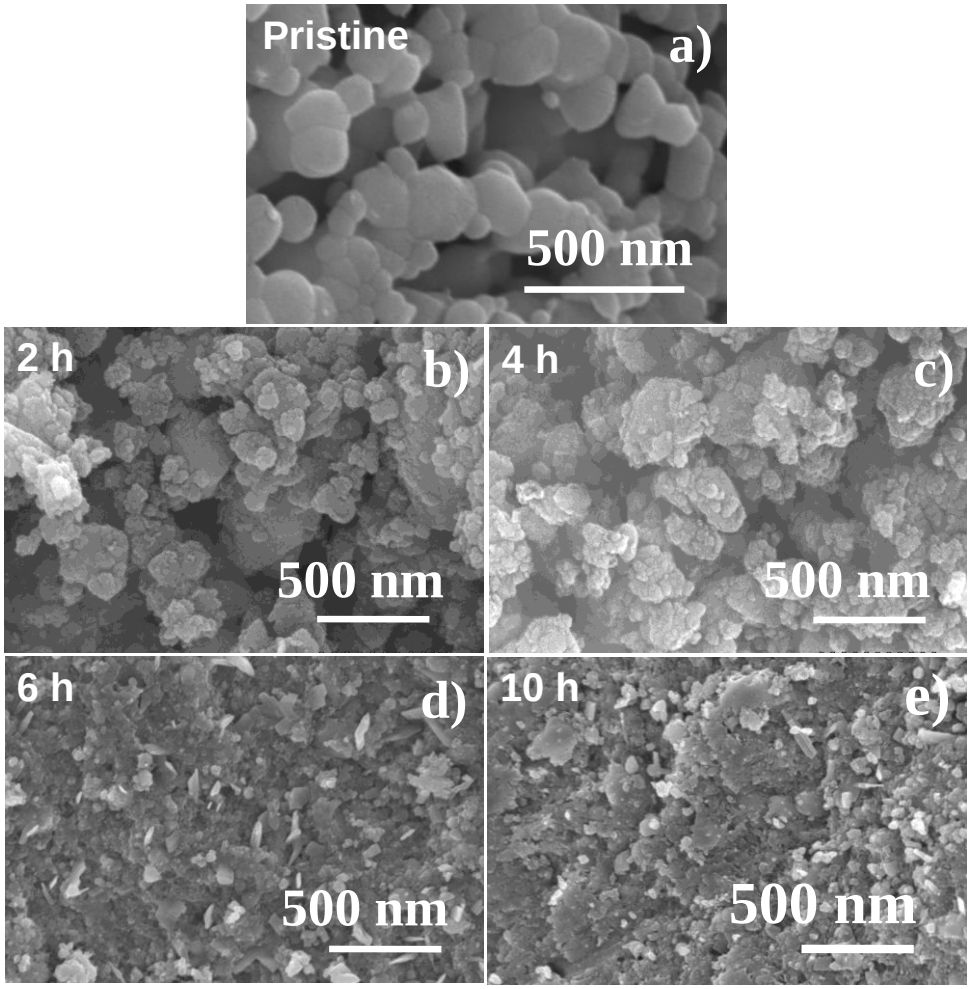

Figure 3.5 FESEM images of pristine and $LiMnPO_4$/C samples with 25 wt% carbon at various milling times; (a) pristine (0 h), (b) 2 h , (c) 4 h, (d) 6 h and (e) 10 h.

Figure 3.6 depicts the elemental mapping images of carbon and manganese of pristine and ball milled samples with 25 wt% carbon at various milling times. It could be seen that with increase in milling time up to 4 h, the distribution of carbon improves as observed in **Figure 3.6e.** However, the samples milled for 6 and 10 h, the distribution is relatively non-uniform **(Figure 3.6h and 3.6k)**. This suggests that increasing the milling time beyond 4 h leads to deterioration of electrical connection due to carbon segregation from the grains.

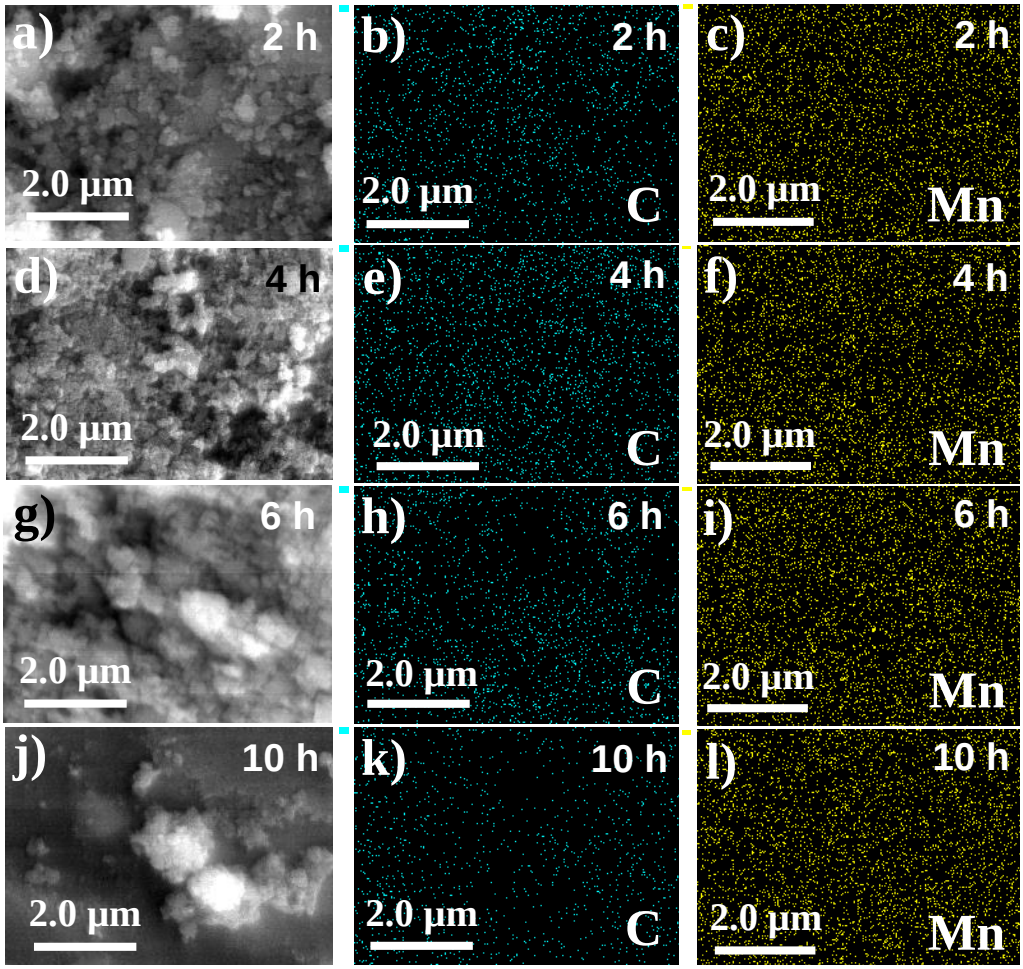

Figure 3.6 Elemental mapping of carbon and manganese of $LiMnPO_4$/C and corresponding SEM images at various milling times; (a-b) 2 h, (c-d) 4 h, (e-f) 6 h and (g-h) 10 h.

Figure 3.7 shows the TEM images of $LiMnPO_4$ pristine and 4 h ball milled $LiMnPO_4$/C. TEM image **(Figure 3.7a)** of the pristine material shows that the average grain size is ~100 ± 10 nm, comparable with Rietveld refinement results (110 ± 3nm) as shown in **Table 3.1.** The corresponding HRTEM image shows **(Figure 3.7b)** clear lattice fringes indicating formation of pure crystallites of $LiMnPO_4$. The observed *d*-spacing 5.23 Å of neighbouring lattice fringes corresponds to (020) plane of $LiMnPO_4$.

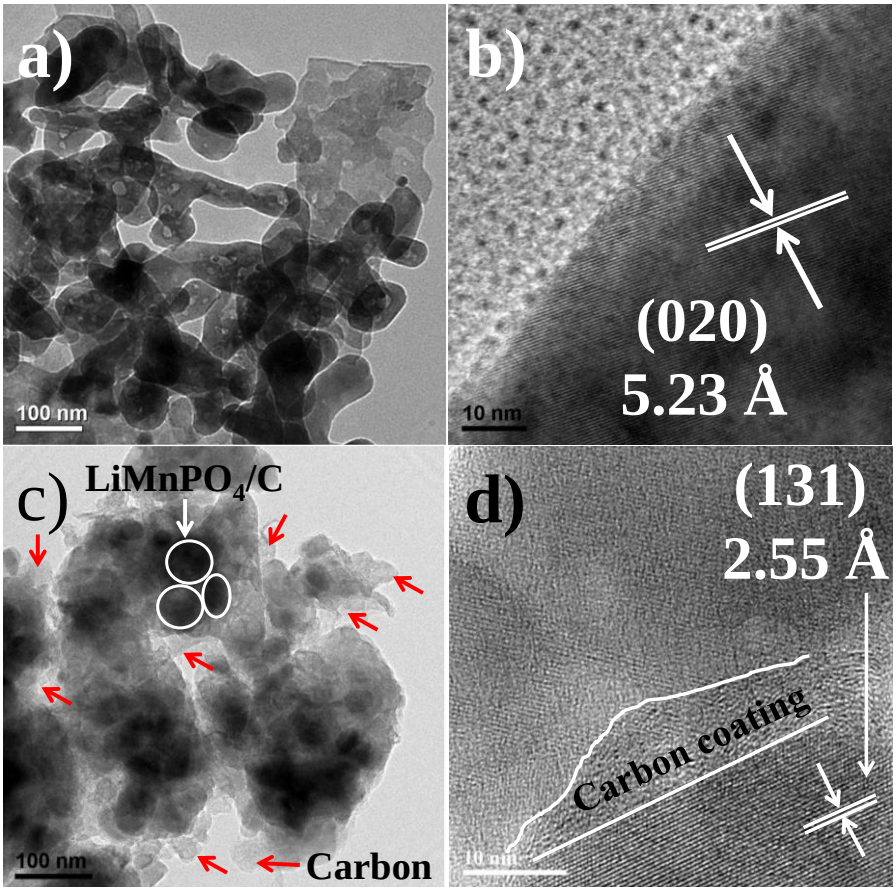

Figure 3.7 TEM and HRTEM images of, (a-b) pristine $LiMnPO_4$ and (c-d) $LiMnPO_4$/C with 25 wt% carbon ball milled for 4 h.

However, after milling for 4 h, the grain size was reduced to ~40 nm and the grains are embedded in a carbon matrix as a cluster forming secondary particles **(Table 3.1, Table 3. and Figure 3.7c).** HRTEM image of nano-structured $LiMnPO_4$/C sample (4 h HEBM) shows clear lattice fringes with observed *d*-spacing, 2.55 Å corresponding to (131) plane of pure $LiMnPO_4$ as shown **Figure 3.7d.** Further, it shows the presence of carbon coating (5 ± 2 nm) around the surface of $LiMnPO_4$ particles. Such a carbon layer around the active surfaces of $LiMnPO_4$ grains acts as an electrically conductive wiring for electrons.

The lithium storage property of these porous materials is tested by galvanostatic cycling. The galvanostatic charge and discharge profiles for

pristine (with no carbon and no ball milling) and HEBM samples (2, 4, 6 and 10 h) with 25 wt% carbon additives at 0.05C rate are shown in **Figure 3.8**.

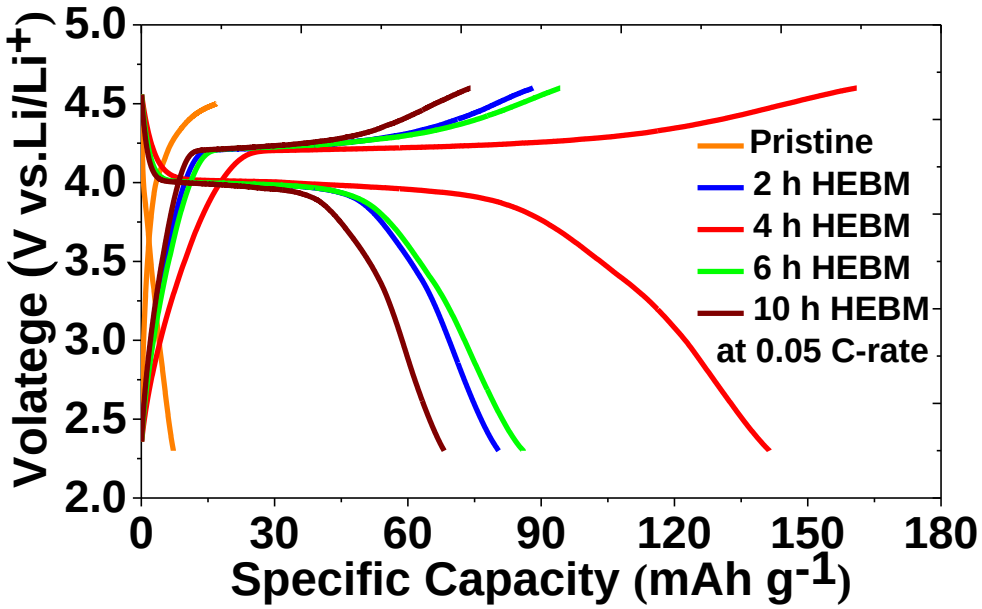

Figure 3.8 Galvanostatic charge and discharge profiles of pristine and $LiMnPO_4$/C at various milling times (2, 4, 6 and 10 h HEBM) with 25 wt% carbon at 0.05C rate (capacity values are calculated based on active material ($LiMnPO_4$) weight in the electrode).

The characteristic lithium ion extraction plateau corresponding to that of Mn^{2+}/Mn^{3+} redox couple at 4.3 V vs. Li/Li^+ was observed in HEBM samples unlike pristine $LiMnPO_4$. In addition, a clear improvement in the storage performance during Li^+ insertion with well-defined plateau for the Mn^{3+}/Mn^{2+} transitions was observed at 3.96 V upon milling with carbon black, representing a gain of ~0.55 V compared to $LiFePO_4$ (3.45 V). The highest storage capacity of 140 mAh g^{-1} at 0.05C rate has been achieved (based on weight of $LiMnPO_4$) for 4 h ball milled sample using galvanostatic charge/discharge mode. This is in contrast to most of the best performing samples reported in the literature that have employed CCCV method for charging.[108, 121, 133, 137, 140-145, 147, 149-154] It is worth noting that the storage capacities of other ball milled samples (2, 6 and 10 h HEBM samples with

25% carbon) were found to be only 82, 85 and 68 mAh g^{-1} at 0.05C respectively. Reasons for such remarkable improvement in the storage performance of 4 h HEBM samples are provided in section 3.4.3 and 3.4.4 . The large polarization observed in pristine $LiMnPO_4$ can be attributed to the poor intrinsic electronic conductivity and sluggish Li^+-ion diffusion kinetics. However, grain size reduction (shorter diffusion length), meso-structuring (high electrolyte wettability) using a systematic milling approach with the addition of carbon has improved both ionic diffusivity and electronic conductivity around the grain surface providing conductive wiring to the current collector thus favouring enhanced lithium storage of $LiMnPO_4$/C samples **(Figure 3.8).**

3.4.2 Formation of mesoporous microstructure

As shown in **Figure 3.9a**, the adsorption and desorption hysteresis loop of the pristine sample is incomplete. In contrast, 4 h HEBM sample exhibits a well-defined hysteresis loop characteristic of mesoporous materials referred as Type IV isotherm associated with capillary condensation in mesopores **(Figure 3.9b)**.[369, 370] Mesoporosity is also confirmed by the V-t plot **(inset II of Figure 3.9b).**[371, 382] BJH pore size distribution of the 4 h HEBM sample shows presence of two types of pores in the mesoporous region with an average pore diameter of 3.43 nm and 25.20 nm **(inset I of Figure 3.9b)**. The former mesopores could be related to pores formed by the primary particles (grains), while the latter mesopores could be associated with pores formed by the secondary particles.

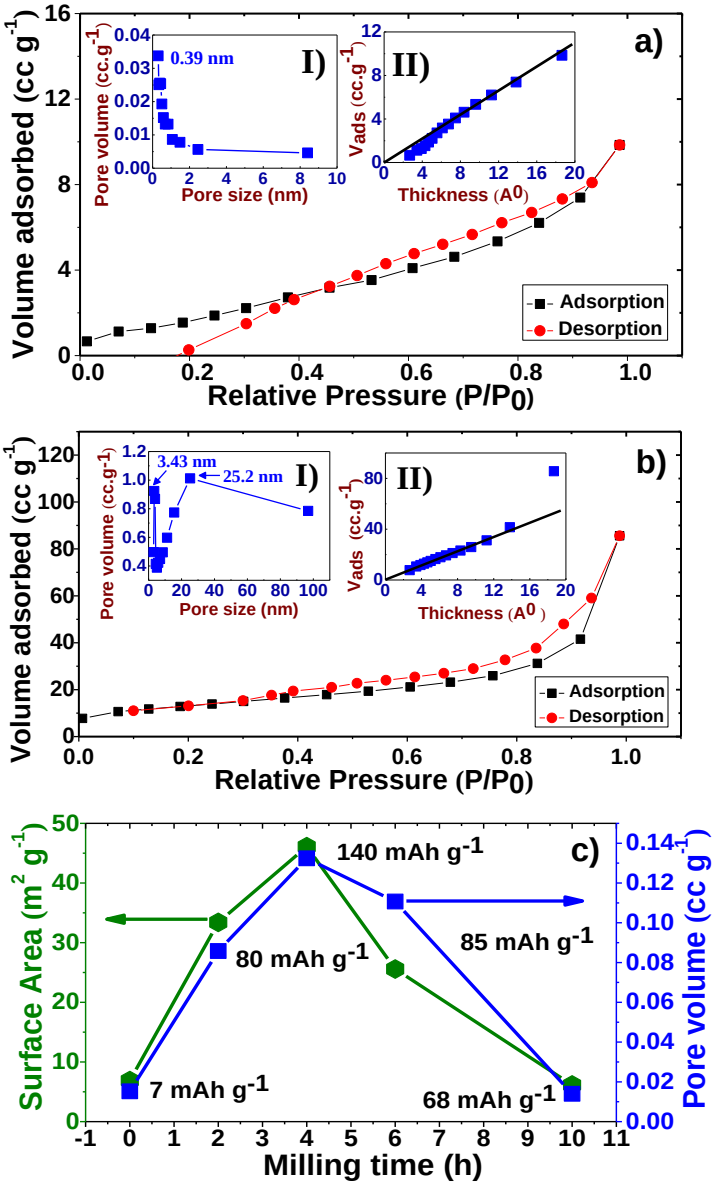

Figure 3.9 (a) Nitrogen physisorption isotherms of pristine sample with inset I showing pore size distribution and inset II showing V-t plots (b) Nitrogen physisorption isotherms of 4 h HEBM sample with inset I showing pore size distribution and inset II showing V-t plots (c) Variation of specific capacity as a function of surface area, pore volume and milling time at 0.05C.

During ball milling, large grains are divided into small grains and new surfaces are created. These small grains tend to aggregate during course of milling and heat treatment forming secondary particles. Pores are developed in this process within/between secondary particles as depicted in **Scheme 1**.

3.4.3 Effect of porous characteristics on lithium storage performance

Figure 3.9c illustrates the surface area, pore volume and corresponding storage performance at 0.05C rate as a function of milling time. Upon increasing the ball milling time to 4 h, the specific surface area, pore volume and pore size increases gradually. However, these parameters decrease with further increase in the milling time beyond 4 h. Agglomeration and pore narrowing witnessed for 6 and 10 h ball milled samples results in lower surface area and pore volume **(Table 3., Figure 3.10 and Figure 3.6c)**. The above observed pore-structural and surface area differences are vital in understanding the differences in the storage performance of $LiMnPO_4$/C. The specific capacity increases as a function of milling time up to 4h beyond which the capacity decreases. For example, the 4 h ball milled sample with grain size: ~40 nm, surface area: 46.60 m^2 g^{-1}, pore sizes: 3.43 and 25.20 nm and pore volume: 0.132 cc g^{-1} delivered lithium storage performance of 140 mAh g^{-1} with attractive voltage profile and less polarization. This was in sharp contrast to pristine $LiMnPO_4$ with grain size: ~120 nm, surface area: 6.9 m^2 g^{-1}, pore size: 0.39 nm and pore volume: 0.015 cc g^{-1} that delivered only 7 mAh g^{-1} with a huge polarization. Such significant difference in the lithium storage performance suggests the need for careful control of grain size, surface area, pore size and pore volume of the active material.

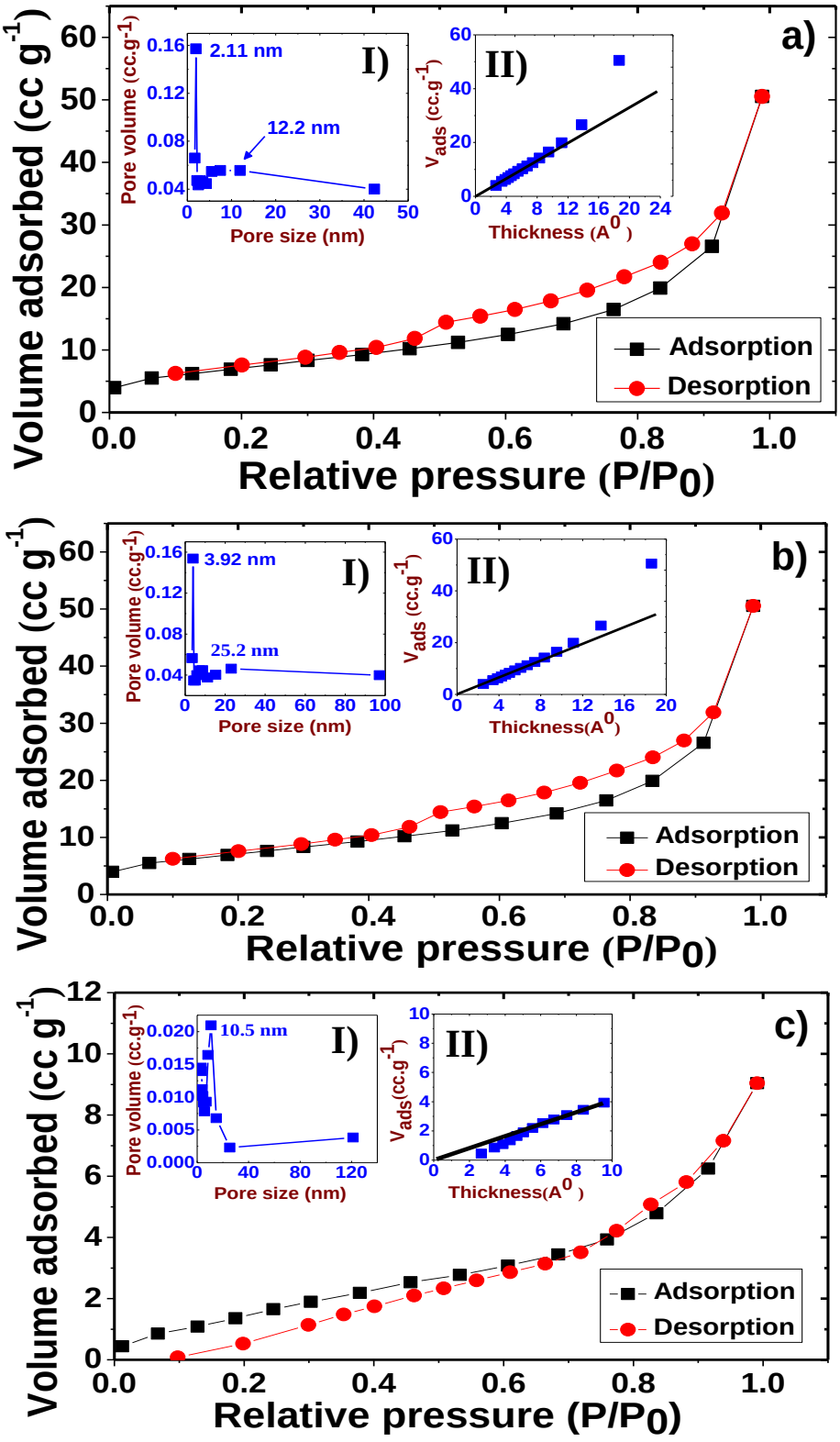

Figure 3.10 Nitrogen sorption isotherm, pore size distribution (inset (I)) and V-t plots (inset (II)) of various samples, (a) 2 h HEBM, (b) 6 h HEBM and (c) 10 h HEBM.

Table 3.4 Nitrogen adsorption and desorption data as a function of milling time.

HEBM time (h)	0	2	4	6	10
Surface Area (*S_{BET}) ($m^2.g^{-1}$) (±0.5)	6.9	33.4	46.6	26.7	9.5
Surface Area (*S_t) ($m^2.g^{-1}$) (±0.5)	6.9	33.4	46.6	26.7	9.5
Pore volume ($cc.g^{-1}$) (±0.005)	0.015	0.085	0.132	0.110	0.014
Pore size (nm) (±0.05)	0.39	2.11 (12.20)	3.43 (25.20)	3.92 (25.20)	10.5

S_{BET} – Surface area by Brunauer–Emmet–Teller equation; S_t –Surface area derived from V-t plot.

3.4.4 Diffusion study

We consider here the 4 h HEBM $LiMnPO_4$/C as a representative sample to study the diffusion limitation of electrochemical process. The anodic peak at 4.3 V (anodic oxidation) and the cathodic peak at 3.96 V (cathodic reduction) are attributed to the Mn^{2+}/Mn^{3+} redox couple which is in good agreement with galvanostatic cycling **(Figure 3.11a)**. The voltage hysteresis (ΔV, difference between the anodic and cathodic peak voltages) increased with increasing scan rates **(Figure 3.11b)**. The current ratio of the anodic and cathodic peaks being unity **(Figure 3.11b),**[383] there are no perceivable side reactions during the insertion and extraction processes. The linear relationship between the peak current (i_p) and the square root of the scan rate ($v^{1/2}$) suggests that the electrochemical process is purely limited by diffusion **(Figure 3.11c)**.[383] Hence, to calculate the diffusion coefficients,

electrochemical impedance spectroscopy (EIS) studies were carried out on fresh cells.

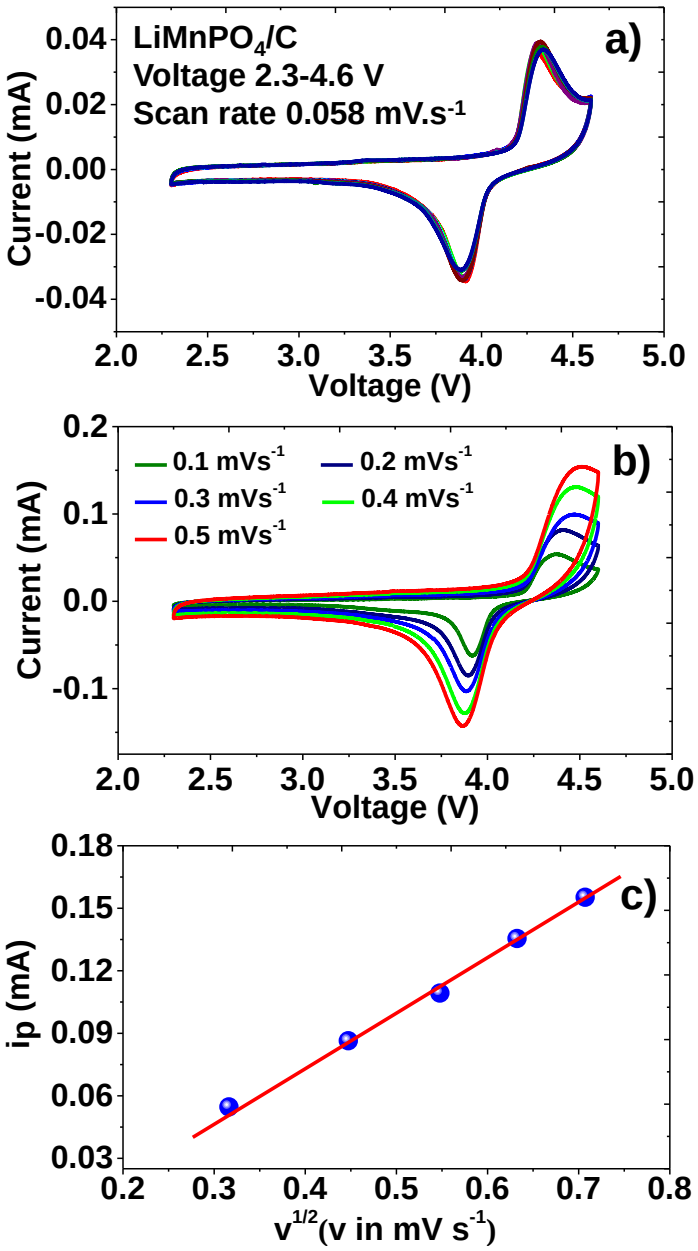

Figure 3.11 Cyclic Voltammograms (CV) of ball milled sample for 4 h with 25 wt% $LiMnPO_4$/C (a) at a scan rate of 0.058 mV s^{-1}, (b) CV plots at different scan rates 0.1, 0.2, 0.3, 0.4 and 0.5 mV s^{-1} and (c) the relationship between the peak current (i_p) and the square root of scan rate ($v^{1/2}$).

Figure 3.12a shows the fitting of experimental data using the following equivalent circuit model **(Equation 3.1) (Figure 3.12b).**[137]

$$\mathbf{R_S + (R_1||CPE_1) + (R_2 || CPE_2) + W_o} \qquad \mathbf{(3.1)}$$

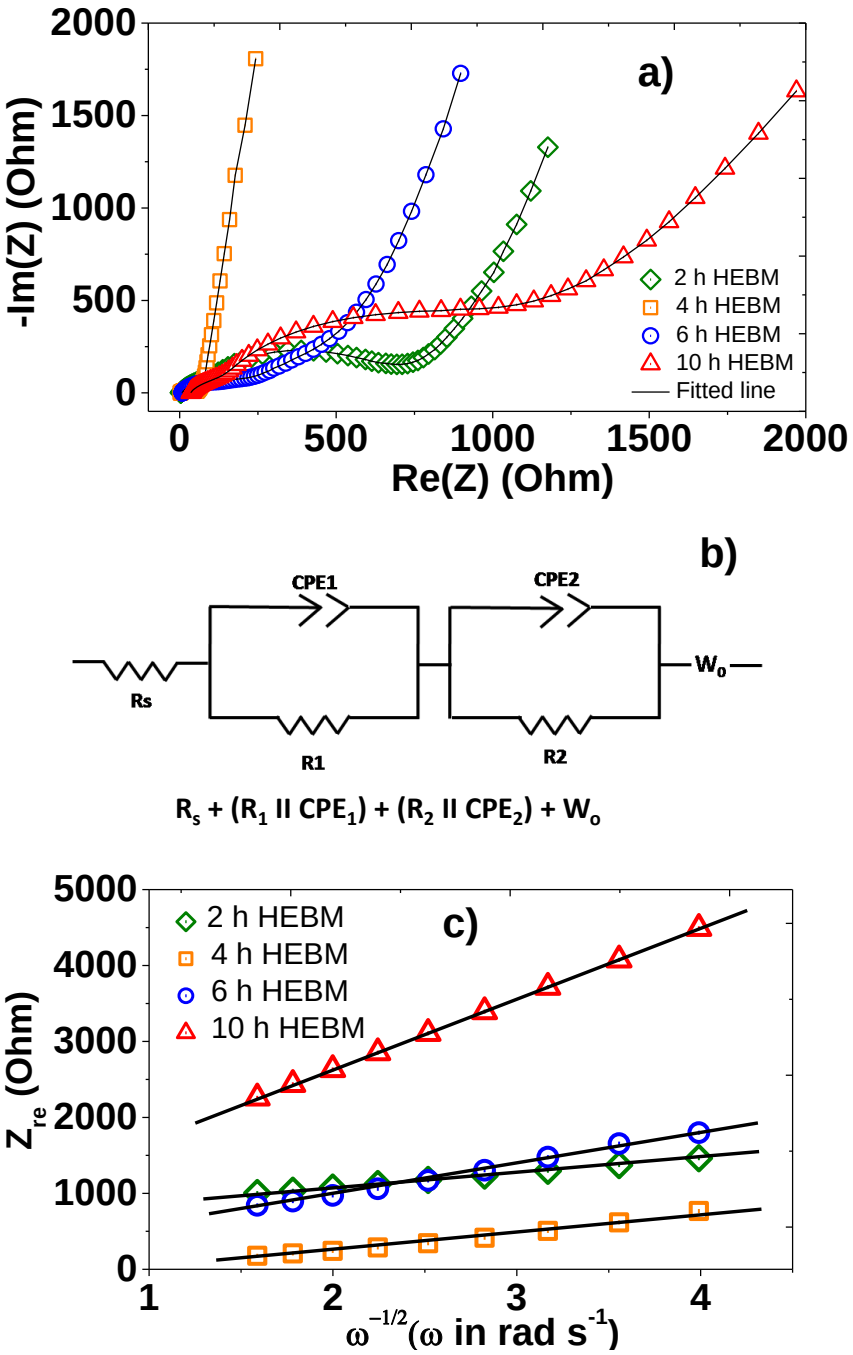

Figure 3.12 (a) Nyquist impedance spectra of $LiMnPO_4$/C of fresh cell at various milling times, (b) equivalent circuit, (c) linear fittings between Z_{re} and reciprocal square root of the angular frequency in low frequency region.

where, R_S is the solution resistance associated with the electrolyte and electrical contacts. $(R_1||CPE_1) + (R_2||CPE_2)$ refers to two depressed semicircles associated with the charge transfer process (R_1 and R_2 - charge transfer resistance; CPE_1 and CPE_2 - constant phase element and W_o is Warburg

element associated with solid state Li^+ ions diffusion in the bulk electrode. The fitted values of R_S, R_1 and R_2 for fresh cells are given in **Table 3..**

Table 3.5 Impedance parameters derived using equivalent circuit model for $LiMnPO_4$/C at various milling time.

Fresh cells					
Milling time	$R_s(\Omega)$	$R_1(\Omega)$	$CPE_1(x10^{-6}\,F)$	$R_2(\Omega)$	$CPE_2(x10^{-6}\,F)$
2 h	2.9	550.0	34.7	69.4	11.4
4 h	4.5	46.9	24.0	9.8	25.4
6 h	7.7	179.2	21.7	81.5	16.2
10 h	5.2	658.7	43.5	66.2	11.3

In this study, the mid frequency semi-circular arc is fitted with two overlapped depressed semicircles corresponding to ($R_1\|CPE_1$) and ($R_2\|CPE_2$) which can be attributed to the complex charge transfer processes from the electrolyte to bulk of the electrode surfaces. It is suggested that R_1 and R_2 relates to the resistance associated with Li^+-ion transfer resistance at the electrode-electrolyte interface (surface film resistance) and charge transfer resistance respectively.[137] The improvement in the Warburg inclined lines at low frequency region of the spectra strongly suggests[137] that the Li^+-ion diffusion in 4 h ball milled mesoporous $LiMnPO_4$/C is better than other ball milled samples (2, 6 and 10 h HEBM). Apparent lithium-ion diffusion coefficient (D_{Li^+}) has been calculated for all the HEBM samples using the **Equation (3.2).**

$$D_{Li^+} = \frac{R^2T^2}{2A^2n^4F^4C^2\sigma^2} \quad \textbf{(3.2)}$$

where R is the gas constant (8.314 J mol^{-1} K^{-1}), T is the absolute temperature, A is the contact area of the electrode (2.01 cm^2), n is the number of electrons per molecule, F is the Faraday constant (96485 C mol^{-1}), C is the concentration of Li^+-ion (6.38 x 10^{-3} mol cm^{-3}) (ratio between the tap density of the prepared material and molecular weight) and σ is the Warburg coefficient associated with the slope of the linear fittings between Z_{re} and reciprocal square root of the angular frequency at low frequency region[187] **(Figure 3.12c)**.

Note that the apparent D_{Li^+} for 4 h HEBM mesoporous electrode is 7.09 x10^{-14} cm^2 s^{-1} which is higher than the values for other HEBM electrodes (3.96x10^{-15} , 1.55 x10^{-14} and 2.72 x10^{-16} cm^2 s^{-1} for 2, 6 and 10 h HEBM electrodes respectively), consistent with the literature.[177, 384] Further, the 4 h HEBM electrode exhibits the lowest impedance compared to other ball milled samples which is consistent with the changes in the lithium storage performance. Finally, it may be noted that the limiting factor in $Li_{1-x}MnPO_4/Li_xMnPO_4$ intercalation/deintercalation reaction is due to the ionic conductivity and/or electronic conductivity.[89]

3.4.5 Lithium storage performance of mesoporous $LiMnPO_4$/C

The cycle life, rate capability and full cell testing of the $LiMnPO_4$/C ball milled for 4 h are demonstrated in the **Figure 3.13.** The specific discharge profiles of corresponding electrode at different current rates are shown in **Figure 3.13a**. This electrode exhibits lithium storage capacities of 140, 120, 98, 94 and 61 mAh g^{-1} (based on active material weight ($LiMnPO_4$)) at 0.05,

0.1, 0.2, 0.5 and 1C respectively. **Figure 3.13b** illustrates the specific discharge capacities for 30 cycles at various rates. Further, when cycled from 0.1C to 5C and upon further cycling at 0.1C, the cells could retain more than 92% of their initial capacity **(Figure 3.13c)** which shows the robustness of the electrode material.

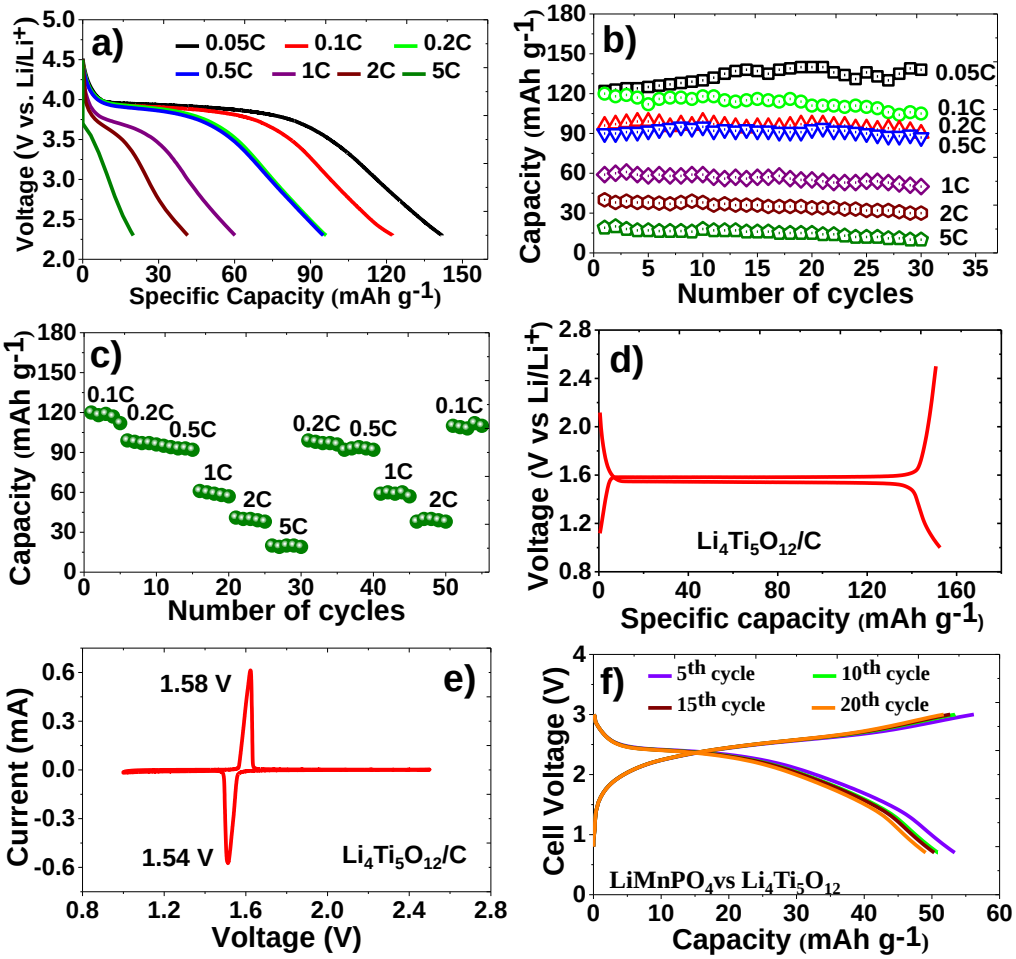

Figure 3.13 (a) Voltage profiles of mesoporous $LiMnPO_4$/C at different current rates at Constant Current mode (b) Cyclability at various current rates, (c) Rate capability, (d) Charge and discharge profiles of $Li_4Ti_5O_{12}$/C vs. Li metal, (e) Cyclic Voltammograms (CV) of $Li_4Ti_5O_{12}$/C vs. Li metal in EC-DEC/ 1 M $LiPF_6$ solutions at room temperature (f) Voltage profile of $LiMnPO_4$/C vs. $Li_4Ti_5O_{12}$/C up to 20 cycles at 1C, the voltage window of 0.5-3.2 V (capacity values are calculated based on active material ($LiMnPO_4$) weight in the electrode).

In order to validate the capability of $LiMnPO_4$/C electrode as a possible cathode material for the Li-ion battery application, preliminary full

cell test was performed using $Li_4Ti_5O_{12}$/C anode material. **Figure 3.13d-3.13e** shows the voltage profile and CV of $Li_4Ti_5O_{12}$/C against Li metal in a half cell in EC-DEC/1 M $LiPF_6$ solutions at room temperature (RT). **Figure 3.13f** presents a typical voltage profile of full cell consisting of $LiMnPO_4$/C vs. $Li_4Ti_5O_{12}$/C up to 20 cycles at 1C in the voltage window of 0.5-3.2 V at room temperature (initial formation cycles are not shown). During charging, Li^+ ions are removed from $LiMnPO_4$ cathode and inserted into $Li_4Ti_5O_{12}$ anode resulting in the formation of $Li_{1-x}MnPO_4$ and $Li_7Ti_5O_{12}$ at cathode and anode respectively.[125] During discharge, the Li^+-ions are extracted from the anode and inserted back into the cathode. The average voltage and capacity of this full cell was ~2.3 V and 54 mAh g^{-1} at a current rate of 1C which is close to half cell capacity at 1C using lithium metal as a counter electrode.

3.5 Summary

In summary, the preparation of mesoporous carbon coated $LiMnPO_4$ cathodes featuring interconnected nano-grains, using a high energy ball mill assisted soft template method was demonstrated. Such mesoporous $LiMnPO_4$/C delivered lithium storage performance of 140 mAh g^{-1} at 0.05C with flat operating voltage. This was in sharp contrast to pristine microporous $LiMnPO_4$ that delivered only 7 mAh g^{-1} at 0.05C with no perceivable plateaus. This study also underlined the interdependence of lithium storage performance of $LiMnPO_4$/C on carbon content, milling time, grain size and porous characteristics namely, surface area, pore size and pore volume.

As seen, the lithium storage performance of mesoporous $LiMnPO_4$/C is one of highest reported values. However, the capacity is lower than the theoretical capacity of $LiMnPO_4$ (140 mAh g^{-1} < 170 mAh g^{-1}) especially at

higher current rates. In the next chapter, the storage capacity of $LiMnPO_4$ will be enhanced by combining above architecture with isovalent co-doping (Fe^{2+} and Mg^{2+}).

Chapter 4

4. Enhancing the electrochemical kinetics of high voltage olivine $LiMnPO_4$ by isovalent co-doping

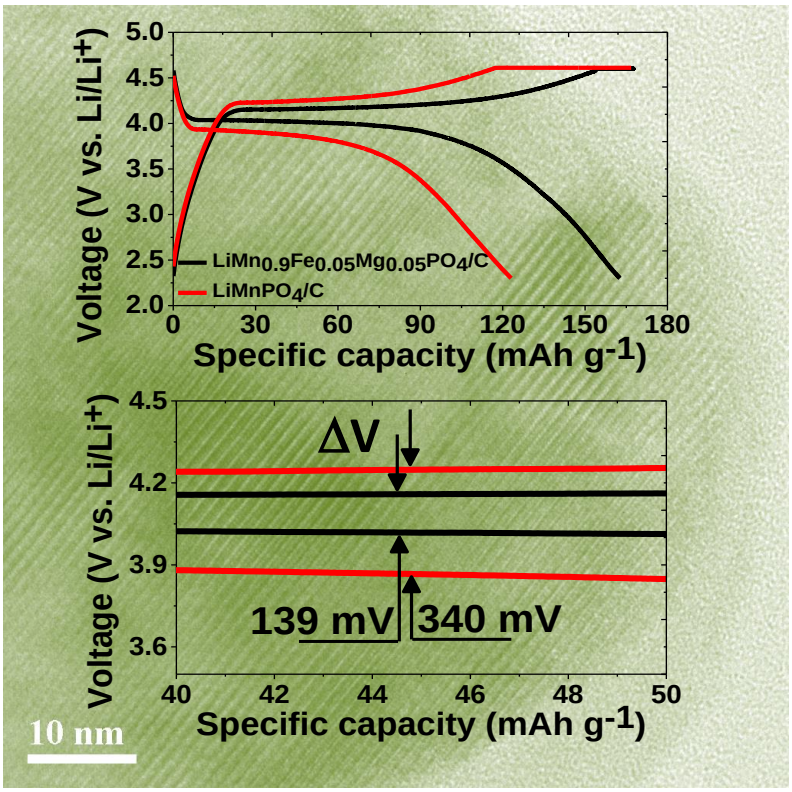

4.1 Preface to Chapter 4

Doping of Fe^{2+} and/or Mg^{2+} in $LiMnPO_4$ cathode material was carried out to enhance its lithium storage performance and appraise the effect of doping. For this purpose, $LiMn_{0.9}Fe_{(0.1-x)}Mg_xPO_4/C$ (x = 0 and 0.05) and $LiMn_{0.95}Mg_{0.05}PO_4/C$ have been prepared by a ball mill assisted soft template method. These materials were prepared with similar morphology, particles size and carbon content. Amongst them, the isovalent co-doped $LiMn_{0.9}Fe_{0.05}Mg_{0.05}PO_4/C$ sample shows better electrochemical performance compared to $LiMn_{0.9}Fe_{0.1}PO_4/C$ and $LiMn_{0.95}Mg_{0.05}PO_4/C$ samples. The improved electrochemical performance of co-doped $LiMnPO_4$ is thus explained in terms of (i) favorable extraction and insertion reactions, (ii) partial suppression of Mn dissolution in the electrolyte and (ii) enhanced transport properties.

4.2 Introduction

Previous reports in enhancing the storage performance of $LiMnPO_4$ has focused on (i) particle size reduction;[108, 125, 138-140, 385-387] (ii) carbon coating,[121, 136, 142, 143, 149] (iii) forming Mn-Fe solid solutions[94, 131, 161, 388, 389] and (iv) doping using transition metals[137, 150, 151, 176-181, 183, 390] such as Fe^{2+}, Mg^{2+}, Zn^{2+}, Cu^{2+}, Ni^{2+} and Co^{2+}. Among these the Mn-Fe solid solutions have attracted great attention due to high storage capacity. However, the disadvantage with Mn-Fe solid solutions is that the overall energy density could be lowered owing to the lower equilibrium potential of Fe^{2+}/Fe^{3+} (3.45 V) redox couple.[11, 22, 31-34, 391] On the other hand, divalent metal doping such as Fe^{2+}, Mg^{2+}, Zn^{2+}, Cu^{2+}, Ni^{2+} and Co^{2+} enables to enhance the storage performance of $LiMnPO_4$ without compromising the energy density significantly as the presence of dopant is much smaller and is not reflected in the voltage profiles.[180]

The lithium storage performance of mesoporous $LiMnPO_4$/C is lower than the theoretical capacity of $LiMnPO_4$ especially at higher current rates **(chapter 3)**. Keeping this in mind, we discuss in this chapter the doping of Fe^{2+} and/or Mg^{2+} in $LiMnPO_4$/C cathode material to enhance its lithium storage performance. For this purpose, $LiMn_{0.9}Fe_{(0.1-x)}Mg_xPO_4$/C (x = 0 and 0.05) and $LiMn_{0.95}Mg_{0.05}PO_4$/C samples were synthesized by ball mill assisted soft template approach **(Scheme 1).** Among these compositions, isovalent co-doped $LiMn_{0.9}Fe_{0.05}Mg_{0.05}PO_4$/C electrode delivers discharge capacities of 159, 155, 141, 118, 104, 81 and 51 mAh g^{-1} at 0.1, 0.2, 0.5, 1, 2, 5 and 10C rates respectively with less polarization of ~139 mV compared to other samples investigated. This electrode material also retains capacity of 116 mAh

g^{-1} at 1C after 200 cycles, which is 96% of its initial capacity. The storage performance achieved here for co-doped $LiMn_{0.9}Fe_{0.05}Mg_{0.05}PO_4/C$ is the highest among the reports in literature for $LiMnPO_4$ using divalent doping technique in the transition metal (Mn) site especially at low rates.[151, 176, 178, 180, 181, 392] The role of divalent doping or co-doping on the dissolution of Mn is also elucidated. Further, possible reasons for improved storage performance of isovalent co-doped $LiMnPO_4$ is demonstrated in terms of (i) the favourable redox combination which in turn provides beneficial environment for the delithiation and lithiation processes and (ii) enhanced transport properties.

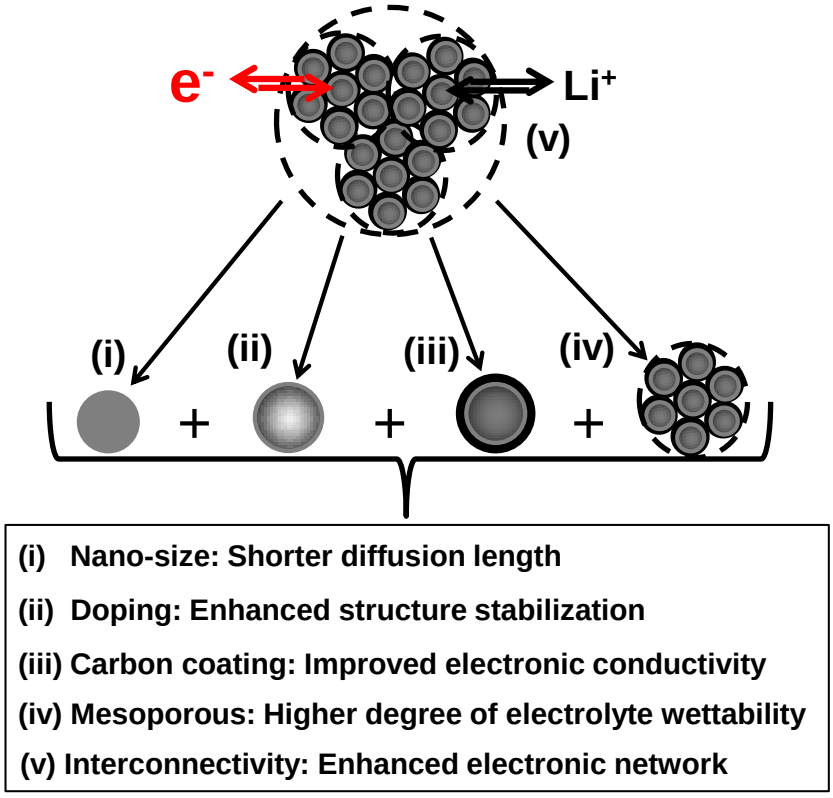

Scheme 1 Schematic illustration of strategies employed in this work to enhance the electrochemical kinetics of $LiMnPO_4/C$.

4.3 Experimental

4.3.1 Synthesis of doped and co-doped $LiMnPO_4/C$

Fe^{2+} and/or Mg^{2+} doped and co-doped $LiMn_{0.9}Fe_{(0.1-x)}Mg_xPO_4/C$ (x = 0 and 0.05) and $LiMn_{0.95}Mg_{0.05}PO_4/C$ were synthesized using soft template method followed by high energy ball milling process **(see chapter 3, scheme 2)**. In the synthesis, 0.01 M of CTAB ($(C_{16}H_{33})N(CH_3)_3Br$, Sigma Aldrich) was dissolved in a round bottom flask with a mixture of millQ water and absolute ethanol in the volume ratio of 1:5 and the solution was stirred for 90 min. to initiate micellar formation, followed by the addition of lithium dihydrogen phosphate (LiH_2PO_4, Sigma Aldrich), manganese (II) acetate tetrahydrate ($Mn(CH_3CO_2)_2.4H_2O$, Sigma Aldrich), iron (II) acetate tetrahydrate ($Fe(CH_3CO_2)_2.4H_2O$, Sigma Aldrich) and magnesium (II) acetate tetrahydrate ($Mg(CH_3CO_2)_2.4H_2O$, Sigma Aldrich) in stoichiometric proportion. The solution was further stirred for 24 h. The solvents were evaporated using an IKA RV10 roto-evaporator. The precipitate was calcined in a tubular furnace at 650 $^{\circ}$C for 6 h in an $Ar:H_2$ (95:5) atmosphere.[135] The calcined sample was ball-milled with 25 wt% acetylene black using FRITSCH premium line – pulverisette 7 instrument at 500 rpm for 4 h with the weight ratio of sample: balls = 1:40 Further, the ball milled sample was heat-treated again at 500 $^{\circ}$C for 3 h in an $Ar:H_2$ atmosphere.

4.3.2 Material and electrochemical characterization

Above samples were characterized using PXRD, Rietveld refinement, FESEM, EDXS, TEM, BET, XPS, galvanostatic cycling, cyclic voltammetry and electrochemical impedance spectroscopy. The details are given in chapter 2, section 2.2.1 section 2.3 , section 2.4 and section 2.5 .

4.4 Results and discussion

4.4.1 Structural and morphological characterization

Figure 4.1 shows PXRD of $LiMn_{0.9}Fe_{(0.1-x)}Mg_xPO_4/C$ (x = 0 and 0.05) and $LiMn_{0.95}Mg_{0.05}PO_4/C$. All the diffraction peaks could be indexed to $LiMnPO_4$ which belongs to the *Pmnb* space group (JCPDS card no. 33-0803) with an orthorhombic structure. No other perceivable impurity phases were observed.

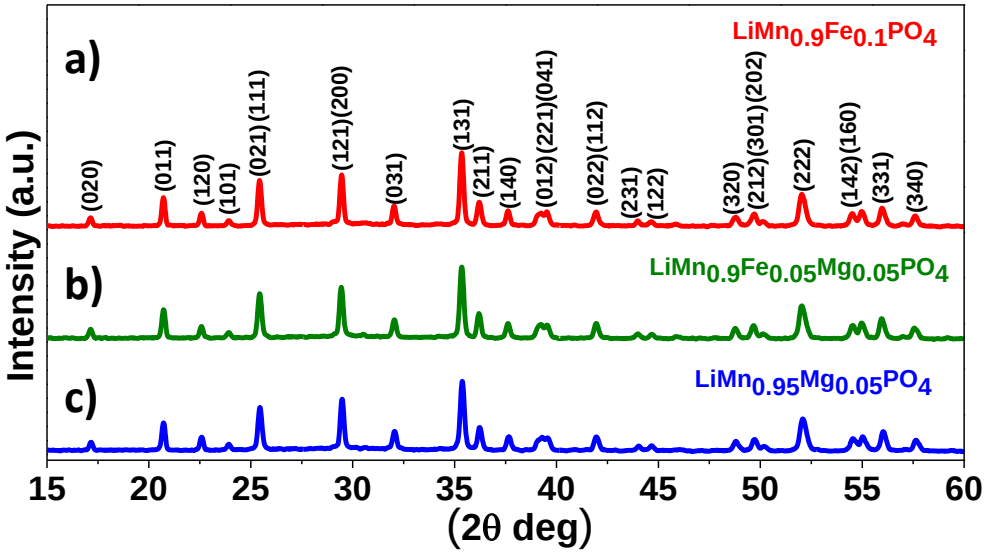

Figure 4.1 PXRD patterns of (a) $LiMn_{0.9}Fe_{0.1}PO_4/C$, (b) $LiMn_{0.9}Fe_{0.05}Mg_{0.05}PO_4/C$ and (c) $LiMn_{0.95}Mg_{0.05}PO_4/C$.

Changes in the lattice parameters and unit cell volume of the above samples compared to parent member ($LiMnPO_4$) are presented in **Table 4.1,** which are in good agreement with the literature.[143, 151, 178, 180, 181, 390] The differences in the cell volume of the various samples could be understood by the change in the ionic radii of the transition metals (Mn^{2+} = 0.97 Å, Fe^{2+} = 0.92 Å and Mg^{2+} = 0.86 Å) in the active material.[151, 176, 178-181, 393]

Table 4.1 Lattice parameters and cell volume of doped and co-doped $LiMnPO_4$/C materials obtained by Rietveld refinement.

Electrode material	a (Å)	b (Å)	c (Å)	V ($Å^3$)	Changes in the cell volume in (%) with respect to $LiMnPO_4$ (reference) *Pmnb* space group (*JCPDS card no. 33-0803*)
$LiMnPO_4$ (reference) *Pmnb* space group (*JCPDS card no. 33-0803*)	6.108	10.459	4.732	302.29	-
$LiMn_{0.9}Fe_{0.1}PO_4$	6.102(6)	10.447(4)	4.726(6)	301.33	0.32
$LiMn_{0.9}Fe_{0.05}Mg_{0.05}PO_4$	6.091(4)	10.427(5)	4.720(6)	299.83	0.81
$LiMn_{0.95}Mg_{0.05}PO_4$	6.104(5)	10.436(3)	4.718(7)	300.62	0.55

Further, we have carried out Rietveld refinement for XRD data to check the position of dopants (Fe^{2+} and/or Mg^{2+}) using TOPAS 3.0 version. The quality of the refinement and dopant position were determined based on R_{exp}, R_{wp} and R_p values **(Figure 4.2 and Table 4.2)**.[114, 180, 394]

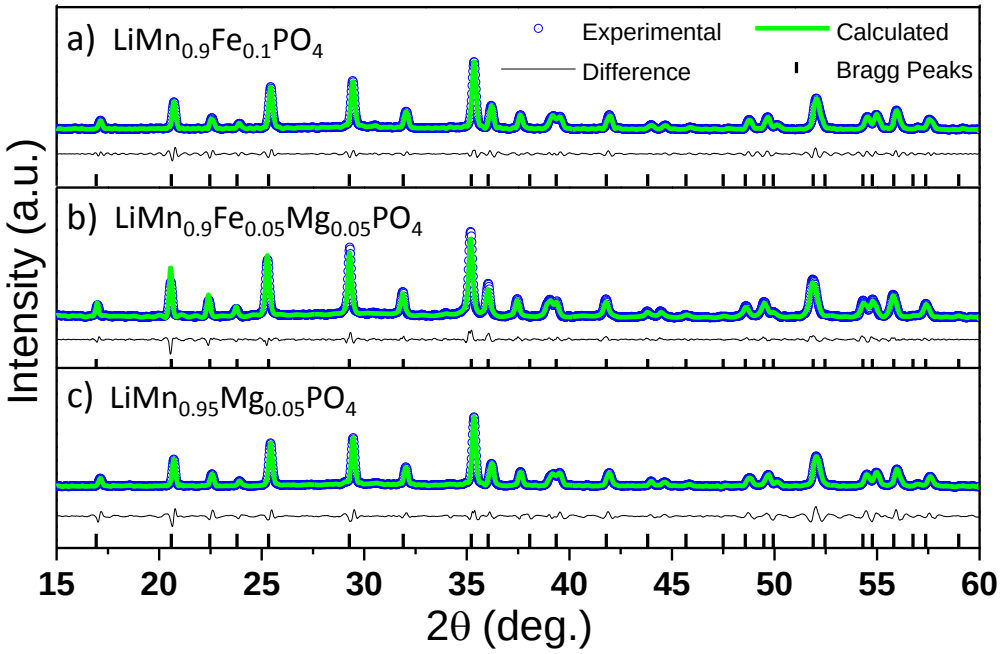

Figure 4.2 Rietveld refinement of (a) $LiMn_{0.9}Fe_{0.1}PO_4$ (R_{exp}:4.91, R_{wp}:1.04 and R_p:0.61), (b) $LiMn_{0.9}Fe_{0.05}Mg_{0.05}PO_4$ (R_{exp}:6.77, R_{wp}:1.65 and R_p:0.99) and (c) $LiMn_{0.95}Mg_{0.05}PO_4$ (R_{exp}:6.79, R_{wp}:1.71 and R_p:1.08).

For instance in the case of $LiMn_{0.9}Fe_{0.05}Mg_{0.05}PO_4$ firstly, assuming the Mg^{2+} and Fe^{2+} occupy only Li sites, the reliability factor were R_{exp}:6.77, R_{wp}:1.83 and R_p:1.10; secondly, assuming the Mg^{2+} and Fe^{2+} occupy only Mn sites, then the reliability factors R_{exp}:6.77, R_{wp}:1.80 and R_p:1.07; thirdly, assuming the Mg^{2+} and Fe^{2+} occupy simultaneously both Li and Mn sites, then the reliability factors are R_{exp}:6.77, R_{wp} : 1.65 and R_p:0.99. Based on good reliability factors as seen from the third case and observed site occupancies as shown in **Table 4.2**, Mg^{2+} and Fe^{2+} are most likely to occupy Mn sites. Under these lines, $LiMn_{0.9}Fe_{0.1}PO_4$ and $LiMn_{0.95}Mg_{0.05}PO_4$ were also refined based on above three possibilities. Similarly, we found that Fe^{2+} or Mg^{2+} occupy

simultaneously both Li and Mn sites as inferred from the better reliability factors (R_{exp}:4.91, R_{wp}:1.04 and R_p:0.61 for $LiMn_{0.9}Fe_{0.1}PO_4$; R_{exp}:6.79, R_{wp}:1.71 and R_p:1.08 for $LiMn_{0.95}Mg_{0.05}PO_4$). Hence, as seen from the site occupancies in all the samples **(Table 4.2)** from Rietveld refinement, Fe^{2+} and/or Mg^{2+} is found to be substituted mostly in the Mn site , not in the Li site.

Table 4.2 Site occupancies of $LiMn_{0.9}Fe_{(0.1-x)}Mg_xPO_4/C$ (x = 0 and 0.05) and $LiMn_{0.95}Mg_{0.05}PO_4/C$. Data for $LiMnPO_4/C$ is given for the sake comparison, whose Mn, P and O refined positions are consistent with literature report.[36, 42, 43]

$LiMnPO_4$ (R_{exp}:11.24 R_{wp}:4.04 R_p:3.21)						
Atom	Site	x	y	z	Occupancy (theoretical)	Occupancy (Observed)
Li1 (Li^{+1})	4a	0.0	0.0	0.0	1	1
Mn1(Mn^{+2})	4c	0.2500	0.2817	0.0281	1	1
P1(P^{+5})	4c	0.2500	0.0923	0.4081	1	1
O1(O^{-2})	4c	0.2500	0.0968	0.2664	1	1
O2(O^{-2})	4c	0.2500	0.4561	0.2073	1	1
O3(O^{-2})	8d	0.0492	0.1609	0.2781	1	1
$LiMn_{0.9}Fe_{0.1}PO_4$ (R_{exp}:4.91 R_{wp}:1.04 R_p:0.61)						
Li1 (Li^{+1})	4a	0.0	0.0	0.0	1	0.9994
Li2 (Li^{+1})	4c	0.2500	0.2817	0.0281	0	0.0006
Fe1(Fe^{+2})	4a	0.0	0.0	0.0	0	0.0006
Fe2(Fe^{+2})	4c	0.2500	0.2817	0.0281	0.1	0.0994
Mn1(Mn^{+2})	4c	0.2500	0.2817	0.0281	0.90	0.90
P1(P^{+5})	4c	0.2500	0.0923	0.4081	1	1
O1(O^{-2})	4c	0.2500	0.0968	0.2664	1	1
O2(O^{-2})	4c	0.2500	0.4561	0.2073	1	1
O3(O^{-2})	8d	0.0492	0.1609	0.2781	1	1
$LiMn_{0.9}Fe_{0.05}Mg_{0.05}PO_4$ (R_{exp}:6.77 R_{wp}:1.65 R_p:0.99)						
Li1 (Li^{+1})	4a	0.0	0.0	0.0	1	0.9987
Li2 (Li^{+1})	4c	0.2500	0.2817	0.0281	0	0.0013
Mg1(Mg^{+2})	4a	0.0	0.0	0.0	0	0.0013
Mg2(Mg^{+2})	4c	0.2500	0.2817	0.0281	0.05	0.0487
Fe2(Fe^{+2})	4c	0.2500	0.2817	0.0281	0.05	0.05
Mn1(Mn^{+2})	4c	0.2500	0.2817	0.0281	0.90	0.90
P1(P^{+5})	4c	0.2500	0.0923	0.4081	1	1
O1(O^{-2})	4c	0.2500	0.0968	0.2664	1	1
O2(O^{-2})	4c	0.2500	0.4561	0.2073	1	1
O3(O^{-2})	8d	0.0492	0.1609	0.2781	1	1

$LiMn_{0.95}Mg_{0.05}PO_4$ (R_{exp}:6.79 R_{wp}:1.71 R_p:1.08)						
Li1 (Li^{+1})	4a	0.0	0.0	0.0	1	0.9986
Li2 (Li^{+1})	4c	0.2500	0.2817	0.0281	0	0.0014
Mg1(Mg^{+2})	4a	0.0	0.0	0.0	0	0.0014
Mg2(Mg^{+2})	4c	0.2500	0.2817	0.0281	0.05	0.0486
Mn1(Mn^{+2})	4c	0.2500	0.2817	0.0281	0.95	0.95
P1(P^{+5})	4c	0.2500	0.0923	0.4081	1	1
O1(O^{-2})	4c	0.2500	0.0968	0.2664	1	1
O2(O^{-2})	4c	0.2500	0.4561	0.2073	1	1
O3(O^{-2})	8d	0.0492	0.1609	0.2781	1	1

FESEM images of $LiMn_{0.9}Fe_{(0.1-x)}Mg_xPO_4/C$ (x = 0 and 0.05) and $LiMn_{0.95}Mg_{0.05}PO_4/C$ samples are shown in **Figure 4.3**. FESEM images of all the samples show presence of similar particle size with a pseudo-spherical morphology. EDXS analysis confirms presence of magnesium and/or iron uniformly within the active material **(Figure 4.4)**. Further, a uniform distribution of carbon around the active materials is also seen.

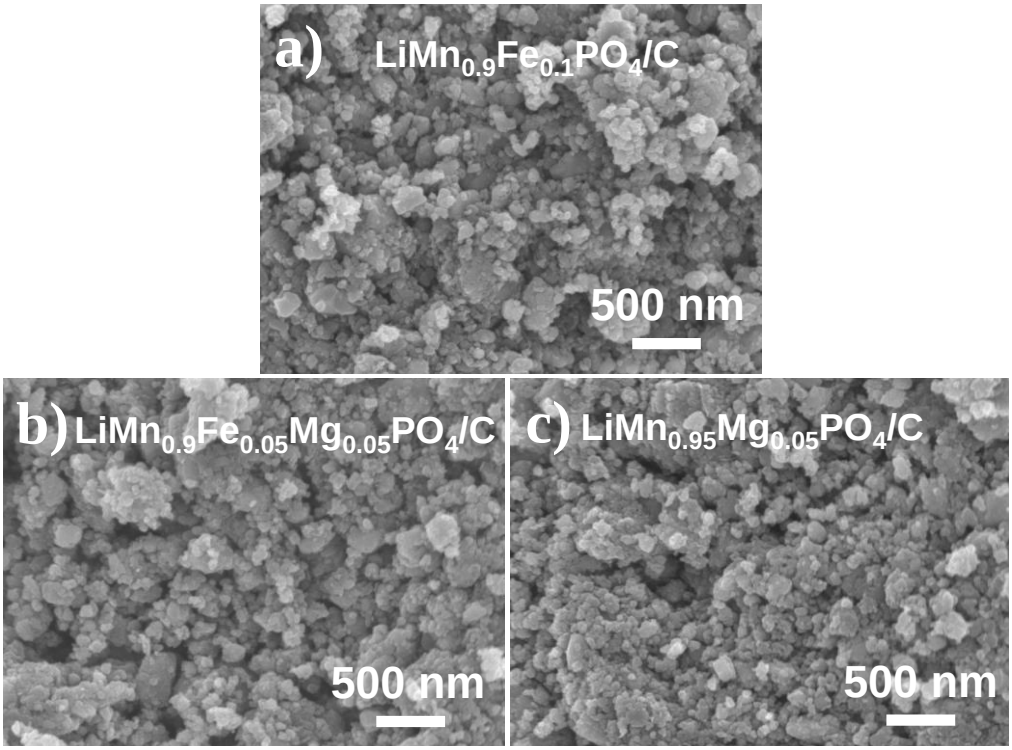

Figure 4.3 FESEM images of (a) $LiMn_{0.9}Fe_{0.1}PO_4$, (b) $LiMn_{0.9}Fe_{0.05}Mg_{0.05}PO_4$ and (c) $LiMn_{0.95}Mg_{0.05}PO_4$.

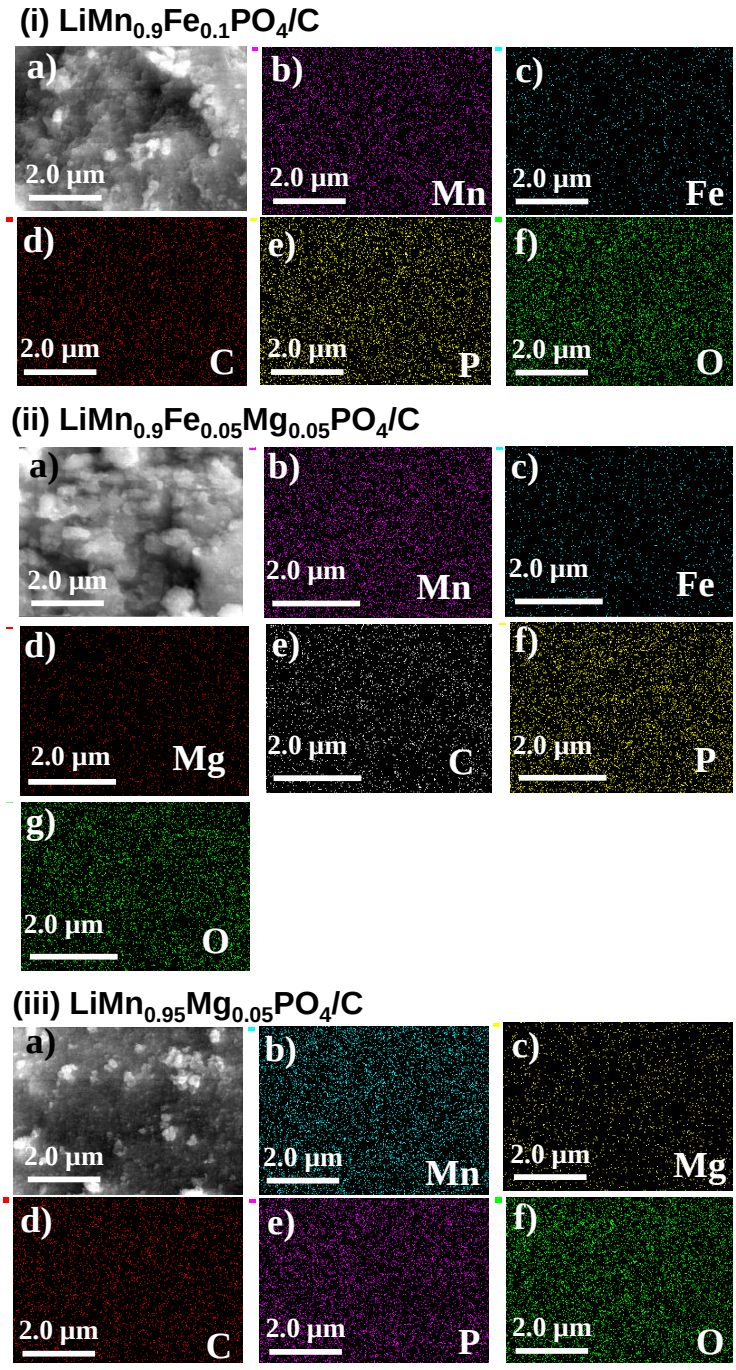

Figure 4.4 Elemental mapping images and corresponding SEM images of (i) $LiMn_{0.9}Fe_{0.1}PO_4/C$, (ii) $LiMn_{0.9}Fe_{0.05}Mg_{0.05}PO_4/C$ and (iii) $LiMn_{0.95}Mg_{0.05}PO_4/C$.

Figure 4.5 shows the bright field TEM and HRTEM images of $LiMn_{0.9}Fe_{(0.1-x)}Mg_xPO_4/C$ (x = 0 and 0.05) and $LiMn_{0.95}Mg_{0.05}PO_4/C$ materials. The particles appear to be interconnected with an individual particle size in the range of 20 - 40 nm **(Figure 4.5a, 4.5c and 4.5e)**. HRTEM images shows the

lattice fringes with *d*-spacing of 4.32 Å ($LiMn_{0.9}Fe_{0.1}PO_4/C$), 5.23 Å ($LiMn_{0.9}Fe_{0.05}Mg_{0.05}PO_4/C$) and 3.97 Å ($LiMn_{0.95}Mg_{0.05}PO_4/C$) corresponding to (011), (020) and (120) planes respectively of pure $LiMnPO_4$ **(Figure 4.5b, 4.5d and 4.5f)**. HRTEM images also show the presence of carbon coating (~5±2 nm) around the active materials.

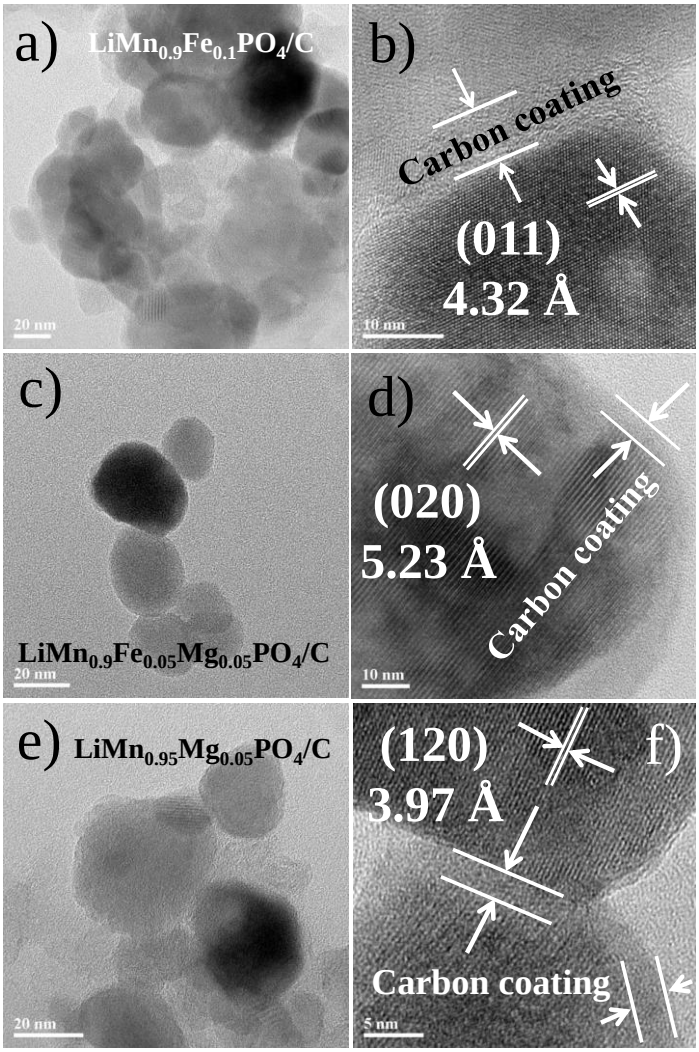

Figure 4.5 TEM and HRTEM images of (a and b) $LiMn_{0.9}Fe_{0.1}PO_4/C$, (c and d) $LiMn_{0.9}Fe_{0.05}Mg_{0.05}PO_4/C$ and (e and f) $LiMn_{0.95}Mg_{0.05}PO_4/C$.

The BET surface area of the various samples were analysed by N_2 adsorption and desorption isotherms **(Figure 4.6 and Table 4.3)**. All three samples are mesoporous in nature; the mesoporosity was confirmed from the Type IV hysteresis loops as seen in **Figure 4.6**.

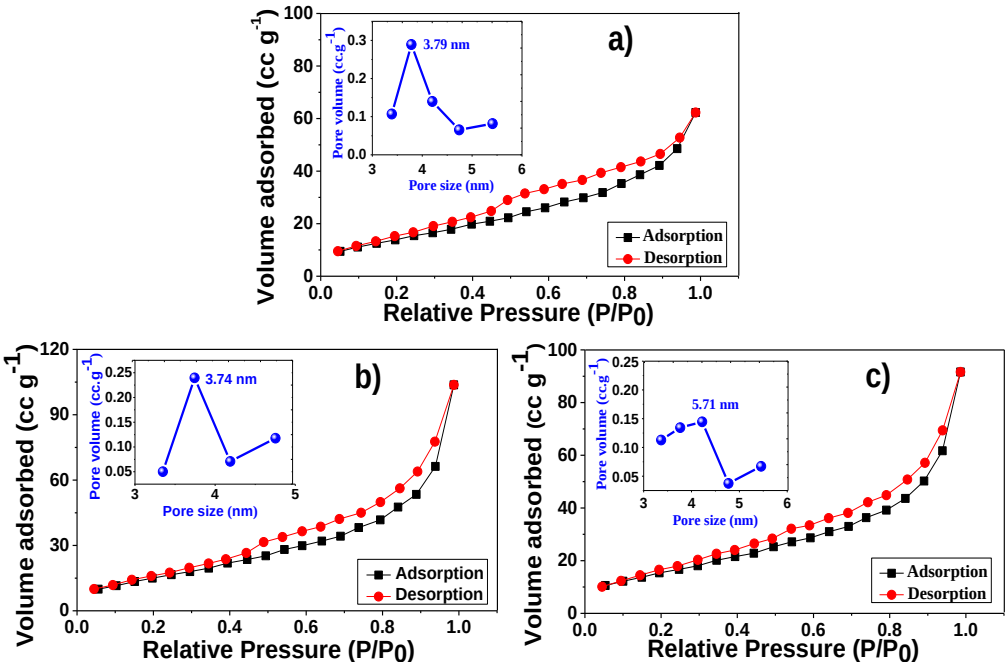

Figure 4.6 Nitrogen sorption isotherm with pore size distribution (inset) of, (a) $LiMn_{0.9}Fe_{0.1}PO_4/C$, (b) $LiMn_{0.9}Fe_{0.05}Mg_{0.05}PO_4/C$ and (c) $LiMn_{0.95}Mg_{0.05}PO_4/C$.

The BET surface area of $LiMn_{0.9}Fe_{0.1}PO_4/C$, $LiMn_{0.9}Fe_{0.05}Mg_{0.05}PO_4/C$ and $LiMn_{0.95}Mg_{0.05}PO_4/C$ samples was found to be 45, 52 and 48 $m^2\ g^{-1}$ with a pore size distribution of 3.7, 3.7 and 5.7 nm respectively **(inset of Figure 4.6)**.[369, 370]

Table 4.3 Nitrogen adsorption and desorption data of $LiMn_{0.9}Fe_{(0.1-x)}Mg_xPO_4/C$ (x = 0 and 0.05) and $LiMn_{0.95}Mg_{0.05}PO_4/C$.

Nitrogen sorption data of Fe^{2+} and/or Mg^{2+} doped $LiMnPO_4$	$LiMn_{0.9}Fe_{0.1}PO_4$	$LiMn_{0.9}Fe_{0.05}Mg_{0.05}PO_4$	$LiMn_{0.95}Mg_{0.05}PO_4$
Surface area ($^*S_{BET}$) ($m^2.g^{-1}$) (±1)	45	52	48
Pore volume (cc g^{-1}) (±0.05)	0.08	0.13	0.10
Pore size (nm) (±0.1)	3.7	3.7	5.7

S_{BET} – Surface area by Brunauer–Emmet–Teller equation.

The pore volumes of these samples are 0.084, 0.132 and 0.1 cc g^{-1} respectively **(Table 4.3)** These pores provide better penetration of the liquid electrolyte which allows easy access to Li^+-ions and hence enhancing the storage performance as shown later.

4.4.2 Lithium storage performance

Figure 4.7 presents the galvanostatic charge and discharge profiles of $LiMn_{0.9}Fe_{(0.1-x)}Mg_xPO_4/C$ (x = 0 and 0.05), $LiMn_{0.95}Mg_{0.05}PO_4/C$ and un-doped $LiMnPO_4/C$ samples at 0.1C in the voltage window 2.3-4.6 V. $LiMnPO_4/C$ is shown here for the sake of comparison. $LiMn_{0.9}Fe_{0.05}Mg_{0.05}PO_4/C$ exhibits the highest lithium storage capacity of 159 mAh g^{-1} with a polarization of ~139 mV while $LiMn_{0.9}Fe_{0.1}PO_4/C$ and $LiMn_{0.95}Mg_{0.05}PO_4/C$ exhibit capacities and polarization of 136 mAh g^{-1}, ~222 mV and 128 mAh g^{-1}, ~334 mV respectively. It is worth noting that the un-doped $LiMnPO_4/C$ delivered the lowest storage capacity of 123 mAh g^{-1} at 0.1C with a polarization of ~340 mV. The facile electrochemical reaction in $LiMn_{0.9}Fe_{0.05}Mg_{0.05}PO_4/C$ material could be inferred from the lowest polarization value witnessed during the galvanostatic cycling.

The voltage profiles of $LiMn_{0.9}Fe_{(0.1-x)}Mg_xPO_4/C$ (x = 0 and 0.05), and $LiMn_{0.95}Mg_{0.05}PO_4/C$ at various current rates namely 0.1, 0.2, 0.5, 1, 2, 5 and 10 C are shown in **Figure 4.7b, 4.7c and 4.7**d. The storage performances of above samples at various rates are summarized in **Table 4.4**. For rapid charge and discharge in 30 min. (2C), $LiMn_{0.9}Fe_{0.05}Mg_{0.05}PO_4/C$ delivers discharge capacities of 105 mAh g^{-1} which is higher than $LiMn_{0.9}Fe_{0.1}PO_4/C$ and $LiMn_{0.95}Mg_{0.05}PO_4/C$ which deliver only 80 mAh g^{-1} and 69 mAh g^{-1} respectively **(Figure 4.7c-4.7d)**. The storage performance of

$LiMn_{0.9}Fe_{0.05}Mg_{0.05}PO_4/C$ is the highest among the reports in literature for $LiMnPO_4$ using divalent doping technique in the transition metal (Mn) site especially at low rates (summary in **Table 4.5**).[151, 176, 178, 180, 181, 395]

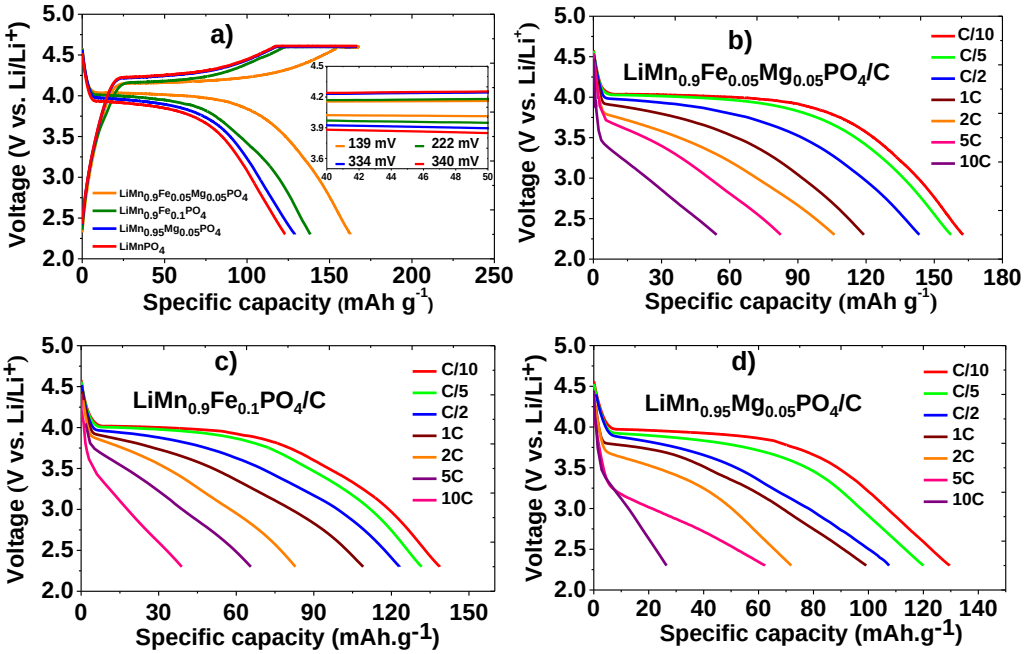

Figure 4.7 (a) Galvanostatic cycling profiles and polarization potential (inset) of $LiMn_{0.9}Fe_{(0.1-x)}Mg_xPO_4/C$ (x = 0 and 0.05), $LiMn_{0.95}Mg_{0.05}PO_4/C$ and $LiMnPO_4/C$ (for the sake of comparison) at 0.1C, (b) Discharge profiles of co-doped $LiMn_{0.9}Fe_{0.05}Mg_{0.05}PO_4/C$ at different current rates, (c) Discharge profiles of $LiMn_{0.9}Fe_{0.1}PO_4/C$ at different current rates, (d) Discharge profiles of $LiMn_{0.9}Mg_{0.05}PO_4/C$ at different current rates (capacity values are calculated based on the active material weight).

Table 4.4 A summary of lithium storage performance of all the composition at different current rates.

C-rates							
Specific discharge capacity in mAh g^{-1}							
Electrode materials	0.1C	0.2C	0.5C	1C	2C	5C	10C
$LiMn_{0.9}Fe_{0.1}PO_4$	136	130	119	105	80	62	35
$LiMn_{0.9}Fe_{0.05}Mg_{0.05}PO_4$	159	155	141	118	104	81	51
$LiMn_{0.95}Mg_{0.05}PO_4$	128	118	105	98	69	59	24

Table 4.5 A summary of lithium storage performance and carbon content from the literature.*

S.N	Electrode composition	Carbon content	Maximum Capacity (in mAh g^{-1})	References
1	$LiMn_{0.9}Fe_{0.05}Mg_{0.05}PO_4$	25wt % carbon	159	Present work
2	$LiMn_{0.9}Mg_{0.1}PO_4$	25wt % carbon + 5 % synthetic flake graphite	120	176
3	$LiMn_{0.99}Mg_{0.01}PO_4$	25wt % carbon	145	151
4	$LiMn_{0.8}Mg_{0.2}PO_4$	25wt % carbon + 5 % synthetic flake graphite	150	178
5	$LiMn_{0.9}Fe_{0.05}Mg_{0.05}PO_4$	31wt % carbon	140	180
6	$LiMn_{0.9}Fe_{0.09}Mg_{0.01}PO_4$	20wt % carbon	140	181
7	$LiMn_{0.8}Mg_{0.2}PO_4$	12.1wt % carbon +8wt % synthetic flake graphite	70	392

In this summary, the active material loading is not taken into account.

The rate performances of the various samples are shown in **Figure 4.8**. After testing at 10C rate, all the cells were again tested at 0.5C rate **(see Figure 4.8a)**. The electrodes show excellent recovery, for example $LiMn_{0.9}Fe_{0.05}Mg_{0.05}PO_4$/C retains 97% of its initial capacity. $LiMn_{0.9}Fe_{0.05}Mg_{0.05}PO_4$/C showed the better long term cycling stability compared to $LiMn_{0.9}Fe_{0.1}PO_4$/C and $LiMn_{0.95}Mg_{0.05}PO_4$/C. For instance, the capacity retention of 96.7% is obtained for $LiMn_{0.9}Fe_{0.05}Mg_{0.05}PO_4$/C after 100

cycles at 1C rate with an average coulombic efficiency of 98.3%. In contrast, $LiMn_{0.9}Fe_{0.1}PO_4/C$ and $LiMn_{0.95}Mg_{0.05}PO_4/C$ show capacity retention of 83.7% and 94.3% with the average coulombic efficiencies of 98.2% and 98.0% respectively **(Figure 4.8b-4.8c)**. This trend is in good agreement with the Mn dissolution observation. Further, even after 200 cycles at 1C rate, $LiMn_{0.9}Fe_{0.05}Mg_{0.05}PO_4/C$ electrode material retained 96% of its initial capacity, delivering 116 mAh g^{-1} with the average coulombic efficiency of 98.2% **(Figure 4.8)**. As mentioned, these materials have similar morphology, particle sizes and carbon content. To a larger extent, the observed differences in the electrochemical performance amongst these materials are not biased by factors such as morphology, particle size and carbon content.

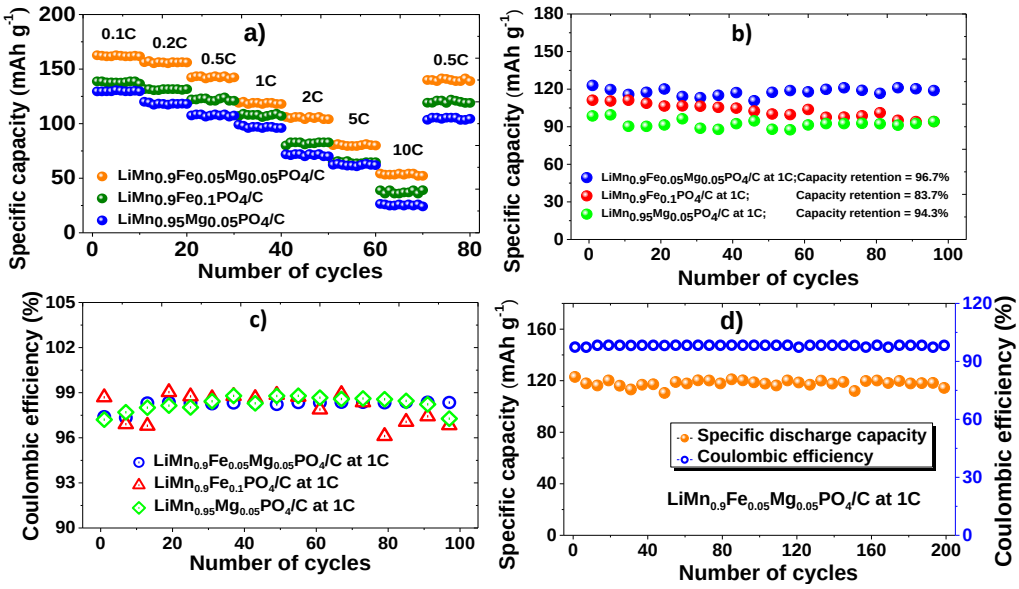

Figure 4.8 (a) Rate capability of $LiMn_{0.9}Fe_{(0.1-x)}Mg_xPO_4/C$ (x = 0 and 0.05) and $LiMn_{0.95}Mg_{0.05}PO_4/C$ at different current rates, (b) Capacity retention of $LiMn_{0.9}Fe_{(0.1-x)}Mg_xPO_4/C$ (x = 0 and 0.05) and $LiMn_{0.95}Mg_{0.05}PO_4/C$ up to 100 cycles at 1C, (c) Corresponding coulombic efficiency (shown in the magnified scale for the sake of clarity) and (d) Cycling stability of $LiMn_{0.9}Fe_{0.05}Mg_{0.05}PO_4/C$ up to 200 cycles at 1C corresponding coulombic efficiency (capacity values are calculated based on the active material weight).

4.4.3 Manganese dissolution

To understand the better storage performance and stability of $LiMn_{0.9}Fe_{0.05}Mg_{0.05}PO_4/C$, manganese dissolution analysis was performed on fully charged electrode using ICP-OES technique. Similar analysis was also performed on $LiMn_{0.9}Fe_{0.1}PO_4/C$, $LiMn_{0.95}Mg_{0.05}PO_4/C$ and un-doped $LiMnPO_4/C$ electrodes for the sake of comparison. The amounts of Mn dissolution were obtained after soaking the charged (4.6 V) electrodes in the electrolyte at room temperature for 20 days. **Table 4.6** compares the amount of Mn dissolved in the electrolyte (in ppm) for various samples.

Table 4.6 Mn dissolution in the electrolyte of the doped, co-doped and un-doped $LiMnPO_4$ electrodes charged to 4.6 V after 20 days of storage in electrolyte (1M $LiPF_6$ in EC/DEC = 1:1) at room temperature.

Electrode material	$LiMnPO_4$	$LiMn_{0.9}Fe_{0.1}PO_4$	$LiMn_{0.9}Fe_{0.05}Mg_{0.05}PO_4$	$LiMn_{0.95}Mg_{0.05}PO_4$
Mn dissolution (in ppm)	21.95	4.56	2.89	3.48

The Mn dissolution in $LiMn_{0.9}Fe_{0.05}Mg_{0.05}PO_4/C$ was 2.89 ppm which is lower than the dissolution observed in $LiMn_{0.9}Fe_{0.1}PO_4/C$ (4.56 ppm), $LiMn_{0.95}Mg_{0.05}PO_4/C$ (3.48 ppm) and $LiMnPO_4/C$ (21.95 ppm). Such a trend is suggestive of the fact that co-doping with 5% of Fe^{2+} and inactive Mg^{2+} ions suppresses the Mn dissolution in the electrolyte compared to the other samples. Further, the overall Mn dissolution of all doped samples is lower compared to the un-doped $LiMnPO_4/C$. The stability of the delithiated phase of doped $LiMnPO_4$ has been attributed to (i) the unchanged ionic radii of Mg^{2+} in the lattice during charging/discharging and (ii) partial removal of Li^+ ions

from the lattice owing to inactive Mg^{2+} dopant in $LiMnPO_4$.[176, 178] Hence the suppressed Mn dissolution seen in our doped samples (compared to un-doped $LiMnPO_4$) could possibly arise from stabilization of the delithiated phase ($Li_{1-x}MnPO_4$).

4.4.4 Enhanced lithium extraction/insertion mechanism in $LiMn_{0.9}Fe_{0.05}Mg_{0.05}PO_4$

Ex-situ XPS measurements were carried out to study the Li^+ ion extraction/insertion mechanism in $LiMn_{0.9}Fe_{0.05}Mg_{0.05}PO_4$ and to appraise the reasons for enhanced lithium storage performance. XPS spectra were recorded on partially charged (4 V), fully charged (4.6 V) and fully discharged (2.3 V) electrodes **(Figure 4.9(i)).** During the process of lithium extraction up to 4 V, there is a redox transition from $LiMn^{2+}Fe^{2+}Mg^{2+}PO_4$ (pristine) to $Li_{(1-x)}Mn^{2+}(Fe^{3+})Mg^{2+}PO_4$ (partially charged to 4 V) which is seen from XPS spectra **(Figure 4.9(ii)).** Accordingly, peaks are found to be located at binding energy of 641.1, 712.3 and 50.2 eV, corresponding to Mn^{2+}, Fe^{3+} and Mg^{2+} respectively **(Figure 4.9(ii))**. A charge capacity of ~25 mAh g^{-1} witnessed up to 4 V corresponds to Fe^{2+}/Fe^{3+} redox transition and not from the Mn^{2+}/Mn^{3+} **(Figure 4.9(i))**. The possibility of capacity contribution from Mn^{2+}/Mn^{3+} is ruled out as the equilibrium potential for this redox couple occurs at 4.1 V. The delithiated phase formed owing to Fe^{2+}/Fe^{3+} redox further facilitates the favorable electrochemical activity of Mn^{2+}/Mn^{3+} in this material.[180] During further lithium extraction up to 4.6 V, there is a redox transition from $Li_{(1-x)}Mn^{2+}(Fe^{3+})Mg^{2+}PO_4$ (partially charged to 4 V) to $Li_{(1-x)}(Mn^{3+}\ Fe^{3+})Mg^{2+}PO_4$ (fully charged to 4.6 V, $0< x >1$) owing to transition of Mn^{2+}/Mn^{3+} at 4.1 V in the sample while electrochemically inactive Mg^{2+} does not contribute to

charge capacity as seen from XPS spectra **(Figure 4.9(iii))**. XPS spectra shows peaks at 642.2, 712.3 and 50.2 eV corresponding to Mn^{3+}, Fe^{3+} and Mg^{2+} respectively.[161, 177, 396-402] Since Mg^{2+} ions do not undergo any change in its oxidation state, lithiated phases associated Mg^{2+} still exist in the structure.

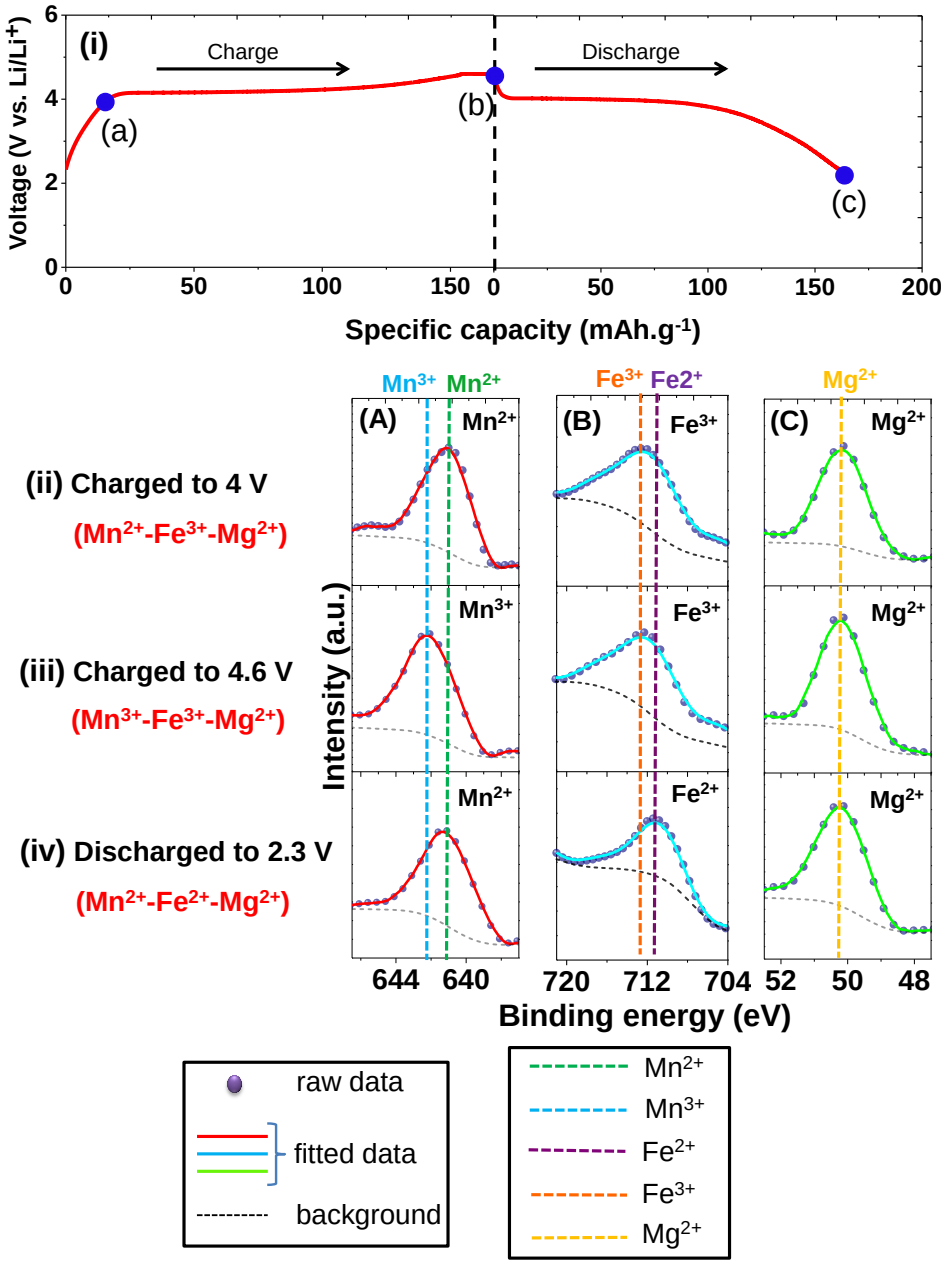

Figure 4.9 (i) Charge/discharge profile of $Li_xMn_{0.9}Fe_{0.05}Mg_{0.05}PO_4/C$: [(a) a state of partially charged to 4 V, (b) a state of fully charged to 4.6 V, (c) a state of fully discharged to 2.3 V]; ex-situ XPS spectra of $Li_xMn_{0.9}Fe_{0.05}Mg_{0.05}PO_4/C$: [(ii) partially charged to 4 V, (iii) fully charged to 4.6 V and (iv) fully discharged to 2.3 V]; (A) refers to Mn $2p_{3/2}$, (B) refers to Fe $2p_{3/2}$ and (C) refers to Mg $2p_{3/2}$.

Presence of such partial lithiated phase prior to lithium insertion (discharge) cycle, promotes enhanced electrochemical activity of Mn^{3+}/ Mn^{2+} in the material. After complete discharge to 2.3 V, peaks at 641.1 and 711.2 eV corresponding to Mn^{2+} and Fe^{2+} were seen, while Mg^{2+} (50.2 eV) showed no change **(Figure 4.9(iv))**.[154, 161, 177, 400-402] E*x-situ* XRD patterns of these samples charged to 4 and 4.6 V and discharged to 2.3 V does not show any significant changes **(Figure 4.10)**. The subsequent charge and discharge cycles follow the above mechanism which facilitates enhanced lithium storage performance of Fe^{2+}/Mg^{2+} doped samples. The mechanism of enhanced Li^{+} ion extraction/insertion in $LiMn_{0.9}Fe_{0.05}Mg_{0.05}PO_4$ could be summarised in **Equation (4.1).**

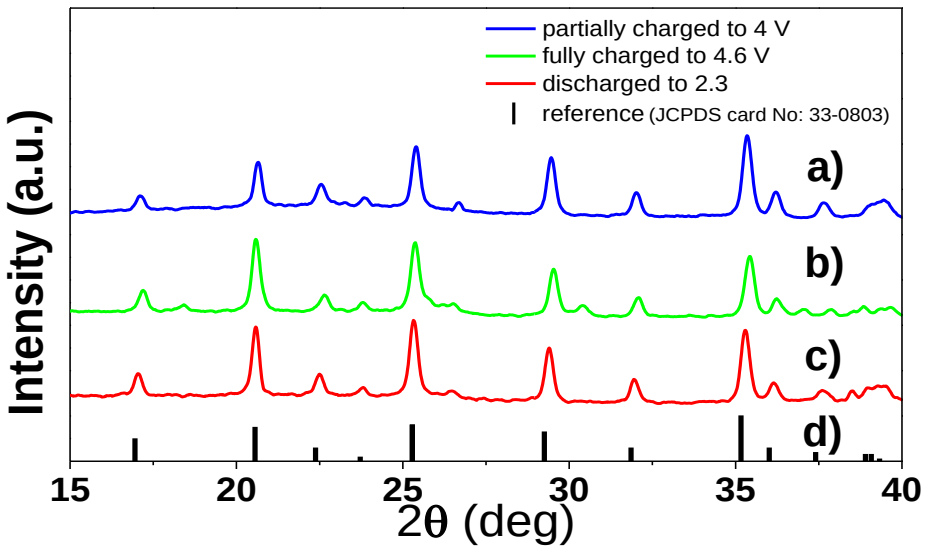

Figure 4.10 *Ex-situ* PXRD patterns of $LiMn_{0.9}Fe_{0.05}Mg_{0.05}PO_4$ (a) fully charged to 4 V, (b) partially charged to 4.6 V, (c) discharged to 2.3 V and (d) standard powder pattern of $LiMnPO_4$ (JCPDS card No: 33-0803).

In short, during Li extraction process, delithiated phases created from Fe^{2+}/Fe^{3+} redox (~ 3.45 V) favours facile electrochemical activity of the succeeding Mn^{2+}/Mn^{3+} redox. The fully charged product ($Li_{(1-x)}Mn_{0.9}Fe_{0.05}Mg_{0.05}PO_4$/C at 4.6 V) contains partial lithiated phase owing to the

presence of electrochemically inactive Mg^{2+}. Presence of such lithiated phase provides favourable environment for the subsequent lithium insertion process.

$$\underset{LiMn^{2+}Fe^{2+}Mg^{2+}PO_4}{\text{at OCV / 2.3 V}} \rightleftharpoons \underset{Li_{(1-x)}Mn^{2+}(Fe^{3+})Mg^{2+}PO_4}{\text{at 4 V}} \rightleftharpoons \underset{Li_{(1-x)}(Mn^{3+}Fe^{3+})Mg^{2+}PO_4}{\text{at 4.6 V}} \quad (4.1)$$

4.4.5 Diffusion study

Cyclic voltammograms (CV) was recorded on $LiMn_{0.9}Fe_{(0.1-x)}Mg_xPO_4/C$ (x = 0 and 0.05) and $LiMn_{0.95}Mg_{0.05}PO_4/C$ at different scan rates (0.1, 0.2, 0.3, 0.4 and 0.5 mV s^{-1}) as shown **Figure 4.11a, 4.11c and 4.11e**.

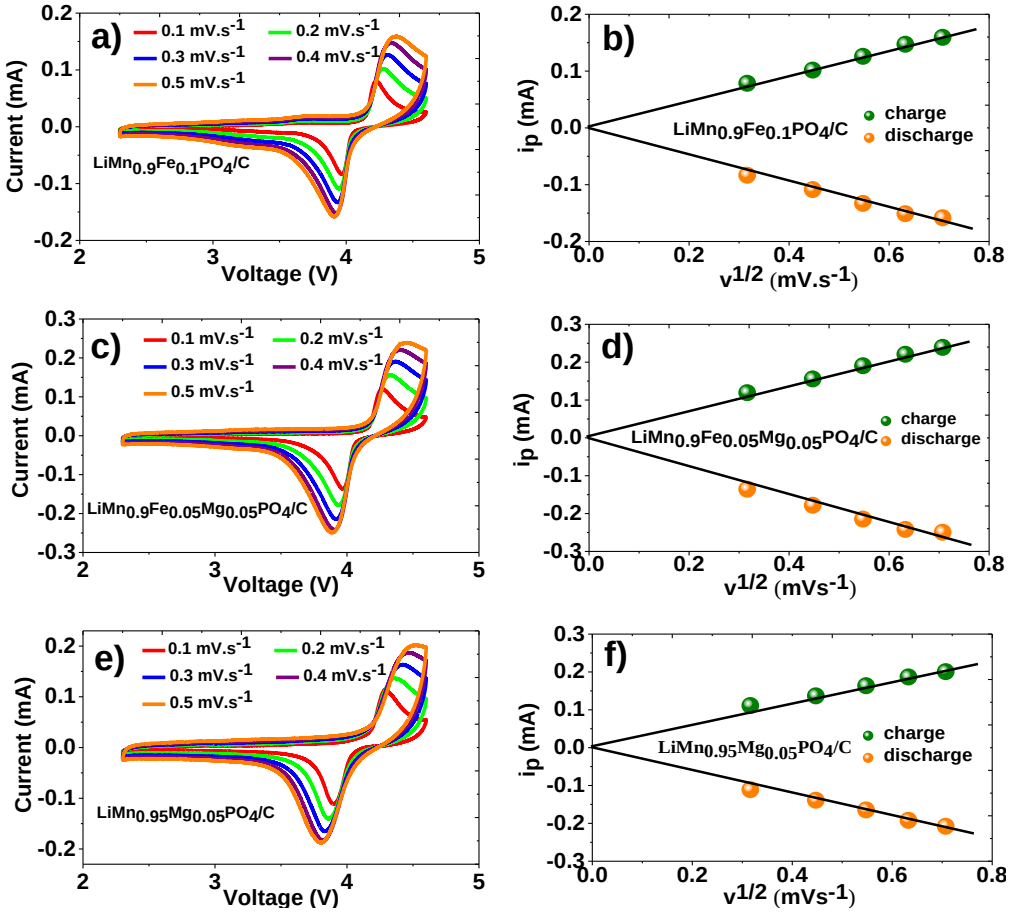

Figure 4.11 Cyclic voltammograms (CV) at different scan rates (0.1, 0.2, 0.3, 0.4 and 0.5 mV s^{-1}) and corresponding plots of linear relationship between the peak current (i_p) and the square root of scan rate ($v^{1/2}$) for both the charge and discharge states of (a and b) $LiMn_{0.9}Fe_{0.1}PO_4$, (c and d) $LiMn_{0.9}Fe_{0.05}Mg_{0.05}PO_4$ and (e and f) $LiMn_{0.95}Mg_{0.05}PO_4$.

The voltage hysteresis (ΔV, difference between the anodic and cathodic peak voltages) increases with the increasing scan rate. However, the

ratio of the anodic to the cathodic peak currents being unity,[383] there are no side reactions during the insertion and extraction processes. The linear relationship observed between the both anodic/cathodic peak currents (i_p) and the square root of the scan rate ($v^{1/2}$) **(Figure 4.11b, 4.11d and 4.11f)** indicates that the electrochemical storage process is diffusion limited. To estimate the apparent D_{Li}^{+} of $LiMn_{0.9}Fe_{(0.1-x)}Mg_xPO_4/C$ (x = 0 and 0.05) and $LiMn_{0.95}Mg_{0.05}PO_4/C$, EIS studies were performed on fresh cells at OCV (3.0 V) **(Figure 4.12)**. The experimental data were fitted using the equivalent circuit model shown as inset in **Figure 4.12a**.[134, 137]

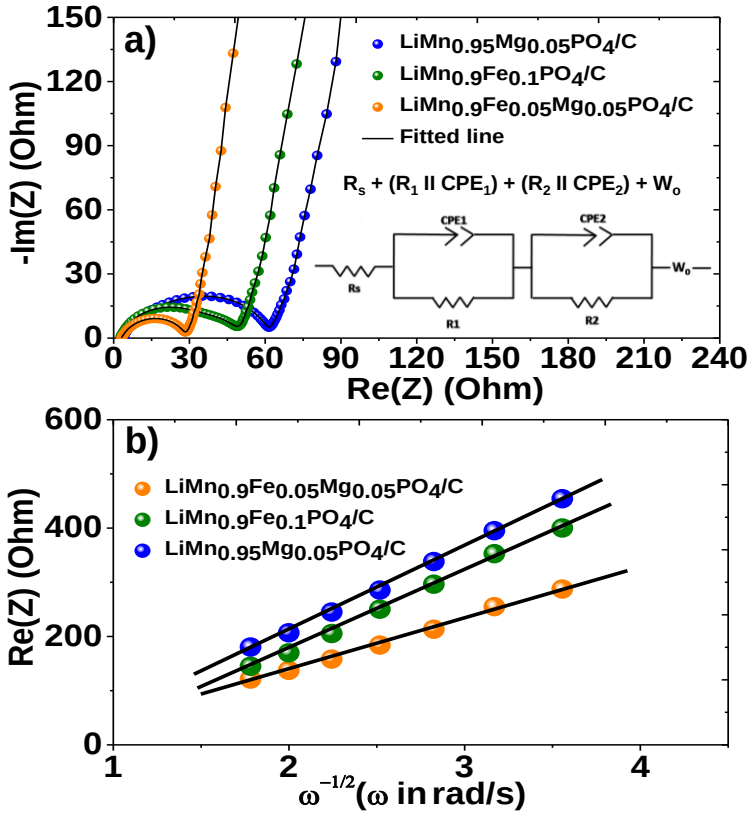

Figure 4.12 (a) Nyquist impedance spectra of $LiMn_{0.9}Fe_{(0.1-x)}Mg_xPO_4/C$ (x = 0 and 0.05) and $LiMn_{0.95}Mg_{0.05}PO_4/C$ of fresh cell (OCV) at room temperature and equivalent circuit (inset) and (b) linear fittings between Z_{re} and reciprocal square root of the angular frequency in low frequency region.

The fitted values of R_S, R_1 and R_2 are given in **Table 4.7**. R_S is the effective resistance due to electrolyte impedance and electrical contacts and

obtained from the intercept of semicircle at high frequency with x-axis. W_o, the Warburg element seen as a slope in low frequency regime is associated with Li^+-ion diffusion in the bulk of the electrode. The mid-frequency semicircle is fitted with two depressed semicircles, corresponding to ($R_1||CPE_1$) and ($R_2||CPE_2$) which can be attributed to the complex charge transfer processes from the electrolyte to bulk of the electrode surfaces. It is suggested that the R_2 refers to the charge transfer resistance, while R_1 which is an elevated resistance at high frequency region is associated with the Li^+-ion transfer resistance at electrode-electrolyte interface (surface film resistance).[137]

Table 4.7 Impedance parameters derived using equivalent circuit model for $LiMn_{0.9}Fe_{(0.1-x)}Mg_xPO_4/C$ (x = 0 and 0.05) and $LiMn_{0.95}Mg_{0.05}PO_4/C$.

Fresh cells					
Electrode material	$R_s(\Omega)$	$R_1(\Omega)$	CPE_1 (x 10^{-6} F)	$R_2(\Omega)$	CPE_2 (x 10^{-6} F)
$LiMn_{0.9}Fe_{0.1}PO_4$	3.39	41.94	15.14	6.03	6.67
$LiMn_{0.9}Fe_{0.05}Mg_{0.05}PO_4$	2.14	25.73	21.15	2.47	7.93
$LiMn_{0.95}Mg_{0.05}PO_4$	3.89	52.04	11.91	4.68	1.93

The apparent D_{Li}^+ was calculated for these samples using **Equation (3.2).**

where, R is the gas constant, T is the absolute temperature (K), A is the contact area of the electrode (2.01 cm^2), n is the number of electrons per molecule, F is the Faraday constant, C is the concentration of Li^+-ions (6.38 x 10^{-3} mol cm^{-3}) (ratio between the tap density of the prepared material and molecular weight) and σ is the Warburg coefficient (obtained from **Figure 4.12b)**.[134, 187, 403] The apparent D_{Li}^+ values obtained from EIS measurements are shown in **Table 4.8**. The obtained D_{Li}^+ values are comparable with the

literature **(Table 4.8)**.[177, 384] It is interesting to note that the diffusion coefficient of $LiMn_{0.9}Fe_{0.05}Mg_{0.05}PO_4/C$ is higher than the rest of the electrodes $LiMn_{0.9}Fe_{0.1}PO_4/C$ and $LiMn_{0.95}Mg_{0.05}PO_4/C$ which is consistent with the changes in the lithium storage performance.

Table 4.8 Apparent diffusion coefficient derived from EIS measurements of $LiMn_{0.9}Fe_{(0.1-x)}Mg_xPO_4/C$ (x= 0 and 0.05) and $LiMn_{0.95}Mg_{0.05}PO_4/C$.

Electrode material	$LiMn_{0.9}Fe_{0.1}PO_4$	$LiMn_{0.9}Fe_{0.05}Mg_{0.05}PO_4$	$LiMn_{0.95}Mg_{0.05}PO_4$
Diffusion coefficient (D_{Li}^+) by EIS ($cm^2\ s^{-1}$)	4.84×10^{-14}	1.04×10^{-13}	3.26×10^{-14}

4.5 Summary

In summary, the influence of Fe^{2+} and/or Mg^{2+} doping in high potential olivine $LiMnPO_4/C$ and its electrochemical performance were investigated. $LiMn_{0.9}Fe_{(0.1-x)}Mg_xPO_4/C$ (x = 0 and 0.05) and $LiMn_{0.95}Mg_{0.05}PO_4/C$ were synthesized using ball-mill assisted soft template approach. Among them, co-doped $LiMn_{0.9}Fe_{0.05}Mg_{0.05}PO_4/C$ exhibits the best storage performance delivering capacities of 159, 155, 141, 118, 104, 81 and 51 mAh g^{-1} at 0.1, 0.2, 0.5, 1, 2, 5 and 10C rates respectively with less polarization ~139 mV. On the other hand $LiMn_{0.9}Fe_{0.1}PO_4/C$ and $LiMn_{0.95}Mg_{0.05}PO_4/C$ show only 136 and 128 mAh g^{-1} at 0.1C with the polarization of ~222 and 334 mV respectively. This electrode material also retains capacity of 116 mAh g^{-1} at 1C after 200 cycles, which is 96% of its initial capacity. Such improved cycling stability of $LiMn_{0.9}Fe_{0.05}Mg_{0.05}PO_4/C$ is attributed to the suppressed Mn dissolution in the electrolyte compared to the other samples. The possible reasons for enhanced electrochemical performance in

$LiMn_{0.9}Fe_{0.05}Mg_{0.05}PO_4/C$ was demonstrated in terms of (i) redox combination which provides favourable lithiation and delithiation processes owing to low equilibrium potential of Fe^{2+}/Fe^{3+} and electrochemically inactive Mg^{2+} and (iii) enhanced transport properties. Thus, isovalent co-doping provides a positive influence on the lithium storage performance of olivine $LiMnPO_4$.

As seen, isovalent co-doped $LiMn_{0.9}Fe_{0.05}Mg_{0.05}PO_4/C$ exhibits higher storage capacity compared to doped and un-doped sample at slow current rates. However, the storage capacity reduced significantly at higher current rates. In the next chapter, the electrochemical performance of $LiMnPO_4$ will be further enhanced especially at high current rates by preparing Mn-Fe mixed transition metal phosphate.

Chapter 5

5. Understanding the electrochemical kinetics and redox potential shift of olivine cathode materials $Li(Mn_{1-x}Fe_x)PO_4/C$ (x = 0, 0.2, 0.5 and 0.8)

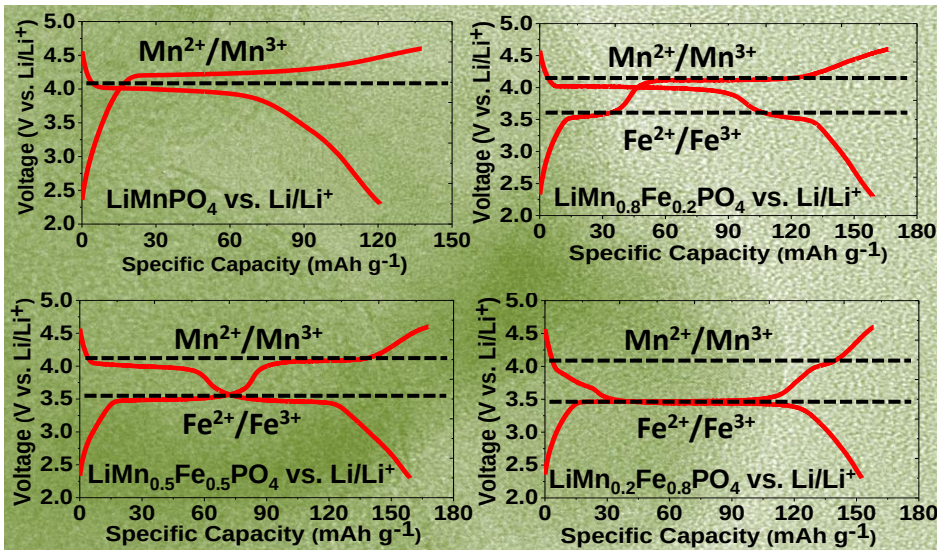

5.1 Preface to Chapter 5

Mn-Fe mixed transition metal phosphates were prepared to enhance its electrochemical kinetics. For this purpose, $Li(Mn_{1-x}Fe_x)PO_4/C$ (x = 0, 0.2, 0.5 and 0.8) cathode materials were synthesized by high energy ball mill assisted soft template method. $LiMn_{1-x}Fe_xPO_4/C$ (x = 0.2, 0.5 and 0.8) showed better lithium storage performance as compared to parent material $LiMnPO_4/C$. For instance, $LiMn_{0.8}Fe_{0.2}PO_4/C$, $LiMn_{0.5}Fe_{0.5}PO_4/C$ and $LiMn_{0.2}Fe_{0.8}PO_4/C$ Mn-Fe mixed compositions showed two distinct charge and discharge profiles and improved lithium storage performance of 160, 159, 158 mAh g^{-1} at 0.1C rate respectively. In contrast, $LiMnPO_4/C$ exhibited lithium storage performance of 120 mAh g^{-1} at 0.1C. The voltage polarization of Mn-Fe mixed composition electrodes was found to be ~85 mV:20 mV in the Mn:Fe redox potential region unlike $LiMnPO_4/C$ (340 mV) at 0.1C. Mn-rich $LiMn_{0.8}Fe_{0.2}PO_4/C$ electrode retains 86% of its initial capacity at 1C after 700 cycles. Moreover, this electrode exhibits stable discharge capacity of ~155 mAh g^{-1} over a wide operating temperature of RT - 60°C. The enhanced electrochemical kinetics of $LiMn_{0.8}Fe_{0.2}PO_4/C$ is demonstrated in terms of (i) redox combination which in turn provides favourable environment for the lithiation and delithiation processes owing to difference in the equilibrium potential of Fe^{2+}/Fe^{3+} and Mn^{2+}/Mn^{3+} unlike $LiMnPO_4$, (ii) partial suppression of Jahn-Teller distortion, (iii) good structural and thermal stability of delithiated phase and (iv) enhanced transport properties. Finally, $LiMn_{0.8}Fe_{0.2}PO_4/C$ electrode also shows feasible operation in full cells when combined with insertion anode $Li_4Ti_5O_{12}/C$ and conversion anode Fe_2O_3/C.

5.2 Introduction

Previous reports on $LiMnPO_4$ indicate that the complete extraction of Li^+-ion was not possible.[13, 94, 131, 132] To improve the electrochemical performance of $LiMnPO_4$ various novel synthetic approaches such as sol-gel method,[108, 133] polyol method,[121] soft template method,[134, 135] spray pyrolysis with wet ball milling,[137] ultrasonic spray pyrolysis,[140] direct precipitation,[141] solid state reactions,[142] hydrothermal synthesis[143] and off-stoichiometry[148] synthesis have been reported. Besides all these, partial substitution of cations such as Mg^{2+}, Fe^{2+}, Ni^{2+}, Zn^{2+}, Ca^{2+} and Zr^{4+} have also been attempted to improve the electrochemical activity of Mn^{2+}/Mn^{3+} redox couples,[135, 137, 150, 151, 160, 176, 177] but this results in relatively less capacity and high polarization especially at higher current rates. Recently, the mixed transition metal phospho-olivine $LiMn_xFe_{1-x}PO_4$ has drawn attention as it exhibits improved bulk conductivity.[164-167] Several reports on the electrochemical performance of $LiMn_xFe_{1-x}PO_4$ (x = 0.25, 0.50 and 0.75) Mn-Fe mixed compositions have showed that the manganese rich [$LiMn_xFe_{1-x}PO_4$ (x > 0.75)] component is not an appropriate cathode material for LIBs owing to its sluggish electrochemical activity of manganese and huge anisotropic distortion of Mn^{3+} in charge state[13, 120, 131, 160, 168, 169]. In contrast, Martha *et al.*[161] and Wang *et al.*[170] demonstrated that the Mn-rich component [$LiMn_xFe_{1-x}PO_4$ (x = 0.8 or 0.75)] can be an excellent advanced cathode material for LIBs. A study on $LiFe_{1-y}Mn_yPO_4$ by Molenda *et al.*[164, 171] shows that manganese is more electrochemically active in Mn rich Mn-Fe mixed phospho-olivine than $LiMnPO_4$ owing to its lower activation energy and enhanced bulk conductivity.

Co-doped $LiMn_{0.9}Fe_{0.05}Mg_{0.05}PO_4/C$ **(chapter 4)** cathode material exhibited higher storage capacity compared to pure $LiMnPO_4/C$ (chapter 3). However, the storage capacity and voltage reduced significantly at higher current rates. In this chapter, $Li(Mn_{1-x}Fe_x)PO_4/C$ (x = 0, 0.2, 0.5 and 0.8) cathode materials were synthesized by high energy ball mill assisted soft template method to enhance the manganese utilization. $LiMn_{1-x}Fe_xPO_4/C$ (x = 0.2, 0.5 and 0.8) showed better lithium storage performance compared to $LiMnPO_4/C$. Among these, $LiMn_{0.8}Fe_{0.2}PO_4/C$ exhibits higher energy density owing to the 80% of the capacity at higher potential Mn^{2+}/Mn^{3+} redox region. Mn-rich $LiMn_{0.8}Fe_{0.2}PO_4/C$ exhibits enhanced manganese utilization, thermal stability, cycling stability and reduced voltage polarization. The enhanced electrochemical kinetics of $LiMn_{0.8}Fe_{0.2}PO_4/C$ has been attributed in terms of (i) favourable redox combination which in turn provides better environment for the lithiation and delithiation processes owing to difference in the equilibrium potential of Fe^{2+}/Fe^{3+} and Mn^{2+}/Mn^{3+}, (ii) partial suppression of Jahn-Teller distortion and (iii) good structural and thermal stability of delithiated phase and (iv) enhanced transport properties.

5.3 Experimental

5.3.1 Synthesis of $Li(Mn_{1-x}Fe_x)PO_4/C$ (x = 0, 0.2, 0.5 and 0.8)

Carbon coated $Li(Mn_{1-x}Fe_x)PO_4/C$ (x = 0, 0.2, 0.5 and 0.8) was synthesized using soft template method followed by high energy ball milling process **(see chapter 3, scheme 2)**. 0.01 M of CTAB ($(C_{16}H_{33})N(CH_3)_3Br$, Sigma Aldrich) was dissolved in a round bottom flask with a mixture of millQ water and absolute ethanol in the volume ratio of 1:5. The solution was stirred for 90 min. to initiate micellar formation, followed by the addition of lithium

dihydrogen phosphate (LiH_2PO_4, Sigma Aldrich), manganese (II) acetate tetrahydrate ($Mn(CH_3CO_2)_2.4H_2O$, Sigma Aldrich) and iron (II) acetate tetrahydrate ($Fe(CH_3CO_2)_2.4H_2O$, Sigma Aldrich) in stoichiometric proportion. The solution was further stirred for 24 h and the solvent evaporated using an IKA RV10 roto-evaporator. The precipitate was annealed in a tubular furnace at 650 $^{\circ}$C for 6 h in an Ar-H_2 (95:5) atmosphere. The calcined product was ball-milled with 25 wt% acetylene black using FRITSCH premium line – pulverisette 7 instrument at 500 rpm for 4 h with the weight ratio of sample:balls = 1:40. Further, the ball milled sample was heat-treated again at 500 $^{\circ}$C for 3 h in an Ar:H_2 atmosphere.[135]

5.3.2 Material and electrochemical characterization

Above samples were characterized using PXRD, Rietveld refinement, FESEM, EDXS, TEM, BET, XPS, temperature dependent PXRD, RT and high temperature galvanostatic cycling, cyclic voltammetry and electrochemical impedance spectroscopy. The details are given in chapter 2, section 2.2.1 , section 2.3 , section 2.4 and section 2.5

5.4 Results and discussion

5.4.1 Structural and morphological characterization

Figure 5.1a illustrates the PXRD of the $LiMn_{1-x}Fe_xPO_4/C$ (x = 0, 0.2, 0.5 and 0.8) samples. All peaks in the diffraction patterns belong to the *Pmnb* space group (*JCPDS card no. 33-0803*) with an orthorhombic structure. The expanded 2θ region as illustrated in **Figure 5.1b** indicates a continuous shift in the positions of the (031), (311) and (121) peaks and this reveals the formation of Mn-Fe mixed compositions.

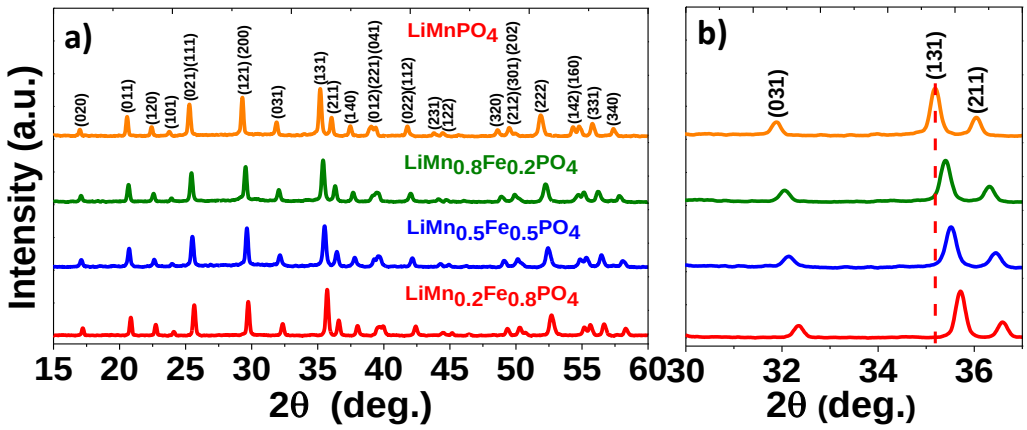

Figure 5.1 (a) PXRD patterns of the $LiMn_{1-x}Fe_xPO_4/C$ (x = 0, 0.2, 0.5 and 0.8) solid solution, (b) expanded 2θ region showing the continuous shift in the positions of the reflections to the higher angles with the substitution of the smaller Fe^{2+} for Mn^{2+} in the $LiMn_{1-x}Fe_xPO_4$.

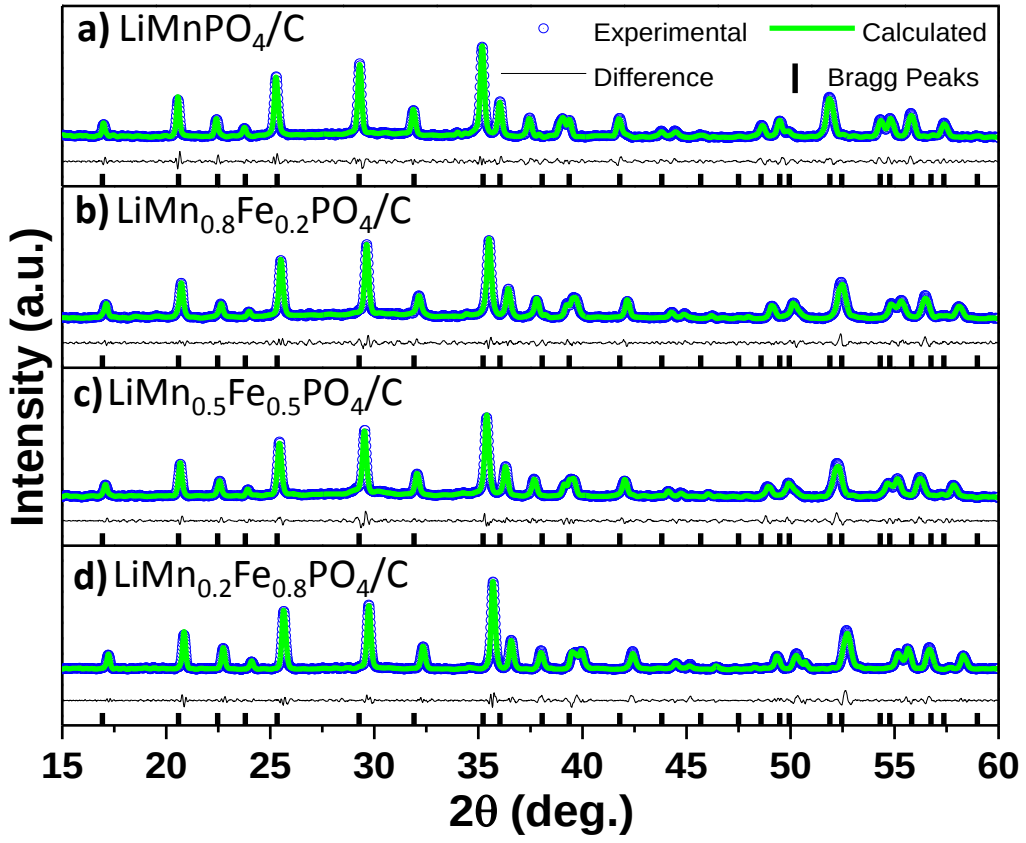

Figure 5.2 Rietveld refinement of (a) $LiMnPO_4/C$ (R_{exp}:10.46, R_{wp}:4.04 and R_p:3.21), (b) $LiMn_{0.8}Fe_{0.2}PO_4/C$ (R_{exp}:9.05, R_{wp}:5.46 and R_p:4.21), (c) $LiMn_{0.5}Fe_{0.5}PO_4/C$ (R_{exp}:8.71, R_{wp}:4.79 and R_p:3.76) and (d) $LiMn_{0.2}Fe_{0.8}PO_4/C$ (R_{exp}:8.86, R_{wp}:4.90 and R_p:3.76).

Rietveld refinement was performed on PXRD data of $LiMn_{1-x}Fe_xPO_4/C$ (x = 0, 0.2, 0.5 and 0.8) **(Figure 5.2)**. The quality of the refinement is determined based on low reliability factors R_{exp}, R_{wp} and R_p, which confirms the formation of orthorhombic structure. **Figure 5.3** shows the variations in the lattice parameters and unit cell volume of the $LiMn_{1-x}Fe_xPO_4/C$ (x = 0, 0.2, 0.5 and 0.8).

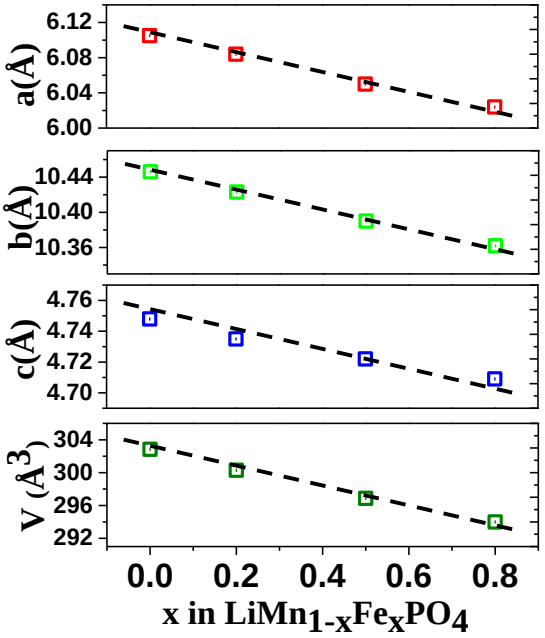

Figure 5.3 Variations of the unit cell parameters of $LiMn_{1-x}Fe_xPO_4$ with x.

The systematic changes in the unit cell parameters and cell volume can be understood by ionic radii of the transition ions (Mn^{2+} = 0.97 Å, Fe^{2+} = 0.92 Å) in the system.[179, 393] This linear variation in the unit cell parameters also confirms the formation of identical $LiMn_{1-x}Fe_xPO_4/C$ (x = 0.2, 0.5 and 0.8) solid solution with an orthorhombic structure.

FESEM images of $LiMn_{1-x}Fe_xPO_4/C$ (x = 0, 0.2, 0.5 and 0.8) samples are shown in **Figure 5.4**. FESEM images show presence of particles with a pseudo-spherical morphology.

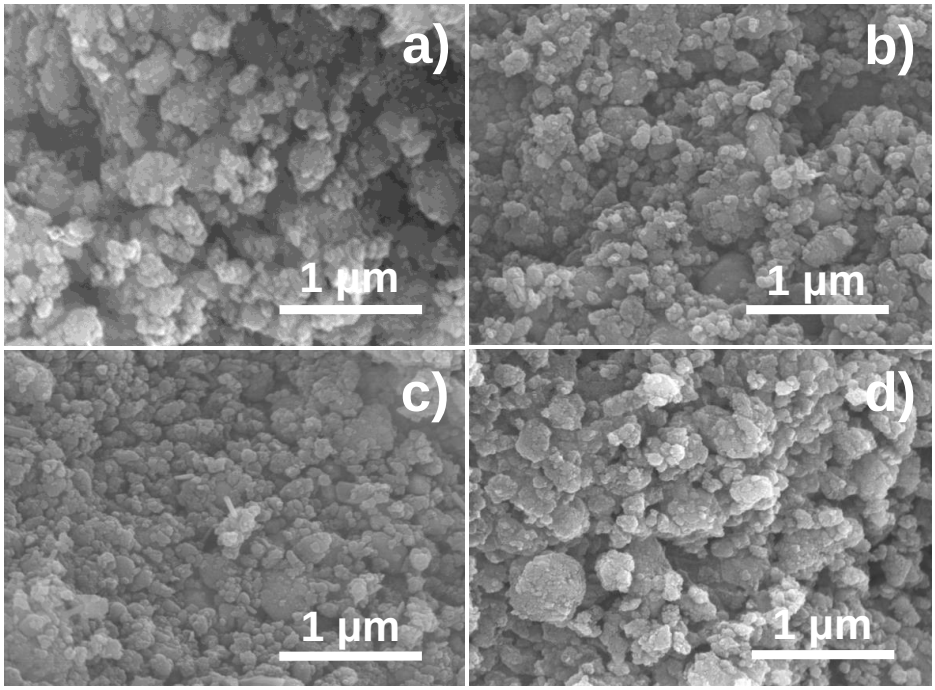

Figure 5.4 FESEM images of (a) $LiMnPO_4/C$, (b) $LiMn_{0.8}Fe_{0.2}PO_4/C$, (c) $LiMn_{0.5}Fe_{0.5}PO_4/C$ and (d) $LiMn_{0.2}Fe_{0.8}PO_4/C$.

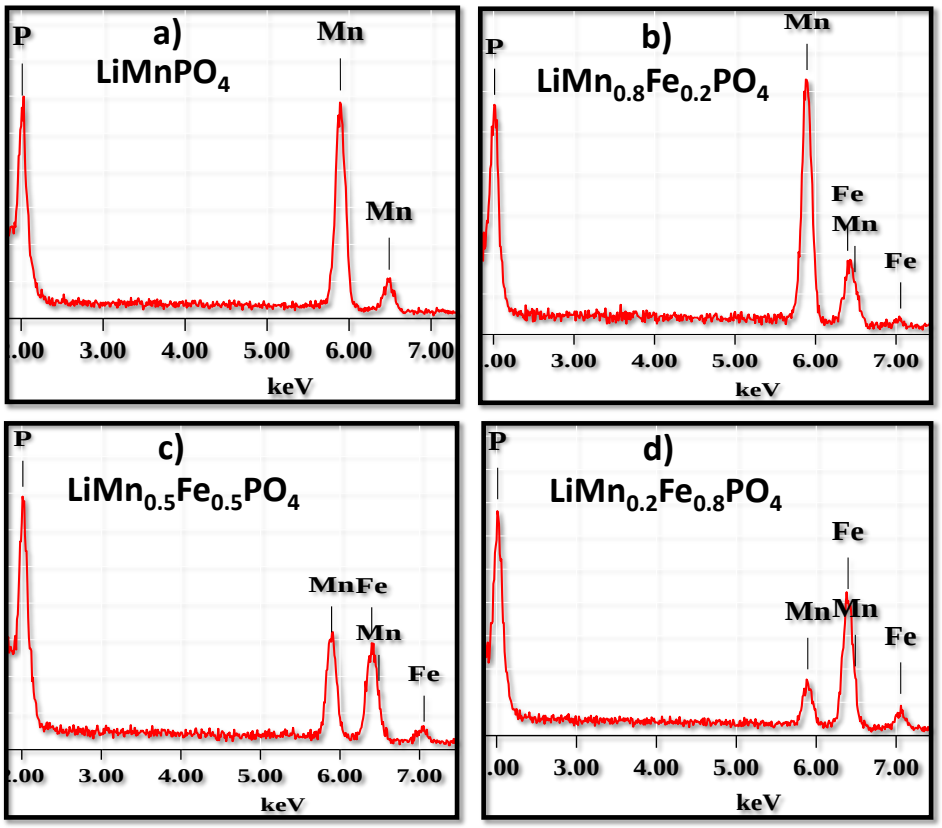

Figure 5.5 Energy dispersive spectra of $LiMn_{1-x}Fe_xPO_4/C$ (x = 0, 0.2, 0.5 and 0.8): Distribution trend of Mn and Fe in the composition (a) $LiMnPO_4/C$, (b) $LiMn_{0.8}Fe_{0.2}PO_4/C$, (c) $LiMn_{0.5}Fe_{0.5}PO_4/C$ and (d) $LiMn_{0.2}Fe_{0.8}PO_4/C$.

Energy dispersive spectrum **(Figure 5.5)** and elemental mapping images **(Figure 5.6)** confirm uniform distribution of manganese and/or iron within the active material, and this trend is in accordance with the Mn and Fe content in the material composition. Further, a uniform distribution of carbon, phosphorus and oxygen around the active materials are also seen **(Figure 5.7)**.

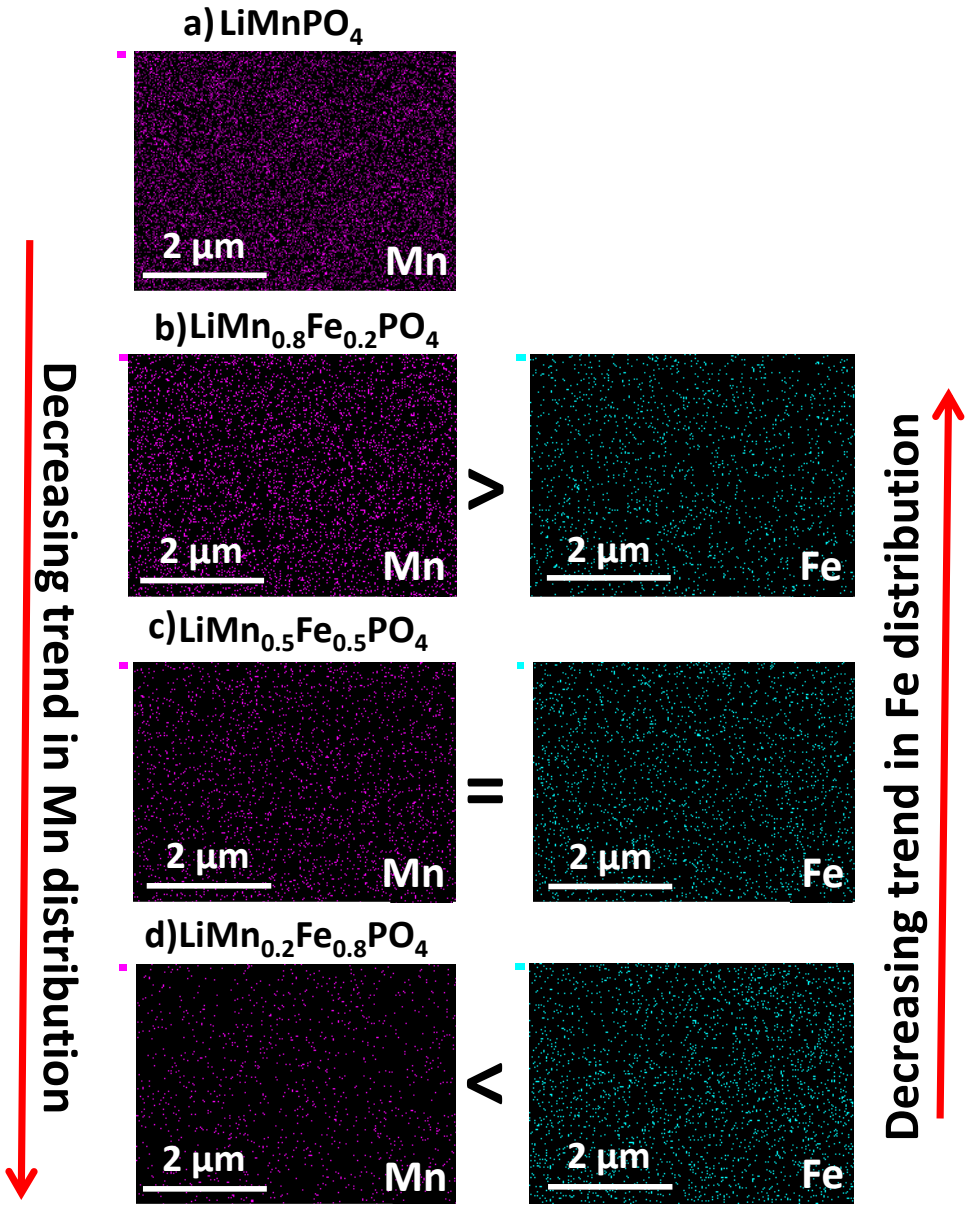

Figure 5.6 Elemental mapping images of $LiMn_{1-x}Fe_xPO_4/C$ (x = 0, 0.2, 0.5 and 0.8): Distribution trend of Mn and Fe in the composition (a) $LiMnPO_4/C$, (b) $LiMn_{0.8}Fe_{0.2}PO_4/C$, (c) $LiMn_{0.5}Fe_{0.5}PO_4/C$ and (d) $LiMn_{0.2}Fe_{0.8}PO_4/C$.

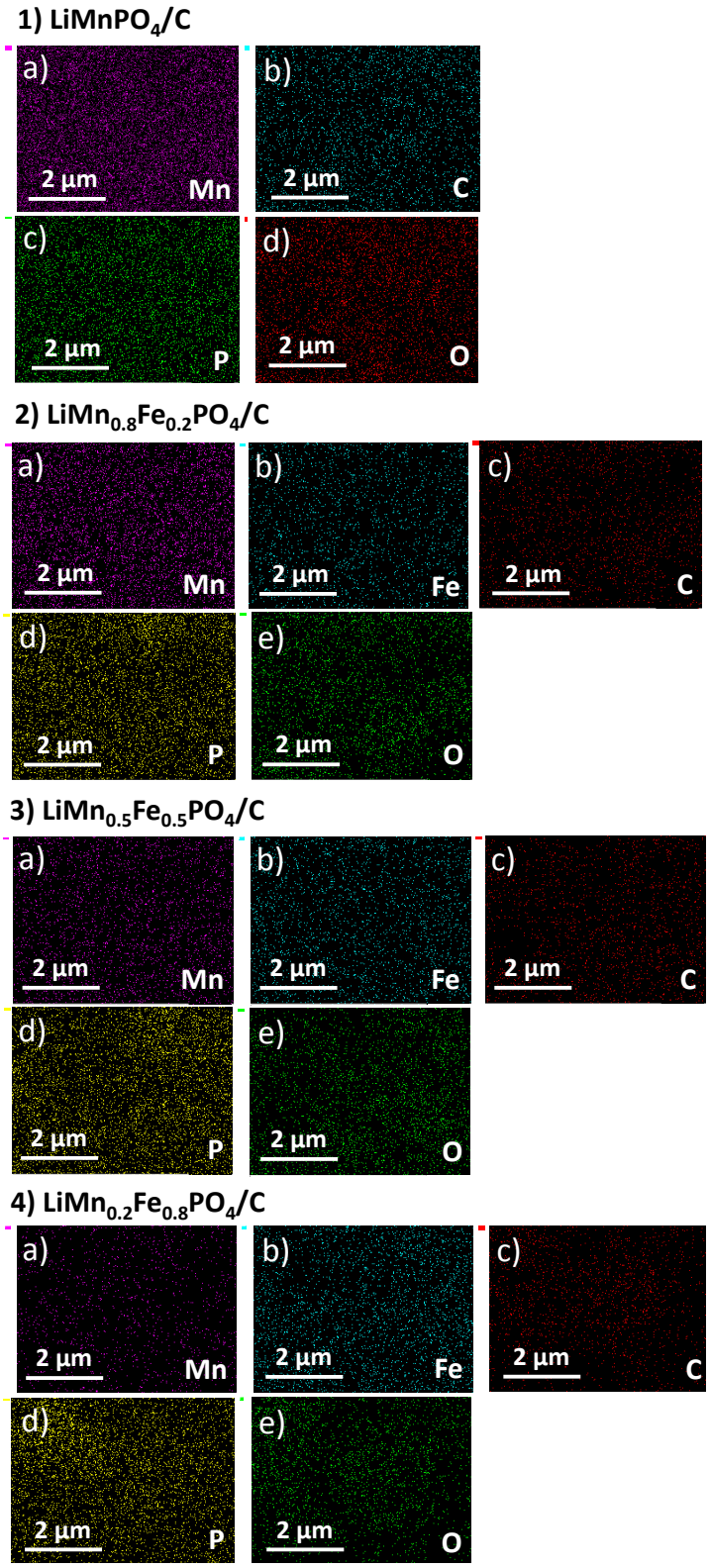

Figure 5.7 Elemental mapping of various compositions $LiMn_{1-x}Fe_xPO_4/C$ (x = 0, 0.2, 0.5 and 0.8): [(1) $LiMnPO_4$, (2) $LiMn_{0.8}Fe_{0.2}PO_4$, (3) $LiMn_{0.5}Fe_{0.5}PO_4$, (4) $LiMn_{0.2}Fe_{0.8}PO_4$]; Distribution of elements, (a) manganese (purple), (b) iron (cyan), (c) carbon (red), (d) phosphorus (yellow), and (e) oxygen (green) in $LiMn_{1-x}Fe_xPO_4/C$ (x = 0, 0.2, 0.5 and 0.8).

TEM images of $LiMn_{1-x}Fe_xPO_4$/C (x = 0, 0.2, 0.5 and 0.8) materials are shown in **Figure 5.8** The particles in the size range 30-50 nm appear to be embedded in a carbon matrix. The TEM images of $LiMn_{1-x}Fe_xPO_4$/C (x = 0, 0.2, 0.5 and 0.8) also show the presence of carbon coating (5 ± 2 nm) around the active materials. Such carbon coating facilitates electronic wiring between the particles and the Al current collector.

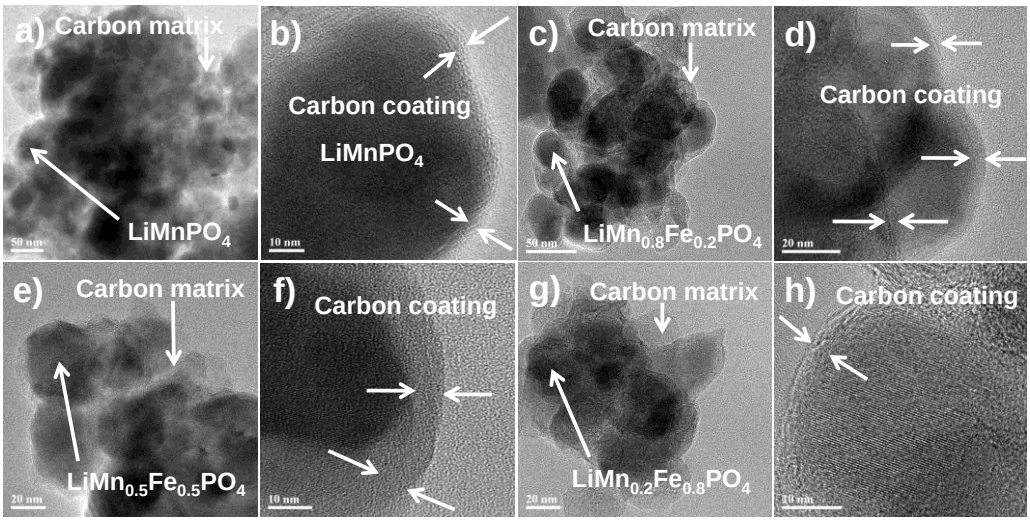

Figure 5.8 TEM images of (a-b) $LiMnPO_4$/C, (c-d) $LiMn_{0.8}Fe_{0.2}PO_4$/C, (e-f) $LiMn_{0.5}Fe_{0.5}PO_4$/C and (g-h) $LiMn_{0.2}Fe_{0.8}PO_0$/C at different magnification.

The BET surface area of $LiMn_{1-x}Fe_xPO_4$/C (x = 0, 0.2, 0.5 and 0.8) was analyzed by N_2 sorption isotherms **(Figure 5.9)**. Nitrogen adsorption and desorption isotherms of $LiMn_{1-x}Fe_xPO_4$/C (x = 0, 0.2, 0.5 and 0.8) sample exhibits clear hysteresis loop of Type IV.[370, 371, 382] The BET surface area of $LiMn_{1-x}Fe_xPO_4$/C (x = 0, 0.2, 0.5 and 0.8) samples were found to be 40.6, 34.2 33.2 and 31.6 m^2 g^{-1} with a pore size of 4.83, 3.85, 3.84 and 3.75 nm respectively **(inset of Figure 5.9 and Table 5.1)**. The pore volumes of these samples are 0.11, 0.12, 0.13 and 0.13 cc g^{-1} respectively **(Table 5.1)**. These pores provide better penetration of the liquid electrolyte which allows easy access to Li^+-ions from the bulk of the electrode.

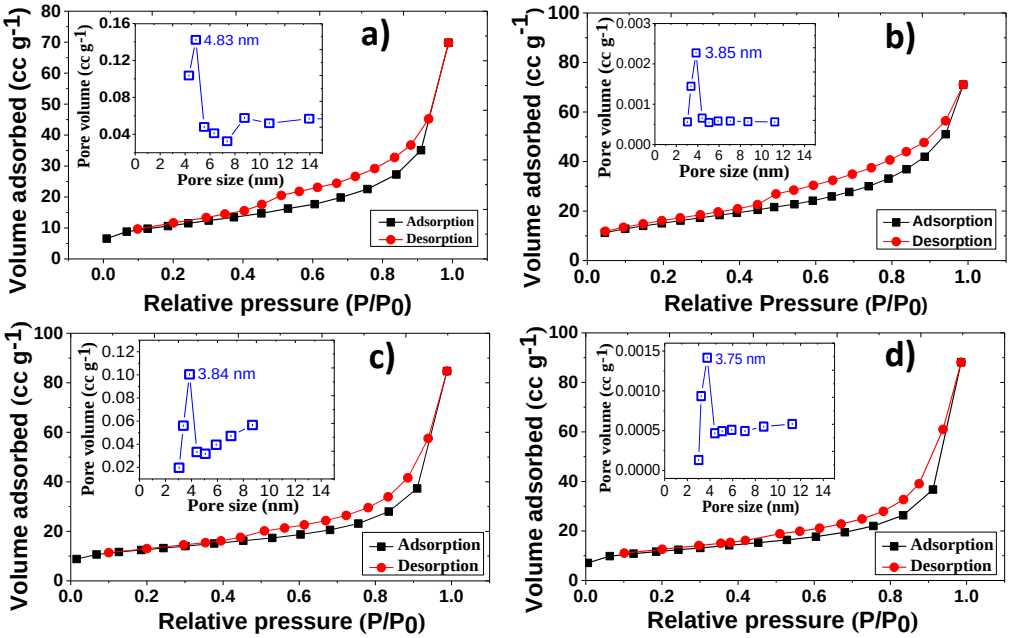

Figure 5.9 Nitrogen adsorption and desorption isotherms and pore size distribution (inset) of (a) $LiMnPO_4/C$, (b) $LiMn_{0.8}Fe_{0.2}PO_4/C$, (c) $LiMn_{0.5}Fe_{0.5}PO_4/C$ and (d) $LiMn_{0.2}Fe_{0.8}PO_4/C$.

Table 5.1 Nitrogen adsorption and desorption data LiMn1-xFexPO4/C (x = 0, 0.2, 0.5 and 0.8).

Electrode materials	$LiMnPO_4$	$LiMn_{0.8}Fe_{0.2}PO_4$	$LiMn_{0.5}Fe_{0.5}PO_4$	$LiMn_{0.2}Fe_{0.8}PO_4$
Surface area (*S_{BET}) (m^2g^{-1}) (±0.5)	40.6	34.2	33.2	31.6
Pore volume (cc g^{-1}) (±0.05)	0.11	0.12	0.13	0.13
Pore size (nm) (±0.05)	4.83	3.85	3.84	3.75

S_{BET} – Surface area by Brunauer–Emmet–Teller equation.

5.4.2 Redox potential shift in $LiMn_{1-x}Fe_xPO_4/C$ (x = 0, 0.2, 0.5 and 0.8)

Changes in the overall cell potential and the energy density of $LiMn_{1-x}Fe_xPO_4/C$ (x = 0, 0.2, 0.5, 0.8 and 1) are demonstrated in the schematic given below (**Figure 5.10)**. It shows the position of redox potential of Mn^{2+}/Mn^{3+}

and Fe^{2+}/Fe^{3+} redox couples with respect to that of Li/Li^{+}. The effect of Fe^{2+} substitutions in the lattice of Mn^{2+}, showing subsequent changes in cell potentials and energy density of $LiMn_{1-x}Fe_xPO_4$ (x = 0, 0.2, 0.5, 0.8 and 1). The amount of Mn^{2+}/Mn^{3+} redox in the electrode composition decides the energy density and the overall cell voltage.[160]

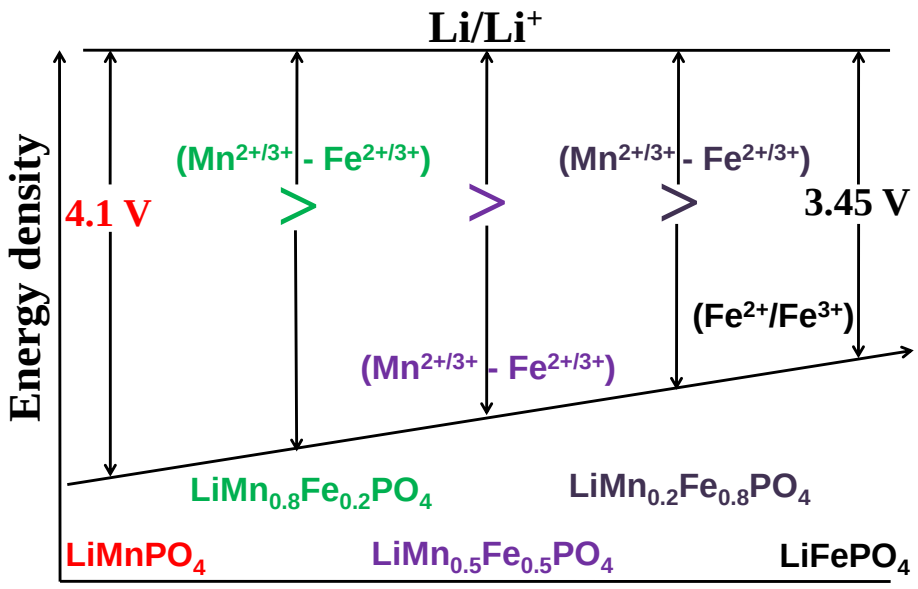

Figure 5.10 Positions of the Mn^{2+}/Mn^{3+} and Fe^{2+}/Fe^{3+} redox couples with respect to that of Li/Li^{+} and the effect of Fe^{2+} substitution on the overall cell potentials and energy density.

Figure 5.11 represents the cyclic voltammograms (CV) of carbon coated electrode compositions. The CV was recorded with Li metal as the counter and reference electrodes in the voltage range of 2.3-4.6 V at a scan rate of 0.058 mV s^{-1} up to 10 cycles at room temperature. **Figure 5.11a** shows the anodic oxidation peak in $LiMnPO_4$/C at ~4.3 V and the cathodic reduction peak at 3.96 V which are attributed exclusively to the consecutive oxidation and reduction of the Mn^{2+}/Mn^{3+} redox couple. Further, the CV of $LiMn_{1-x}Fe_xPO_4$ (x = 0.2, 0.5 and 0.8) shows two distinct anodic peaks approximately at 3.45 and 4.12 V and cathodic peaks at ~3.43 and 4.03 V and these observed

peak scan be attributed exclusively to the consecutive oxidation and reduction of Fe^{2+}/Fe^{3+} and Mn^{2+}/Mn^{3+} redox couples. The peak height of Mn^{2+}/Mn^{3+} and Fe^{2+}/Fe^{3+} redox couples are proportionate to the amount of Mn and Fe in the electrode composition as shown in **Figure 5.11a - 5.11e**.

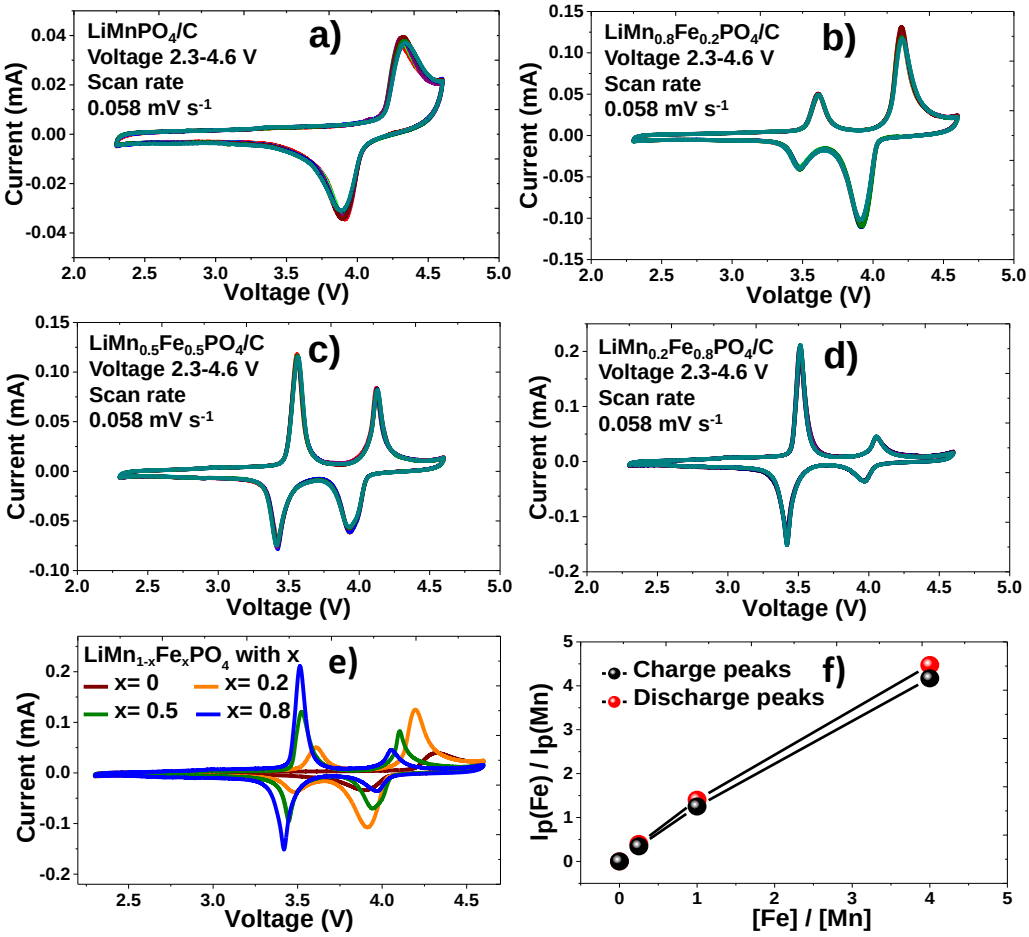

Figure 5.11 Cyclic Voltammograms profiles for $LiMn_{1-x}Fe_xPO_4/C$ (x = 0, 0.2, 0.5 and 0.8) at 0.058 mV s^{-1} scan rates up to 10 cycles; (a) $LiMnPO_4/C$, (b) $LiMn_{0.8}Fe_{0.2}PO_4/C$, (c) $LiMn_{0.5}Fe_{0.5}PO_4/C$, (d) $LiMn_{0.2}Fe_{0.8}PO_4/C$, (e) CV profiles of $LiMn_{1-x}Fe_xPO_4/C$ with x and (f) the linear relationship of the ratio of current peaks for Fe [I_p (Fe)] and Mn [I_p (Mn)] from CVs recorded at 0.058 mV s^{-1} and the ratio of composition.

Figure 5.11f shows the ratio between Mn and Fe redox current peaks corresponding to the electrode composition, where a linear behaviour is seen. As could be seen the slope of these lines are close to unity and it passes through the origin.[404] Hence, the oxidation and reduction peaks for both

Mn^{2+}/Mn^{3+} and Fe^{2+}/Fe^{3+} redox couples with varying redox current peaks depend on the degree of Mn and Fe substitution in the electrode composition which is in good agreement with the galvanostatic cycling profiles **(shown later in Figure 5.14)**. Further, the systematic shifts in the redox potentials were confirmed by CV measurements and voltage profiles (voltage profile is measured by galvanostatic method where a constant current was applied to battery to obtain voltage values at different SOC) of $LiMn_{1-x}Fe_xPO_4/C$ (x = 0, 0.2, 0.5, 0.8 and 1) as shown in **Figure 5.11e and Figure 5.12.**

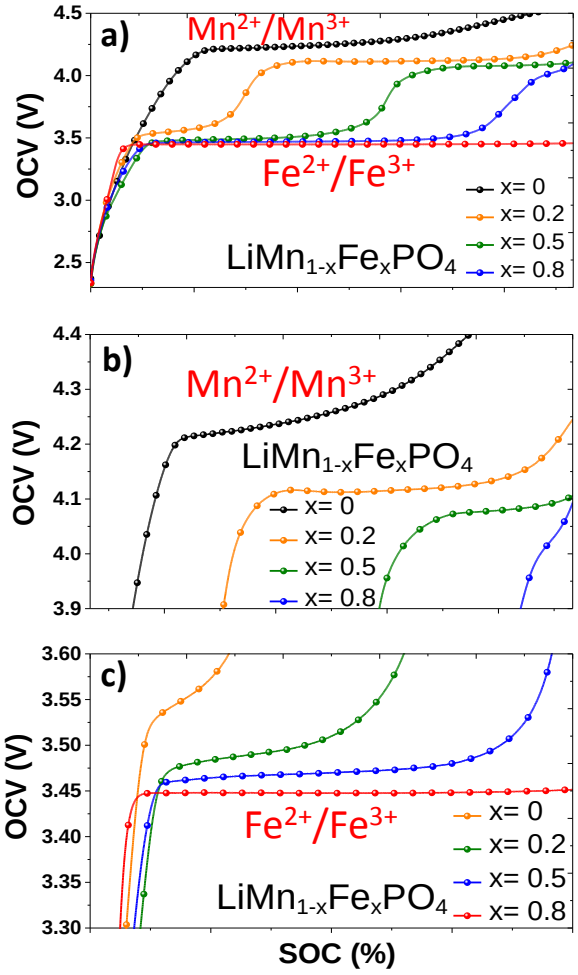

Figure 5.12 (a) A comparative chart of voltage profiles of charge cycle of $LiMn_{1-x}Fe_xPO_4$ (x = 0, 0.2, 0.5, 0.8 and 1) with x ($LiFePO_4$ voltage profile of charge cycle for sake comparison), (b) Expanded view of Mn^{2+}/Mn^{3+} redox profiles and (c) Expanded view of Fe^{2+}/Fe^{3+} redox profiles.

It clearly shows that the redox potential is progressively decreased for Mn^{3+}/Mn^{2+} and it is progressively increased for Fe^{3+}/Fe^{2+} as a function of the Fe content (x) owing to Fe-O-Mn superexchange interaction.[13, 120] The augmentation in the Mn/Fe ratio leads to the shift in the cathodic and anodic peaks towards higher potential for Mn^{3+}/Mn^{2+} and Fe^{3+}/Fe^{2+} redox couples, where the overall potential shifts are approximately 0.1 V, consistent with the previous reports.[13, 120]

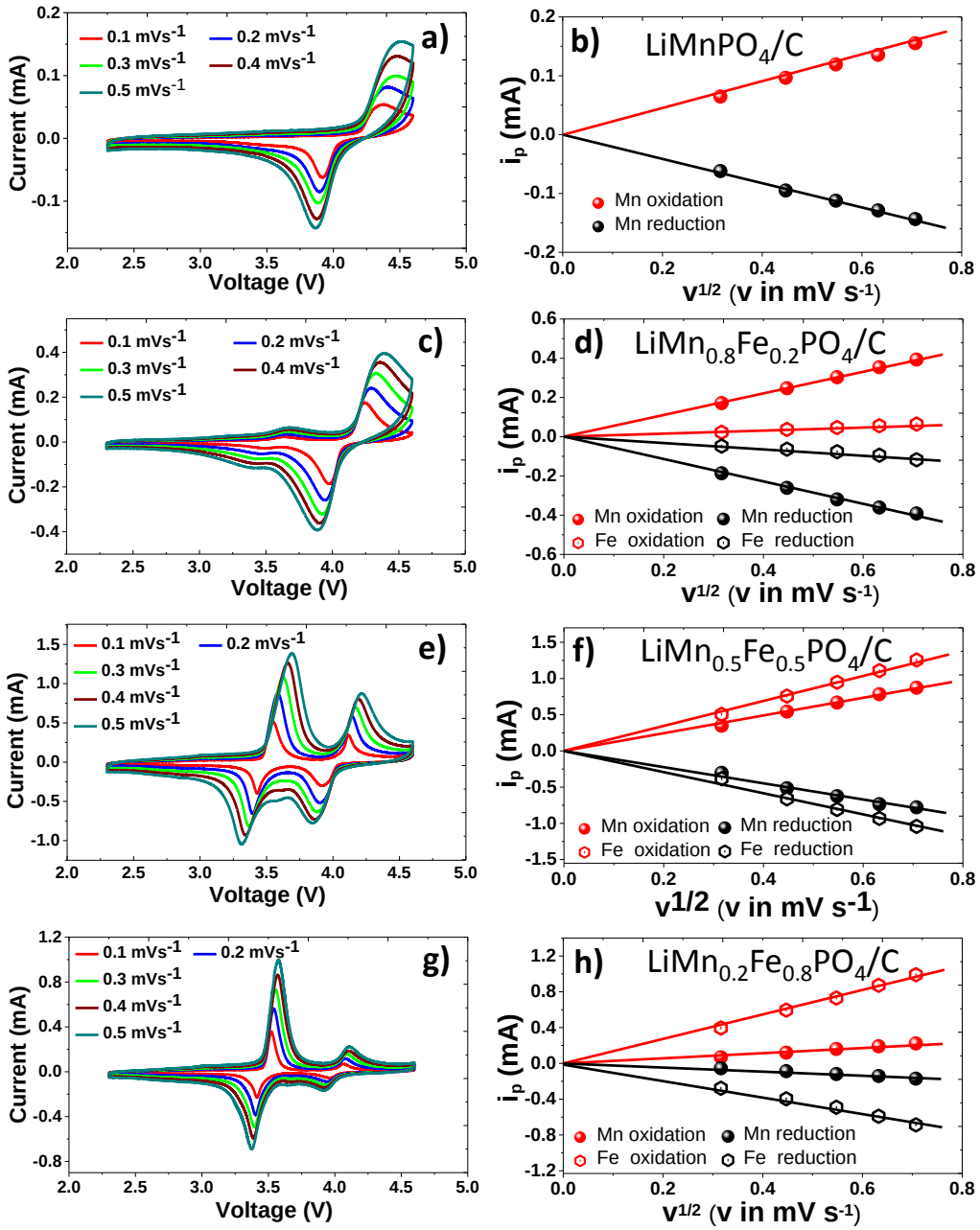

Figure 5.13 Cyclic voltammograms (CV) at different scan rates (0.1, 0.2, 0.3, 0.4 and 0.5 mV s^{-1}) and corresponding plots of linear relationship between the peak current (i_p) and the square root of scan rate ($v^{1/2}$) for both the charge and discharge states of (a-b) $LiMnPO_4/C$, (c-d) $LiMn_{0.8}Fe_{0.2}PO_4/C$, (e-f) $LiMn_{0.5}Fe_{0.5}PO_4/C$ and (g-h) $LiMn_{0.2}Fe_{0.8}PO_4/C$.

The symmetrical nature of the redox peaks in the CV at different scan rates are shown in **Figure 5.13a, 5.13c, 5.13e and 5.13g.** In the subsequent scan rates, the anodic peaks and the corresponding cathodic peaks of Mn and Fe are unaltered; this infers good reversibility of mesoporous $LiMn_{1-}$

$_x Fe_x PO_4$/C (x = 0, 0.2, 0.5 and 0.8). The voltage hysteresis (ΔV, the difference between the anodic and cathodic peaks voltage) increased with the increasing scan rate whereas the peak ratio of the anodic current to the cathodic current was unity (i.e. $|i_{ap}/i_{cp}| = 1$).[383] This shows the absence of side reactions during this insertion and extraction process. **Figure 5.13b, 5.13d, 5.13f and 5.13h** clearly illustrates the linear relationship between the peak current (i_p) and the square root of the scan rate ($v^{1/2}$). This indicates that the electrochemical extraction and insertion process of $LiMn_{1-x}Fe_xPO_4$/C (x = 0, 0.2, 0.5 and 0.8) is mainly limited by diffusion. Therefore, the diffusion of Li^+-ion is a key factor for electrochemical kinetics of the system. Further, the change in steepness of linear relationship between the peak current (i_p) and the square root of the scan rate ($v^{1/2}$) confirms the augmentation in the Mn/Fe ratio in the electrode compositions.

5.4.3 Lithium storage performance

Figure 5.14a represents the galvanostatic cycling profiles of $LiMnPO_4$/C, the charge profile at 4.3 V corresponding to the Mn oxidation (Mn^{2+}/Mn^{3+}) followed by discharge cycle potential at 3.96 V corresponding to the Mn reduction (Mn^{3+}/Mn^{2+}), resulting in a storage performance of 120 mAh g^{-1} at 0.1C corresponding to ~0.71 moles of Li^+ insertion. **Figure 5.14b - 5.14d** shows the voltage profiles of $LiMn_{1-x}Fe_xPO_4$ (x = 0.2, 0.5 and 0.8) Mn-Fe mixed phospho-olivine in which two distinct charge and discharge plateaus corresponding to Mn and Fe redox couples are seen. The lithium storage performance of these solid solutions are 160, 159, 158 mAh g^{-1} at 0.1C rate corresponding to ~0.94, 0.93 and 0.93 moles of Li^+ insertion at room temperature. Though the discharge capacity is almost similar in all these

electrode compositions, $LiMn_{0.8}Fe_{0.2}PO_4/C$ exhibits high energy density as 80% of the storage capacity occurs at the higher potential Mn^{2+}/Mn^{3+} redox region. However, the total discharge capacity delivery is a contribution of both oxidation and reduction of Fe^{2+}/Fe^{3+} (~3.45 V) and Mn^{2+}/Mn^{3+} (~4.1 V) redox couples in the Mn-Fe mixed electrode compositions unlike $LiMnPO_4/C$. This favourable redox combination exhibits attractive electrochemical activity of Mn in the phospho-olivine.[161, 164, 171]

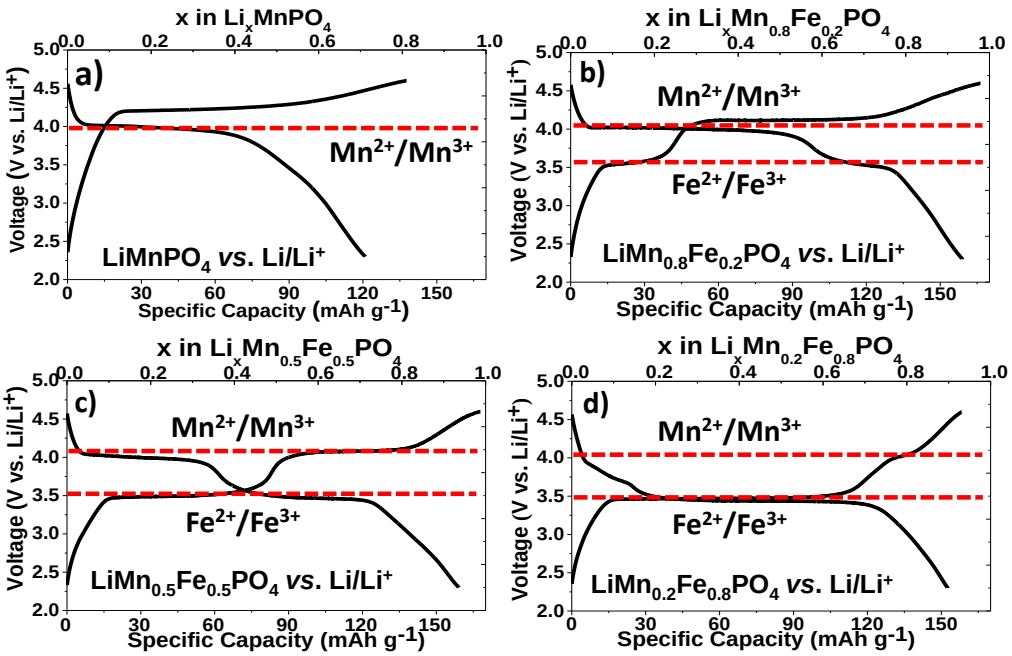

Figure 5.14 Specific charge and discharge characteristic profiles of $LiMn_{1-x}Fe_xPO_4/C$ (x = 0, 0.2, 0.5 and 0.8) at 0.1C, (a) $LiMnPO_4/C$, (b) $LiMn_{0.8}Fe_{0.2}PO_4/C$, (c) $LiMn_{0.5}Fe_{0.5}PO_4/C$, (d) $LiMn_{0.2}Fe_{0.8}PO_4/C$ in a voltage window of 2.3 - 4.6V at room temperature.

The voltage polarization between intercalation/deintercalation plateau for solid solution electrodes was found to be ~85 mV:20 mV in the Mn:Fe potential regions at 0.1C which is consistent with our earlier report.[136] The voltage polarization of the $LiMnPO_4$ was found to be 340 mV.[134, 135] The huge reduction in the voltage polarization, particularly at Mn^{2+}/Mn^{3+} redox region and improved lithium storage performance could be attributed to Fe-O-Mn

superexchange interaction, lower activation energy and electronic configuration of Mn^{2+} ($3d^5$) and Fe^{2+} ($3d^6$) of Mn-Fe mixed phospho-olivines.[13, 123, 164, 171, 174]

The discharge profiles and cycling stability of $LiMn_{1-x}Fe_xPO_4$/C (x = 0, 0.2, 0.5 and 0.8) at various current rates namely 0.1, 0.2, 0.5, 1, 2, 5 and 10 C are shown in **Figure 5.15**. The storage performances of above samples at various rates are summarized in **Table 5.2**. For instance, $LiMn_{0.8}Fe_{0.2}PO_4$/C delivers discharge capacity of 141 mAh g^{-1} compared to $LiMn_{0.5}Fe_{0.5}PO_4$/C, $LiMn_{0.2}Fe_{0.8}PO_4$/C and $LiMnPO_4$/C which deliver only 134, 126 and 61 mAh g^{-1} at 1C respectively.

Table 5.2 A summary of lithium storage performance of $LiMn_{1-x}Fe_xPO_4$/C (x =0, 0.2, 0.5, 0.8) at various current rates.

	C rates							
	Specific discharge capacity in mAh g^{-1}							
Electrode materials	0.05C	0.1C	0.2C	0.5C	1C	2C	5C	10C
$LiMnPO_4$/C	140	120	98	94	61	41	20	-
$LiMn_{0.8}Fe_{0.2}PO_4$/C	-	160	156	154	141	125	106	88
$LiMn_{0.5}Fe_{0.5}PO_4$/C	-	159	155	145	134	122	100	82
$LiMn_{0.2}Fe_{0.8}PO_4$/C	-	158	147	136	126	115	93	70

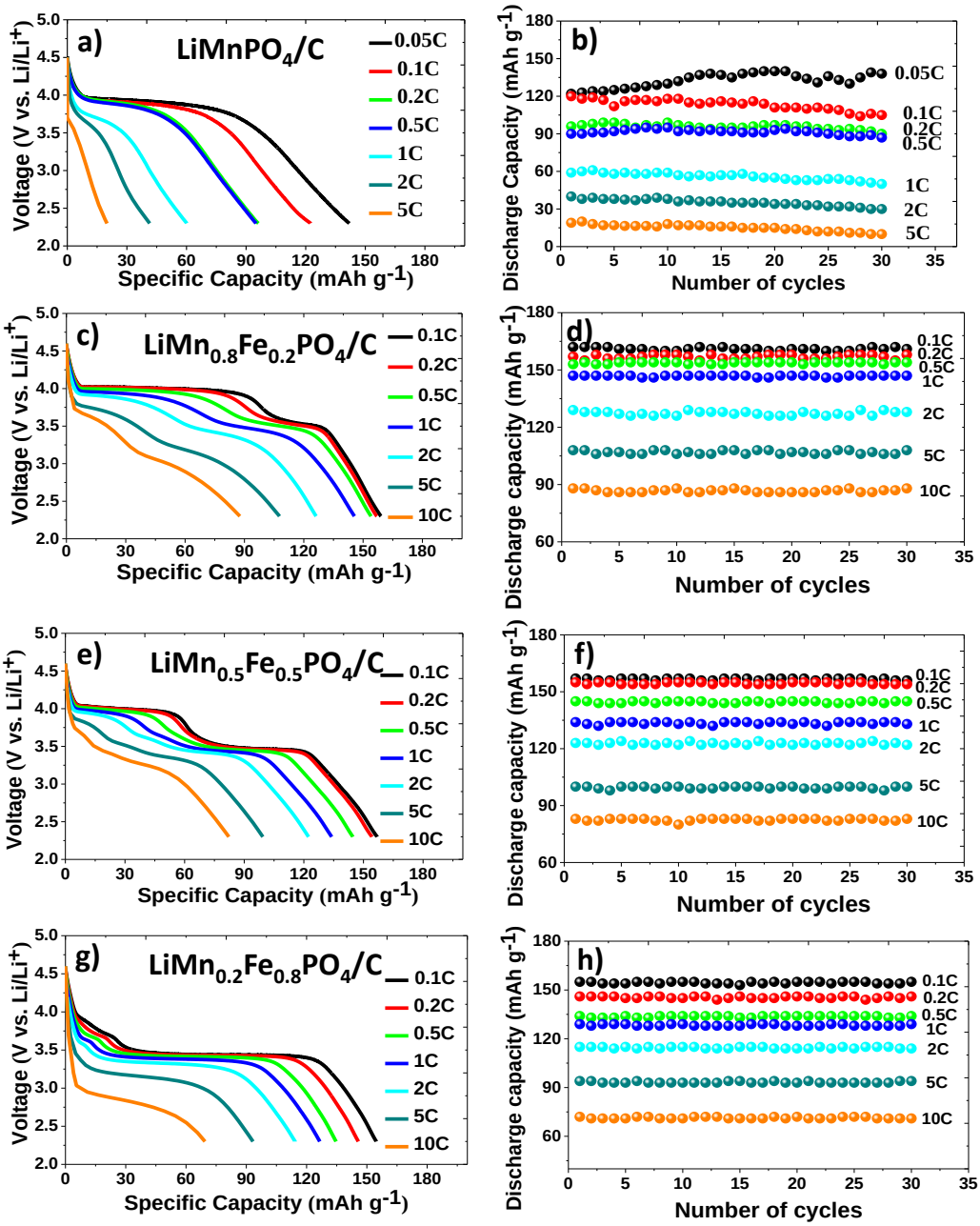

Figure 5.15 Galvanostatic discharge profiles of $LiMn_{1-x}Fe_xPO_4/C$ (x = 0, 0.2, 0.5 and 0.8) at different C-rates and corresponding cycling stability up to 30 cycles, (a-b) $LiMnPO_4/C$ (c-d) $LiMn_{0.8}Fe_{0.2}PO_4/C$, (e-f) $LiMn_{0.5}Fe_{0.5}PO_4/C$, (g-h) $LiMn_{0.2}Fe_{0.8}PO_4/C$ in a voltage window of 2.3 - 4.6 V at room temperature.

$LiMn_{0.8}Fe_{0.2}PO_4/C$ electrode delivers discharge capacities of 160, 156, 154, 125, 106 and 88 mAh g^{-1} at 0.1, 0.2, 0.5, 2, 5, and 10C respectively **(Figure 5.15a–5.15b).** Further, the lithium storage performance of $LiMn_{0.8}Fe_{0.2}PO_4/C$ is one of the highest reported so far.[160, 161, 391] Similarly,

$LiMn_{0.5}Fe_{0.5}PO_4/C$ electrode delivers discharge capacities of 159, 155, 145, 122, 100 and 82 mAh g^{-1} at 0.1, 0.2, 0.5, 2, 5, and 10C respectively **(Figure 5.15c–5.15d)** and $LiMn_{0.2}Fe_{0.8}PO_4/C$ electrode delivers discharge capacities of 157, 146, 136, 115, 93 and 70 mAh g^{-1} at 0.1, 0.2, 0.5, 2, 5, and 10C respectively **(Figure 5.15e–5.15f)**. Mn-Fe mixed phospho-olivines samples showed good cyclic stability compared to $LiMnPO_4/C$ up to 30 cycles **(Figure 5.15)**.

Fast charging at 1C followed by slow discharge at 0.2C was performed to evaluate the stability of the $LiMn_{1-x}Fe_xPO_4$ (x= 0.2, 0.5 and 0.8) electrodes and the results are shown in **Figure 5.16**. Such fast charge galvanostatic cycling is required for electric automotives to reduce charging time to minute/seconds. $LiMn_{1-x}Fe_xPO_4$ (x= 0.2, 0.5 and 0.8) electrode exhibits the lithium storage performance of 155, 150 and 142 mAh g^{-1} at 0.2C respectively.

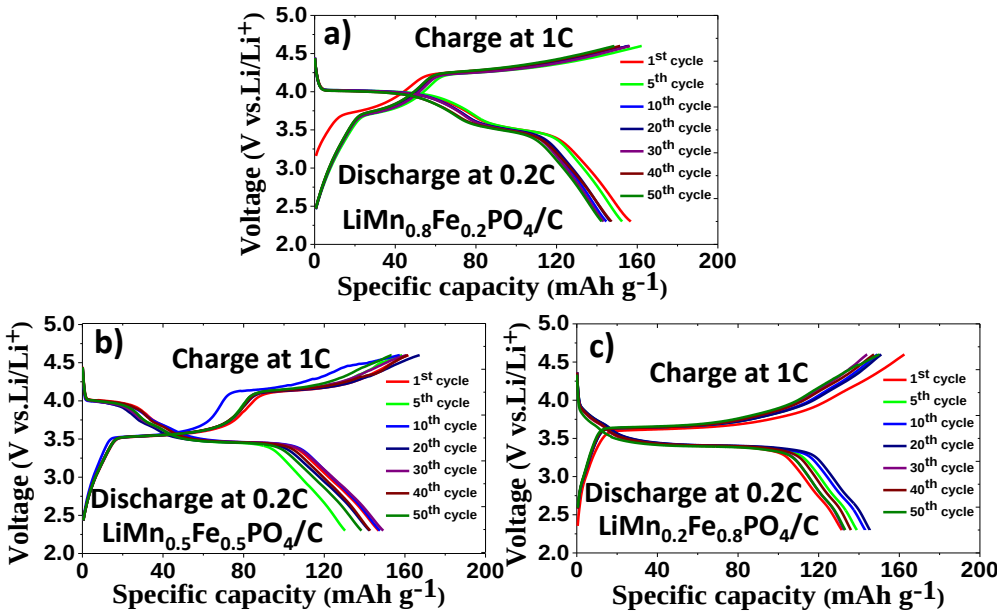

Figure 5.16 Fast charge (1C) and slow discharge (0.2C) lithium storage performance profiles of $LiMn_{1-x}Fe_xPO_4/C$ (x = 0.2, 0.5 and 0.8) up to 50 cycles in a voltage window of 2.3-4.6 V at 25 °C temperature, (a) $LiMn_{0.8}Fe_{0.2}PO_4/C$, (b) $LiMn_{0.5}Fe_{0.5}PO_4/C$, (c) $LiMn_{0.2}Fe_{0.8}PO_4/C$.

The rate performances of the various samples are summarized in **Figure 5.17a**. After testing at 10C rate, all the cells were again tested at 0.1C rate. The electrodes show excellent recovery, for example $LiMn_{0.8}Fe_{0.2}PO_4/C$, $LiMn_{0.5}Fe_{0.5}PO_4/C$ and $LiMn_{0.2}Fe_{0.8}PO_4/C$ retains 97%, 96% and 96% of its initial capacity respectively (92% for $LiMnPO_4/C$ after 5C).[134]

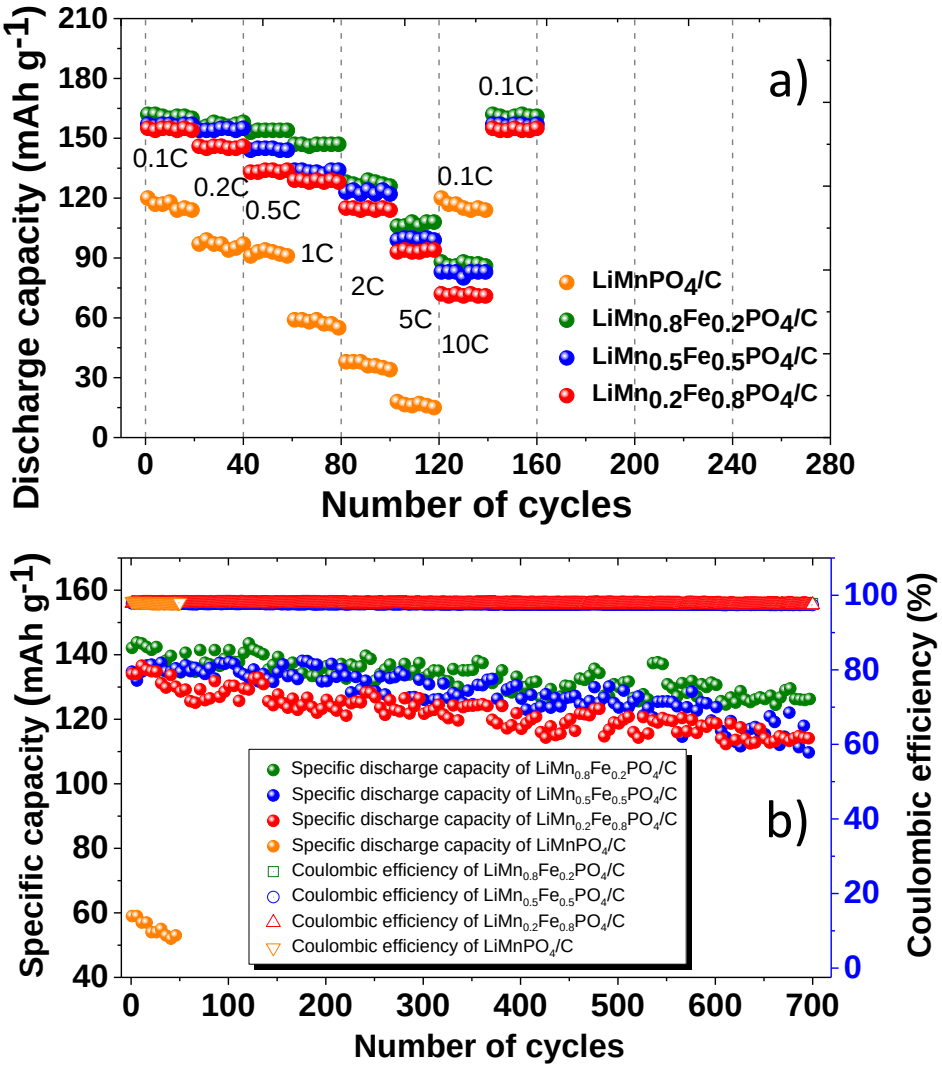

Figure 5.17 (a) Rate performance of $LiMn_{1-x}Fe_xPO_4/C$ (x = 0, 0.2, 0.5 and 0.8) at different C-rates, (b) Long term cyclability of $LiMn_{1-x}Fe_xPO_4/C$ (x = 0.2, 0.5 and 0.8) up to 700 cycles and $LiMnPO_4/C$ up to 50 cycles at 1C ($LiMnPO_4/C$ for sake comparison).

$LiMn_{1-x}Fe_xPO_4/C$ (x = 0.2, 0.5, 0.8) showed good long term cycling stability compared to $LiMnPO_4/C$ which shows capacity retention of 85% after

50 cycles with an average coulombic efficiency of 98.2% **(Figure 5.17b)**. Capacity retention of 86% was obtained for $LiMn_{0.8}Fe_{0.2}PO_4/C$ after 700 cycles at 1C with an average coulombic efficiency of 97.9%. Similarly, $LiMn_{0.5}Fe_{0.5}PO_4/C$ and $LiMn_{0.2}Fe_{0.8}PO_4/C$ show capacity retention of 85.8% and 83.6% with average coulombic efficiencies of 97.7% and 97.6% respectively. As mentioned, these materials were prepared with the similar morphology, particle sizes and carbon content. To a large extent, the observed differences in the electrochemical performance of these materials are not biased by factors such as morphology, particle size and carbon content. Hence, the enhanced electrochemical kinetics are clearly associated with the improved bulk electronic conduction, lower activation energy[164, 171] and favourable redox combination (Fe^{2+}/Fe^{3+} and Mn^{2+}/Mn^{3+}) as shown later in $LiMn_{0.8}Fe_{0.2}PO_4/C$.

To calculate the D_{Li}^{+} of $LiMn_{1-x}Fe_xPO_4/C$ (x = 0.2, 0.5, 0.8), EIS studies were performed on cells after 700 cycles as shown in **Figure 5.18a and 5.18b**. The experimental data were fitted using the equivalent circuit model shown as in **Figure 5.18c**.[134, 135, 137] The fitted values of R_S, R_1 and R_2 are given in **Table 5.3**. It is suggested that the R_1 refers to the charge transfer resistance, while R_2 which is an elevated resistance at high frequency region is associated with the Li^+-ion transfer resistance (surface film resistance) at electrode-electrolyte interface.[134, 135, 137]

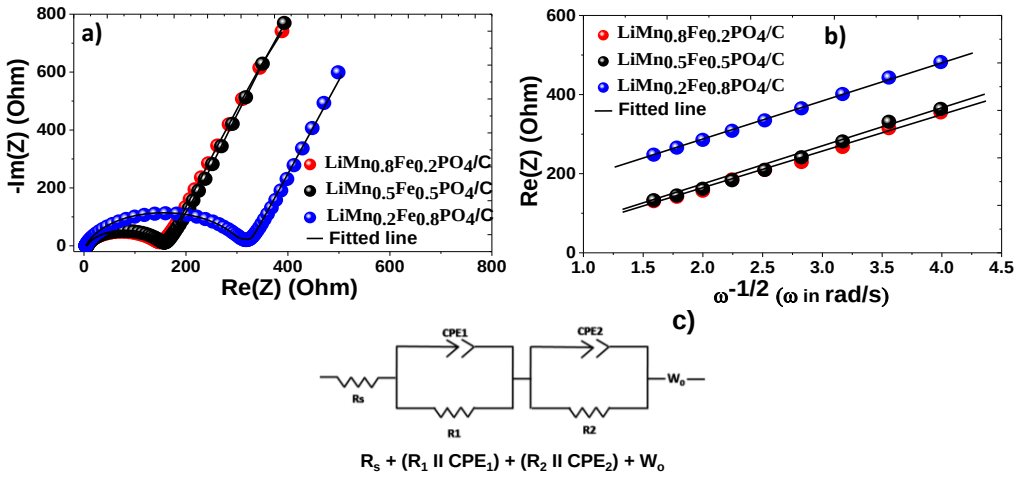

Figure 5.18 (a) Nyquist impedance spectra of $LiMn_{1-x}Fe_xPO_4/C$ (x = 0.2, 0.5, 0.8) after 700 cycles at room temperature, (b) corresponding linear fittings between Z_{re} and reciprocal square root of the angular frequency in low frequency region and (c) equivalent circuit.

Table 5.3 Impedance parameters derived using equivalent circuit model for $LiMn_{1-x}Fe_xPO_4/C$ (x = 0.2, 0.5, 0.8) at room temperature.

	Cell impedance after 700 cycles				
Electrode materials	$R_s(\Omega)$	$R_1(\Omega)$	CPE_1 (x 10^{-6} F)	$R_2(\Omega)$	CPE_2 (x 10^{-6}F)
$LiMn_{0.8}Fe_{0.2}PO_4/C$	3.94	1.97	20.31	136.60	12.62
$LiMn_{0.5}Fe_{0.5}PO_4/C$	2.65	2.83	12.11	151.70	14.32
$LiMn_{0.2}Fe_{0.8}PO_4/C$	1.71	1.77	15.20	301.70	10.66

The D_{Li}^+ was calculated for these samples using **Equation (3. 2).**

where, R is the gas constant, T is the absolute temperature (K), A is the contact area of the electrode (2.01 cm^2), n is the number of electrons per molecule, F is the Faraday constant, C is the concentration of Li ions (6.38 x 10^{-3} $mol.cm^{-3}$) (ratio between the tap density of the prepared material and molecular weight) and σ is the Warburg coefficient (obtained from **Figure**

5.18a-5.18b).[134, 135, 187, 403] The D_{Li}^{+} values obtained from EIS measurements are shown in **Table 5.4**. These obtained D_{Li}^{+} values are comparable with the reported values.[135, 177, 384 134]

Table 5.4 Diffusion coefficient derived from EIS measurements of $LiMn_{1-x}Fe_xPO_4/C$ (x = 0.2, 0.5, 0.8) at after 700 cycles.

Electrode materials	$LiMn_{0.8}Fe_{0.2}PO_4/C$	$LiMn_{0.5}Fe_{0.5}PO_4/C$	$LiMn_{0.2}Fe_{0.8}PO_4/C$
D_{Li}^{+} after 700 cycles ($cm^2\ s^{-1}$)	3.44×10^{-14}	2.96×10^{-14}	2.62×10^{-14}

5.4.4 High temperature galvanostatic cycling

The optimal composition $LiMn_{0.8}Fe_{0.2}PO_4/C$ was chosen for high temperature galvanostatic cycling, *ex-situ* FTIR, XRD, thermal XRD, XPS studies and diffusion coefficient studies at various stages of lithium extraction and insertion owing to its superior energy density.

Figure 5.19 shows the high temperature galvanostatic cycling (RT, 45, 55 and 60°C) of $LiMn_{0.8}Fe_{0.2}PO_4/C$ at 0.2C up to 50 cycles at each temperature. $LiMn_{0.8}Fe_{0.2}PO_4/C$ shows stable discharge capacity of ~155 mAh g^{-1}. However, there is a fading in the voltage as well as the capacity at the Mn region with increase in temperature. Such a trend is believed to be attributed to the increase in Mn dissolution with temperature.[72, 405] *Ex-situ* PXRD patterns of this sample cycled up to 150 cycles at high temperature (50 cycles at each temperature - 45, 55 and 60°C) show all the corresponding peaks of olivine phase with the additional peak of delithiated $Mn_{0.8}Fe_{0.2}PO_4$ at 30.70° and a strong peak of Al at 44.77° **(Figure 5.20)**.

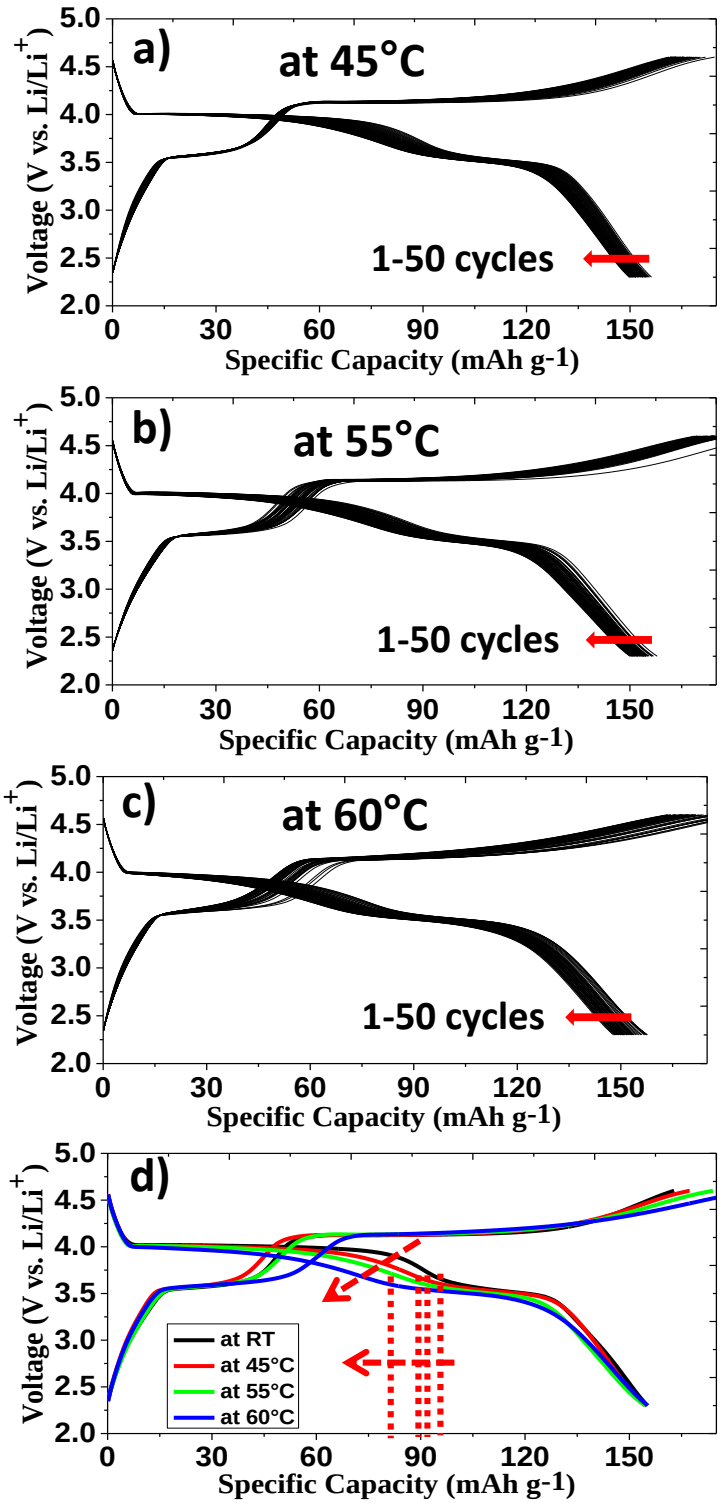

Figure 5.19 Charge and discharge profiles of $LiMn_{0.8}Fe_{0.2}PO_4/C$ at different temperature (RT, 45, 55 and 60°C) at 0.2C; $LiMn_{0.8}Fe_{0.2}PO_4/C$: (a) at 45°C, (b) at 55°C (c) at 60°C and (d) comparison of galvanostatic charge and discharge profiles at different temperature (RT, 45, 55, 60°C).

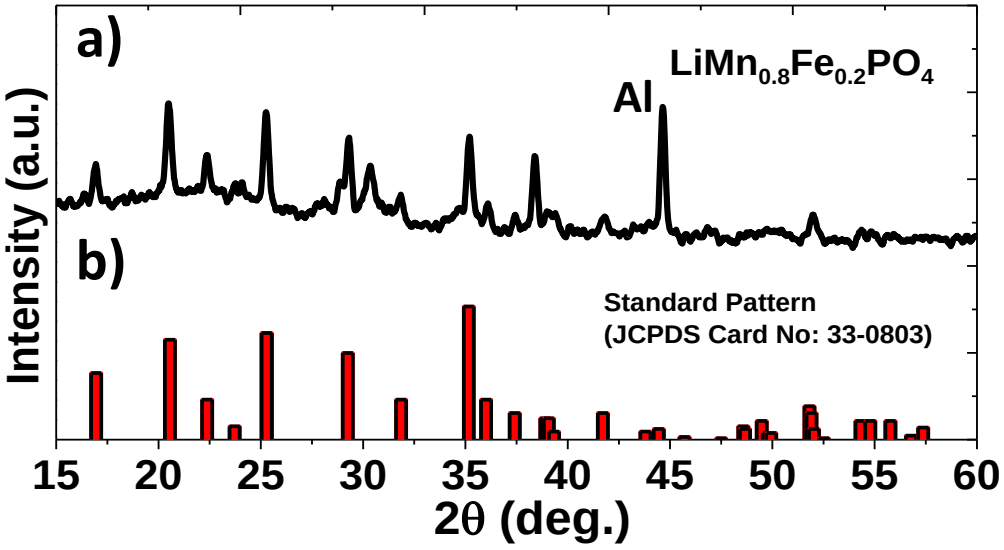

Figure 5.20 *Ex-situ* PXRD patterns of $LiMn_{0.8}Fe_{0.2}PO_4$/C after 150 cycles at high temperature (50 cycles at each temperature - 45, 55 and 60°C); (a) $LiMn_{0.8}Fe_{0.2}PO_4$/C and (b) standard powder pattern of $LiMnPO_4$ (JCPDS card No: 33-0803), Aluminium substrate (Al) peak at 44.77°.

Figure 5.21 represents the FESEM images of $LiMn_{0.8}Fe_{0.2}PO_4$/C electrode surface was taken on a sample after 150 cycles in total, but subjected to 50 cycles at 45 °C, 50 cycles at 55 °C and finally 50 cycles at 60 °C. Different FESEM figures (a), (b), (c), (d) and (f) refer to the same sample but at different magnification. This electrode surface image shows clear formation of cracks and electrical disconnectivity between the particles in the electrode. Such cracks seen in this electrode material could possibly arise from volume change during intercalation and deintercalation process (for more details see chapter 6) as well as expansion of electrode material at high temperature (higher than room temperature). Further, as seen from the literature, the introduction of huge volume change during electrochemical intercalation and deintercalation of lithium ions is well-known for causing cracks and disconnections in the electrode materials.[406, 407]

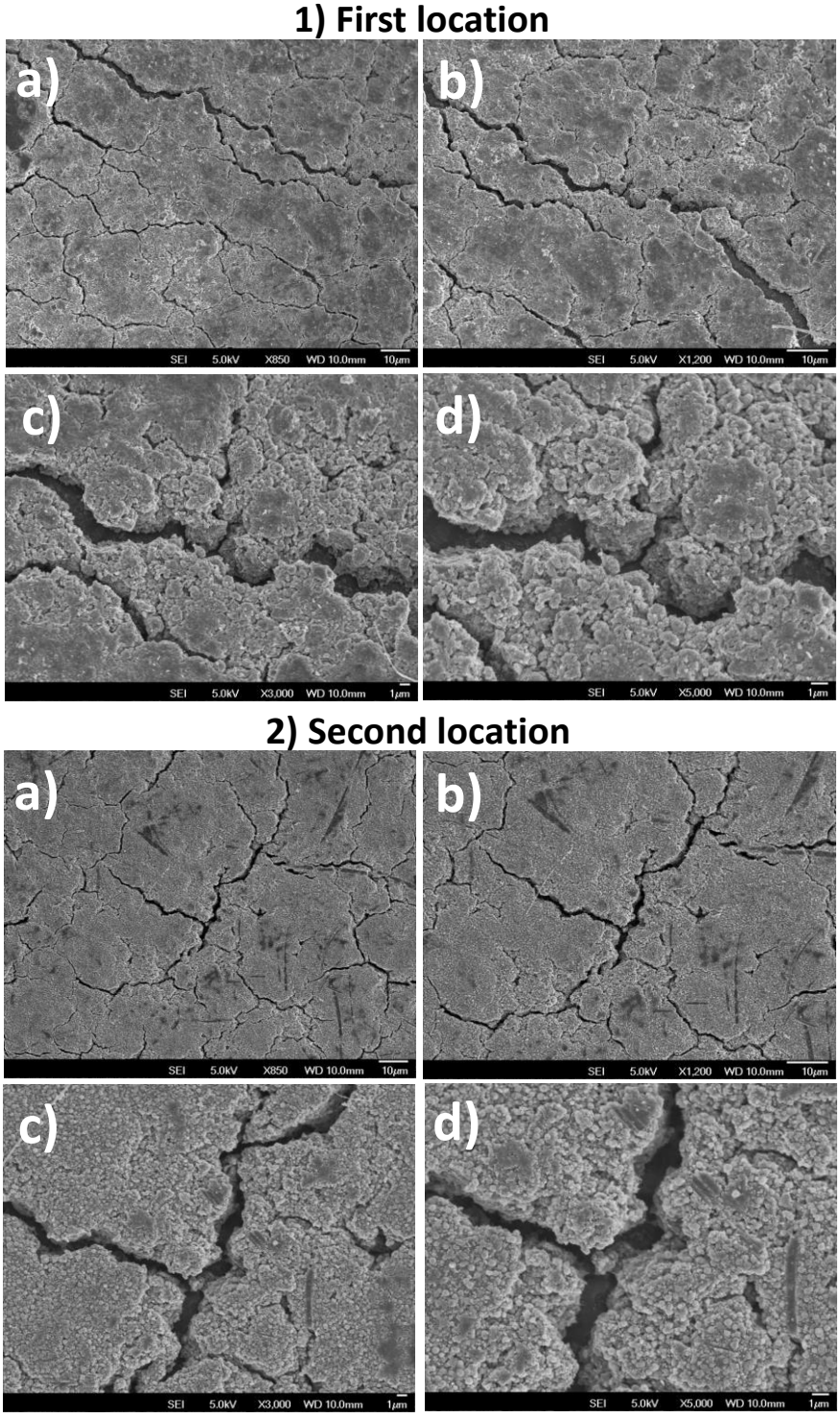

Figure 5.21 FESEM images of $LiMn_{0.8}Fe_{0.2}PO_4$/C electrode surface after 150 cycles in total at various temperature (50 cycles at each temperature - 45, 55 and 60 °C), (1 and 2) at different location and (a, b, c, d, e and f) at different magnification.

5.4.5 *Ex-situ* transmission FTIR spectra study of $LiMn_{0.8}Fe_{0.2}PO_4/C$

Figure 5.22a represents the transmission FTIR absorption spectra of $LiMnPO_4$, $LiMn_{0.8}Fe_{0.2}PO_4/C$ and $LiFePO_4$.

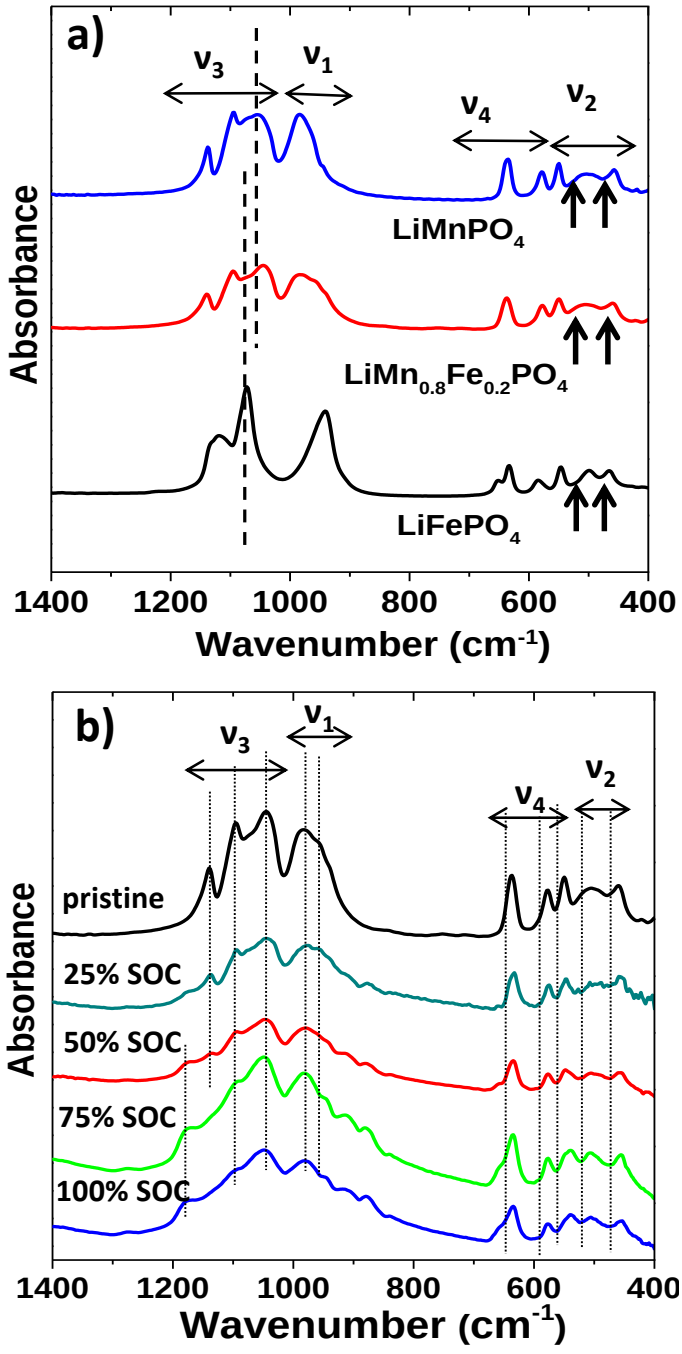

Figure 5.22 (a) Transmission FTIR spectra of ν_3, ν_1, ν_4 and ν_2 the lithium cage modes for $LiMnPO_4$, $LiMn_{0.8}Fe_{0.2}PO_4$ and $LiFePO_4$ ($LiMnPO_4$ and $LiFePO_4$ infrared spectra for sake of comparison), The dashed lines represent the two-mode behaviour in ν_3 and the arrow marks represent the lithium cage modes (ν_2), (b) Transmission FTIR spectra of $LiMn_{0.8}Fe_{0.2}PO_4/C$ at different state of charge (SOC).

These spectra are dominated by the vibrations of the PO_4^{3-} anion, which consist of four modes: (i) anti-symmetric PO_4^{3-} stretching mode ν_3 that lies between 1150 and 1000 cm^{-1}, (ii) symmetric PO_4^{3-} stretching mode ν_1 that lies between 1000 and 800 cm^{-1}, (iii) anti-symmetric bending mode ν_4 seen between 650 and 530 cm^{-1} and (iv) symmetric bending mode ν_2 seen at a frequency lower than ν_4.[408-412] Among these, the stretching mode peaks are more localized than the bending modes.[413] Stretching mode spectral assignments of PO_4^{3-} vibrations in Mn-Fe mixed system is essentially the superposition of the two parent materials namely $LiFePO_4$ and $LiMnPO_4$ **(Figure 5.22a)**.[168, 408-416] The details of the spectral assignments of the pristine samples are mentioned in **Table 5.5**.

Table 5.5 Spectral assignment of $LiMn_{0.8}Fe_{0.2}PO_4/C$ at various state of charge.

$LiMn_{0.8}Fe_{0.2}PO_4/C$ (major peaks - frequency in cm^{-1})				
Sample	ν_3	ν_1	ν_4	ν_2
Pristine	1135, 1096 and 1047	982 and 954	637, 578 and 550	501 and 459
25% SOC	1137, 1098 and 1047	981 and 958	635, 577 and 548	504 and 459
100% SOC	1189, 1095 and 1041	973 and 942	633, 577 and 539	505 and 454

Figure 5.22b shows the transmission FTIR spectra of $LiMn_{0.8}Fe_{0.2}PO_4/C$ at various states of charge (SOC). At 25% SOC where Fe^{2+} is oxidized to Fe^{3+}, there are hardly any changes in the FTIR spectra **(Table 5.5)**. For 50% - 100% SOC where Mn^{2+} is oxidized to Mn^{3+}, noticeable changes could be seen in the spectra. During this redox reaction, the peaks of

the test electrodes broaden as compared to the pristine sample spectrum **(see Figure 5.22b and Table 5.5)**.

As seen from the earlier reports, the P-O stretching mode ν_3 width increased from 84 cm^{-1} to 142 cm^{-1} for $LiFePO_4$ while width increment is from 65 cm^{-1} to 228 cm^{-1} for $LiMnPO_4$.[411, 412, 414] The broadening in the stretching mode ν_3 of $LiMn_{0.8}Fe_{0.2}PO_4$ was 88 cm^{-1} (1135-1047) at 25% SOC while the corresponding broadening after 100% SOC was 148 cm^{-1} (1189-1041 cm^{-1}) **(Table 5.5)**. It is seen that the peak broadening of the $LiMn_{0.8}Fe_{0.2}PO_4$ was less compared to $LiMnPO_4$[411 178, 411, 417] Such a peak broadening is attributed to the Jahn-Teller distortion induced by Mn^{3+} ions owing to strong electron-lattice interaction between these ions in the delithiated structure.[94, 158, 411, 412, 418] This geometrical deformation of the Mn-O structure directly affects the P-O bands, since Mn^{3+} and P^{5+} share oxygen atoms covalently in the structure lattices and a larger separation of the ν_3 bands.[168, 412] The theoretical work by Seo *et al.*[172] also showed that the substitution of transition metal in $LiMnPO_4$ could suppress the Jahn-Teller distortion and enables faster migration of the electrons which are localized around Mn^{3+} ions compared to parent material $LiMnPO_4$.[90, 411] Hence, the presence of Fe^{3+} ions in the place of Mn^{3+} ions in the olivine structure could suppress the strain that is created by the Jahn-Teller Mn^{3+} ions.[176, 178]

5.4.6 Reaction mechanism

It is known from the previous studies that the mixed phospho-olivine $LiMn_{1-x}Fe_xPO_4$ follows a two phase mechanism similar to $LiFePO_4$.[13, 97, 123, 124, 419, 420] $LiMn_{0.8}Fe_{0.2}PO_4$/C shows similar behavior as seen from the *ex-situ* PXRD in **Figure 5.23**.

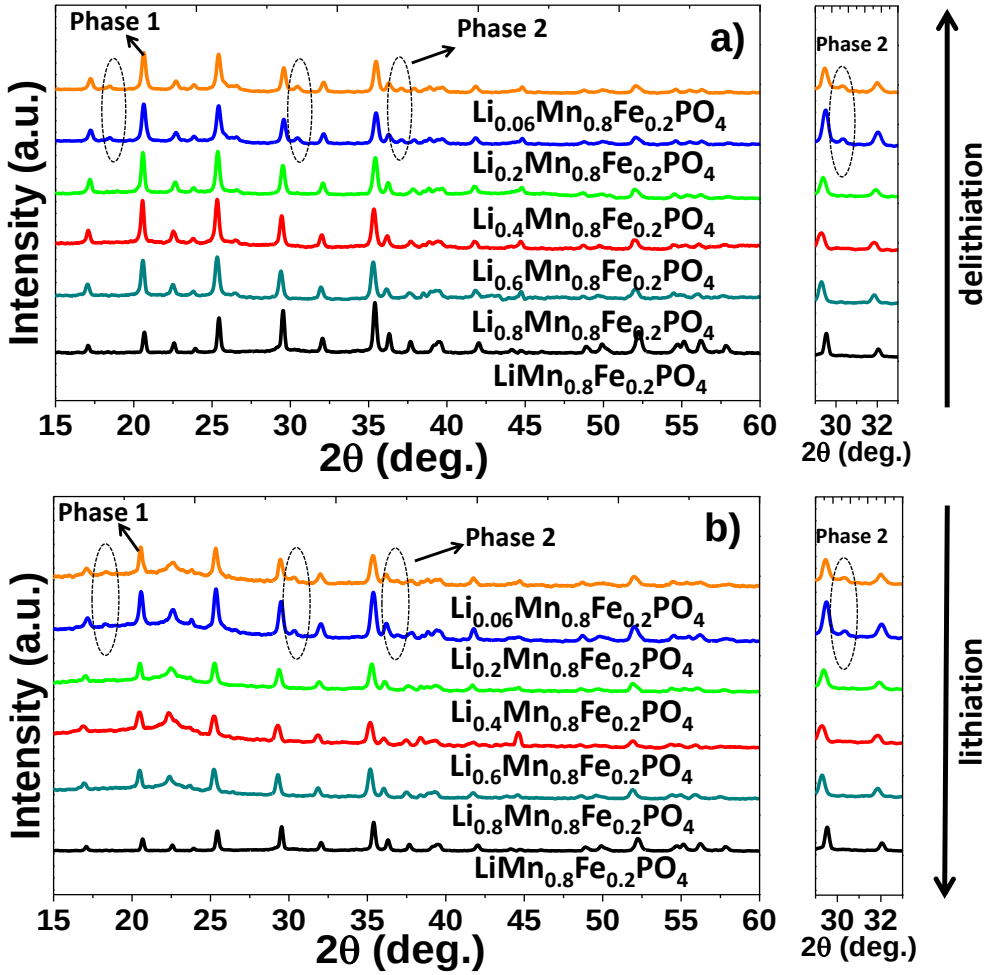

Figure 5.23 (a) *Ex-situ* PXRD patterns of $LiMn_{0.8}Fe_{0.2}PO_4/C$ at different stages of electrochemical extraction of lithium (charge), (b) *Ex-situ* PXRD patterns of $LiMn_{0.8}Fe_{0.2}PO_4/C$ at different stages of electrochemical insertion of lithium (discharge), (Phase 1 refers to lithiated phase and Phase 2 refers to delithiated phase).

During Fe^{2+}/Fe^{3+} redox reaction, the initial delithiation of $LiMn_{0.8}Fe_{0.2}PO_4/C$ proceeds through a single-phase mechanism to produce $Li_{1-y}Mn_{0.8}Fe_{0.2}PO_4/C$.[123, 124, 419] During Mn^{2+}/Mn^{3+} redox reaction, the particle surfaces become enclosed with a thin layer of delithiated $Li_{1-y}Mn_{0.8}Fe_{0.2}PO_4/C$ that migrates towards the lithium rich core. This single-phase mechanism continues until $y \leq 0.8$ as inferred from the XRD pattern as there are no evident changes in the XRD pattern. However, when $y \geq 0.8$, new peaks emerge at $2\theta = 18.49°$, $30.46°$ and $37.10°$ suggesting the onset of the two phase

behavior **(Figure 5.23a)**. Similarly, during lithiation, the initial lithiation of $Li_{1-y}Mn_{0.8}Fe_{0.2}PO_4/C$ occurs via two-phase mechanism followed by single-phase process ($y \geq 0.8$) that migrates towards lithium deficient core. At the end of lithiation process, lithiated $LiMn_{0.8}Fe_{0.2}PO_4/C$ is formed by single-phase process **(Figure 5.23b)**. This two-phase mechanism was also confirmed by the FTIR spectra of $Li_{1-x}Mn_{0.8}Fe_{0.2}PO_4/C$ in which peak broadening and increase in the peak intensity were significant during Mn^{2+}/Mn^{3+} redox reaction at >75% of SOC.[412] This observation is analogous with the FTIR spectral changes witnessed in the two-phase mechanism of $LiFePO_4$.[408]

Yamada et al.,[120, 124, 378] has shown that manganese redox reaction in $Li_{1-y}Mn_{1-x}Fe_xPO_4$, y = 0.6 happens through a two-phase mechanism while the iron redox reaction occurs via single-phase mechanism. In accordance to this report, we also observe two-phase mechanism in $Li_{1-y}Mn_{0.8}Fe_{0.2}PO_4/C$ (y = 0.8) during the Mn redox reaction. However, there is a narrow shift in the state of charge/state of discharge point where the two-phase mechanism is observed. This is related to the fact that we extracted lithium by electrochemical means, while Yamada's study focused on chemical delithiation.[124] It must be noted that the mechanism of lithium extraction/insertion is essentially different in the electrochemical cell than the chemical extraction.[421]

5.4.7 Structural and thermal stability

High structural and thermal stability of the cathode materials particularly at fully charge state is essential to enhance the reliability of the rechargeable batteries. *Ex-situ* temperature dependent PXRD were carried out at charged state (at 4.6 V) from RT to 500°C to understand the structural and

thermal stability of $LiMn_{0.8}Fe_{0.2}PO_4/C$. All the major peaks in $Li_{1-x}Mn_{0.8}Fe_{0.2}PO_4$ are seen even at 400°C **(Figure 5.24)**; however the peaks decrease/disappear at 450°C. The structure and thermal stability of fully charged Mn-rich $Li_{1-x}Mn_{0.8}Fe_{0.2}PO_4$ sample is reasonably high considering the observed thermal XRD patterns at high temperature.

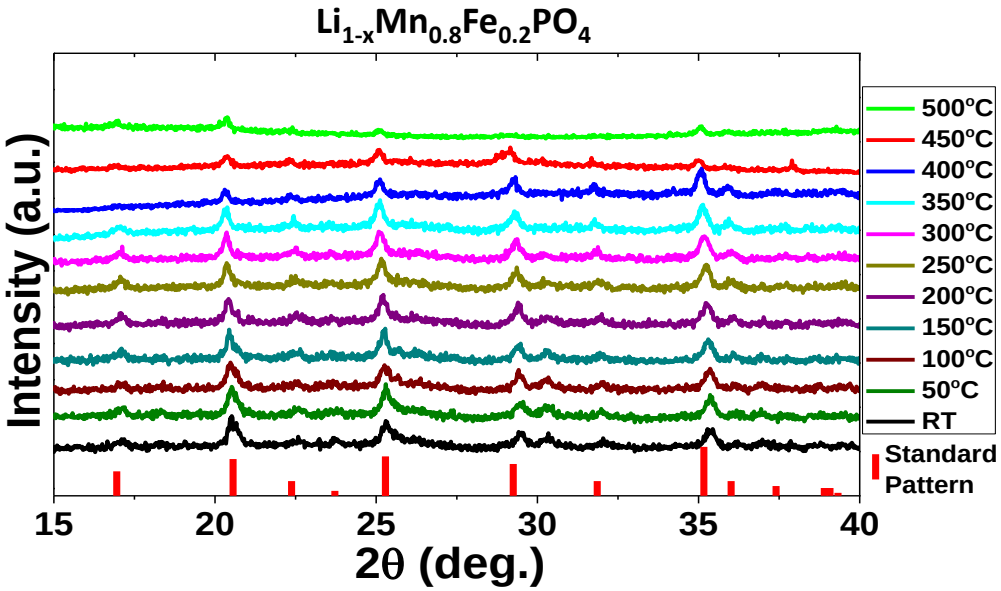

Figure 5.24 *Ex-situ* temperature dependent PXRD of $Li_{1-x}Mn_{0.8}Fe_{0.2}PO_4/C$ at charged state (at 4.6 V).

5.4.8 Enhanced Li^+-ion shuttling in the mixed transition metal Mn-Fe phospho-olivine: Facile transition mechanism

Ex-situ XPS experiments were carried out to study the Li^+ ion extraction/insertion mechanism in $LiMn_{0.8}Fe_{0.2}PO_4$ and to understand the reasons for enhanced manganese activity and lithium storage performance. XPS spectra were also recorded in $LiMn_{0.8}Fe_{0.2}PO_4$ sample on partially charged (4 V), fully charged (4.6 V) and fully discharged (2.3 V) electrodes **(Figure 5.25(i))**. During the process of lithium extraction up to 4 V, there is a redox transition from $LiMn^{2+}Fe^{2+}PO_4$ (pristine) to $Li_{(1-x)}Mn^{2+}(Fe^{3+})PO_4$ (partially charged to 4V) which is shown in XPS spectra **(Figure 5.25(ii))**.

Accordingly, spectra peaks are found to be located at binding energy of 641.3 and 712.6 eV corresponding to Mn^{2+} and Fe^{3+}, respectively **(Figure 5.25(ii))**.

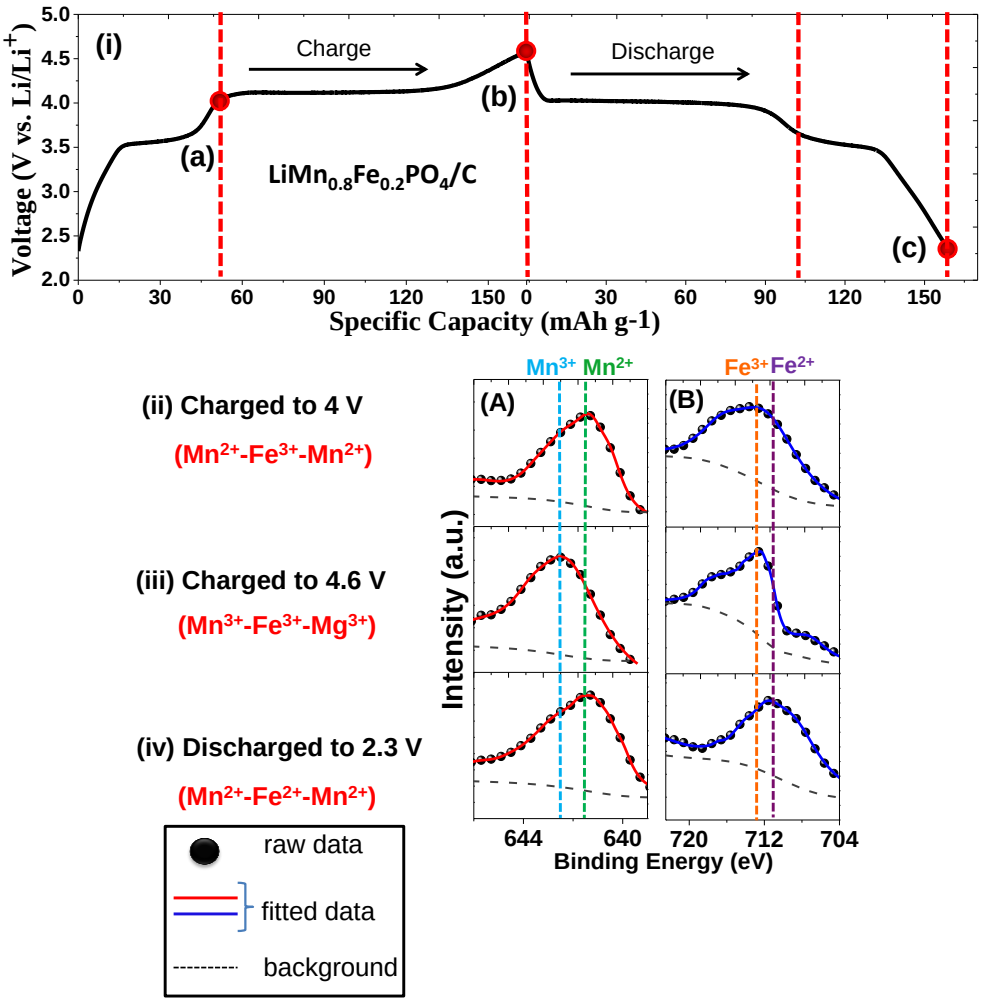

Figure 5.25 (i) Charge/discharge profile of $LiMn_{0.8}Fe_{0.2}PO_4/C$: [(a) a state of partially charged to 4 V, (b) a state of fully charged to 4.6 V, (c) a state of fully discharged to 2.3 V]; *ex-situ* XPS spectra of $LiMn_{0.8}Fe_{0.2}PO_4/C$: [(ii) partially charged to 4 V, (iii) fully charged to 4.6 V and (iv) fully discharged to 2.3 V]; (A) refers to Mn $2p_{3/2}$ and (B) refers to Fe $2p_{3/2}$.

A charge capacity of ~52 mAh g^{-1} witnessed up to 4 V corresponds to Fe^{2+}/Fe^{3+} redox transition and not from the Mn^{2+}/Mn^{3+} **(Figure 5.25(i))**. The possibility of capacity contribution from Mn^{2+}/Mn^{3+} is ruled out here as the equilibrium potential for such a redox couple occurs at ~4.1 V. The delithiated phase formed owing to Fe^{2+}/Fe^{3+} redox couple (favourable redox combination of Fe^{3+}-Mn^{2+}) facilitates further electrochemical redox activity of Mn^{2+}/Mn^{3+}

in $Li_{1-x}Mn_{0.8}Fe_{0.2}PO_4$.[180] During lithium extraction up to 4.6V, there is a redox transition from $Li_{(1-x)}Mn^{2+}$ $(Fe^{3+})PO_4$ (partially charged to 4 V) to $Li_{(1-x)}(Mn^{3+}$ $Fe^{3+})PO_4$ (fully charged to 4.6 V, 0< x >1) owing to transition of Mn^{2+}/Mn^{3+} at ~4.1 V as seen from XPS spectrum **(Figure 5.25(iii))**. XPS spectra show peaks at 642.5 and 712.6 eV corresponding to Mn^{3+} and Fe^{3+} respectively. During the process of lithium insertion, there is redox transition from Mn^{3+} to Mn^{2+} owing to higher equilibrium potential of Mn (~4.1 V), then followed by Fe^{3+} to Fe^{2+} redox transition. The delithiated phase created by Mn^{3+}/Mn^{2+} redox couples (redox combination of Fe^{2+}-Mn^{3+}), favours succeeding redox reaction of Fe^{3+}/Fe^{2+}. After complete discharge to 2.3V, peaks at 641.3 and 711.4 eV corresponding to Mn^{2+} and Fe^{2+} were seen **(Figure 5.25(iv))**. The subsequent charge and discharge cycles follow the above mechanism (combined Fe^{2+}/Fe^{3+} and Mn^{2+}/Mn^{3+} redox transition) which facilitates to enhance lithium storage performance of $LiMn_{0.8}Fe_{0.2}PO_4$ samples unlike parent material $LiMnPO_4$. The mechanism of enhanced Li^+ ion extraction/insertion in $LiMn_{0.8}Fe_{0.2}PO_4$ could be summarized in **Equation (5.2)**.

$$\underset{\mathbf{LiMn^{2+}Fe^{2+}PO_4}}{\mathbf{at\ OCV\ /\ 2.3\ V}} \rightleftharpoons \underset{\mathbf{Li_{(1-x)}Mn^{2+}(Fe^{3+})PO_4}}{\mathbf{at\ 4\ V}} \rightleftharpoons \underset{\mathbf{Li_{(1-x)}Mn^{3+}Fe^{3+}PO_4}}{\mathbf{at\ 4.6\ V}} \qquad \mathbf{(5.2)}$$

In short, during Li^+ ion extraction process, delithiated phase created from Fe^{2+}/Fe^{3+} redox (~3.45 V) favors facile electrochemical activity of the succeeding Mn^{2+}/Mn^{3+} redox of $LiMn_{0.8}Fe_{0.2}PO_4$ unlike $LiMnPO_4$. During the insertion process, there is redox transition from Mn^{3+} to Mn^{2+} owing to higher equilibrium potential of Mn redox (~4.1 V), then followed by Fe^{3+} to Fe^{2+} redox transition. The delithiated phase created by Mn^{3+}/Mn^{2+} redox, further

favours the succeeding redox reaction of Fe^{3+}/Fe^{2+}. Apart from electronic configuration of mixed transition metals ($Fe^{2+}(3d^6)$-$Mn^{2+}(3d^5)$),[164] the presence of such favourable redox combination provides favourable environment owing to difference in the equilibrium potential of Fe^{2+}/Fe^{3+} and Mn^{2+}/Mn^{3+} for the enhanced manganese utilization in the subsequent lithium ions extraction/insertion process unlike $LiMnPO_4$.

5.4.9 Diffusion study of $LiMn_{0.8}Fe_{0.2}PO_4/C$ at various stages of electrochemical extraction and insertion of lithium ion

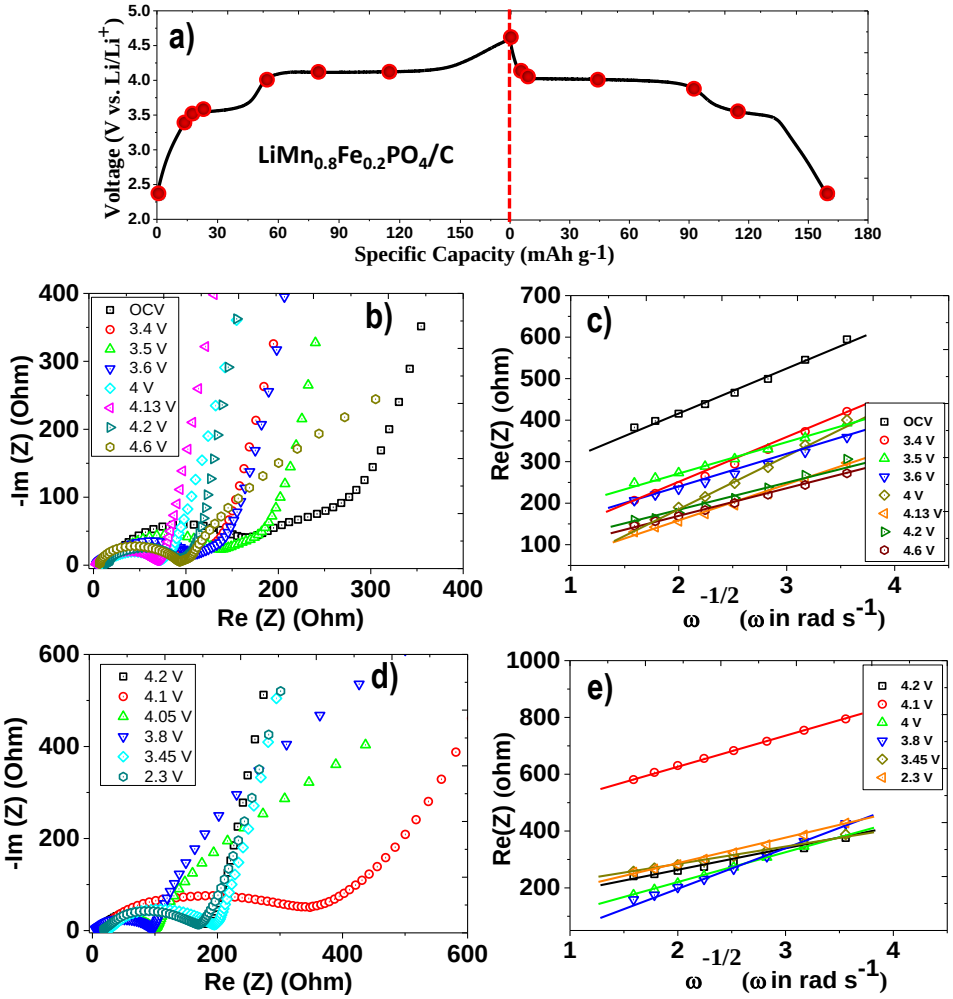

Figure 5.26 Impedance spectra of $LiMn_{0.8}Fe_{0.2}PO_4/C$ and corresponding linear fittings between Z_{re} and reciprocal square root of the angular frequency in the low frequency region of impedance spectra of $LiMn_{0.8}Fe_{0.2}PO_4/C$ at different stages of charge and discharge potentials, (a) charge and discharge profiles of $LiMn_{0.8}Fe_{0.2}PO_4/C$ (different stages were marked with red dots in the charge and

discharge profiles), (b-c) at different charge potential of $LiMn_{0.8}Fe_{0.2}PO_4/C$ and (d-e) at different discharge potential of $LiMn_{0.8}Fe_{0.2}PO_4/C$.

To estimate the apparent D_{Li}^+ of $LiMn_{0.8}Fe_{0.2}PO_4/C$ at various stages of electrochemical extraction and insertion of lithium ion, EIS studies were performed **(Figure 5.26a, 5.26b and 5.26d)**. The Warburg coefficient (σ) was calculated by taking the linear fittings between Z_{re} and reciprocal square root of the angular frequency in the low frequency region **(Figure 5.26c and 5.26e)**. The apparent D_{Li+} was calculated for these samples using **Equation (5.1).** where, σ is the Warburg coefficient (obtained from **Figure 5.26c and 5.26e**).[134, 187, 403] The apparent D_{Li}^+ values obtained from EIS measurements are shown in shown in **Figure 5.27** at various stages of lithium insertion and extraction and found to be comparable with earlier reports.[177, 384] The value of apparent D_{Li}^+ $LiMn_{0.8}Fe_{0.2}PO_4/C$ is higher compared to parent material $LiMnPO_4/C$[134] in both Fe^{2+}/Fe^{3+} and Mn^{2+}/Mn^{3+} redox region in charge and discharge process.

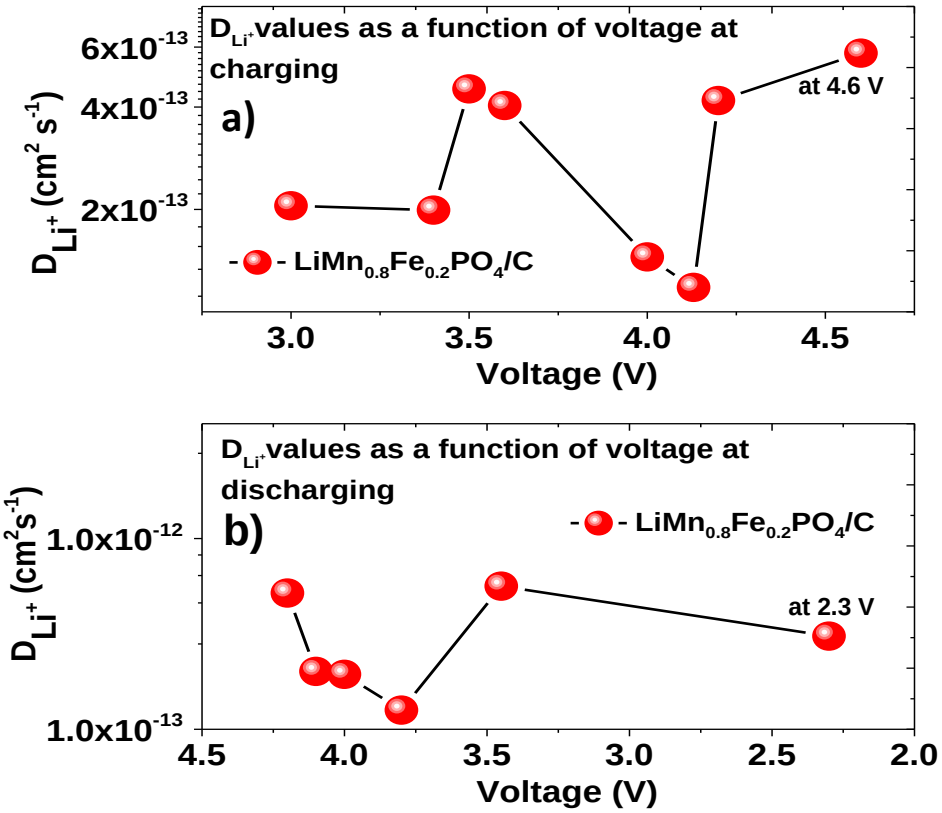

Figure 5.27 Apparent diffusion coefficient (D_{Li}^+) of $LiMn_{0.8}Fe_{0.2}PO_4/C$ (red dots) at different stages of electrochemical extraction and insertion of lithium calculated using impedance spectroscopy (taking the linear fittings between Z_{re} and reciprocal square root of the angular frequency in the low frequency region): (a) diffusion coefficient at different stages of charge and (b) diffusion coefficient at different stages of discharge.

5.4.10 Full cell performance $LiMn_{0.8}Fe_{0.2}PO_4/C$ vs. $Li_4Ti_5O_{12}/C$ and Fe_2O_3/C

In order to validate the capability of Mn-rich $LiMn_{0.8}Fe_{0.2}PO_4/C$ cathode material for the rechargeable Li-ion battery applications, full cell was fabricated using $Li_4Ti_5O_{12}/C$ and Fe_2O_3/C as anode materials **(Figure 5.28)**.[125,

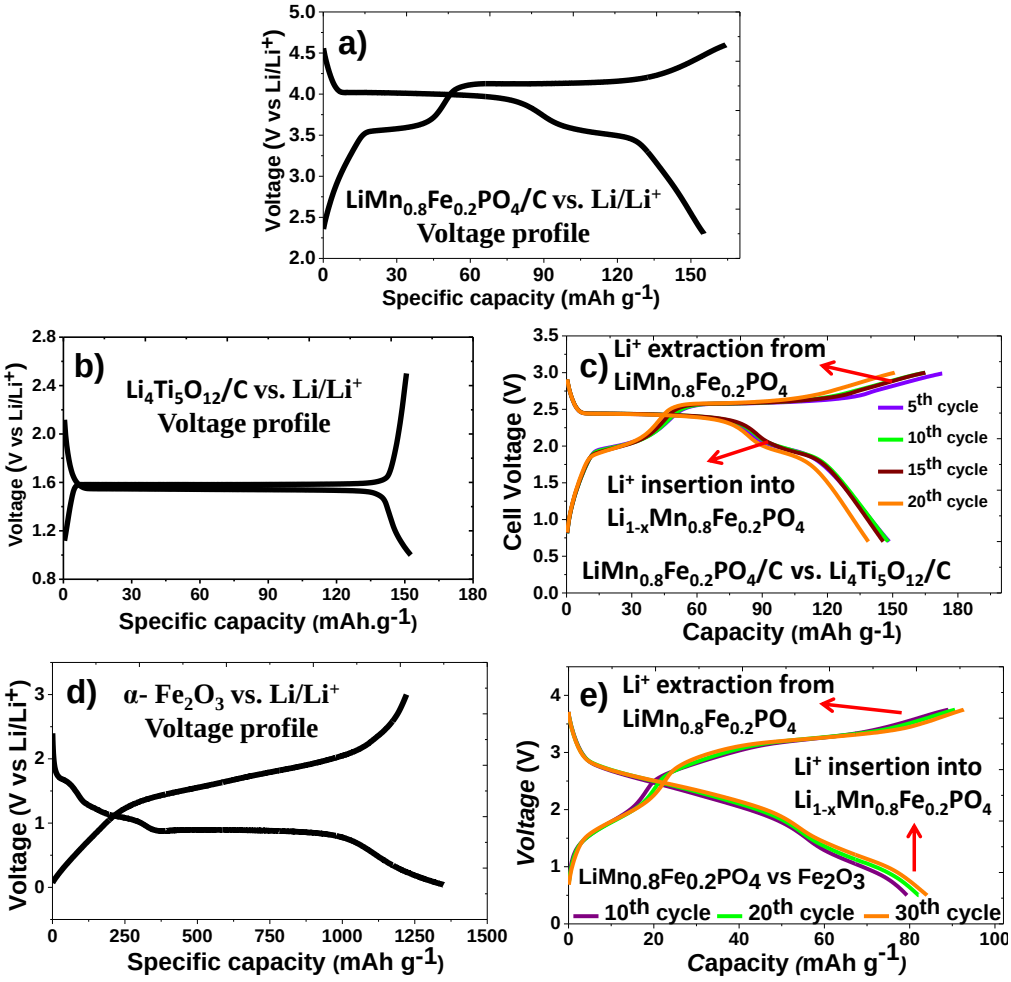

Figure 5.28 (a) Charge and discharge profiles of $LiMn_{0.8}Fe_{0.2}PO_4$/C at 0.5C, (b) Charge and discharge profiles of $Li_4Ti_5O_{12}$/C at 0.5C, (C) Charge and discharge profiles of full cell consist of $LiMn_{0.8}Fe_{0.2}PO_4$/C *vs.* $Li_4Ti_5O_{12}$/C in EC-DEC/1 M $LiPF_6$ electrolyte solution at 0.5C, (d) Charge and discharge profiles of Fe_2O_3/C at 0.1C, (e) Charge and discharge profiles of full cell consist of $LiMn_{0.8}Fe_{0.2}PO_4$/C *vs.* Fe_2O_3/C in EC-DEC/1 M $LiPF_6$ electrolyte solution at 0.5C.

Figure 5.28a, 5.28b and 5.28d shows a typical voltage profile of $LiMn_{0.8}Fe_{0.2}PO_4$/C, $Li_4Ti_5O_{12}$/C and Fe_2O_3/C against Li metal in a half cell. **Figure 5.28c** presents a typical voltage profile of full cell consisting of $LiMn_{0.8}Fe_{0.2}PO_4$/C vs. $Li_4Ti_5O_{12}$/C which clearly exhibits the behaviour of Mn^{2+}/Mn^{3+} and Fe^{2+}/Fe^{3+} redox couples. The full cell delivers discharge capacity of 147 mAh g^{-1} at 0.5C (close to discharge capacity of 153 mAh g^{-1} observed in the $LiMn_{0.8}Fe_{0.2}PO_4$/C vs. Li/Li^+ half-cell). The cells could retain

relatively stable discharge capacity of 139 mAh g^{-1} after 20 cycles at 0.5C. **Figure 5.28e** shows the charge and discharge profiles of full cell consisting of $LiMn_{0.8}Fe_{0.2}PO_4/C$ vs. Fe_2O_3/C which exhibits the behaviour of Mn^{2+}/Mn^{3+} and Fe^{2+}/Fe^{3+} redox couples. It delivers discharge capacity of 80 mAh g^{-1} couples (initial formation cycles are not shown). It could retain relatively stable discharge capacity of 85 mAh g^{-1} after 30 cycles at 0.5C. This preliminary full cell performance demonstrates potential capability of $LiMn_{0.8}Fe_{0.2}PO_4/C$ as cathode for rechargeable Li-ion batteries.

5.5 Summary

In summary, $LiMn_{1-x}Fe_xPO_4/C$ (x = 0, 0.2, 0.5 and 0.8) was synthesized with similar morphology, particles size (30 - 50 nm) and carbon content by a ball mill assisted soft template method to enhance the manganese utilization. $LiMn_{1-x}Fe_xPO_4$ (x = 0.2, 0.5 and 0.8) Mn-Fe mixed phosphate showed two distinct charge and discharge profiles, resulting in lithium storage performance of 160, 159, 158 mAh g^{-1} at 0.1C rate compared to $LiMnPO_4/C$ (120 mAh g^{-1}). The voltage polarization for solid solution electrodes was found to be ~85 mV:20 mV in the Mn:Fe redox potential region unlike $LiMnPO_4/C$ (340 mV) at 0.1 C. The capacity retention of 86% is obtained for $LiMn_{0.8}Fe_{0.2}PO_4/C$ after 700 cycles at 1C. Mn-rich $LiMn_{0.8}Fe_{0.2}PO_4/C$ looks attractive owing to the fact that most of the electrochemical activity occurs at ~4.1 V, high temperature cycling, quick charging/discharging and long-term stable operations. The enhanced electrochemical kinetics is clearly associated with the (i) redox combination which in turn provides favourable environment for the lithiation and delithiation processes owing to difference in the

equilibrium potential of Fe^{2+}/Fe^{3+} and Mn^{2+}/Mn^{3+} unlike $LiMnPO_4$, (ii) partial suppression of Jahn-Teller distortion, (iii) reasonably good structural and thermal stability of delithiated phase ($Li_{1-x}Mn_{0.8}Fe_{0.2}PO_4$) and (iv) enhanced transport properties.

Despite successful high rate operation of $LiMn_{0.8}Fe_{0.2}PO_4$ at 10C; the capacity associated with the Mn^{2+}/Mn^{3+} redox regime was only 32 mAh g^{-1} which lowered the energy density of the battery. In the next chapter, the electrochemical activity of Mn^{2+}/Mn^{3+} will be enhanced by Mg^{2+} substitution.

Chapter 6

6. Influence of Mg^{2+} substitution on the manganese utilization of olivine based cathode material $Li(Mn_{0.8}Fe_{0.15}Mg_{0.05})PO_4/C$ for rechargeable Li-ion battery

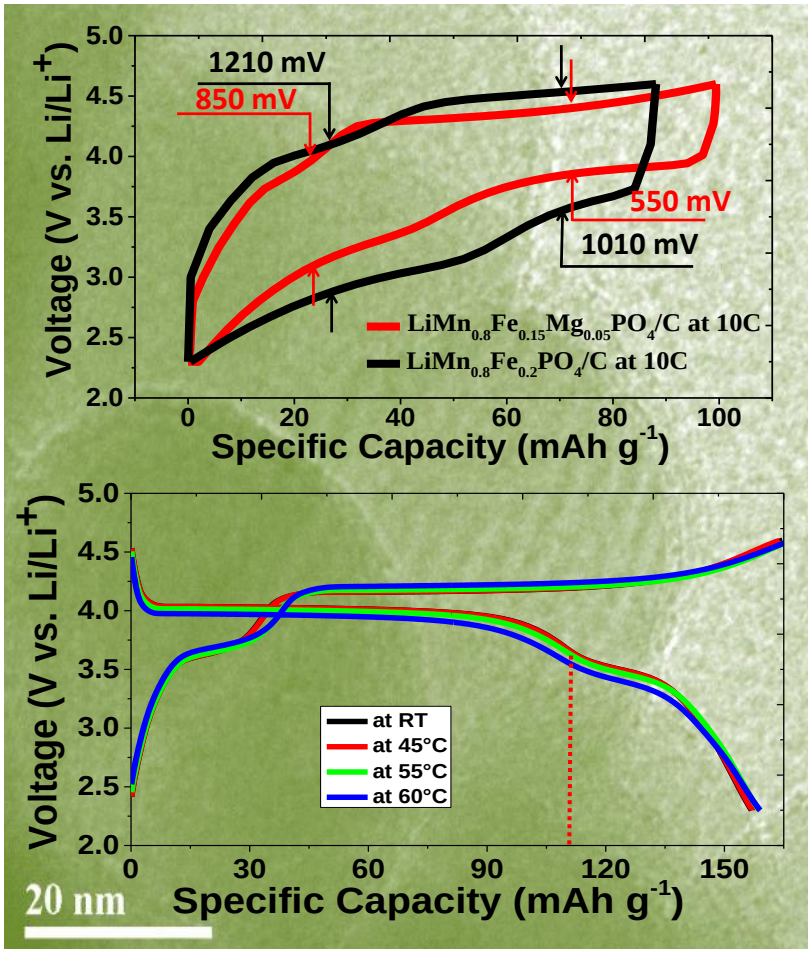

6.1 Preface to Chapter 6

The influence of Mg^{2+} substitution on the electrochemical performance of Mn-rich Mn-Fe mixed phospho-olivine ($LiMn_{0.8}Fe_{0.15}Mg_{0.05}PO_4/C$) is presented in this chapter. Presence of Mg^{2+} in Mn-Fe mixed phospho-olivine positively influences the lithium storage performance. For instance, the voltage polarization at 10C for $LiMn_{0.8}Fe_{0.15}Mg_{0.05}PO_4/C$ is 550 and 850 mV for Mn^{3+}/Mn^{2+} and Fe^{3+}/Fe^{2+} redox couples compared to $LiMn_{0.8}Fe_{0.2}PO_4/C$ (details are presented in chapter 5) sample that shows voltage polarization of 1010 and 1210 mV for Mn^{2+}/Mn^{3+} and Fe^{2+}/Fe^{3+} redox couples respectively. Further, the manganese utilization of $LiMn_{0.8}Fe_{0.15}Mg_{0.05}PO_4/C$ is found to be higher than that of $LiMn_{0.8}Fe_{0.2}PO_4/C$ at all current rates. $LiMn_{0.8}Fe_{0.15}Mg_{0.05}PO_4/C$ electrode retains 82% of its initial capacity at 1C after over 1000 cycles. The capacity of Mg^{2+} substituted samples is also extremely stable (~157 mAh g^{-1}) over a wide operating temperature of RT – 60 °C. Such robustness of high temperature cycling seen in $LiMn_{0.8}Fe_{0.15}Mg_{0.05}PO_4/C$ samples could possibly arise from stabilization of the delithiated phase ($Li_{1-x}Mn_{0.8}Fe_{0.15}Mg_{0.05}PO_4/C$). The possible reasons for the enhanced electrochemical kinetics of $LiMn_{0.8}Fe_{0.15}Mg_{0.05}PO_4/C$ is discussed in terms of (i) redox combination which provides favourable environment for the lithiation and delithiation processes owing to low equilibrium potential of Fe^{2+}/Fe^{3+} and electrochemically inactive Mg^{2+}, (ii) partial suppression of Jahn-Teller distortion, (iii) structural and thermal stability of delithiated phase ($Li_{1-x}Mn_{0.8}Fe_{0.15}Mg_{0.05}PO_4$) and (iv) enhanced transport properties.

6.2 Introduction

Previous reports in enhancing the lithium storage performance of $LiMnPO_4$ has focused on (i) particle size reduction;[108, 125, 138-140, 385-387] (ii) carbon coating;[121, 136, 142, 143, 149] (iii) forming Mn-Fe mixed transition metals olivine phosphates ($LiMn_{1-x}Fe_xPO_4$);[136, 161, 388, 389] and (iv) partial substitution of divalent metals[137, 150, 151, 176-178, 180, 181, 392] such as Mg^{2+}, Zn^{2+}, Cu^{2+}, Ni^{2+} and Co^{2+}. It has been reported previously that manganese is more electrochemically active in Mn-Fe mixed olivine phosphate than in $LiMnPO_4$.[120, 136, 160, 161, 168, 171, 391] Further, considering that the ionic radii of Mg^{2+} (0.86 Å) is smaller than the Mn^{2+} (0.97 Å) but larger than that of Mn^{3+} (0.78 Å),[179, 393] presence of Mg^{2+} ions improves the structure stability and reduces volume mismatch between delithiated and lithiated phases.[135, 176, 178]

Despite successful high rate operation of $LiMn_{0.8}Fe_{0.2}PO_4$ at 10C; the capacity associated with the Mn^{2+}/Mn^{3+} redox regime was only 32 mAh g^{-1} which lowered the energy density of the battery. In this chapter, the influence of Mg^{2+} substitution on the lithium storage performance and manganese utilization of Mn-rich Mn-Fe mixed olivine phosphates is discussed. For this purpose, we have prepared $LiMn_{0.8}Fe_{0.2}PO_4$/C (details are presented in chapter 5) and $LiMn_{0.8}Fe_{0.15}Mg_{0.05}PO_4$/C cathode material with similar morphology, particles size and carbon content. These two samples are compared throughout the discussion for their electrochemical behaviour. The presence of Mg^{2+} in Mn-Fe mixed transition metal phospho-olivine compound showed better electrochemical kinetics, manganese utilization, rate performance, cycling stability, thermal stability, structural stability, reduced voltage polarization and reduced volume change during the electrochemical delithiation. During Li^+ ion

extraction, delithiated phases created from Fe^{2+}/Fe^{3+} redox reaction at relatively low potential (~3.45 V) favors enhanced electrochemical activity of the succeeding Mn^{2+}/Mn^{3+} redox reaction at high potential. The fully charged sample (4.6 V) contains partially lithiated phase owing to the presence of electrochemically inactive Mg^{2+}. Presence of such lithiated phase provides favourable environment for the subsequent lithium insertion reaction resulting in improved electrochemical performance. Furthermore, the presence of Mg^{2+} also resulted in partial suppression of Jahn-Teller distortion, leading to stable cyclic performance. $LiMn_{0.8}Fe_{0.15}Mg_{0.05}PO_4/C$ is attractive especially for high temperature cycling, reduced polarization and long-term stable operations.

6.3 Experimental

6.3.1 Synthesis of $LiMn_{0.8}Fe_{0.15}Mg_{0.05}PO_4/C$

Carbon coated mesoporous $LiMn_{0.8}Fe_{(0.2-x)}Mg_xPO_4/C$ (x = 0 and 0.05) was synthesized using soft template method followed by high energy ball milling process **(in chapter 3, scheme 2)**. 0.01 M of CTAB ($(C_{16}H_{33})N(CH_3)_3Br$, Sigma Aldrich) was dissolved in a round bottom flask with a mixture of millQ water and absolute ethanol in the volume ratio of 1:5. The solution was stirred for 90 min. to initiate micellar formation, followed by the addition of lithium dihydrogen phosphate (LiH_2PO_4, Sigma Aldrich), manganese (II) acetate tetrahydrate ($Mn(CH_3CO_2)_2.4H_2O$, Sigma Aldrich), iron (II) acetate tetrahydrate ($Fe(CH_3CO_2)_2.4H_2O$, Sigma Aldrich) and magnesium (II) acetate tetrahydrate ($Mg(CH_3CO_2)_2.4H_2O$, Sigma Aldrich) in stoichiometric proportion. The solution was further stirred for 24 h and the solvent was evaporated using an IKA RV10 roto-evaporator. The precipitate was calcined in a tubular furnace at 650 $^{\circ}C$ for 6 h in an Ar-H_2 (95:5)

atmosphere. The calcined product was ball-milled with 25 wt% acetylene black using FRITSCH premium line – pulverisette 7 instrument at 500 rpm for 4 h with the weight ratio of sample: balls = 1:40 Further, the ball milled sample was heat-treated again at 500 $^{\circ}$C for 3 h in an Ar:H_2 atmosphere.[135]

6.3.2 Material and electrochemical characterization

Above samples were characterized using PXRD, Rietveld refinement, FESEM, EDXS, TEM, BET, XPS, temperature dependent PXRD, RT and high temperature galvanostatic cycling, cyclic voltammetry and electrochemical impedance spectroscopy. The details are given in chapter 2, section 2.2.1 , section 2.3 , section 2.4 and section 2.5 .

6.4 Results and discussion

6.4.1 Structural and morphological characterization

Figure 6.1a shows the PXRD of $LiMn_{0.8}Fe_{0.15}Mg_{0.05}PO_4$/C sample. All the diffraction peaks could be indexed to $LiMnPO_4$ which belongs to the *Pmnb* space group (JCPDS card no. 33-0803) with an orthorhombic structure. No other perceivable impurity phases are observed. The Rietveld refined pattern and lattice parameters for this sample are shown in the **Figure 6.1b and Table 6.1** respectively, which are in good agreement with the literature.[161, 180] Changes in the lattice parameters and unit cell volume of the above samples compared to parent member ($LiMnPO_4$) are presented in. **Table 6.1.** The differences in the cell volume of the samples could be understood by the change in ionic radii of the transition metals (Mn^{2+} = 0.97 Å, Fe^{2+} = 0.92 Å and Mg^{2+} = 0.86 Å) in the active material.[179, 393]

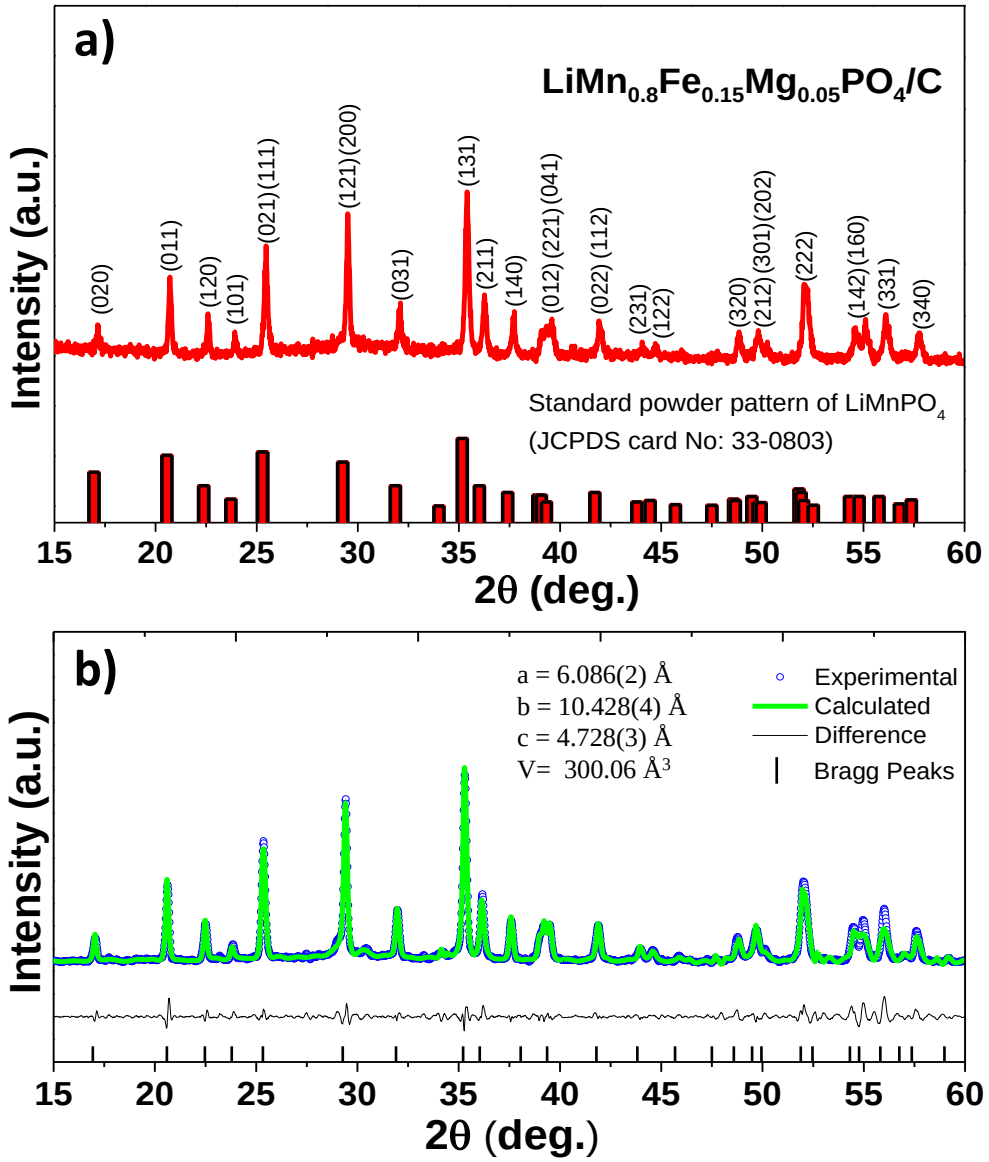

Figure 6.1 (a) PXRD patterns of $LiMn_{0.8}Fe_{0.15}Mg_{0.05}PO_4/C$, (b) Rietveld refinement of $LiMn_{0.8}Fe_{0.15}Mg_{0.05}PO_4/C$ (R_{exp}: 4.77, R_{wp}: 2.64 and R_p: 2.03).

Rietveld refinement was performed to check the position of dopants in $LiMn_{0.8}Fe_{0.15}Mg_{0.05}PO_4/C$ using TOPAS 3.0 version. The dopant position and quality of the refinement were determined based on R_{exp}, R_{wp} and R_p values **(Figure 6.1b and Table 6.2)**.[114, 180, 394] For instance in the case of $LiMn_{0.8}Fe_{0.15}Mg_{0.05}PO_4$ firstly, assuming the Mg^{2+} and Fe^{2+} occupy only Li sites, the reliability factor were R_{exp}:4.77, R_{wp}:3.36 and R_p:2.61; secondly, assuming the Mg^{2+} and Fe^{2+} occupy only Mn sites, then the reliability factors

Table 6.1 Lattice parameters and cell volume of $LiMn_{0.8}Fe_{0.15}Mg_{0.05}PO_4$/C materials obtained by Rietveld refinement.

Electrode material	a (Å)	b (Å)	c (Å)	V ($Å^3$)	Changes in the cell volume in (%) with respect to $LiMnPO_4$ (reference) *Pmnb* space group (*JCPDS card no. 33-0803*)
$LiMnPO_4$ (reference) *Pmnb* space group (*JCPDS card no. 33-0803*)	6.108	10.459	4.732	302.29	-
$LiMn_{0.8}Fe_{0.15}Mg_{0.05}PO_4$	6.086(2)	10.428(4)	4.728(3)	300.06	0.74

R_{exp}:4.77, R_{wp}:3.04 and R_p:2.29; thirdly, assuming the Mg^{2+} and Fe^{2+} occupy simultaneously both Li and Mn sites, then the reliability factors are R_{exp}:4.77, R_{wp}:2.64 and R_p:2.03. Based on good reliability factors as seen from the third case and observed site occupancies as shown in **Table 6.2**, Mg^{2+} and Fe^{2+} are most likely to occupy Mn sites. Hence, as seen from the site occupancies that the Fe^{2+} and Mg^{2+} substitute mostly the Mn site, not the Li site.[180]

Table 6.2 Site occupancies of $LiMn_{0.8}Fe_{0.15}Mg_{0.05}PO_4/C$.

$LiMn_{0.8}Fe_{0.15}Mg_{0.05}PO_4$ (R_{exp}:4.77, R_{wp}:2.64 and R_p:2.03)						
Atom	Site	x	y	z	Occupancy (theoretical)	Occupancy (Observed)
Li1 (Li^{+1})	4a	0.0	0.0	0.0	1	0.9994
Li2 (Li^{+1})	4c	0.2500	0.2817	0.0281	0	0.0006
Mg1(Mg^{+2})	4a	0.0	0.0	0.0	0	0.0006
Mg2(Mg^{+2})	4c	0.2500	0.2817	0.0281	0.05	0.0494
Fe2(Fe^{+2})	4c	0.2500	0.2817	0.0281	0.15	0.15
Mn1(Mn^{+2})	4c	0.2500	0.2817	0.0281	0.80	0.80
P1(P^{+5})	4c	0.2500	0.0923	0.4081	1	1
O1(O^{-2})	4c	0.2500	0.0968	0.2664	1	1
O2(O^{-2})	4c	0.2500	0.4561	0.2073	1	1
O3(O^{-2})	8d	0.0492	0.1609	0.2781	1	1

FESEM images of $LiMn_{0.8}Fe_{0.15}Mg_{0.05}PO_4/C$ samples are shown in **Figure 6.2**. FESEM images of the samples show presence of particles with a pseudo-spherical morphology. The carbon content and elemental composition were estimated by CHNX analysis using Elementar Vario Micro Cube analyser. Elemental mapping images and energy dispersive spectrum confirm presence of magnesium and iron uniformly within the active material **(Figure 6.3)**. Further, uniform distribution of carbon around the active materials is also

seen.

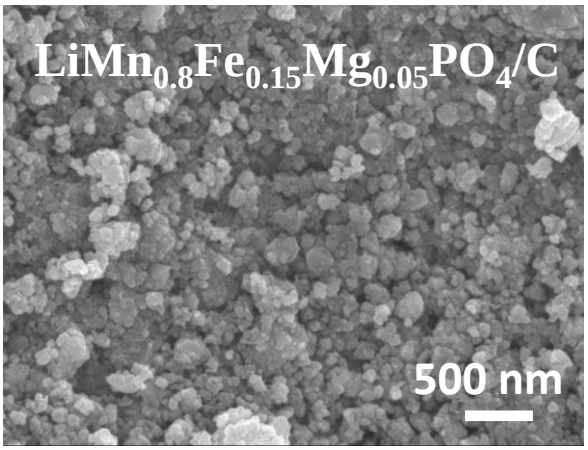

Figure 6.2 FESEM images of $LiMn_{0.8}Fe_{0.15}Mg_{0.05}PO_4/C$.

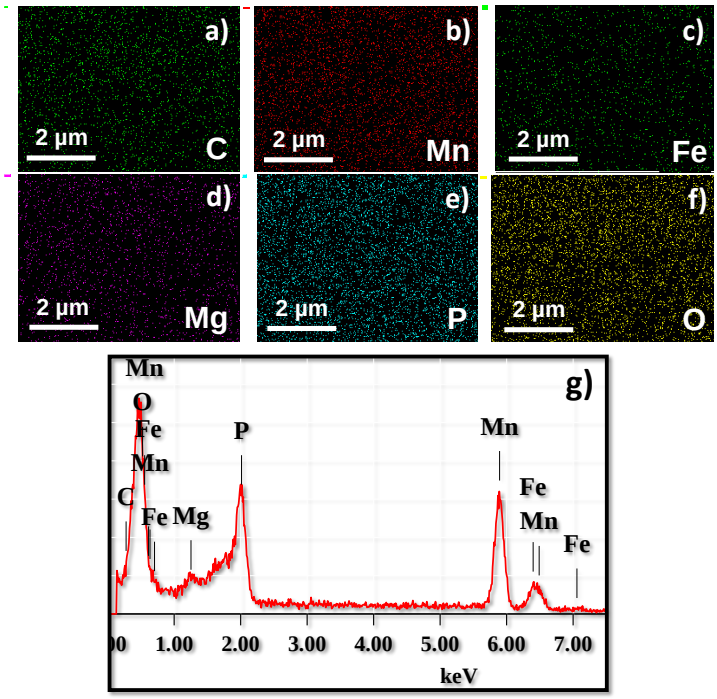

Figure 6.3 Elemental images of (a) carbon (white), (b) manganese (red), (c) iron (green), (d) magnesium (purple), (e) phosphorus (cyan), (f) oxygen (yellow) and (g) energy dispersive spectrum of $LiMn_{0.8}Fe_{0.15}Mg_{0.05}PO_4/C$.

TEM images of $LiMn_{0.8}Fe_{0.15}Mg_{0.05}PO_4/C$ materials are shown in **Figure 6.4**. The particles appear to be well connected within the carbon matrix with size in the range 30-50 nm. TEM images of $LiMn_{0.8}Fe_{0.15}Mg_{0.05}PO_4/C$ also show the presence of carbon coating (5±2 nm) around the active materials which act as electronic wiring for the electrons from particle to particle and to

the Al current collector.

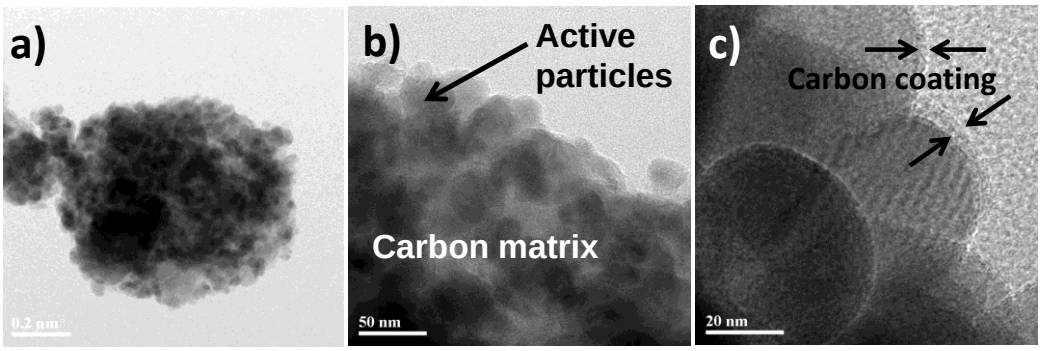

Figure 6.4 (a-c) TEM images of $LiMn_{0.8}Fe_{0.15}Mg_{0.05}PO_4/C$ at different magnification.

The BET surface area of $LiMn_{0.8}Fe_{0.15}Mg_{0.05}PO_4/C$ was analysed by N_2 sorption isotherms **(Figure 6.5)**. Nitrogen adsorption and desorption isotherms of $LiMn_{0.8}Fe_{0.15}Mg_{0.05}PO_4/C$ sample exhibits clear hysteresis loop of Type IV.

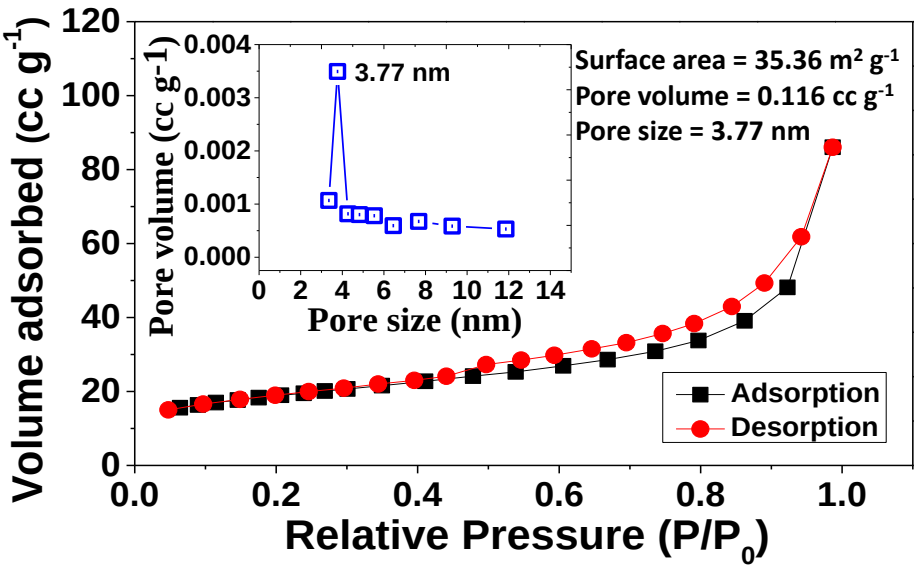

Figure 6.5 Nitrogen adsorption and desorption isotherm with pore size distribution (inset) of $LiMn_{0.8}Fe_{0.15}Mg_{0.05}PO_4/C$.

The BET surface area and pore volume of this sample was found to be 35.36 m^2 g^{-1} and 0.116 cc g^{-1} respectively with a pore size distribution of 3.77 nm **(inset of Figure 6.5)**. These pores provide better penetration of the liquid electrolyte which allows easy access to Li^+-ions.

6.4.2 *Ex-situ* transmission FTIR spectra study of $LiMn_{0.8}Fe_{0.15}Mg_{0.05}PO_4/C$

Figure 6.6a represents the transmission FTIR spectra of $LiMnPO_4$, $LiMn_{0.8}Fe_{0.15}Mg_{0.05}PO_4/C$ and $LiFePO_4$.

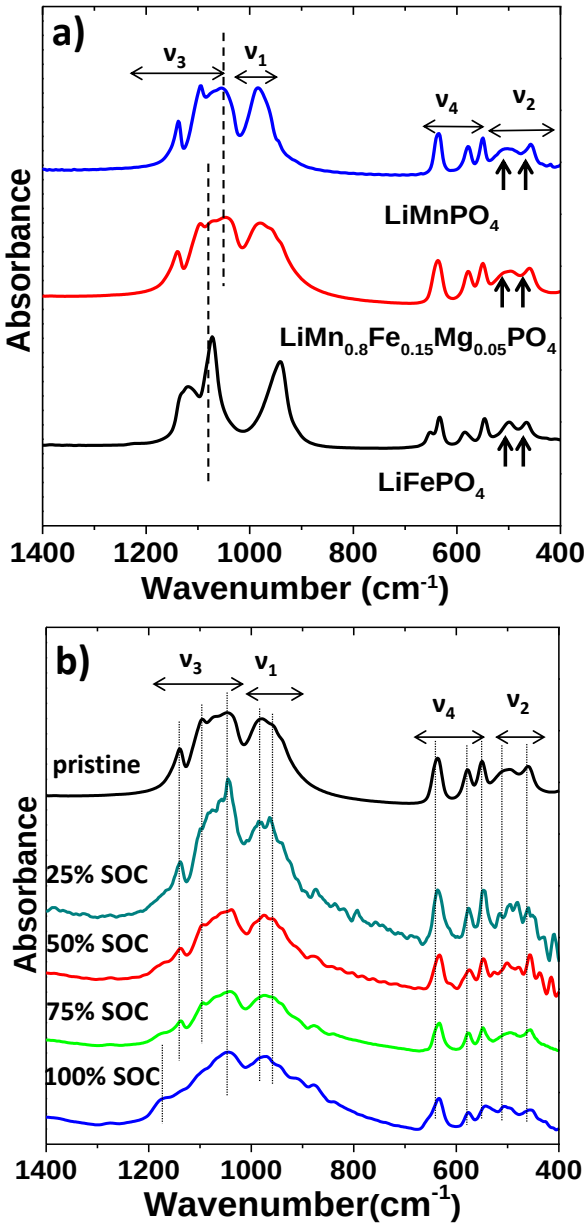

Figure 6.6 (a) Transmission FTIR spectra of ν_3, ν_1, ν_4 and ν_2 the lithium cage modes for $LiMnPO_4$, $LiMn_{0.8}Fe_{0.15}Mg_{0.05}PO_4$ and $LiFePO_4$ ($LiMnPO_4$ and $LiFePO_4$ infrared spectra for sake of comparison), The dashed lines represent the two-mode behaviour in ν_3 and the arrow marks represent the lithium cage modes (ν_2), (b) Transmission FTIR spectra of $LiMn_{0.8}Fe_{0.15}Mg_{0.05}PO_4/C$ at different state of charge.

These spectra are dominated by the vibrations of the PO_4^{3-} anion, which consist of four modes: (i) anti-symmetric PO_4^{3-} stretching mode ν_3 that lies between 1150 and 1000 cm^{-1}, (ii) symmetric PO_4^{3-} stretching mode ν_1 that lies between 1000 and 800 cm^{-1}, (iii) anti-symmetric bending mode ν_4 seen between 650 and 530 cm^{-1} and (iv) symmetric bending mode ν_2 seen at a frequency lower than ν_4.[408-412] Among them, the stretching mode peaks are more localized than the bending modes.[413] Stretching mode spectral assignments of PO_4^{3-} vibrations in Mn-Fe mixed system is essentially the superposition of the two parent materials namely $LiFePO_4$ and $LiMnPO_4$ **(Figure 6.6a)**.[168, 408-416] The details of the spectral assignments of the pristine samples are mentioned in **Table 6.3**.

Table 6.3 Spectral assignments of $LiMn_{0.8}Fe_{0.15}Mg_{0.05}PO_4/C$ at differe nt state of charge.

$LiMn_{0.8}Fe_{0.15}Mg_{0.05}PO_4/C$ (major peaks - frequency in cm^{-1})				
SOC	ν_3	ν_1	ν_4	ν_2
Pristine	1136, 1096 and 1048	983 and 955	637, 578 and 550	501 and 459
25% SOC	1137, 1099 and 1047	982 and 960	636, 577 and 546	502 and 459
100% SOC	1183, 1097 and 1044	979 and 944	633, 577 and 542	505 and 454

Figure 6.6b shows the transmission FTIR spectra of $LiMn_{0.8}Fe_{0.15}Mg_{0.05}PO_4/C$ at different states of charge. At 25% SOC where Fe^{2+} is oxidized to Fe^{3+}, there are hardly any changes in the FTIR spectra (**Table 6.3**). For 50% - 100% SOC where Mn^{2+} is oxidized to Mn^{3+}, noticeable changes could be seen in the spectra. During this redox reaction, the

peaks of the test electrodes broaden compared to their parent material **(see Table 6.3).**

As seen from the earlier reports, the anti-symmetric P-O stretching mode ν_3 width increased from 84 cm^{-1} to 142 cm^{-1} for $LiFePO_4$ while width increment is from 65 cm^{-1} to 228 cm^{-1} for $LiMnPO_4$.[411, 412, 414] The broadening in the stretching mode ν_3 of $LiMn_{0.8}Fe_{0.15}Mg_{0.05}PO_4/C$ was 88 cm^{-1} (1136-1048) at 25% SOC while the respective values for 100% SOC sample was 139 cm^{-1} (1183-1044 cm^{-1}). Similarly, the broadening in the stretching mode ν_3 of $LiMn_{0.8}Fe_{0.2}PO_4/C$ was 88 cm^{-1} (1135-1047) at 25% SOC while the corresponding broadening after 100% SOC was 148 cm^{-1} (1189-1041 cm^{-1}) (for more details, see chapter 5). It is seen that the peak broadening is more pronounced for the completely delithiated Mg^{2+} un-doped sample and $LiMnPO_4$[411] compared to the Mg^{2+} doped Mn-rich Mn-Fe mixed sample.[178, 411, 417] Such a peak broadening is attributed to the Jahn-Teller distortion induced by Mn^{3+} ions owing to strong electron-lattice interaction between these ions in the delithiated structure.[94, 158, 411, 412, 418] This geometrical deformation of the Mn-O structure directly affects the P-O bands, since Mn^{3+} and P^{5+} share oxygen atoms covalently in the structure lattices and a larger separation of the ν_3 bands.[168, 412] The presence of more compatible large ions Mg^{2+} in the olivine structure could stabilize the structure and the lattice against the strain that is created by the Jahn-Teller Mn^{3+} ions.[176, 178] A recent work by Jang et al.,[422] showed that the Mg^{2+} substitution causes smaller local structural distortion during lithium extraction. Further, the theoretical work by Seo *et al.*[172] also showed that the substitution of transition metal in $LiMnPO_4$ could suppress the Jahn-Teller distortion and enables faster migration of the

electrons which are localized around Mn^{3+} ions compared to parent material $LiMnPO_4$.[90, 411]

6.4.3 Reaction mechanism

It is known that the mixed phospho-olivine $LiMn_{1-x}Fe_xPO_4$ follows a two phase mechanism similar to $LiFePO_4$.[13, 97, 120, 124, 419, 420] *Ex-situ* PXRD patterns recorded on the $LiMn_{0.8}Fe_{0.15}Mg_{0.05}PO_4/C$ also shows a similar behavior **(Figure 6.7).** During Fe^{2+}/Fe^{3+} redox reaction, the initial delithiation of $LiMn_{0.8}Fe_{0.15}Mg_{0.05}PO_4/C$ proceeds through a single-phase mechanism to produce $Li_{1-y}Mn_{0.8}Fe_{0.15}Mg_{0.05}PO_4/C$.[120, 124, 419] During Mn^{2+}/Mn^{3+} redox reaction, the particle surfaces become enclosed with a thin layer of delithiated $Li_{1-y}Mn_{0.8}Fe_{0.15}Mg_{0.05}PO_4/C$ that migrates towards the lithium rich core. This single-phase mechanism continues until $y \leq 0.8$ as inferred from the XRD pattern as there are no evident changes in the XRD pattern. However, when $y \geq 0.8$, new peaks emerge at $2\theta=18.49°$, 30.46° and 37.10° suggesting the onset of the two phase behavior **(Figure 6.7a)**. Similarly, during lithiation, the initial lithiation of $Li_{1-y}Mn_{0.8}Fe_{0.15}Mg_{0.05}PO_4/C$ ($y \geq 0.8$) occurs via two-phase mechanism followed by single-phase process that migrates towards lithium deficient core. At end of the lithiation process, lithiated $LiMn_{0.8}Fe_{0.15}Mg_{0.05}PO_4/C$ is formed by single-phase process **(Figure 6.7b)**. This two-phase mechanism is also confirmed by the FTIR spectra of $LiMn_{0.8}Fe_{0.15}Mg_{0.05}PO_4/C$ in which peak broadening and increase in the peak intensity are significant during Mn^{2+}/Mn^{3+} redox reaction at > 75% of SOC.[412] This observation is analogous with the spectral changes witnessed in the two-phase mechanism of $LiFePO_4$.[408]

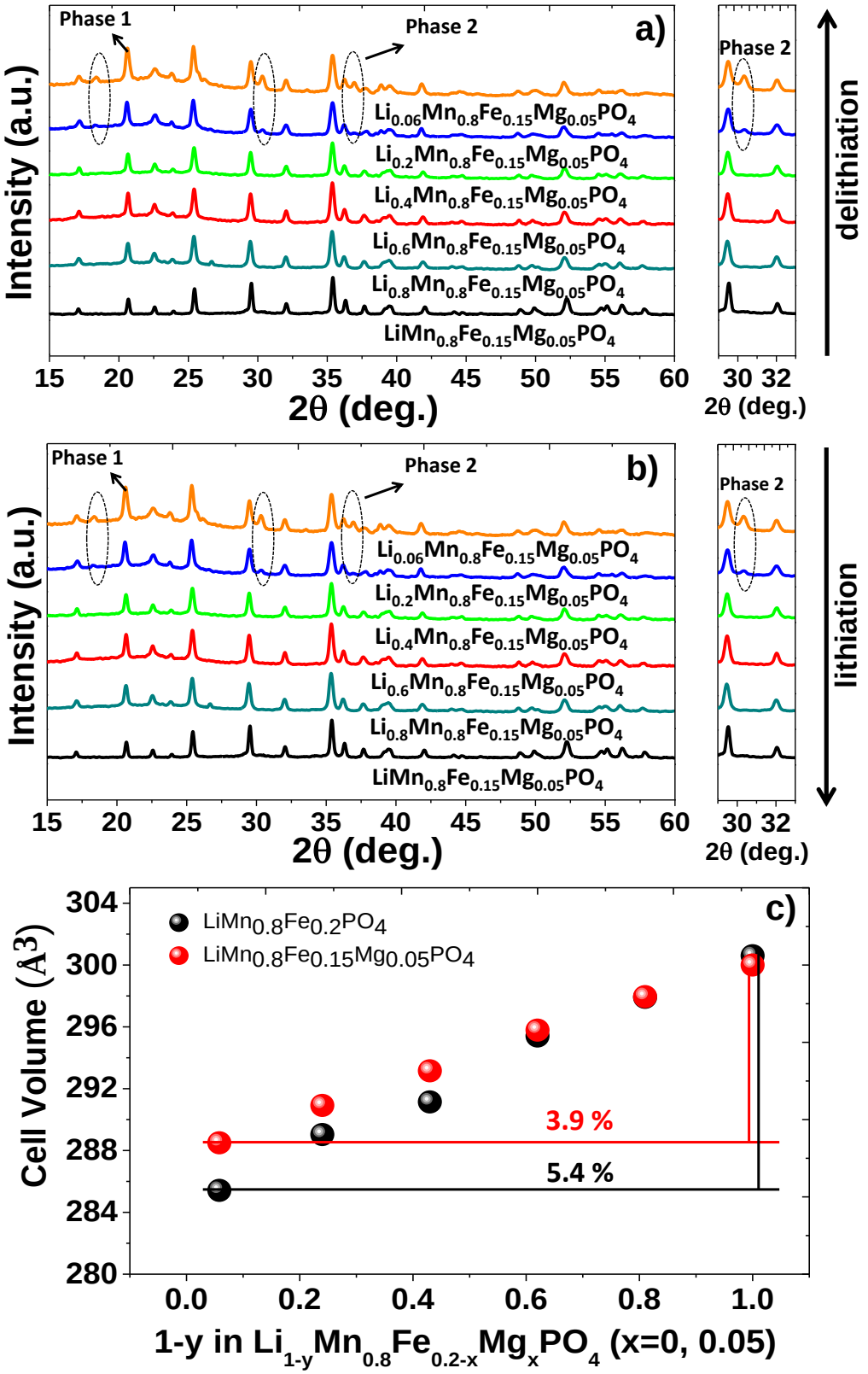

Figure 6.7 (a) *Ex-situ* PXRD patterns of $LiMn_{0.8}Fe_{0.15}Mg_{0.05}PO_4$/C at different stages of electrochemical extraction of lithium (charge), (b) *Ex situ* PXRD patterns of $LiMn_{0.8}Fe_{0.15}Mg_{0.05}PO_4$/C at different stages of electrochemical insertion of lithium (discharge), (c) change in cell volume of $LiMn_{0.8}Fe_{0.15}Mg_{0.05}PO_4$/C (Phase 1 refers to lithiated phase and Phase 2 refers to delithiated phase).

Yamada *et al.*[120, 124, 378] has shown that manganese redox reaction in $Li_{1-y}Mn_{1-x}Fe_xPO_4$, y=0.6 happens through a two-phase mechanism while the iron redox reaction occurs via single-phase mechanism. In accordance to Yamada *et al.*, we also observed two-phase mechanism in Mg^{2+} substituted $Li_{1-y}Mn_{0.8}Fe_{0.15}Mg_{0.05}PO_4/C$ (y = 0.8) during the Mn redox reaction. However, there is a narrow shift in the point where the two-phase mechanism is observed. This is related to the fact that we extracted lithium by electrochemical means, while Yamada *et al.* study focused on chemical delithiation.[124] It must be noted that the mechanism of lithium extraction/insertion is essentially different in the electrochemical cell than the chemical extraction.[421]

During delithiation, the overall cell volume change in Mg^{2+} substituted $LiMn_{0.8}Fe_{0.15}Mg_{0.05}PO_4/C$ is relatively small compared to Mg^{2+} un-doped $LiMn_{0.8}Fe_{0.2}PO_4/C$ **(Figure 6.77c)**, which is believed to be highly beneficial for repeated electrochemical extraction and insertion of lithium from/into the structure. For the Mg^{2+} substituted sample, the volume change between lithiated and delithiated phase is 3.9% while the volume change is 5.4% for Mg^{2+} un-doped sample $LiMn_{0.8}Fe_{0.2}PO_4/C$ which is consistent with the recent report by Jang *et al.*[422] The reduced change in the cell volume of Mg-substituted Mn-Fe mixed sample could be understood by the ionic radii of the Mg^{2+} (Mg^{2+} (0.86 Å) > Mn^{3+} (0.78 Å) and Fe^{3+} (0.78 Å)) in the olivine structure.[176, 178] Volume change during electrochemical intercalation and deintercalation of lithium is well-known to induce crack formation creating disconnections in the electrode material leading to capacity loss during the cycling.[406, 407] This seems less likely in the Mg^{2+} substituted Mn-Fe mixed

sample compared to Mg^{2+} un-doped $LiMn_{0.8}Fe_{0.2}PO_4/C$ (details are presented in chapter 5) which is beneficial to achieve stable cyclability **(Figure 6.10 and Figure 6.11)**.

6.4.4 Structural and thermal stability

Safety is a major concern for LIBs and high structural and thermal stability of the cathode materials; particularly at fully delithiated state is critical. *Ex-situ* thermal XRD was carried out at delithiated state (at 4.6 V) from RT to 500°C to understand the structure and thermal stability of $LiMn_{0.8}Fe_{0.15}Mg_{0.05}PO_4/C$. All the major peaks in $Li_{1-x}Mn_{0.8}Fe_{0.15}Mg_{0.05}PO_4$ are seen even at 500°C **(Figure 6.8),** while the peaks in $Li_{1-x}Mn_{0.8}Fe_{0.2}PO_4$ disappear at 450°C and above (details are presented in chapter 5). The presence of more compatible large ions Mg^{2+} (Mg^{2+} (0.86 Å) >Mn^{3+} and Fe^{3+} (0.78 Å)) is believed to stabilize the delithiated olivine structure at high temperature. Hence, the structural and thermal stability of fully charged Mg-substituted Mn-Fe mixed sample are relatively higher than the Mg^{2+} un-doped Mn-Fe mixed sample.

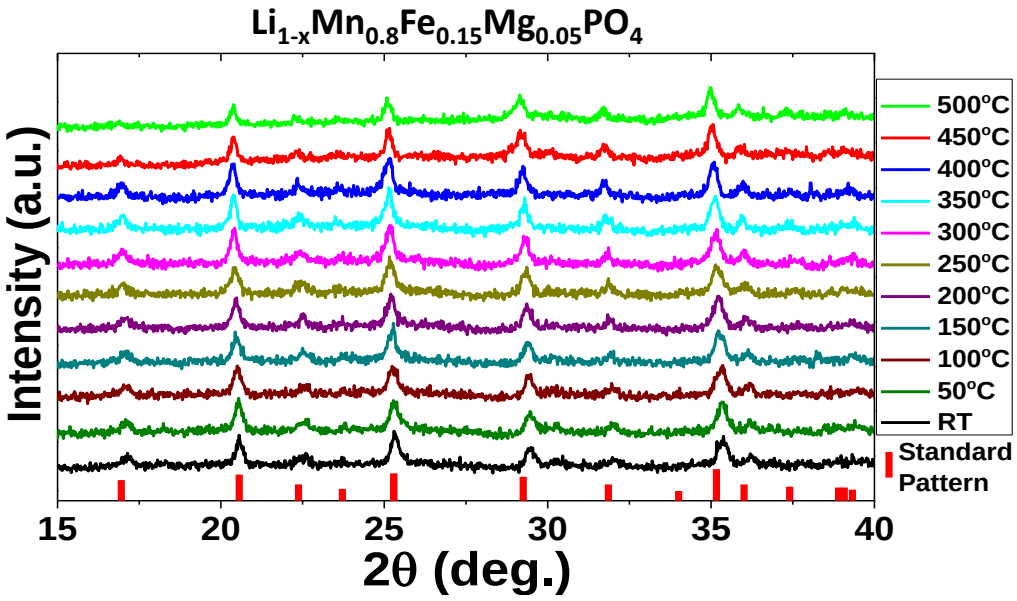

Figure 6.8 *Ex-situ* thermal XRD of $Li_{1-x}Mn_{0.8}Fe_{0.15}Mg_{0.05}PO_4$/C at charged state (at 4.6 V).

6.4.5 Lithium storage performance

Figure 6.9 shows the charge and discharge profiles of $LiMn_{0.8}Fe_{0.15}Mg_{0.05}PO_4$/C and $LiMn_{0.8}Fe_{0.2}PO_4$/C at 0.1C (In this section, the results of $LiMn_{0.8}Fe_{0.2}PO_4$/C is used for sake of comparison and details are presented in chapter 5). Both the samples deliver similar charge capacities of 163 mAh g^{-1} **(Figure 6.9a-6.9b)**. The charge capacity contribution of Fe^{2+}/Fe^{3+} redox in $LiMn_{0.8}Fe_{0.2}PO_4$/C is 52 mAh g^{-1} compared to $LiMn_{0.8}Fe_{0.15}Mg_{0.05}PO_4$/C which shows 39 mAh g^{-1}. During discharge, the capacity contribution of Fe^{2+}/Fe^{3+} redox in $LiMn_{0.8}Fe_{0.2}PO_4$/C and $LiMn_{0.8}Fe_{0.15}Mg_{0.05}PO_4$/C were 57 and 43 mAh g^{-1}. Thus, the capacity contribution from the Fe^{2+}/Fe^{3+} redox in $LiMn_{0.8}Fe_{0.2}PO_4$ is slightly higher than $LiMn_{0.8}Fe_{0.15}Mg_{0.05}PO_4$. Such variation in charge and discharge capacity is due to the difference in the Fe content in these compositions. However, the capacity contribution from the Mn^{2+}/Mn^{3+} redox is lower in $LiMn_{0.8}Fe_{0.2}PO_4$ compared to $LiMn_{0.8}Fe_{0.15}Mg_{0.05}PO_4$. For instance, the charge capacity

contribution from Mn^{2+}/Mn^{3+} redox in $LiMn_{0.8}Fe_{0.2}PO_4/C$ is only 111 mAh g^{-1} compared to $LiMn_{0.8}Fe_{0.15}Mg_{0.05}PO_4/C$ in which Mn^{2+}/Mn^{3+} redox delivers higher capacity of 124 mAh g^{-1}. The discharge capacity of $LiMn_{0.8}Fe_{(0.2-x)}Mg_xPO_4/C$ (x = 0 and 0.05) is 160 mAh g^{-1} as shown in **Figure 6.9a-6.9b**. During discharge, the capacity contribution from Mn^{3+}/Mn^{2+} redox is 117 mAh g^{-1} of $LiMn_{0.8}Fe_{0.15}Mg_{0.05}PO_4/C$. In contrast, $LiMn_{0.8}Fe_{0.2}PO_4/C$ shows only 103 mAh g^{-1} for Mn^{3+}/Mn^{2+} region. This shows the maximum utilization of the high voltage Mn^{2+}/Mn^{3+} redox reaction of $LiMn_{0.8}Fe_{0.15}Mg_{0.05}PO_4/C$.

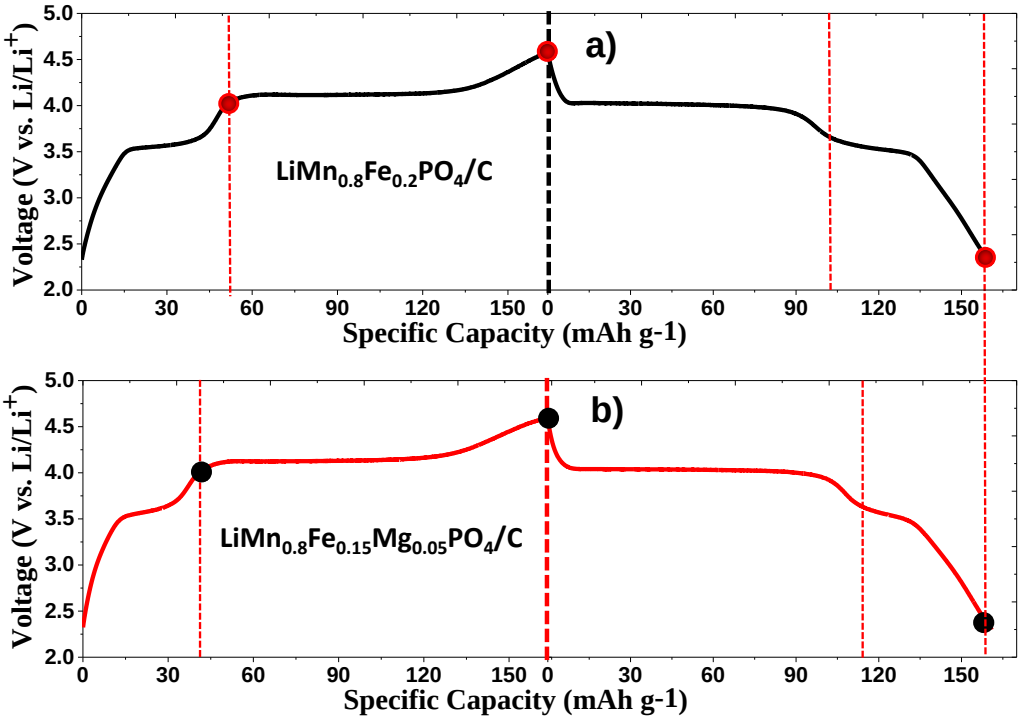

Figure 6.9 Capacity comparison/contribution chart of Mn and Fe redox reaction for (a) $LiMn_{0.8}Fe_{0.2}PO_4/C$ (for sake of comparison) and (b) $LiMn_{0.8}Fe_{0.15}Mg_{0.05}PO_4/C$ at 0.1C rate.

Figure 6.10a-6.10b shows the lithium storage performance of $LiMn_{0.8}Fe_{(0.2-x)}Mg_xPO_4/C$ (x = 0 and 0.05) at selected C rates. Even at higher rate of 10C, the lithium storage performance of Mg^{2+} substituted $LiMn_{0.8}Fe_{0.15}Mg_{0.05}PO_4/C$ was found to be higher (97 mAh g^{-1}) compared to the parent material $LiMn_{0.8}Fe_{0.2}PO_4/C$ which shows only 88 mAh g^{-1} **(Figure**

6.10a-6.10b).

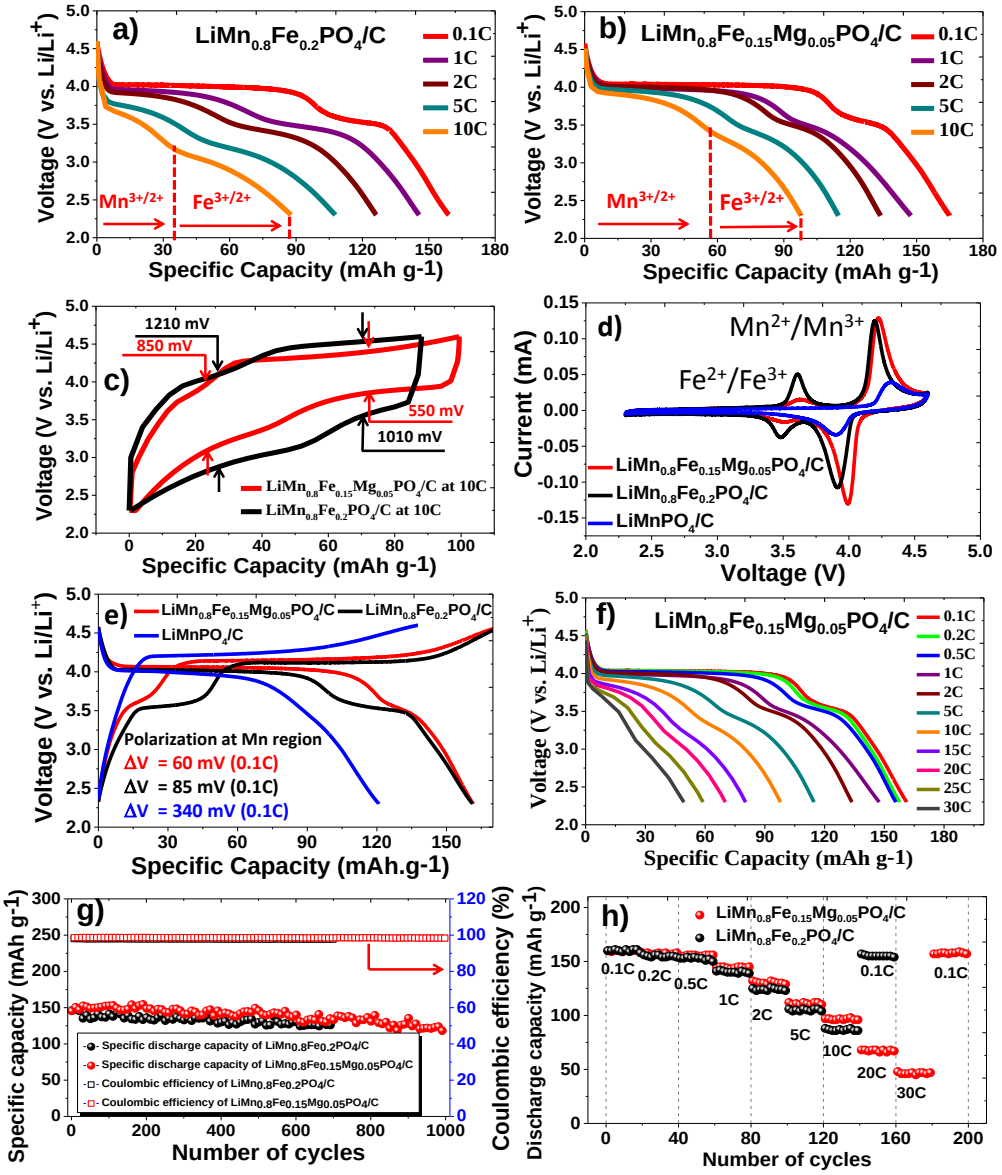

Figure 6.10 (a) Discharge profiles of $LiMn_{0.8}Fe_{0.2}PO_4/C$ at selected C-rates, (b) Discharge profiles of $LiMn_{0.8}Fe_{0.15}Mg_{0.05}PO_4/C$ at selected C-rates, (c) Voltage polarization comparison of $LiMn_{0.8}Fe_{(0.2-x)}Mg_xPO_4/C$ (x = 0 and 0.05) at 10C, (d) Cyclic voltammetry of $LiMn_{0.8}Fe_{(0.2-x)}Mg_xPO_4/C$ (x = 0 and 0.05) and $LiMnPO_4/C$ at 0.058 mV ($LiMnPO_4/C$ for sake of comparison), (e) Comparison of charge and discharge profiles of $LiMn_{0.8}Fe_{(0.2-x)}Mg_xPO_4/C$ (x = 0 and 0.05) and $LiMnPO_4/C$ at 0.1C, (f) Discharge profiles of $LiMn_{0.8}Fe_{0.15}Mg_{0.05}PO_4/C$ at different C-rates (0.1C to 30C) (g) Long term cyclability of $LiMn_{0.8}Fe_{(0.2-x)}Mg_xPO_4/C$ (x = 0 and 0.05) at 1C,and (h) Rate performance of $LiMn_{0.8}Fe_{(0.2-x)}Mg_xPO_4/C$ (x = 0 and 0.05). (capacity values are calculated based on the active material weight).

It is worth noting that the manganese utilization of $LiMn_{0.8}Fe_{0.15}Mg_{0.05}PO_4/C$ is higher than that of $LiMn_{0.8}Fe_{0.2}PO_4/C$ at all C rates. Most importantly, the

voltage polarization at 10C for $LiMn_{0.8}Fe_{0.15}Mg_{0.05}PO_4/C$ is 550 and 850 mV for Mn^{2+}/Mn^{3+} and Fe^{2+}/Fe^{3+} redox couples compared to $LiMn_{0.8}Fe_{0.2}PO_4/C$ sample that show higher voltage polarization of 1010 and 1210 mV for Mn^{3+}/Mn^{2+} and Fe^{3+}/Fe^{2+} redox couples respectively **(Figure 6.10c)**. The polarization at Mn region for $LiMn_{0.8}Fe_{0.15}Mg_{0.05}PO_4/C$ is relatively less about 60 mV compared to $LiMn_{0.8}Fe_{0.2}PO_4/C$ (85 mV) and $LiMnPO_4$ (340 mV)[134, 135] (for sake comparison) at 0.1C **(Figure 6.10d-6.10e)**. In can be suggested that both Fe^{2+} (improved bulk conductivity and activation energy)[164, 171] and Mg^{2+} (narrow Fe-O-Mn bond gap)[172, 423] substitution facilitated improvement in the electronic and ionic conductivity of the sample. $LiMn_{0.8}Fe_{0.15}Mg_{0.05}PO_4/C$ electrode delivers discharge capacities of 160, 157, 156, 145, 132, 112, 97, 70 and 48 mAh g^{-1} at 0.1, 0.2, 0.5, 1, 2, 5, 10, 20 and 30C respectively **(Table 6.2 and Figure 6.10f)**.

$LiMn_{0.8}Fe_{0.15}Mg_{0.05}PO_4/C$ showed better long term cycling stability compared to $LiMn_{0.8}Fe_{0.2}PO_4/C$ **(Figure 6.10g).** Mg-substituted samples retain 91% of its initial capacity at 1C after 700 cycles with an average coulombic efficiency of 98.5 % compared to $LiMn_{0.8}Fe_{0.2}PO_4/C$ that retains only 86% over 700 cycles with an average coulombic efficiency of 98.2% **(Figure 6.10g).** Even after 1000 cycles at 1C rate, $LiMn_{0.8}Fe_{0.15}Mg_{0.05}PO_4/C$ electrode material retained 82% of its initial capacity, delivering 120 mAh g^{-1} with an average coulombic efficiency of 98.5% **(Figure 6.10g).** The rate performance of $LiMn_{0.8}Fe_{(0.2-x)}Mg_xPO_4/C$ (x = 0 and 0.05) samples are shown in **Figure 6.10h.** After testing at high C-rate, all the cells were again tested at 0.1C rate. The electrodes show excellent recovery, for example $LiMn_{0.8}Fe_{0.15}Mg_{0.05}PO_4/C$ retains 98% after 30C. Notably,

$LiMn_{0.8}Fe_{0.15}Mg_{0.05}PO_4/C$ electrode material exhibits capacity up to 30C **(Figure 6.10f)**, while $LiMn_{0.8}Fe_{0.2}PO_4/C$ material only shows capacity up to 10C **(Figure 6.10a).** The facile electrochemical kinetics of $LiMn_{0.8}Fe_{0.15}Mg_{0.05}PO_4/C$ material could be inferred from the lowest polarization value, enhanced Mn utilization and lithium storage performance witnessed during the galvanostatic cycling. As mentioned, these materials have similar morphology, particle size and carbon content. Hence, to a larger extent, the observed differences in the electrochemical performance amongst these materials are not biased by these factors. Therefore, the kinetic difference especially at high rate and enhanced Mn redox reaction is believed to be associated with the structural stability and enhanced transport properties (shown later in diffusion study) of $LiMn_{0.8}Fe_{0.15}Mg_{0.05}PO_4/C$ electrode material.

Table 6.4 A summary of lithium storage performance of $LiMn_{0.8}Fe_{0.15}Mg_{0.05}PO_4/C$ at various current rates.

C rates									
Specific discharge capacity in mAh g^{-1}									
Electrode material	0.1C	0.2C	0.5C	1C	2C	5C	10C	20C	30C
$LiMn_{0.8}Fe_{0.15}Mg_{0.05}PO_4$	160	157	156	145	132	112	97	70	48

6.4.6 High temperature galvanostatic cycling

Figure 6.11 shows the high temperature galvanostatic cycling (50 cycles at each temperature-RT, 45, 55 and 60°C) of $LiMn_{0.8}Fe_{0.15}Mg_{0.05}PO_4/C$ at 0.2C up to 50 cycles.

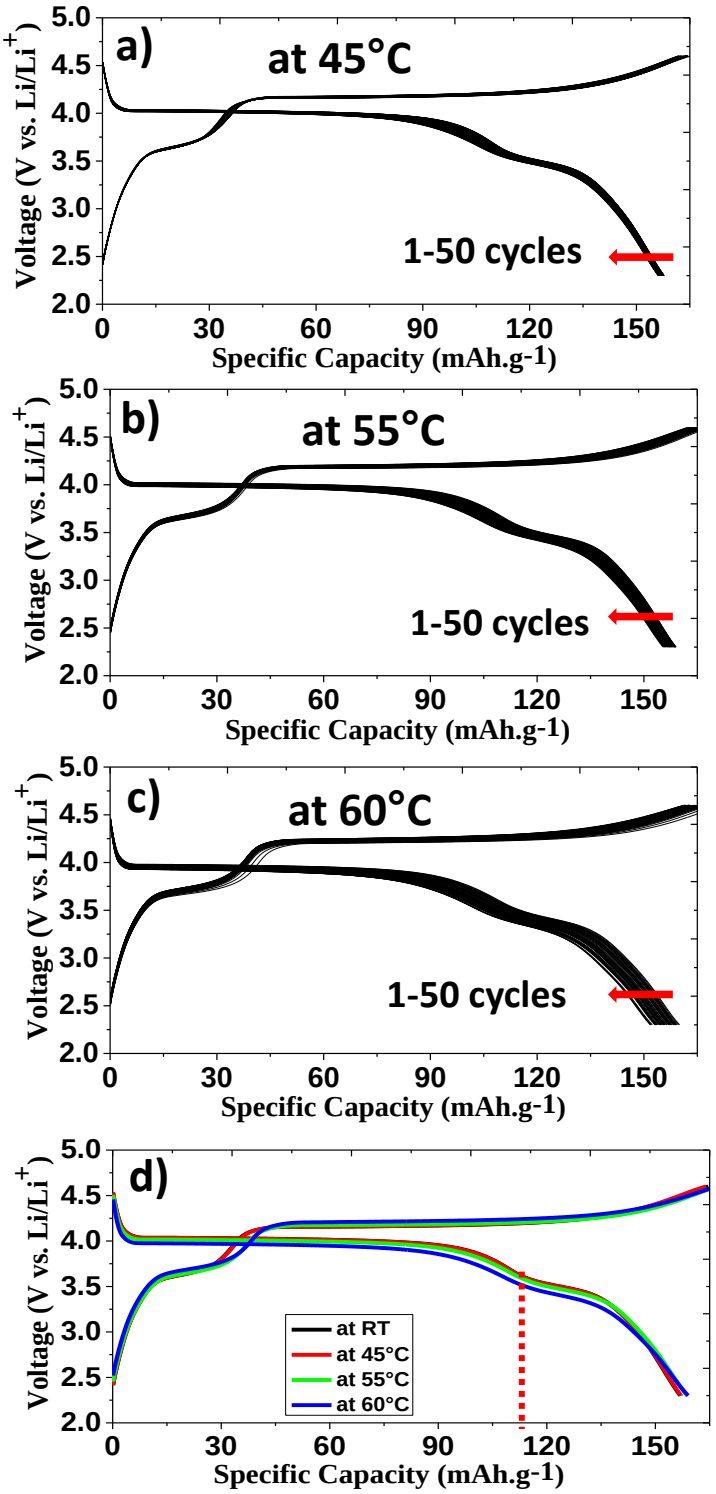

Figure 6.11 Charge and discharge profiles of $LiMn_{0.8}Fe_{0.15}Mg_{0.05}PO_4/C$ at different temperature (RT, 45, 55 and 60°C) at 0.2C; $LiMn_{0.8}Fe_{0.15}Mg_{0.05}PO_4/C$: (a) at 45°C, (b) at 55°C (c) at 60°C and (d) comparison of galvanostatic charge and discharge profiles at different temperature (RT, 45, 55, 60°C).

$LiMn_{0.8}Fe_{0.15}Mg_{0.05}PO_4/C$ shows extremely stable discharge capacity ~157-160 mAh g^{-1} without significant drop in the high voltage regime at all

temperature range RT-60°C compared to $LiMn_{0.8}Fe_{0.2}PO_4/C$ (details are presented in chapter 5) **Figure 6.11a-6.11d** Similarly, electrochemical performance improvement was reported in Mg^{2+} substituted spinel $LiMn_2O_4$ at elevated temperature.[73] *Ex-situ* PXRD patterns of this sample cycled up to 150 cycles at high temperature (50 cycles at each temperature - 45, 55 and 60°C) show all the corresponding peaks of olivine phase with the additional peak of delithiated $Mn_{0.8}Fe_{0.15}Mg_{0.05}PO_4$ at 30.70° and a strong peak of Al at 44.77° (**Figure 6.12**).

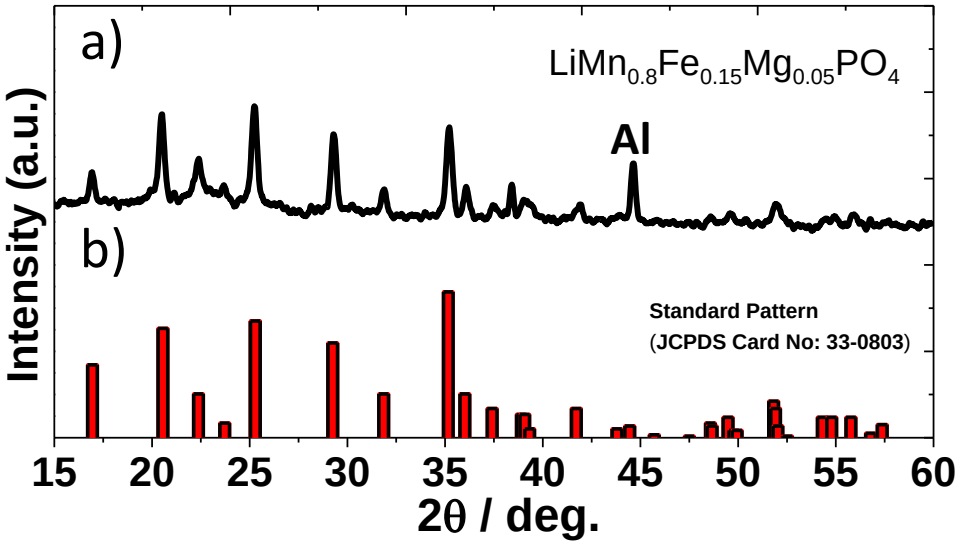

Figure 6.12 *Ex-situ* PXRD patterns of $LiMn_{0.8}Fe_{0.15}Mg_{0.05}PO_4/C$ after 150 cycles at high temperature (50 cycles at each temperature - 45, 55 and 60°C); (a) $LiMn_{0.8}Fe_{0.15}Mg_{0.05}PO_4/C$ and (b) standard powder pattern of $LiMnPO_4$ (JCPDS card No: 33-0803), Aluminium substrate (Al) peak at 44.77°

Figure 6.13 shows the FESEM images of $LiMn_{0.8}Fe_{0.15}Mg_{0.05}PO_4/C$ electrode surface were taken on a sample after 150 cycles in total, but subjected to 50 cycles at 45, 50 cycles at 55 and finally 50 cycles at 60 °C. Different FESEM figures (a), (b), (c), (d) and (f) refer to same sample but at different magnification. This electrode has still sufficient porosity and good connectivity between the particles (**Figure 6.13**) rather than cracks compared to $LiMn_{0.8}Fe_{0.2}PO_4/C$ electrode (details are presented in chapter 5).

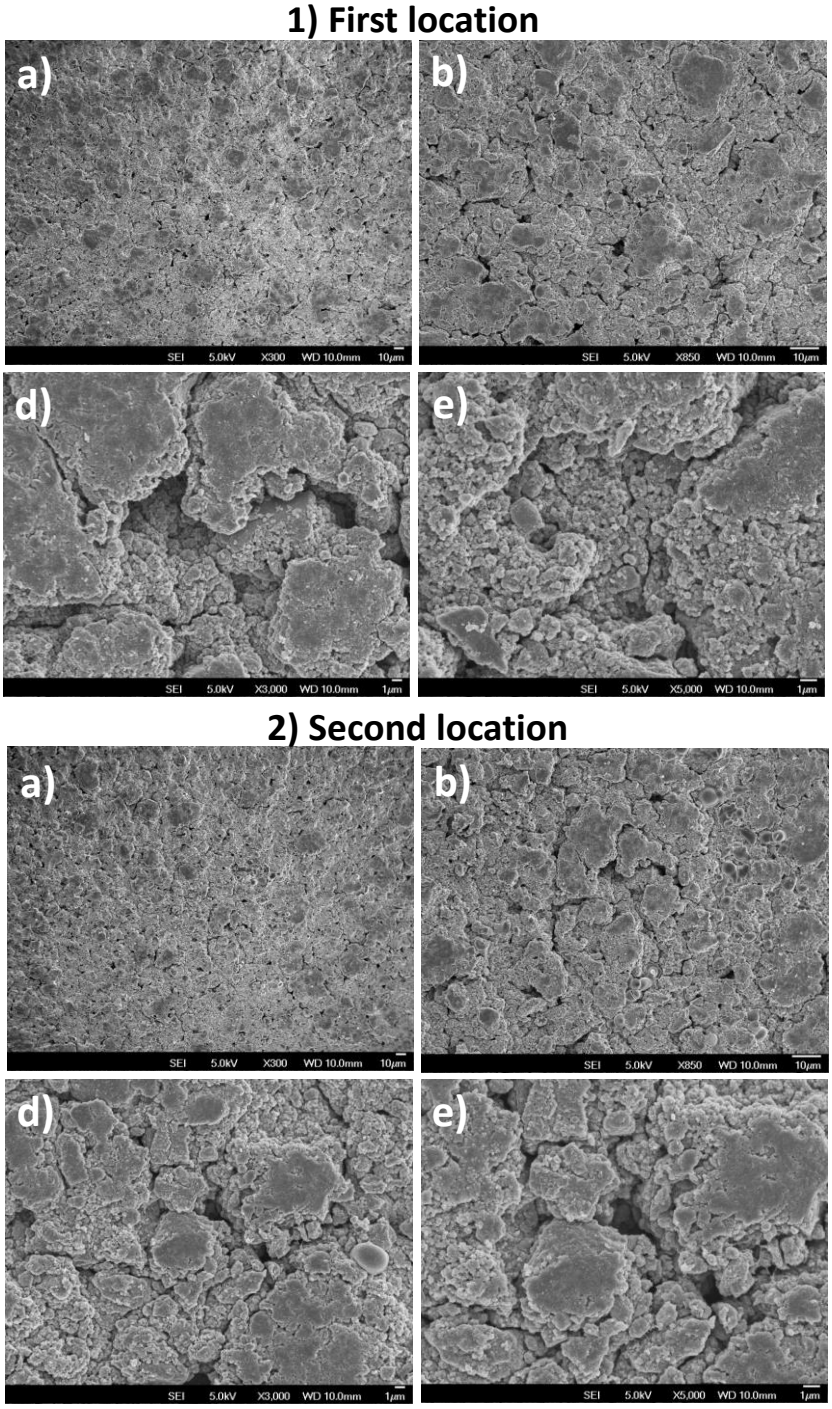

Figure 6.13 FESEM images of $LiMn_{0.8}Fe_{0.15}Mg_{0.05}PO_4/C$ electrode surface after 150 cycles in total at various temperatures (50 cycles at each temperature - 45, 55 and 60 °C), (1 and 2) at different locations and (a, b, c, d, e and f) at different magnifications.

Such extreme robustness of high temperature cycling seen in our Mg^{2+} substituted $LiMn_{0.8}Fe_{0.15}Mg_{0.05}PO_4/C$ samples could possibly arise from stabilization of the delithiated phase ($Li_{1-x}Mn_{0.8}Fe_{0.15}Mg_{0.05}PO_4/C$). The

stability of the delithiated phase of $LiMn_{0.8}Fe_{0.15}Mg_{0.05}PO_4/C$ has been attributed to (i) the unchanged ionic radii of Mg^{2+} in the lattice during charging and discharging and (ii) partial removal of Li^+ ions from the lattice owing to inactive Mg^{2+} dopant in $LiMn_{0.8}Fe_{0.15}Mg_{0.05}PO_4/C$.[176, 178]

6.4.7 Enhanced lithium extraction/insertion mechanism in $LiMn_{0.8}Fe_{0.15}Mg_{0.05}PO_4$

Previously in chapter 4, we have demonstrated that the enhanced manganese electrochemical activity of co-substituted $LiMn_{0.9}Fe_{0.05}Mg_{0.05}PO_4$ can be significantly improved over $LiMnPO_4$ owing to the role of Fe^{2+} and Mg^{2+} in the structure.[135] In this study, we have further extended this mechanism in Mn-rich Mn-Fe-Mg mixed phosphate where most of the capacity arises at high potential manganese redox domain. *Ex-situ* XPS experiments were carried out to study the Li^+ ion extraction/insertion mechanism in $LiMn_{0.8}Fe_{0.15}Mg_{0.05}PO_4$, to appraise the reasons for enhanced manganese utilization and lithium storage performance. XPS spectra were recorded on partially charged (4 V), fully charged (4.6 V) and fully discharged (2.3 V) electrodes **(Figure 6.14(i)).** During the process of lithium extraction up to 4 V, there is a redox transition from $LiMn^{2+}Fe^{2+}Mg^{2+}PO_4$ (pristine) to $Li_{(1-x)}Mn^{2+}(Fe^{3+})Mg^{2+}PO_4$ (partially charged to 4 V) which is shown in XPS spectra **(Figure 6.14(ii)).** Accordingly, spectra peaks are found to be located at binding energy of 641.3, 712.6 and 50.3 eV, corresponding to Mn^{2+}, Fe^{3+} and Mg^{2+} respectively **(Figure 6.14(ii)).** A charge capacity of ~39 mAh g^{-1} witnessed up to 4 V corresponds to Fe^{2+}/Fe^{3+} redox transition and not from the Mn^{2+}/Mn^{3+} **(Figure 6.14(i)).** The possibility of capacity contribution from Mn^{2+}/Mn^{3+} is ruled out here as the equilibrium potential for this redox couple

occurs at ~4.1 V. The delithiated phase formed owing to Fe^{2+}/Fe^{3+} redox further facilitates the favourable redox electrochemical activity of Mn^{2+}/Mn^{3+} in $LiMn_{0.8}Fe_{0.15}Mg_{0.05}PO_4$ material.[180]

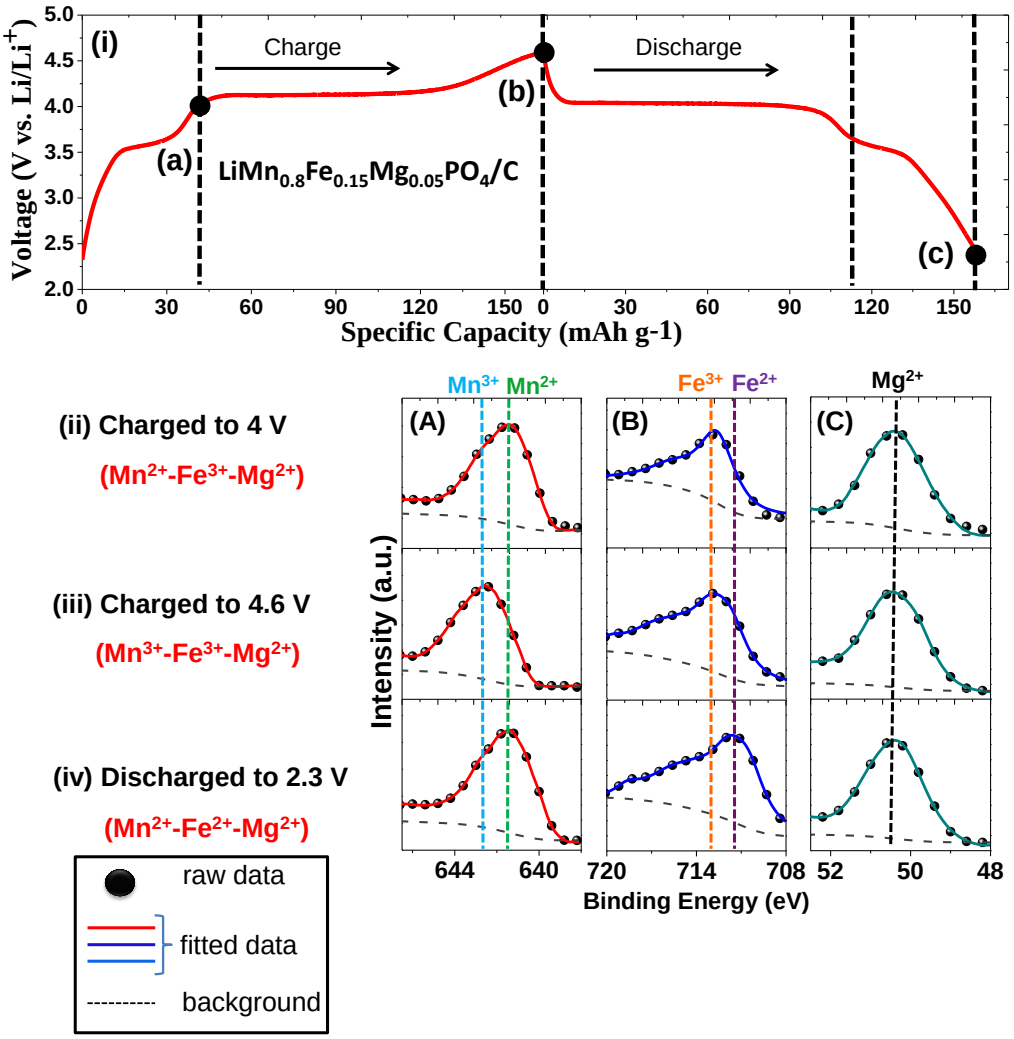

Figure 6.14 (i) Charge/discharge profile of $LiMn_{0.8}Fe_{0.15}Mg_{0.05}PO_4/C$: [(a) a state of partially charged to 4 V, (b) a state of fully charged to 4.6 V, (c) a state of fully discharged to 2.3 V]; *ex-situ* XPS spectra of $LiMn_{0.8}Fe_{0.15}Mg_{0.05}PO_4/C$: [(ii) partially charged to 4 V, (iii) fully charged to 4.6 V and (iv) fully discharged to 2.3 V]; (A) refers to Mn $2p_{3/2}$, (B) refers to Fe $2p_{3/2}$ and (C) refers to Mg $2p_{3/2}$.

During further lithium extraction up to 4.6V, there is a redox transition from $Li_{(1-x)}Mn^{2+}(Fe^{3+})Mg^{2+}PO_4$ (partially charged to 4 V) to $Li_{(1-x)}(Mn^{3+}Fe^{3+})Mg^{2+}PO_4$ (fully charged to 4.6 V, $0< x >1$) owing to transition of Mn^{2+}/Mn^{3+} at ~4.1 V while electrochemically inactive Mg^{2+} does not

contribute to charge capacity as seen from XPS spectra **(Figure 6.14 (iii)).** These XPS spectra show peaks at 642.5, 712.6 and 50.3 eV corresponding to Mn^{3+}, Fe^{3+} and Mg^{2+} respectively.[161, 177, 396-402] Since Mg^{2+} ions do not undergo any change in its oxidation state, lithiated phase associated Mg^{2+} still exists in the structure. Presence of such partial lithiated phase prior to lithium insertion (discharge) cycle, promotes enhanced electrochemical activity of Mn^{2+}/Mn^{3+} in this material. After complete discharge to 2.3V, peaks at 641.3 and 711.4 eV corresponding to Mn^{2+} and Fe^{2+} were seen, while Mg^{2+} (50.3 eV) showed no change **(Figure 6.14 (iv)).**[154, 161, 177, 400-402] The subsequent charge and discharge cycles follow the above mechanism which facilitates enhanced manganese utilization and lithium storage performance of Fe^{2+} and Mg^{2+} substituted $LiMn_{0.8}Fe_{0.15}Mg_{0.05}PO_4$ samples. The mechanism of enhanced Li^+ ion extraction/insertion in $LiMn_{0.8}Fe_{0.15}Mg_{0.05}PO_4$ could be summarized in **Equation. (6.1)**.

$$\underset{\mathbf{LiMn^{2+}Fe^{2+}Mg^{2+}PO_4}}{\overset{\mathbf{at\ OCV\ /\ 2.3\ V}}{}} \rightleftharpoons \underset{\mathbf{Li_{(1-x)}Mn^{2+}(Fe^{3+})Mg^{2+}PO_4}}{\overset{\mathbf{at\ 4\ V}}{}} \rightleftharpoons \underset{\mathbf{Li_{(1-x)}(Mn^{3+}Fe^{3+})Mg^{2+}PO_4}}{\overset{\mathbf{at\ 4.6\ V}}{}} \quad \mathbf{(6.1)}$$

In short, during Li^+ ions extraction process, delithiated phase created from Fe^{2+}/Fe^{3+} redox (~3.45 V) favours facile electrochemical activity of the succeeding Mn^{2+}/Mn^{3+} redox of $LiMn_{0.8}Fe_{0.15}Mg_{0.05}PO_4$ and $LiMn_{0.8}Fe_{0.2}PO_4$ unlike $LiMnPO_4$. The fully charged product ($Li_{(1-x)}Mn_{0.8}Fe_{0.15}Mg_{0.05}PO_4$/C at 4.6V) contains partial lithiated phase owing to the presence of electrochemically inactive Mg^{2+}. Apart from electronic configuration of mixed transition metals (Mn-Fe), the presence of such lithiated phase provides favourable environment for the enhanced manganese utilization in the subsequent lithium ions insertion process unlike $LiMn_{0.8}Fe_{0.2}PO_4$ and

$LiMnPO_4$.

6.4.8 Diffusion study of $LiMn_{0.8}Fe_{0.15}Mg_{0.05}PO_4/C$ at various stages of electrochemical extraction and insertion of lithium ion

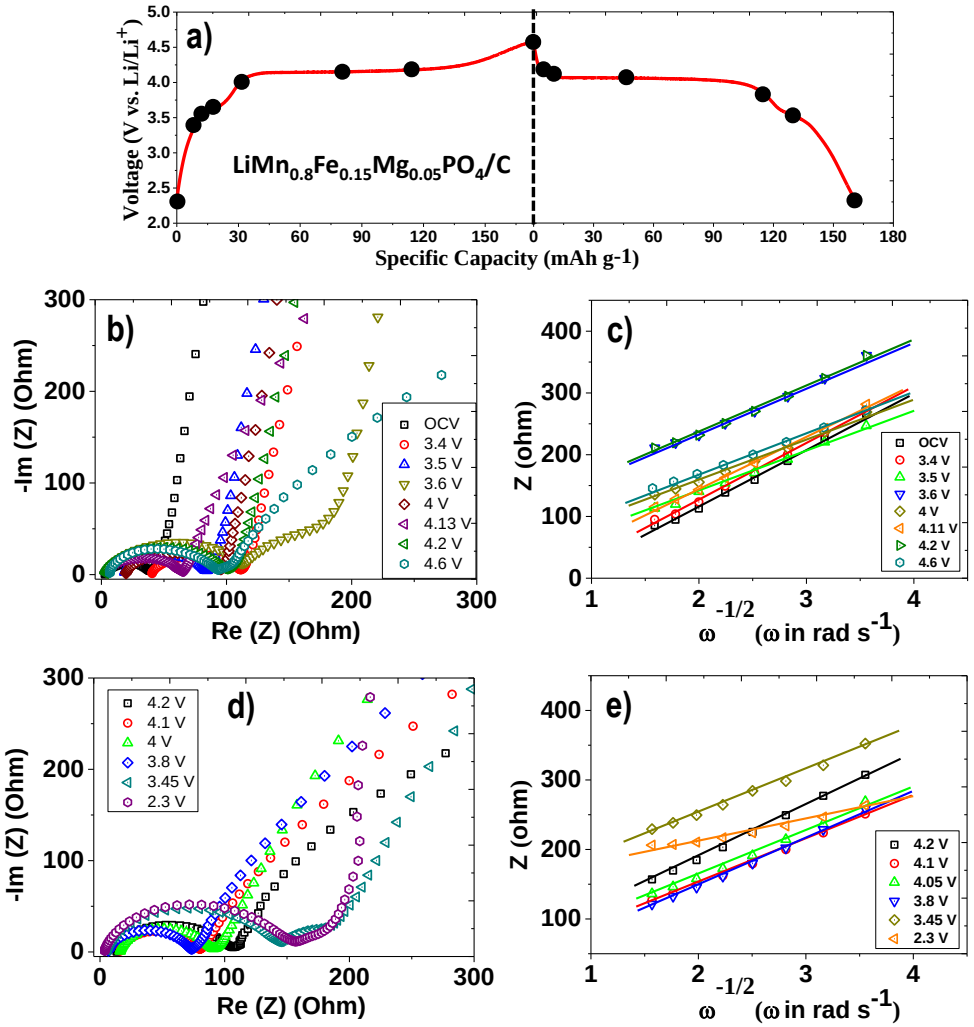

Figure 6.15 Impedance spectra of $LiMn_{0.8}Fe_{0.15}Mg_{0.05}PO_4/C$ and corresponding linear fittings between Z_{re} and reciprocal square root of the angular frequency in the low frequency region of impedance spectra of $LiMn_{0.8}Fe_{0.15}Mg_{0.05}PO_4/C$ at different stages of charge and discharge potentials, (a) charge and discharge profiles of $LiMn_{0.8}Fe_{0.15}Mg_{0.05}PO_4/C$ (different stages were marked with black dots in the charge and discharge profiles), (b-c) at different charge potential of $LiMn_{0.8}Fe_{0.15}Mg_{0.05}PO_4/C$ and (d-e) at different discharge potential of $LiMn_{0.8}Fe_{0.15}Mg_{0.05}PO_4/C$.

The apparent lithium ion diffusion coefficient (D_{Li}^+) of $LiMn_{0.8}Fe_{0.15}Mg_{0.05}PO_4/C$ and $LiMn_{0.8}Fe_{0.2}PO_4/C$ (In this section, the results of $LiMn_{0.8}Fe_{0.2}PO_4/C$ is used for sake of comparison and details are discussed in chapter 5) at different stages of electrochemical extraction and insertion of

lithium is calculated using impedance spectroscopy measurements **(Figure 6.15a, 6.15b and 6.15d)** by taking the linear fittings between Z_{re} and reciprocal square root of the angular frequency in the low frequency region **(Figure 6.15c-6.15e).**

The apparent D_{Li}^{+} was calculated for these samples using **Equation (3.2)**.

where, R is the gas constant, T is the absolute temperature (K), A is the contact area of the electrode (2.01 cm^2), n is the number of electrons per molecule, F is the Faraday constant, C is the concentration of Li ions (6.38 x 10^{-3} $mol.cm^{-3}$) (ratio between the tap density of the prepared material and molecular weight) and σ is the Warburg coefficient (obtained from **(Figure 6.15a-6.15b).**[134, 135, 187, 403] The apparent D_{Li}^{+} values obtained from EIS measurements are shown in **Figure 6.16.**

The apparent D_{Li}^{+} of $LiMn_{0.8}Fe_{0.15}Mg_{0.05}PO_4/C$ and $LiMn_{0.8}Fe_{0.2}PO_4/C$ is almost similar in the iron redox region. In sharp contrast, there is a difference in the diffusion coefficient of lithium ions between Mg^{2+} substituted $LiMn_{0.8}Fe_{0.15}Mg_{0.05}PO_4/C$ and $LiMn_{0.8}Fe_{0.2}PO_4/C$ at the manganese redox (Mn^{2+}/Mn^{3+}) potential region (~4 - 4.15V in both oxidation and reduction process) **(Figure 6.15).** The reduced volume change between lithiated and delithiated phase due to presence of large ions Mg^{2+}, reduced Fe-O-Mn bond, enhanced structural stability and partially suppressed Jahn-Teller distortion in $LiMn_{0.8}Fe_{0.15}Mg_{0.05}PO_4/C$ compared to $LiMn_{0.8}Fe_{0.2}PO_4/C$ could possibly enhance the local ionic transport during the Mn^{2+}/Mn^{3+} redox reaction.[172, 423, 424] This also testifies the enhanced manganese utilization in $LiMn_{0.8}Fe_{0.15}Mg_{0.05}PO_4/C$ than in $LiMn_{0.8}Fe_{0.2}PO_4/C$ **(Figure 6.9 and Figure 6.10).**

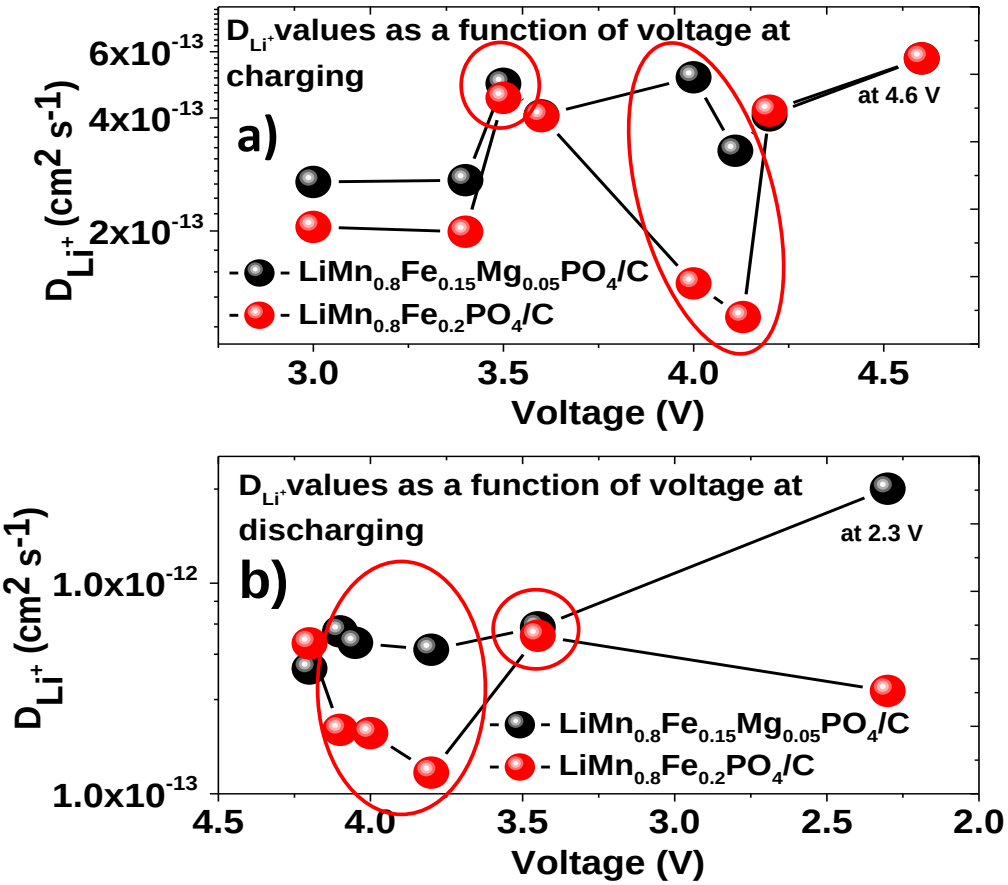

Figure 6.16 Apparent diffusion coefficient (D_{Li}^{+}) of $LiMn_{0.8}Fe_{0.15}Mg_{0.05}PO_4/C$ (black dots) and $LiMn_{0.8}Fe_{0.2}PO_4/C$ (red dots) ($LiMn_{0.8}Fe_{0.2}PO_4/C$, for sake of comparison) at different stages of electrochemical extraction and insertion of lithium using impedance spectroscopy (taking the linear fittings between Z_{re} and reciprocal square root of the angular frequency in the low frequency region); (a) diffusion coefficient at different stages of charge of $LiMn_{0.8}Fe_{0.15}Mg_{0.05}PO_4/C$ and $LiMn_{0.8}Fe_{0.2}PO_4/C$ and (b) diffusion coefficient at different stages of discharge of $LiMn_{0.8}Fe_{0.15}Mg_{0.05}PO_4/C$ and $LiMn_{0.8}Fe_{0.2}PO_4/C$.

6.5 Summary

In summary, the influence of Mg^{2+} substitution on the electrochemical performance of Mn-rich Mn-Fe mixed transition metal phospho-olivine cathode was investigated. The presence of Mg^{2+} ions in Mn-Fe phospho-olivine resulted in enhanced electrochemical kinetics, manganese utilization, rate performance, cycling stability, thermal stability, structural stability, reduced voltage polarization and reduced volume change during the electrochemical delithiation. For example, the discharge capacity of Mg^{2+}

substituted samples was stable (157 mAh g^{-1}) even at wide operating temperature range. The possible reasons for enhanced manganese utilization in $LiMn_{0.8}Fe_{0.15}Mg_{0.05}PO_4/C$ is discussed in terms of (i) redox combination which provides favourable environment for the lithiation and delithiation processes owing to low equilibrium potential of Fe^{2+}/Fe^{3+} and electrochemically inactive Mg^{2+}, (ii) partial suppression of Jahn-Teller distortion, (iii) structural and thermal stability of delithiated phase ($Li_{1-x}Mn_{0.8}Fe_{0.15}Mg_{0.05}PO_4$) and (iv) enhanced transport properties.

In the next chapter, lithium storage properties of low temperature *Pmn*2_1 polymorph and high temperature *P*2_1/*n* polymorph of Li_2MnSiO_4 are investigated.

Chapter 7

7. The effect of polymorphism on the lithium storage performance of Li_2MnSiO_4

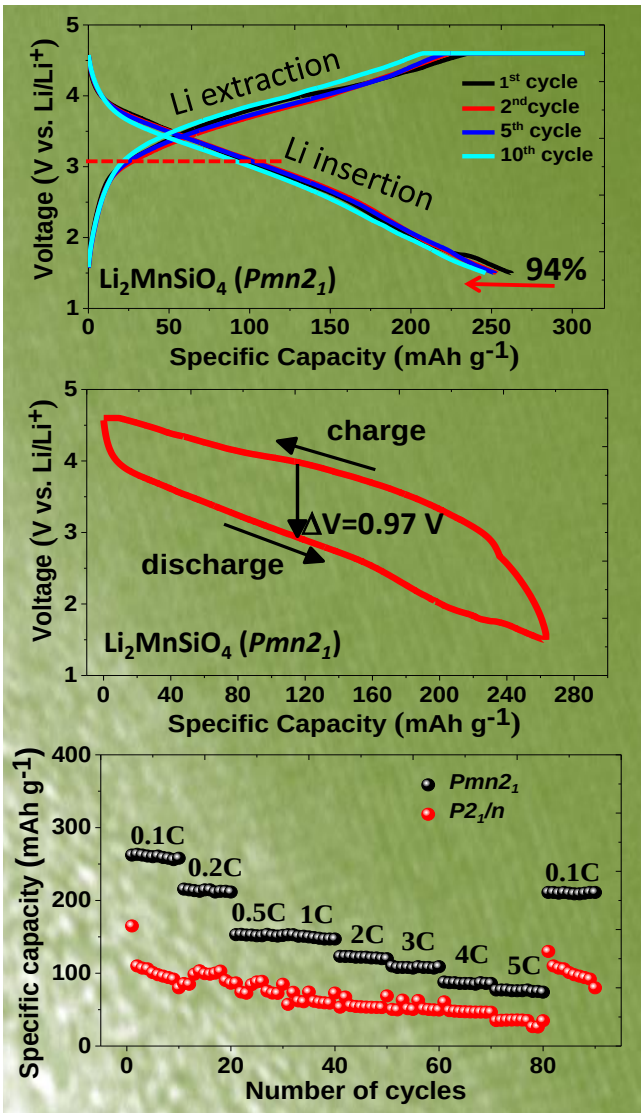

7.1 Preface to Chapter 7

In the previous chapters, we have systematically demonstrated the factors that influence the lithium storage performance of olivine phosphate based cathode materials. In this chapter, we study the role of polymorphism on electrochemical performance in silicate based cathode materials. The synthesis and electrochemical characterization of low and high temperature polymorphs of Li_2MnSiO_4/C cathode material are discussed in this chapter. By controlling the calcination temperature, two different polymorphs of Li_2MnSiO_4/C namely *Pmn*2_1 (low temperature) and *P*2_1/*n* (high temperature) are obtained. The electrochemical performance of low temperature *Pmn*2_1 polymorph is better than the high temperature *P*2_1/*n* polymorph. *Pmn*2_1 polymorph delivers a discharge capacity of 262 mAh g^{-1} while *P*2_1/*n* polymorph delivers a discharge capacity of 164 mAh g^{-1} at 0.1C. The lithium storage performance of *Pmn2$_1$* is almost twice that of *P*2_1/*n* at all current rates. The superior lithium storage performance of *Pmn*2_1 is due to simplest Li^+-ion migration pathway compared to *P*2_1/*n* which has complex Li^+-ion migration path. Besides the role of polymorphs, it is also found that the structural stability after cycling is also critical in achieving high storage performance.

7.2 Introduction

Despite tremendous success of lithium-ion batteries (LIBs), their low energy density has always been a matter of great concern.[119, 425-427] One way of improving the energy density of LIBs is to use cathode materials with high lithium storage capacities.[204, 317, 428] Li_2MnSiO_4 has a high theoretical capacity of 333 mAh g^{-1}, assuming 2 moles of lithium ion transfer per formula unit.[200-203, 217, 223, 239, 240] Besides high capacity, they are attractive owing to their low cost, environmental friendliness and safety which arises from the integration of $(SiO_4)^{4-}$ polyanion (strong Si-O bonds) in the crystal structure.[201, 204, 208, 429] However, Li_2MnSiO_4 suffers from very low intrinsic electronic conductivity (10^{-14} to 10^{-16} S cm^{-1}) resulting in poor electrochemical performance.[235, 430] To improve the lithium storage performance most of the previous works have focused on nano-structuring this active material and providing carbon coating.[234, 239, 240, 244, 245, 431-434] One striking aspect of Li_2MnSiO_4 is their richness in polymorphism.[186, 201-205] Different polymorphs have been previously prepared by carefully controlling the temperature, pressure, temperature ramp up rate and ramp down rate of the synthesis and post-treatment of the materials.[200-204, 211, 217, 223, 237] For instance, two low temperature polymorphs *Pmn*2_1 and *Pmnb* with an orthorhombic structure,[200, 203] a high temperature polymorph *P*2_1/*n* with a monoclinic structure[212] and a meta-stable monoclinic *Pn* polymorph[241] have been reported till date. In general, insertion and extraction of less than one mole of lithium is reported for Li2MnSiO4. However, there are few reports which exploited second lithium exchange. Insertion and extraction of more than one mole of lithium is reported for low temperature *Pmn2*$_1$ polymorph at room temperature[226, 236, 239,

[243, 244] and for high temperature $P2_1/n$ polymorph at elevated temperature.[240, 245] Recently, our group has also observed similar electrochemical performances experimentally on both $Pmn2_1$ and $P2_1/n$ polymorphs with temperature.[239, 240] However, the structural instability caused by Jahn-Teller effect and amorphization of the material during subsequent electrochemical cycling, resulted in capacity fading.[204, 235, 236] A very recent work by Fisher *et al.*[242] showed that $Pmn2_1$ (low temperature polymorph) has simplest Li^+-ion migration pathway and lower energy barrier due to high symmetry of Li sites in the unit cells. This is in contrast to $P2_1/n$ (high temperature polymorph) which has two symmetrically distinct Li sites in the unit cells, whose formation energies are slightly different resulting in complex migration pathway for Li^+-ions. Hence, it is expected that these two polymorphs would show varying electrochemical properties.

The main focus of this chapter is to isolate the polymorphs of Li_2MnSiO_4 by controlling the calcination temperature and to investigate their lithium storage performance. Two polymorphs namely, $Pmn2_1$ and $P2_1/n$ were isolated by exercising judicial control on the calcination temperature. Among these two polymorphs, the electrochemical performance of $Pmn2_1$was found to be better than $P2_1/n$. Further, we could extract and insert more than one mole of lithium successfully from low temperature polymorph ($Pmn2_1$). $Pmn2_1$ exhibits high storage capacity of 262 mAh g^{-1} at 0.1C and rate performance up to 5C; in contrast $P2_1/n$ which delivers only a discharge capacity of 164 mAh g^{-1} at 0.1C at room temperature. The improved storage performance of low temperature polymorph ($Pmn2_1$) is due to simplest Li^+ ions migration pathway compared to high temperature polymorph ($P2_1/n$) which has complex Li^+-ion

migration path way.[242] Besides the role of polymorphism, it is found that the structural stability after cycling is also critical in achieving high storage performance.

7.3 Experimental

7.3.1 Synthesis of Li_2MnSiO_4/C polymorphs by two-step method

Carbon coated Li_2MnSiO_4/C polymorphs were synthesized using soft template method followed by high energy ball milling process **(Scheme 1)**. All the precursors were mixed in stoichiometric ratio. Firstly, manganese (II) acetate tetrahydrate ($Mn(CH_3CO_2)_2{\cdot}4H_2O$, Sigma Aldrich), tetraethyl orthosilicate ($SiC_8H_{20}O_4$, TCI-EP-Japan) and citric acid ($C_6H_8O_7$, Alfa Aesar) for *in-situ* carbon coating were dissolved in a round bottom flask with a mixture of millQ water and absolute ethanol in the volume ratio of 2:1. The solution was stirred for 24 h and the solvent was evaporated using an IKA RV10 roto-evaporator. The precipitate was calcined in a tubular furnace at 700 $^{\circ}$C for 8 h in an Ar atmosphere. The calcined product was ground with lithium hydroxide monohydrate ($Li(OH).H_2O$, Sigma Aldrich) using HEBM at 500 rpm for 60 min. The final product was calcined at different temperatures, between 450 °C and 1000 °C for 8 h in an Ar-H_2 (95:5) atmosphere to isolate the polymorphs. Two polymorphs $Pmn2_1$ (low temperature: 450 °C – 800 °C) and $P2_1/n$ (high temperature: 850 °C – 1000 °C) were isolated by controlling the synthesis temperature. For further experiments, two samples which were calcined at 750 °C and 1000 °C for 8 h in an Ar:H_2 (95:5) atmosphere were taken. Further, the low temperature $Pmn2_1$ polymorph was prepared without carbon coating (control sample) by two-step synthesis method to appraise the effect of carbon coating. Before making the slurry, the active material and

acetylene black were mixed using FRITSCH premium line – pulverisette 7 instrument at 500 rpm for 4 h with the weight ratio of sample: balls = 1:40 and then the samples were re-heated at 750 °C or 1000 °C for 8 h in an Ar-H_2 (95:5) atmosphere.

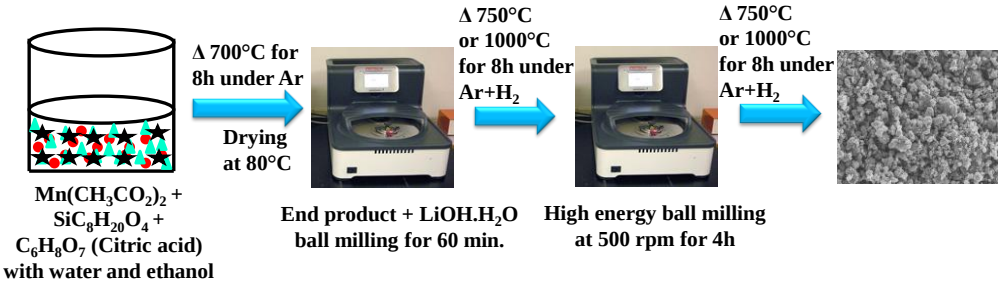

Scheme 1 Schematic illustrations of Li_2MnSiO_4/C preparation by high energy ball mill assisted two-step synthesis.

7.3.2 Material and electrochemical characterization

Above samples were characterized using PXRD, Rietveld refinement, FESEM, EDXS, TEM, BET and galvanostatic cycling. The details are given in chapter 2, section 2.2.2 , section 2.3 , section 2.4 and section 2.5

7.4 Results and discussion

7.4.1 Structural and morphological characterization

Figure 7.1 illustrates the PXRD of Li_2MnSiO_4/C as a function of synthesis temperature, 450 °C - 1000 °C. With increasing the temperature, a clear transition from one polymorph to another could be seen **(refer Figure 7.1 and Figure 7.2)**. The samples which are calcined at low temperature (450 °C to 800 °C) exhibit $Pmn2_1$ polymorph. However, upon calcination at temperatures above 850 °C resulted in the evolution of intensive new peaks at around 22° (shown in red arrow), a signature of high temperature $P2_1/n$ polymorph.[223] All peaks in the sample calcined at 1000 °C correspond to high temperature $P2_1/n$ polymorph. For clarity, XRD patterns of samples calcined

at 750 °C and 1000 °C are shown in **Figure 7.3**. The Rietveld refinements for these samples are shown in the **Figure 7.4** and the cell parameters are listed in **Table 7.1,** which are in good agreement with the earlier reports.[203, 211, 212, 223, 237] This Rietveld analysis suggests that a trace of Mn_2SiO_4 (0.37% for $P2_1/n$ and 1.28% for $Pmn2_1$) is found along with formation of low and high temperature of Li_2MnSiO_4. The *in-situ* carbon content on the low and high temperature polymorphs deduced from CHNX analysis were 6.5 and 4.4 wt% respectively. Accordingly, the *ex-situ* carbon additive is added to maintain the slurry proportion (total carbon content in the electrode is 25%).

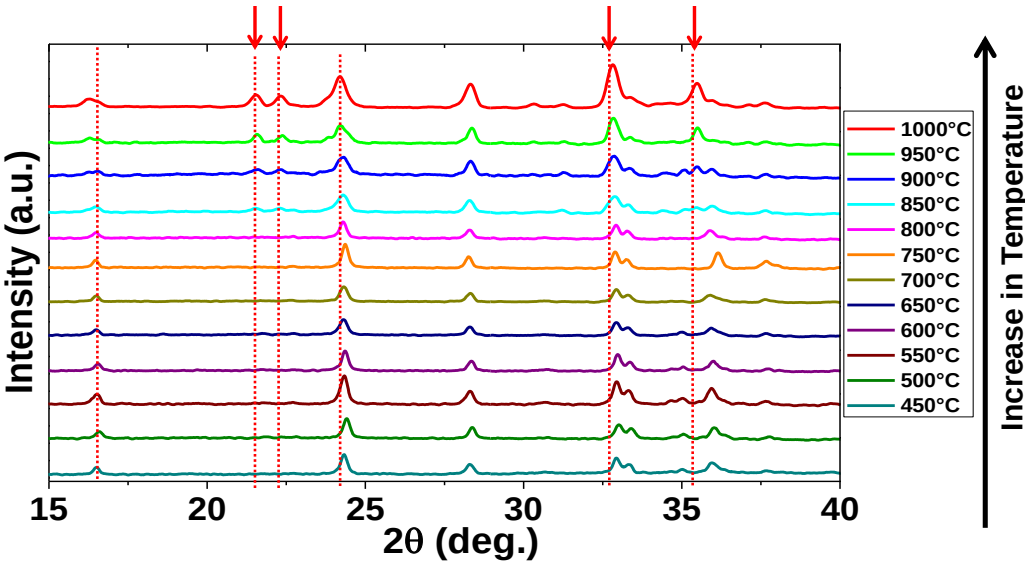

Figure 7.1 PXRD patterns of Li_2MnSiO_4/C polymorphs ($Pmn2_1$ and $P2_1/n$) as a function synthesis temperature (450 – 1000 °C) (arrow in black colour shows increase in temperature).

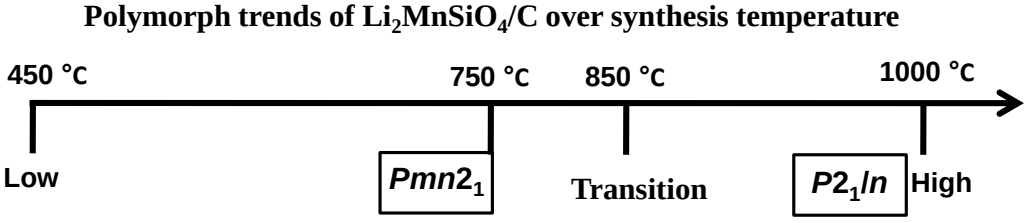

Figure 7.2 Polymorph trends of Li_2MnSiO_4/C over synthesis temperature.

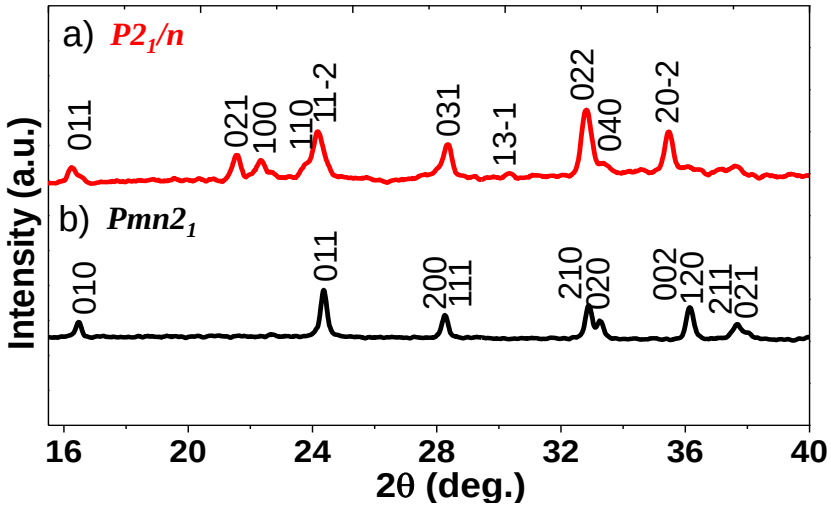

Figure 7.3 PXRD patterns of high and low temperature polymorphs of Li_2MnSiO_4/C, (a) $P2_1/n$ polymorph synthesized at1000 °C and (b) $Pmn2_1$ polymorph synthesized at 750 °C.

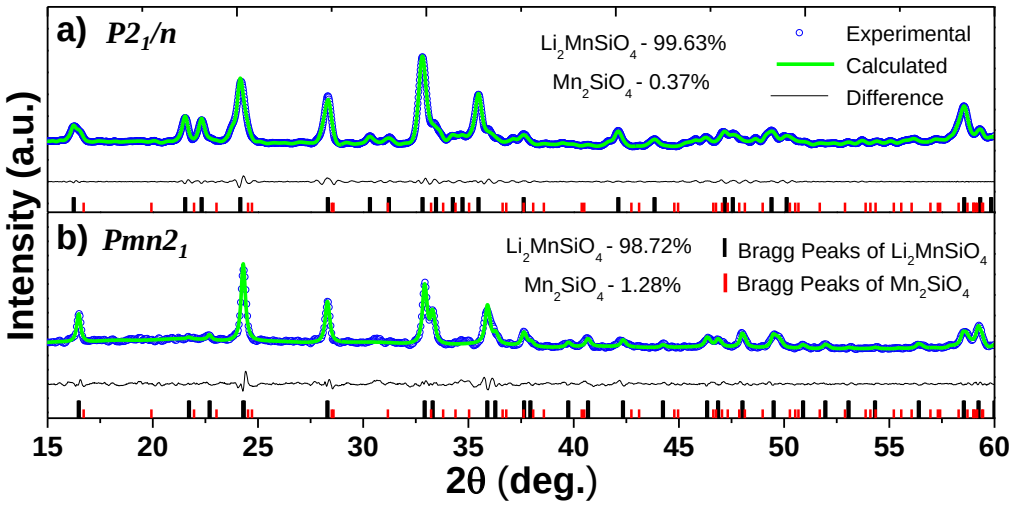

Figure 7.4 Rietveld refinement of high and low temperature polymorphs of Li_2MnSiO_4/C, (a) $P2_1/n$ (R_{exp}:6.69, R_{wp}:3.77 and R_p:2.77) and (b) $Pmn2_1$ (R_{exp}:10.44, R_{wp}:3.49 and R_p:2.69).

Table 7.1 Cell parameters for the low and high temperature polymorphs of Li_2MnSiO_4/C.

Polymorphs	a (Å)	b (Å)	c (Å)	V (Å^3)
$Pmn2_1$ (at 750°C)	6.305(4)	5.381(5)	5.001(5)	169.68
$P2_1/n$ (at 1000°C)	6.312(5)	10.898(6)	5.055(4)	347.81

Figure 7.5 shows the FESEM images of samples which were calcined at 750 °C ($Pmn2_1$) and 1000 °C ($P2_1/n$) for 8h followed by ball milled with carbon and then were re-heated at 750 °C and 1000 °C for 8 h in an Ar:H_2 (95:5) atmosphere.[134, 135] The samples are made of particles in the range of 40 - 60 nm with similar morphology. Elemental mapping images **(Figure 7.6)** show uniform distribution of carbon, silicon, manganese and oxygen within the active material.

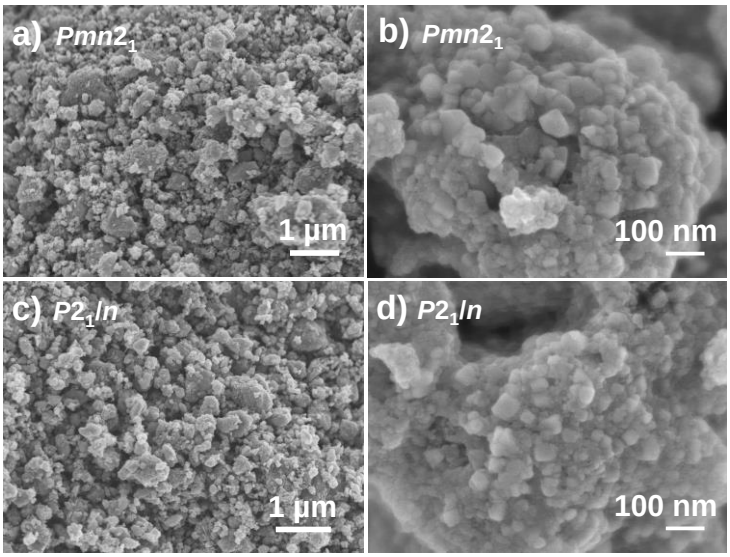

Figure 7.5 FESEM images of Li_2MnSiO_4/C, (a-b) $Pmn2_1$ and (c-d) $P2_1/n$ at different magnification.

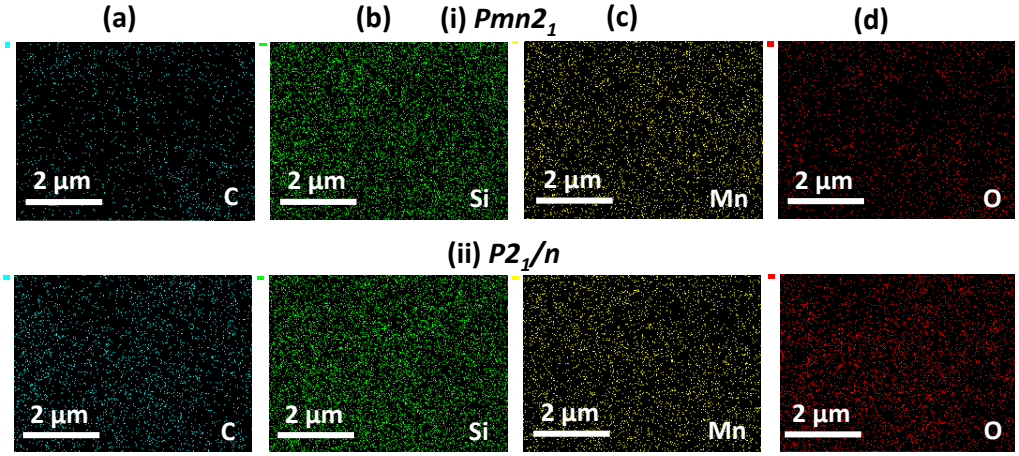

Figure 7.6 Elemental mapping images of low and high temperature polymorphs of Li_2MnSiO_4/C, (i) $Pmn2_1$ and (ii) $P2_1/n$: [(a) carbon (cyan), (b) silicon (green), (c) manganese (yellow) and (d) oxygen (red)].

Figure 7.7 shows the SAED and HRTEM images of *Pmn*2_1 and *P*2_1/*n* samples. The SAED patterns of these two samples calcined at 750 and 1000 °C confirm the formation of low and high temperature polymorphs respectively, a trend consistent with XRD patterns **(Figure 7.3)**.

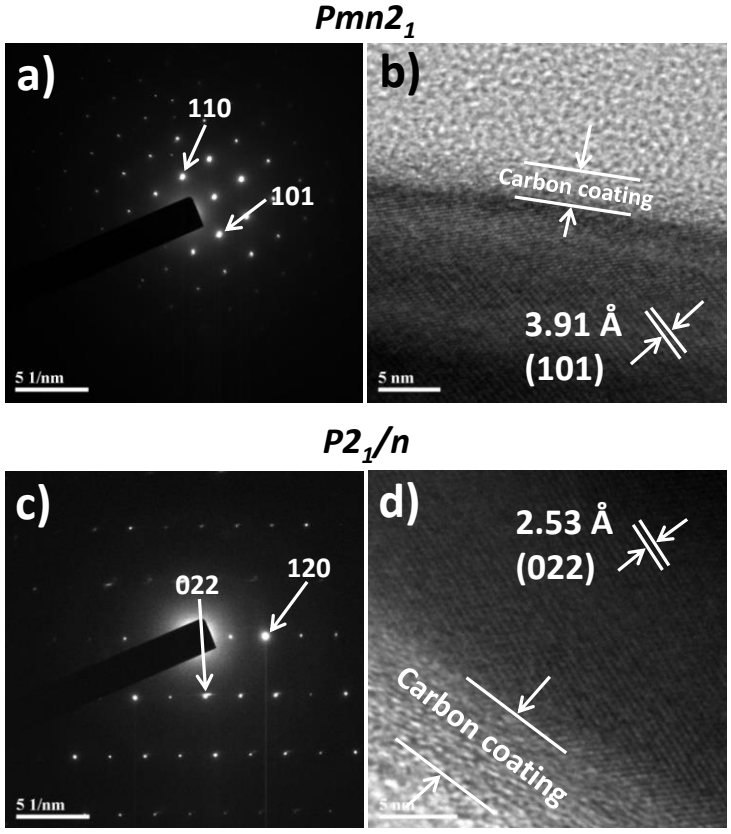

Figure 7.7 SAED patterns and HRTEM images of low and high temperature polymorphs of Li_2MnSiO_4/C, (a-b) *Pmn*2_1 and (c-d) *P*2_1/*n*.

Besides, HRTEM images also show the observed lattice fringes with *d*-spacing of 3.91 Å and 2.53 Å corresponding to (101) and (022) plane of *Pmn*2_1 and *P*2_1/*n* polymorphs of Li_2MnSiO_4 respectively **(Figure 7.7**b **and Figure 7.7d)**. In addition, HRTEM images also show the presence of carbon coating (~5 nm) around the active materials.

The BET surface area of carbon coated *Pmn*2_1 and *P*2_1/*n* samples was analyzed by N_2 sorption isotherms **Figure 7.8**. Nitrogen adsorption and

desorption isotherms of these samples exhibit clear hysteresis loop of Type IV.[370, 371, 382] The BET surface areas of these samples are found to be 22.06 and 20.88 m^2 g^{-1} with a pore size of 3.76 and 3.80 nm respectively **(inset of Figure 7.8)**. The pore volumes of these samples are 0.056 and 0.052 cc g^{-1} respectively.

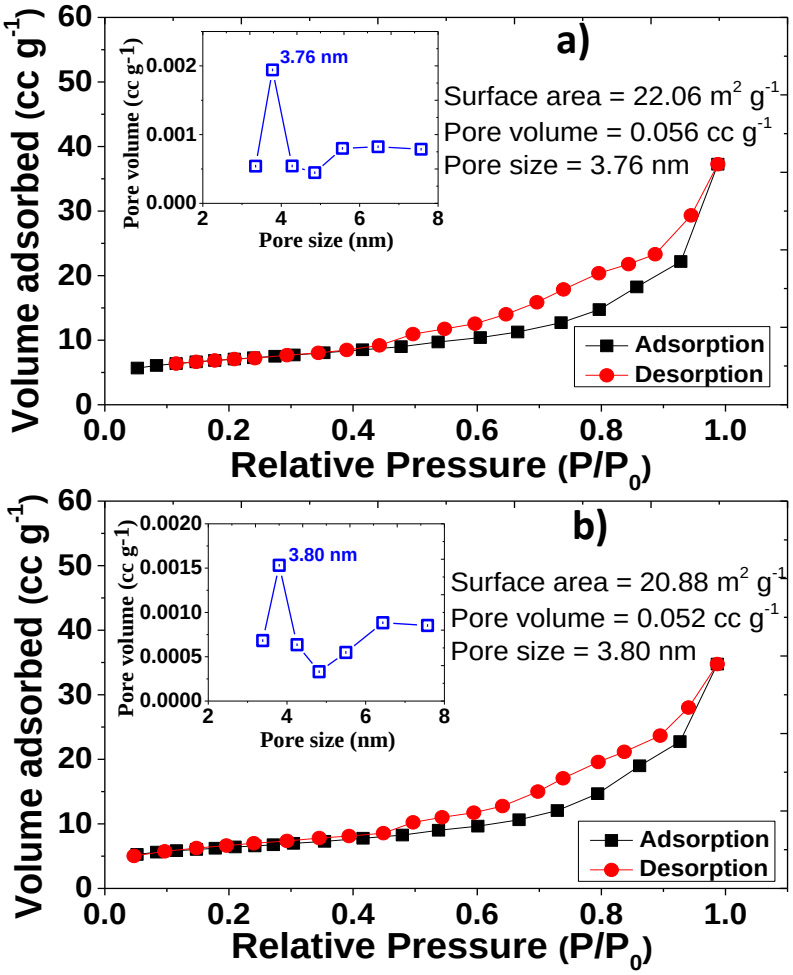

Figure 7.8 Nitrogen adsorption and desorption isotherms and pore size distribution (inset) of Li_2MnSiO_4/C, (a) *Pmn*2_1 and (b) *P*2_1/*n*.

7.4.2 Lithium storage performance

Figure 7.9 demonstrates the lithium storage performance of low and high temperature polymorphs of Li_2MnSiO_4/C with a CC-CV mode of cycling at room temperature. The low temperature polymorph (*Pmn*2_1) exhibits a discharge capacity of 262 mAh g^{-1} with an average potential of ~3.0 V at 0.1C

corresponding to ~1.6 moles of Li^+ ions extraction/insertion from/into the structure. The capacity retention after 10 cycles is 94% of its initial discharge capacity (**Figure 7.9a)**.

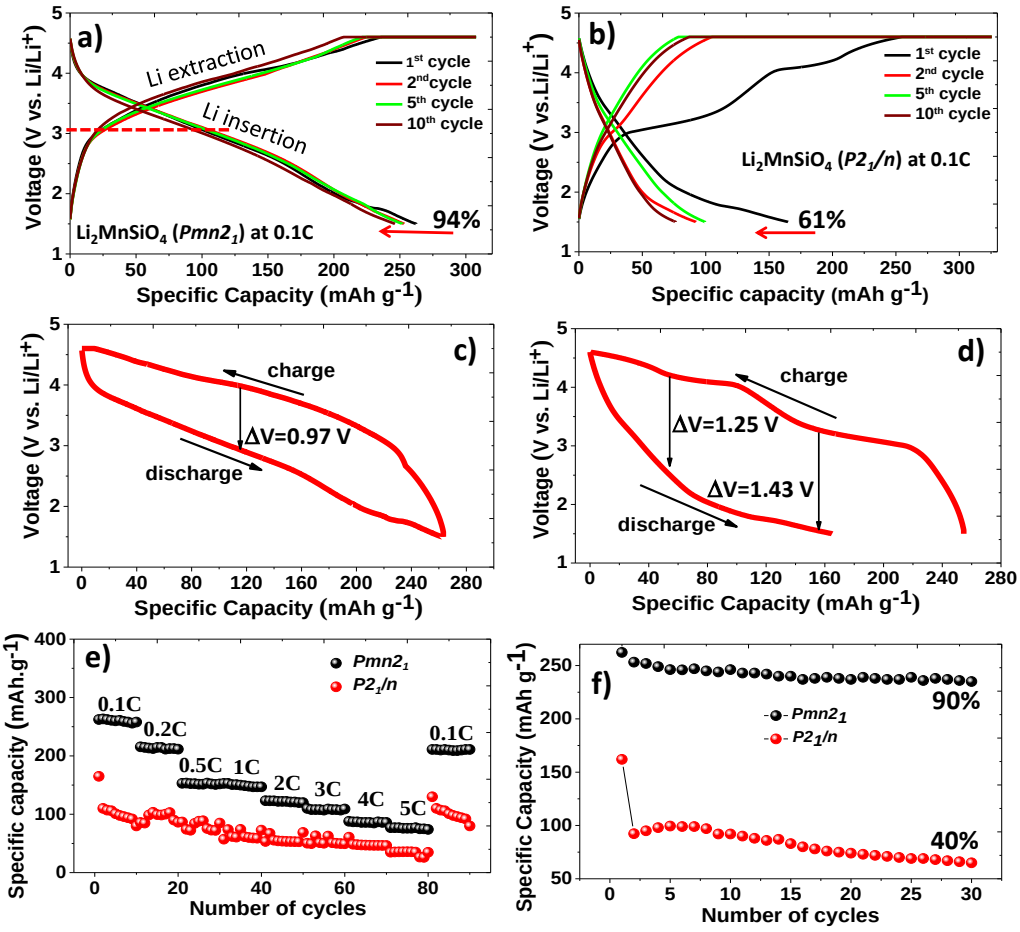

Figure 7.9 Lithium storage performance of Li_2MnSiO_4/C polymorphs at room temperature, (a) Charge and discharge profiles of *Pmn*2$_1$ polymorph up to 10 cycles at 0.1C, (b) Charge and discharge profiles of *P*2$_1$/*n* polymorph up to 10 cycles at 0.1C, (c) Voltage polarization of *Pmn*2$_1$ in the 1st cycle, (d) Voltage polarization of *P*2$_1$/*n* in the 1st cycle, (e) Rate performance of *Pmn*2$_1$ and *P*2$_1$/*n* polymorphs and (f) Cycling stability of *Pmn*2$_1$ polymorph up to 30 cycles (capacity values are calculated based on the active material weight).

On the other hand, high temperature polymorph (*P*2$_1$/*n*), delivers a charge capacity of 250 mAh g^{-1} at 0.1C. However, in the subsequent discharge, only one mole of lithium is inserted into the structure of this sample resulting in low capacity of 164 mAh g^{-1} at 0.1C. In the subsequent cycles, there is a continuous loss in the both Li^+-ion insertion and extraction up to 10

cycles. The capacity retention of the high temperature polymorph ($P2_1/n$) sample after 10 cycles was only 61% **(Figure 7.9b)**.

To understand the differences in the lithium storage performance of low and high temperature phase, we refer to the theoretical work on lithium migration pathway in Li_2MnSiO_4 polymorphs by Fisher *et al.*[242] The low temperature phase which is *Pmn2₁* has the highest symmetry. It provides simplest Li^+ ion migration pathway owing to Li^+-ion sites in the unit cell which are symmetrically equivalent and it has only one jump distance for each direction. In sharp contrast, the high temperature phase ($P2_1/n$) has two symmetrically distinct Li^+-ion sites. The formation energy of these two different sites is slightly different resulting in a more complex migration network with jump distance between 2.7 Å to 3.5 Å. The activation energy for $Pmn2_1$ is uniform in both *a* and *c* direction and its approximately 1 eV. The activation energies for $P2_1/n$ are not uniform, varying from 0.3-1.4 eV depending on the lithium migration directions. Hence, this complex migration pathway and activation energy of $P2_1/n$ ultimately raises the energy barrier for the alkali ions migration resulting in the reduced lithium storage performance which is in good agreement with our electrochemical studies. Therefore, the orthorhombic phase with highest symmetry facilitates easy access to Li^+-ions from the bulk of the electrode delivering enhanced lithium storage performance in contrast to the high temperature monoclinic phase.

The voltage profiles and polarization of orthorhombic phase ($Pmn2_1$) are much better than the monoclinic phase ($P2_1/n$) as shown in **Figure 7.9c-Figure 7.9d. Figure 7.9c** represents the galvanostatic profile of $Pmn2_1$ at the first cycle. The average potentials of lithium extraction and insertion are ~3.97

V and ~3.0 V respectively resulting in a voltage polarization of 0.97 V. It should be noted that the charge and discharge profiles of $Pmn2_1$ are essentially single plateaus owing to similar activation energy in the both the hopping directions.[242] On the other hand, we observe two distinct charge and discharge plateaus for $P2_1/n$ phase in the 1st cycle owing to the variation in the activation energy and hopping distance for different hopping directions.[242] The average potentials of lithium extraction and insertion are ~4.12, 3.85 V and ~3.16, 1.8 V respectively resulting in voltage polarization of 1.26 and 1.43 V. It must be mentioned here that we do not observe distinct voltage plateaus in subsequent cycles and further investigation is needed in this direction.

The rate performance of low and high temperature polymorphs is shown in the **Figure 7.9**e. The cells are cycled from 0.1C to 5C rate. After testing at 5C, all the cells were again tested at 0.1C. The low temperature polymorph retains 80% of its initial capacity at 0.1C while high temperature polymorph retains only 67% of its initial capacity. A summary of lithium storage performance of both polymorphs are listed in the **Table 7.2**. Notably, the capacity of $Pmn2_1$ phase is almost two times higher compare to $P2_1/n$ phase especially at all current rates (**Table 7.2**). The low temperature polymorph of Li_2MnSiO_4/C showed better cycling stability compared to $P2_1/n$ polymorph **(Figure 7.9f)**. The cycling stability of $Pmn2_1$ polymorph is the highest among the reports in literature.[200, 239, 245,229, 234, 235, 240] For instance, a capacity retention of 90% is obtained for low temperature polymorph after 30 cycles at 0.1C. In contrast, high temperature polymorph $P2_1/n$ shows only 40% of its initial capacity after 30 charge and discharge cycles **(Figure 7.9f)**.

As discussed, these materials are prepared with the similar morphology, particle size, mesoporosity and carbon content. Hence, it is believed that the observed differences in the electrochemical performance of these two polymorphs are not biased by factors such as morphology, particle size, mesoporosity and carbon content.

Table 7.2 A summary of lithium storage performance of $Pmn2_1$ and $P2_1/n$ polymorphs of Li_2MnSiO_4/C.

C rates								
Specific discharge capacity in mAh g^{-1}								
Polymorphs	0.1C	0.2C	0.5C	1C	2C	3C	4C	5C
$Pmn2_1$	262	213	152	149	122	108	85	76
$P2_1/n$	164	102	87	74	68	63	48	35

One common problem associated with Li_2MnSiO_4 is their amorphization during cycling. Dominko *et al.*[200, 235] demonstrated that the extraction of more one mole Li^+ ion from the $Pmn2_1$ polymorph leads to the amorphization resulting in low storage performance and there is a continuous fading in the capacity. Here, we show that the amorphization could be suppressed to a greater extent by providing an *in-situ* carbon coating around the active material. **Figure 7.10a** demonstrates the *ex-situ* XRD patterns of carbon coated low temperature polymorph before and after cycling. All the major peaks are seen corresponding to $Pmn2_1$ polymorph suggesting that the carbon coated $Pmn2_1$ polymorphs retains the structure even after 30 cycles **(Figure 7.10a)**. On the other hand, the low temperature $Pmn2_1$ polymorph is prepared without *in-situ* carbon coating (control sample). *Ex-situ* XRD

patterns are recorded on un-coated *Pmn*2$_1$ polymorph electrode at first charge up to 4.6 V and after 10 cycles **(Figure 7.10b)**. The intensity of all major peaks corresponds to *Pmn*2$_1$ polymorph is decreased/disappeared after first charge up to 4.6 V and 10 cycles **(Figure 7.10b)**.

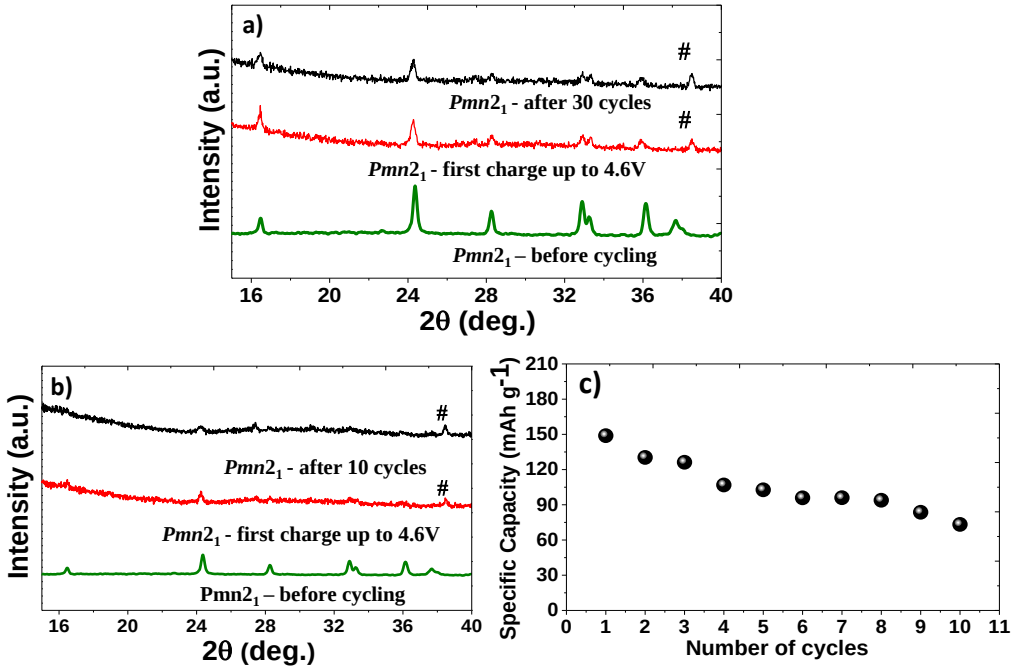

Figure 7.10 (a) *Ex-situ* XRD of low temperature *Pmn*2$_1$ polymorph after a first charge at 4.6 V (black) and after 30 cycles (red), (b) *Ex-situ* XRD of low temperature polymorph of Li_2MnSiO_4 sample without *in-situ* carbon coating after first charge up to 4.6 V (black) and after 10 cycles (red), (substrate peak is marked with symbols, #) and (c) Cyclic behaviour of un-coated low temperature *Pmn*2$_1$ polymorph sample.

It is also worth noting that the un-coated low temperature *Pmn*2$_1$ polymorph delivered discharge capacity of 148 mAh g^{-1} and retained only of 49% capacity after 10th cycle **(Figure 7.10c)** while the carbon coated samples retained 94% **(Figure 7.9f)**. Hence, we believe that the presence of carbon coating around the manganese silicate acts as a buffer layer to accommodate the strain that has been created during the electrochemical intercalation and de-intercalation. Thus, apart from the type of polymorphs, the structural stability is also very important to achieve good lithium storage performance.

7.5 Summary

In summary, two polymorphs of Li_2MnSiO_4 were isolated by carefully controlling the calcination temperature. PXRD patterns, HRTEM images and SAED patterns confirm the presence of the low temperature *Pmn*2_1 polymorph and high temperature *P*2_1/*n* polymorph. The electrochemical performance of *Pmn*2_1 polymorph was much better than *P*2_1/*n* polymorph. *Pmn*2_1 exhibits high lithium storage performance of 262 mAh g^{-1} at 0.1C and impressive rate performance up to 5C at room temperature; in contrast to *P*2_1/*n* which delivers only 164 mAh g^{-1} at 0.1C. Notably, the capacity of *Pmn*2_1 phase is almost two times higher than *P*2_1/*n* phase at all current rates. Such perceivable difference in the storage performance is explained by the simplest migration pathway of Li^+ ion in *Pmn*2_1 polymorph compared to *P*2_1/*n* polymorph. Besides the role of polymorphism, it is also found that the structural stability after cycling is critical in achieving high storage performance. *Ex-situ* XRD pattern of carbon coated samples revealed that the structure was stable upon first charging up to 4.6 V and after 30 electrochemical cycles while un-coated samples underwent amorphization. Thus, carbon coated samples of *Pmn*2_1 retained 94% capacity after 10 cycles while uncoated samples retained only 40% at 0.1C rate. This suggest that the storage performance of Li_2MnSiO_4 can be enhanced by a combination of two effects namely (i) isolating low temperature polymorph and (ii) providing *in-situ* carbon coating.

Chapter 8

8. Conclusions and future research directions

8.1 Conclusions

Besides powering electronic devices, advanced rechargeable lithium-ion batteries must support high energy density applications such as electric vehicles. Increasing the specific capacity and redox potential of cathode material is a crucial approach. In this thesis, we have focused extensively on $LiMnPO_4$ based cathode material owing to its higher operating voltage compared to the well-studied $LiFePO_4$. The following limitations associated with $LiMnPO_4$ have been successfully overcome in this thesis: (i) sluggish Li^+ ions diffusivity, (ii) poor electronic conductivity, (iii) Jahn-Teller distortion in charged state, (iv) interfacial strain owing to large volume change between $LiMnPO_4$ and $Li_{1-x}MnPO_4$, (v) metastable nature of the delithiated $Li_{1-x}MnPO_4$ phase and (vi) huge polarization.

In the first part of the research work **(chapter 3)**, we prepared mesoporous $LiMnPO_4$/C cathodes featuring carbon coated, interconnected nano-grains using a high energy ball mill assisted soft template method. We highlighted the interdependence of lithium storage performance of $LiMnPO_4$/C on carbon content, milling time, grain size and porous characteristics namely, surface area, pore size and pore volume. Such a tailored $LiMnPO_4$/C delivered lithium storage performance of 140 mAh g^{-1} at 0.05C with flat operating voltage. This was in sharp contrast to pristine microporous $LiMnPO_4$ that delivered only 7 mAh g^{-1} at 0.05C with no perceivable plateaus. However, the achievable capacity of mesoporous $LiMnPO_4$/C *vs.* Li/Li^+ is still lower than the theoretical capacity with poor rate and cyclic performances.

To improve the storage performance, $LiMnPO_4$/C was co-doped with Fe^{2+} and/or Mg^{2+} and an optimized composition $LiMn_{0.9}Fe_{0.05}Mg_{0.05}PO_4$/C was obtained **(chapter 4)**. The storage capacity delivered by $LiMn_{0.9}Fe_{0.05}Mg_{0.05}PO_4$/C was 159 mAh g^{-1} at 0.1C with a polarization of ~139 mV. Such capacity and polarization values are much better than those of pure $LiMnPO_4$ (140 mAh g^{-1} and 340 mV). $LiMn_{0.9}Fe_{0.05}Mg_{0.05}PO_4$/C retained 96 % of its initial capacity at 1C rate after 200 cycles. Improved cycling stability of $LiMn_{0.9}Fe_{0.05}Mg_{0.05}PO_4$/C (2.89 ppm) compared to $LiMnPO_4$ (21.95 ppm) was found to stem from suppressed Mn dissolution in the electrolyte. Further, during Li extraction process, the delithiated phases created from Fe^{2+}/Fe^{3+} redox (~ 3.45 V) favoured facile electrochemical activity of the succeeding Mn^{2+}/Mn^{3+} redox. The fully charged product (4.6 V) contained partial lithiated phase owing to the presence of electrochemically inactive Mg^{2+}. Presence of such lithiated phase provided favourable environment for the subsequent lithium insertion process. It was also found that $LiMn_{0.9}Fe_{0.05}Mg_{0.05}PO_4$/C exhibited improved electronic conductivity and Li^+-ion diffusivity compared to $LiMnPO_4$. Thus, isovalent co-doping provided a positive influence on the lithium storage performance of olivine $LiMnPO_4$. However, the storage capacity of $LiMn_{0.9}Fe_{0.05}Mg_{0.05}PO_4$/C at high rate of 10C was only 58 mAh g^{-1}.

To improve the rate performance, we have prepared Mn-Fe mixed transition metal phosphates **(chapter 5)** with varying compositions, namely $LiMn_{1-x}Fe_xPO_4$ (x = 0.2, 0.5 and 0.8). Among them, the optimized $LiMn_{0.8}Fe_{0.2}PO_4$/C composition delivered 88 mAh g^{-1} at 10C while $LiMn_{0.9}Fe_{0.05}Mg_{0.05}PO_4$/C prepared in the previous chapter delivered only 58

mAh g^{-1} at similar current rates. The enhanced electrochemical kinetics was found to be associated with (i) favourable redox combination which in turn provided favourable environment for the lithiation and delithiation processes owing to difference in the equilibrium potential of Fe^{2+}/Fe^{3+} and Mn^{2+}/Mn^{3+} unlike $LiMnPO_4$, (ii) partial suppression of Jahn-Teller distortion, (iii) better structural and thermal stability of delithiated phase ($Li_{1-x}Mn_{0.8}Fe_{0.2}PO_4$) and (iv) enhanced transport properties. $LiMn_{0.8}Fe_{0.2}PO_4/C$ also showed cycle life of 700 cycles while $LiMn_{0.9}Fe_{0.05}Mg_{0.05}PO_4/C$ and $LiMnPO_4$ showed cycle life of 200 and 50 cycles only. Despite delivering 88 mAh g^{-1} at 10C the capacity associated with the high voltage Mn^{2+}/Mn^{3+} redox was only 32 mAh g^{-1} which lowered the energy density of the battery.

To enhance the electrochemical activity of Mn, Mg^{2+} substituted $LiMn_{0.8}Fe_{0.15}Mg_{0.05}PO_4/C$ sample was prepared **(chapter 6)**. The presence of Mg^{2+} ions in Mn-Fe mixed transition metal phospho-olivine resulted in enhanced electrochemical kinetics, manganese utilization, rate performance, cycling stability, thermal stability, structural stability, reduced voltage polarization and reduced volume change during the electrochemical delithiation compared to $LiMn_{0.8}Fe_{0.2}PO_4/C$. At 10C, the $LiMn_{0.8}Fe_{0.15}Mg_{0.05}PO_4/C$ delivered 97 mAh g^{-1} out of which 57 mAh g^{-1} came from the high voltage Mn redox. Further the polarization was only 550 and 850 mV for Mn^{3+}/Mn^{2+} and Fe^{3+}/Fe^{2+} redox couples compared to $LiMn_{0.8}Fe_{0.2}PO_4/C$. Besides, $LiMn_{0.8}Fe_{0.15}Mg_{0.05}PO_4/C$ electrode showed cyclability of over1000 cycles at 1C. Even at wide operating temperature range, the capacity of $LiMn_{0.8}Fe_{0.15}Mg_{0.05}PO_4/C$ sample in the Mn redox regime was relatively stable compared to $LiMn_{0.8}Fe_{0.2}PO_4/C$. It was found that

the volume mismatch between the lithiated and delithiated phase reduced to 3.9% for $LiMn_{0.8}Fe_{0.15}Mg_{0.05}PO_4/C$ while the mismatch was 5.4% for $LiMn_{0.8}Fe_{0.2}PO_4/C$. Such reduced volume mismatch was instrumental in achieving highly reversible insertion and extraction of Li^+-ions. Influence of Mg^{2+} substitution on the manganese utilization in Mn-rich Mn-Fe mixed transition metal phosphate is demonstrated in terms of (i) redox combination which provides favorable environment for the lithiation and delithiation processes owing to low equilibrium potential of Fe^{2+}/Fe^{3+} and electrochemically inactive Mg^{2+}, (ii) partial suppression of Jahn-Teller distortion, (iii) structural and thermal stability of delithiated phase and (iv) enhanced transport properties. Thus we have successfully demonstrated that tailoring the composition of phospho-olivines will benefit the electrochemical performance.

Finally, we have also investigated the lithium storage performance of silicate based polyanion **(chapter 7)** whose theoretical capacities are nearly two times more than phosphate based polyanion. We isolated two polymorphs of Li_2MnSiO_4 by carefully controlling the calcination temperature. XRD patterns, HRTEM images and SAED patterns confirmed the presence of the low temperature $Pmn2_1$ polymorph and high temperature $P2_1/n$ polymorph. The electrochemical performance of $Pmn2_1$ polymorph was much better than $P2_1/n$ polymorph. $Pmn2_1$ exhibited lithium storage performance of 262 mAh g^{-1} at 0.1C and impressive rate performance up to 5C at room temperature while $P2_1/n$ delivered only 164 mAh g^{-1} at 0.1C. Notably, the capacity of $Pmn2_1$ phase was almost two times higher than $P2_1/n$ phase at all current rates. Such perceivable difference in the storage performance is explained by the

simplest migration pathway of Li^+-ion in $Pmn2_1$ polymorph compared to $P2_1/n$ polymorph. Besides the role of polymorphism, it was also found that the structural stability and carbon coating are critical in achieving high storage performance.

8.2 Future research directions

$LiCoPO_4$ owing to its high redox potential (4.8 V *vs.* Li/Li^+) exhibits higher energy density compared to $LiMnPO_4$. However, sluggish mixed conductivity and lack of stable electrolytes with high oxidation potential are major limiting factors. It has been found that the completely delithiated phase of $LiCoPO_4$ is unstable and undergoes amorphization. The slow kinetics accompanied with the electrolyte decomposition contributes to the capacity loss upon cycling.[185, 190, 197] The electrochemical performance of $LiCoPO_4$ can be enhanced by preparing similar solid solutions mentioned in this thesis with various relatively low redox potential transition metals. Secondly, co-doping with Fe^{2+} and Mg^{2+} mentioned in this thesis can be extended to $LiCoPO_4$. Alternately, investigations can also be performed using various additives such as fluoroethylene carbonate (FEC), vinylene carbonate (VC), vinyl acetate (VA) etc. to ensure stability of electrolytes at high potential and hence enhance the compatibility of $LiCoPO_4$ with existing electrolytes.

Employing Li_2MnSiO_4 as a cathode material for LIBs holds great promise for the development of high energy density LIBs. Richness in polymorphism of Li_2MnSiO_4 presents a variety of chemistries that remain unexplored for lithium storage activity. In this thesis, we have isolated only two polymorphs; however the other polymorphs need to be isolated successfully to understand the differences in electrochemical kinetics. Further,

poor cyclability, sluggish rate performance and high voltage polarization of Li_2MnSiO_4 are still an open challenge. The poor mixed conductivity, structural instability caused by Jahn-Teller effect and amorphization of the material during electrochemical cycling could contribute to the poor electrochemical kinetics.[203, 237, 242] Hence, careful *ex-situ* and *in-situ* studies such as XRD, EXAFS, NMR and FTIR are required to gain better understanding on structural changes and amorphization mechanism during electrochemical cycling.

9. References

1. Z. Yang, J. Zhang, M. C. W. Kintner-Meyer, X. Lu, D. Choi, J. P. Lemmon and J. Liu, *Chemical Reviews*, 2011, **111**, 3577-3613.
2. *http://www.worldenergyoutlook.org/publications/weo-2010/*, 2010.
3. V. S. Arunachalam and E. L. Fleischer, *MRS Bulletin*, 2008, **33**, 264-288.
4. J. P. Holdren, *Science*, 2007, **315**, 737.
5. B. Dunn, H. Kamath and J.-M. Tarascon, *Science*, 2011, **334**, 928-935.
6. V. Srinivasan, *AIP Conference Proceedings*, 2008, **1044**, 283-296.
7. J. M. Tarascon and M. Armand, *Nature*, 2001, **414**, 359-367.
8. V. Etacheri, R. Marom, R. Elazari, G. Salitra and D. Aurbach, *Energy & Environmental Science*, 2011, **4**, 3243-3262.
9. E. Karden, S. Ploumen, B. Fricke, T. Miller and K. Snyder, *Journal of Power Sources*, 2007, **168**, 2-11.
10. D. Linden and T. B. Reddy, *Handbook of batteries*, McGraw Hill, 2002.
11. J. O. Besenhard, *Handbook of batteries*, John Willey, NY, 1998.
12. G. A. Nazri and G. Pistoia, *Lithium batteries-science and technology*, Kluwer Academic New York, 2003.
13. A. K. Padhi, K. S. Nanjundaswamy and J. B. Goodenough, *Journal of The Electrochemical Society*, 1997, **144**, 1188-1194.
14. http://batteryuniversity.com/learn/article/lithium_based_batteries, 2013.
15. K. Mizushima, P. C. Jones, P. J. Wiseman and J. B. Goodenough, *Materials Research Bulletin*, 1980, **15**, 783-789.
16. G. G. Amatucci, J. M. Tarascon and L. C. Klein, *Journal of The Electrochemical Society*, 1996, **143**, 1114-1123.
17. R. Koksbang, J. Barker, H. Shi and M. Y. Saïdi, *Solid State Ionics*, 1996, **84**, 1-21.
18. S. Komaba, N. Yabuuchi and Y. Kawamoto, *Chemistry Letters*, 2009, **38**, 954-955.
19. C. Delmas, *Materials Science and Engineering: B*, 1989, **3**, 97-101.
20. R. Alcántara, G. F. Ortiz, P. Lavela, J. L. Tirado, W. Jaegermann and A. Thißen, *Journal of Electroanalytical Chemistry*, 2005, **584**, 147-156.
21. M. Tabuchi, K. Ado, H. Kobayashi, H. Sakaebe, H. Kageyama, C. Masquelier, M. Yonemura, A. Hirano and R. Kanno, *Journal of Materials Chemistry*, 1999, **9**, 199-204.
22. S.-T. Myung, N. Kumagai, S. Komaba and H.-T. Chung, *Solid State Ionics*, 2001, **139**, 47-56.
23. M. Mladenov, R. Stoyanova, E. Zhecheva and S. Vassilev, *Electrochemistry Communications*, 2001, **3**, 410-416.
24. Y. J. Kim, H. Kim, B. Kim, D. Ahn, J.-G. Lee, T.-J. Kim, D. Son, J. Cho, Y.-W. Kim and B. Park, *Chemistry of Materials*, 2003, **15**, 1505-1511.

25. E. Gaudin, F. Taulelle, R. Stoyanova, E. Zhecheva, R. Alcántara, P. Lavela and J. L. Tirado, *The Journal of Physical Chemistry B*, 2001, **105**, 8081-8087.
26. E. Zhecheva, R. Stoyanova, M. Gorova, R. Alcántara, J. Morales and J. L. Tirado, *Chemistry of Materials*, 1996, **8**, 1429-1440.
27. R. Alcántara, P. Lavela, P. L. Relaño, J. L. Tirado, E. Zhecheva and R. Stoyanova, *Inorganic Chemistry*, 1998, **37**, 264-269.
28. R. Alcántara, P. Lavela, J. L. Tirado, E. Zhecheva and R. Stoyanova, *Journal of Solid State Electrochemistry*, 1999, **3**, 121-134.
29. K. Ozawa, *Solid State Ionics*, 1994, **69**, 212-221.
30. T. Nagaura and K. Tozawa, *Prog. Batteries Solar Cells*, 1990, **9**, 209.
31. Y. Shao-Horn, L. Croguennec, C. Delmas, E. C. Nelson and M. A. O'Keefe, *Nat Mater*, 2003, **2**, 464-467.
32. R. Alcántara, P. Lavela, J. L. Tirado, R. Stoyanova, E. Kuzmanova and E. Zhecheva, *Chemistry of Materials*, 1997, **9**, 2145-2155.
33. J. Morales, C. Pérez-Vicente and J. L. Tirado, *Materials Research Bulletin*, 1990, **25**, 623-630.
34. T. Ohzuku, A. Ueda and M. Nagayama, *Journal of the Electrochemical Society*, 1993, **140**, 1862-1870.
35. J. R. Dahn, U. von Sacken, M. W. Juzkow and H. Al-Janaby, *Journal of The Electrochemical Society*, 1991, **138**, 2207-2211.
36. J. N. Reimers, J. R. Dahn, J. E. Greedan, C. V. Stager, G. Liu, I. Davidson and U. Von Sacken, *Journal of Solid State Chemistry*, 1993, **102**, 542-552.
37. S. Yamada, M. Fujiwara and M. Kanda, *Journal of Power Sources*, 1995, **54**, 209-213.
38. Y. Sun, P. Wan, J. Pan, C. Xu and X. Liu, *Solid State Ionics*, 2006, **177**, 1173-1177.
39. A. Rougier, I. Saadoune, P. Gravereau, P. Willmann and C. Delmasa, *Solid State Ionics*, 1996, **90**, 83-90.
40. M. S. Whittingham, *Chemical Reviews*, 2004, **104**, 4271-4302.
41. E. Rossen, C. D. W. Jones and J. R. Dahn, *Solid State Ionics*, 1992, **57**, 311-318.
42. K. S. Kang, Y. S. Meng, J. Breger, C. P. Grey and G. Ceder, *Science*, 2006, **311**, 977-980.
43. Y. Makimura and T. Ohzuku, *Journal of Power Sources*, 2003, **119–121**, 156-160.
44. S.-T. Myung, S. Komaba, N. Hirosaki, K. Hosoya and N. Kumagai, *Journal of Power Sources*, 2005, **146**, 645-649.
45. S.-T. Myung, S. Komaba and N. Kumagai, *Solid State Ionics*, 2004, **170**, 139-144.
46. M. S. Islam, R. A. Davies and J. D. Gale, *Chemistry of Materials*, 2003, **15**, 4280-4286.
47. N. Dupré, J.-F. Martin, J. Oliveri, P. Soudan, D. Guyomard, A. Yamada and R. Kanno, *Journal of The Electrochemical Society*, 2009, **156**, C180-C185.
48. F. Lian, P. Axmann, C. Stinner, Q. G. Liu and M. Wohlfahrt-Mehrens, *J Appl Electrochem*, 2008, **38**, 613-617.

49. Y. K. Sun, Y. C. Bae and S. T. Myung, *J Appl Electrochem*, 2005, **35**, 151-156.
50. T. Ohzuku and Y. Makimura, *Chemistry Letters*, 2001, **30**, 744-745.
51. N. Yabuuchi, K. Yoshii, S.-T. Myung, I. Nakai and S. Komaba, *Journal of the American Chemical Society*, 2011, **133**, 4404-4419.
52. S.-T. Myung, K. Izumi, S. Komaba, Y.-K. Sun, H. Yashiro and N. Kumagai, *Chemistry of Materials*, 2005, **17**, 3695-3704.
53. K.-C. Jiang, S. Xin, J.-S. Lee, J. Kim, X.-L. Xiao and Y.-G. Guo, *Physical Chemistry Chemical Physics*, 2012, **14**, 2934-2939.
54. H. Sclar, D. Kovacheva, E. Zhecheva, R. Stoyanova, R. Lavi, G. Kimmel, J. Grinblat, O. Girshevitz, F. Amalraj, O. Haik, E. Zinigrad, B. Markovsky and D. Aurbach, *Journal of The Electrochemical Society*, 2009, **156**, A938-A948.
55. J. Choi and A. Manthiram, *Electrochemical and Solid-State Letters*, 2005, **8**, C102-C105.
56. N. Yabuuchi and T. Ohzuku, *Journal of Power Sources*, 2003, **119–121**, 171-174.
57. J. Choi and A. Manthiram, *Journal of The Electrochemical Society*, 2005, **152**, A1714-A1718.
58. T. Ohzuku and R. J. Brodd, *Journal of Power Sources*, 2007, **174**, 449-456.
59. C. S. Johnson, N. Li, C. Lefief and M. M. Thackeray, *Electrochemistry Communications*, 2007, **9**, 787-795.
60. M. M. Thackeray, W. I. F. David, P. G. Bruce and J. B. Goodenough, *Materials Research Bulletin*, 1983, **18**, 461-472.
61. J. M. Tarascon, W. R. McKinnon, F. Coowar, T. N. Bowmer, G. Amatucci and D. Guyomard, *Journal of the Electrochemical Society*, 1994, **141**, 1421-1431.
62. H. Kawai, M. Nagata, H. Tukamoto and A. R. West, *Journal of Power Sources*, 1999, **81–82**, 67-72.
63. J. B. Goodenough, *Journal of Power Sources*, 2007, **174**, 996-1000.
64. R. Kanno, A. Kondo, M. Yonemura, R. Gover, Y. Kawamoto, M. Tabuchi, T. Kamiyama, F. Izumi, C. Masquelier and G. Rousse, *Journal of Power Sources*, 1999, **81–82**, 542-546.
65. M. H. Rossouw, A. de Kock, L. A. de Picciotto, M. M. Thackeray, W. I. F. David and R. M. Ibberson, *Materials Research Bulletin*, 1990, **25**, 173-182.
66. C. Masquelier, M. Tabuchi, K. Ado, R. Kanno, Y. Kobayashi, Y. Maki, O. Nakamura and J. B. Goodenough, *Journal of Solid State Chemistry*, 1996, **123**, 255-266.
67. D. H. Jang, Y. J. Shin and S. M. Oh, *Journal of The Electrochemical Society*, 1996, **143**, 2204-2211.
68. D. H. Jang and S. M. Oh, *Journal of The Electrochemical Society*, 1997, **144**, 3342-3348.
69. A. Paolone, C. Castellano, R. Cantelli, G. Rousse and C. Masquelier, *Physical Review B*, 2003, **68**, 014108.
70. R. J. Gummow, A. de Kock and M. M. Thackeray, *Solid State Ionics*, 1994, **69**, 59-67.

71. Y. Xia, Y. Zhou and M. Yoshio, *Journal of The Electrochemical Society*, 1997, **144**, 2593-2600.
72. Y. Xia and M. Yoshio, *Journal of The Electrochemical Society*, 1996, **143**, 825-833.
73. B. Deng, H. Nakamura, Q. Zhang, M. Yoshio and Y. Xia, *Electrochimica Acta*, 2004, **49**, 1823-1830.
74. R. Alcántara, M. Jaraba, P. Lavela and J. L. Tirado, *Journal of Electroanalytical Chemistry*, 2004, **566**, 187-192.
75. R. Alcántara, M. Jaraba, P. Lavela, J. L. Tirado, E. Zhecheva and R. Stoyanova, *Chemistry of Materials*, 2004, **16**, 1573-1579.
76. R. Stoyanova, E. Zhecheva, R. Alcántara, J. L. Tirado, G. Bromiley, F. Bromiley and T. Boffa Ballaran, *Solid State Ionics*, 2003, **161**, 197-204.
77. E. Zhecheva, R. Stoyanova, M. Gorova, P. Lavela and J. L. Tirado, *Solid State Ionics*, 2001, **140**, 19-33.
78. Y. Xia, Q. Zhang, H. Wang, H. Nakamura, H. Noguchi and M. Yoshio, *Electrochimica Acta*, 2007, **52**, 4708-4714.
79. S.-T. Myung, S. Komaba and N. Kumagai, *Journal of The Electrochemical Society*, 2001, **148**, A482-A489.
80. S.-T. Myung, S. Komaba, N. Kumagai, H. Yashiro, H.-T. Chung and T.-H. Cho, *Electrochimica Acta*, 2002, **47**, 2543-2549.
81. S. Komaba, K. Oikawa, S.-T. Myung, N. Kumagai and T. Kamiyama, *Solid State Ionics*, 2002, **149**, 47-52.
82. S. Komaba, T. Ohtsuka, B. Kaplan, T. Itabashi, N. Kumagai and H. Groult, *Chemistry Letters*, 2002, **31**, 1236-1237.
83. S.-T. Myung, H.-T. Chung, S. Komaba, N. Kumagai and H.-B. Gu, *Journal of Power Sources*, 2000, **90**, 103-108.
84. K. Amine, I. Belharouak, Z. Chen, T. Tran, H. Yumoto, N. Ota, S. T. Myung and Y. K. Sun, *Advanced Materials*, 2010, **22**, 3052-3057.
85. A. K. Padhi, K. S. Nanjundaswamy, C. Masquelier, S. Okada and J. B. Goodenough, *Journal of The Electrochemical Society*, 1997, **144**, 1609-1613.
86. A. S. Andersson, J. O. Thomas, B. Kalska and L. Häggström, *Electrochemical and Solid-State Letters*, 2000, **3**, 66-68.
87. M. Herstedt, M. Stjerndahl, A. Nytén, T. Gustafsson, H. Rensmo, H. Siegbahn, N. Ravet, M. Armand, J. O. Thomas and K. Edström, *Electrochemical and Solid-State Letters*, 2003, **6**, A202-A206.
88. L.-X. Yuan, Z.-H. Wang, W.-X. Zhang, X.-L. Hu, J.-T. Chen, Y.-H. Huang and J. B. Goodenough, *Energy & Environmental Science*, 2011, **4**, 269-284.
89. C. Delacourt, L. Laffont, R. Bouchet, C. Wurm, J.-B. Leriche, M. Morcrette, J.-M. Tarascon and C. Masquelier, *Journal of The Electrochemical Society*, 2005, **152**, A913-A921.
90. M. Yonemura, A. Yamada, Y. Takei, N. Sonoyama and R. Kanno, *Journal of The Electrochemical Society*, 2004, **151**, A1352-A1356.
91. K. Rissouli, K. Benkhouja, J. R. Ramos-Barrado and C. Julien, *Materials Science and Engineering: B*, 2003, **98**, 185-189.
92. C. A. J. Fisher, V. M. Hart Prieto and M. S. Islam, *Chemistry of Materials*, 2008, **20**, 5907-5915.

93. M. S. Islam, D. J. Driscoll, C. A. J. Fisher and P. R. Slater, *Chemistry of Materials*, 2005, **17**, 5085-5092.
94. A. Yamada, S. C. Chung and K. Hinokuma, *Journal of The Electrochemical Society*, 2001, **148**, A224-A229.
95. L. Laffont, C. Delacourt, P. Gibot, M. Y. Wu, P. Kooyman, C. Masquelier and J. M. Tarascon, *Chemistry of Materials*, 2006, **18**, 5520-5529.
96. C. Delacourt, P. Poizot, J.-M. Tarascon and C. Masquelier, *Nat Mater*, 2005, **4**, 254-260.
97. A. S. Andersson and J. O. Thomas, *Journal of Power Sources*, 2001, **97–98**, 498-502.
98. W. Ojczyk, J. Marzec, K. Świerczek, W. Zając, M. Molenda, R. Dziembaj and J. Molenda, *Journal of Power Sources*, 2007, **173**, 700-706.
99. D. Morgan, A. Van der Ven and G. Ceder, *Electrochemical and Solid-State Letters*, 2004, **7**, A30-A32.
100. C. Delacourt, L. Laffont, R. Bouchet, C. Wurm, J.-B. Leriche, M. Morcrette, J.-M. Tarascon and C. Masquelier, *Journal of the Electrochemical Society*, 2005, **152**, A913-A921.
101. C. Delacourt, C. Wurm, L. Laffont, J. B. Leriche and C. Masquelier, *Solid State Ionics*, 2006, **177**, 333-341.
102. K. Saravanan, P. Balaya, M. V. Reddy, B. V. R. Chowdari and J. J. Vittal, *Energy & Environmental Science*, 2010, **3**, 457-464.
103. A. Ait Salah, A. Mauger, K. Zaghib, J. B. Goodenough, N. Ravet, M. Gauthier, F. Gendron and C. M. Julien, *Journal of The Electrochemical Society*, 2006, **153**, A1692-A1701.
104. H. Huang, S.-C. Yin and L. F. Nazar, *Electrochemical and Solid-State Letters*, 2001, **4**, A170-A172.
105. Z. Chen and J. R. Dahn, *Journal of The Electrochemical Society*, 2002, **149**, A1184-A1189.
106. K. Saravanan, M. V. Reddy, P. Balaya, H. Gong, B. V. R. Chowdari and J. J. Vittal, *Journal of Materials Chemistry*, 2009, **19**, 605-610.
107. H. Huang, S. C. Yin and L. Nazar, *Electrochemical and Solid-State Letters*, 2001, **4**, A170-A172.
108. T. Drezen, N.-H. Kwon, P. Bowen, I. Teerlinck, M. Isono and I. Exnar, *Journal of Power Sources*, 2007, **174**, 949-953.
109. S.-T. Myung, S. Komaba, N. Hirosaki, H. Yashiro and N. Kumagai, *Electrochimica Acta*, 2004, **49**, 4213-4222.
110. C. Delacourt, P. Poizot, S. Levasseur and C. Masquelier, *Electrochemical and Solid-State Letters*, 2006, **9**, A352-A355.
111. F. Mestre-Aizpurua, S. Hamelet, C. Masquelier and M. R. Palacín, *Journal of Power Sources*, 2010, **195**, 6897-6901.
112. C. A. J. Fisher and M. S. Islam, *Journal of Materials Chemistry*, 2008, **18**, 1209-1215.
113. S.-Y. Chung, J. T. Bloking and Y.-M. Chiang, *Nat Mater*, 2002, **1**, 123-128.
114. P. Zhang, Y. Wang, M. Lin, D. Zhang, X. Ren and Q. Yuan, *Journal of The Electrochemical Society*, 2012, **159**, A402-A409.

115. T. Nakamura, Y. Miwa, M. Tabuchi and Y. Yamada, *Journal of The Electrochemical Society*, 2006, **153**, A1108-A1114.
116. M. Wagemaker, B. L. Ellis, D. Lützenkirchen-Hecht, F. M. Mulder and L. F. Nazar, *Chemistry of Materials*, 2008, **20**, 6313-6315.
117. B. Wang, B. Xu, T. Liu, P. Liu, C. Guo, S. Wang, Q. Wang, Z. Xiong, D. Wang and X. S. Zhao, *Nanoscale*, 2014, **6**, 986-995.
118. P. S. Herle, B. Ellis, N. Coombs and L. F. Nazar, *Nat Mater*, 2004, **3**, 147-152.
119. B. Kang and G. Ceder, *Nature*, 2009, **458**, 190-193.
120. A. Yamada, Y. Kudo and K.-Y. Liu, *Journal of The Electrochemical Society*, 2001, **148**, A747-A754.
121. S. K. Martha, B. Markovsky, J. Grinblat, Y. Gofer, O. Haik, E. Zinigrad, D. Aurbach, T. Drezen, D. Wang, G. Deghenghi and I. Exnar, *Journal of The Electrochemical Society*, 2009, **156**, A541-A552.
122. C. Julien, M. Massot, S. Rangan, M. Lemal and D. Guyomard, *Journal of Raman Spectroscopy*, 2002, **33**, 223-228.
123. G. A. Nazri and G. Pistoia, *Lithium Batteries, Science and Technology,Kluwer Academic Publishers, New york*, 2003, 129.
124. A. Yamada, Y. Kudo and K.-Y. Liu, *Journal of The Electrochemical Society*, 2001, **148**, A1153-A1158.
125. S. K. Martha, O. Haik, V. Borgel, E. Zinigrad, I. Exnar, T. Drezen, J. H. Miners and D. Aurbach, *Journal of The Electrochemical Society*, 2011, **158**, A790-A797.
126. M. Piana, B. L. Cushing, J. B. Goodenough and N. Penazzi, *Solid State Ionics*, 2004, **175**, 233-237.
127. M. Yonemura, A. Yamada, Y. Takei, N. Sonoyama and R. Kanno, *Journal of The Electrochemical Society*, 2004, **151**, A1352-A1356.
128. D. Morgan, A. V. d. Ven and G. Ceder, *Electrochemical and Solid-State Letters*, 2004, **7**, A30-A32.
129. A. Yamada, M. Yonemura, Y. Takei, N. Sonoyama and R. Kanno, *Electrochemical and Solid-State Letters*, 2005, **8**, A55-A58.
130. N. Meethong, H. Y. S. Huang, S. A. Speakman, W. C. Carter and Y. M. Chiang, *Advanced Functional Materials*, 2007, **17**, 1115-1123.
131. T. Nakamura, Y. Miwa, M. Tabuchi and Y. Yamada, *Journal of The Electrochemical Society*, 2006, **153**, A1108-A1114.
132. S. Okada, S. Sawa, M. Egashira, J.-i. Yamaki, M. Tabuchi, H. Kageyama, T. Konishi and A. Yoshino, *Journal of Power Sources*, 2001, **97–98**, 430-432.
133. N.-H. Kwon, T. Drezen, I. Exnar, I. Teerlinck, M. Isono and M. Graetzel, *Electrochemical and Solid-State Letters*, 2006, **9**, A277-A280.
134. V. Ramar, K. Saravanan, S. R. Gajjela, S. Hariharan and P. Balaya, *Electrochimica Acta*, 2013, **105**, 496-505.
135. V. Ramar and P. Balaya, *Physical Chemistry Chemical Physics*, 2013, **15**, 17240-17249.
136. K. Saravanan, V. Ramar, P. Balaya and J. J. Vittal, *Journal of Materials Chemistry*, 2011, **21**, 14925-14935.

137. Z. Bakenov and I. Taniguchi, *Journal of The Electrochemical Society*, 2010, **157**, A430-A436.
138. T. N. L. Doan and I. Taniguchi, *Journal of Power Sources*, 2011, **196**, 1399-1408.
139. T. N. L. Doan, Z. Bakenov and I. Taniguchi, *Advanced Powder Technology*, 2010, **21**, 187-196.
140. Z. Bakenov and I. Taniguchi, *Electrochemistry Communications*, 2010, **12**, 75-78.
141. C. Delacourt, P. Poizot, M. Morcrette, J. M. Tarascon and C. Masquelier, *Chemistry of Materials*, 2003, **16**, 93-99.
142. D. Choi, D. Wang, I.-T. Bae, J. Xiao, Z. Nie, W. Wang, V. V. Viswanathan, Y. J. Lee, J.-G. Zhang, G. L. Graff, Z. Yang and J. Liu, *Nano Letters*, 2010, **10**, 2799-2805.
143. J. Chen, M. J. Vacchio, S. Wang, N. Chernova, P. Y. Zavalij and M. S. Whittingham, *Solid State Ionics*, 2008, **178**, 1676-1693.
144. C. V. Ramana, A. Ait-Salah, S. Utsunomiya, U. Becker, A. Mauger, F. Gendron and C. M. Julien, *Chemistry of Materials*, 2006, **18**, 3788-3794.
145. P. Barpanda, K. Djellab, N. Recham, M. Armand and J.-M. Tarascon, *Journal of Materials Chemistry*, 2011, **21**, 10143-10152.
146. N. Recham, J. Oró-Solé, K. Djellab, M. R. Palacín, C. Masquelier and J. M. Tarascon, *Solid State Ionics*, 2012, **220**, 47-52.
147. H. Ji, G. Yang, H. Ni, S. Roy, J. Pinto and X. Jiang, *Electrochimica Acta*, 2011, **56**, 3093-3100.
148. B. Kang and G. Ceder, *Journal of The Electrochemical Society*, 2010, **157**, A808-A811.
149. S.-M. Oh, S.-W. Oh, C.-S. Yoon, B. Scrosati, K. Amine and Y.-K. Sun, *Advanced Functional Materials*, 2010, **20**, 3260-3265.
150. D. Wang, C. Ouyang, T. Drezen, I. Exnar, A. Kay, N.-H. Kwon, P. Gouerec, J. H. Miners, M. Wang and M. Gratzel, *Journal of The Electrochemical Society*, 2010, **157**, A225-A229.
151. T. Shiratsuchi, S. Okada, T. Doi and J.-i. Yamaki, *Electrochimica Acta*, 2009, **54**, 3145-3151.
152. G. Li, H. Azuma and M. Tohda, *Electrochemical and Solid-State Letters*, 2002, **5**, A135-A137.
153. D. Chen, W. Wei, R. Wang, X.-f. Lang, Y. Tian and L. Guo, *Dalton Transactions*, 2012, **41**, 8822-8828.
154. D. Rangappa, K. Sone, Y. Zhou, T. Kudo and I. Honma, *Journal of Materials Chemistry*, 2011, **21**, 15813-15818.
155. A. K. Padhi, K. S. Nanjundaswamy and J. B. Goodenough, *J. Electrochem. Soc*, 1997, **144**, 1188-1194.
156. Y. Wang and G. Cao, *Advanced Materials*, 2008, **20**, 2251-2269.
157. K. Saravanan, P. Balaya, M. V. Reddy, B. V. R. Chowdari and J. J. Vittal, *Energy & Environmental Science*, 2010, **3**, 457-463.
158. A. Yamada, M. Hosoya, S.-C. Chung, Y. Kudo, K. Hinokuma, K.-Y. Liu and Y. Nishi, *Journal of Power Sources*, 2003, **119–121**, 232-238.
159. X.-L. Wu, L.-Y. Jiang, F.-F. Cao, Y.-G. Guo and L.-J. Wan, *Advanced Materials*, 2009, **21**, 2710-2714.

160. T. Muraliganth and A. Manthiram, *The Journal of Physical Chemistry C*, 2010, **114**, 15530-15540.
161. S. K. Martha, J. Grinblat, O. Haik, E. Zinigrad, T. Drezen, J. H. Miners, I. Exnar, A. Kay, B. Markovsky and D. Aurbach, *Angewandte Chemie International Edition*, 2009, **48**, 8559-8563.
162. H. Wang, Y. Yang, Y. Liang, L. F. Cui, H. Sanchez Casalongue, Y. Li, G. Hong, Y. Cui and H. Dai, *Angewandte Chemie*, 2011, **123**, 7502-7506.
163. P. Balaya and V. Ramar, *Patent : WO2013002730*, 2013.
164. J. Molenda, W. Ojczyk and J. Marzec, *Journal of Power Sources*, 2007, **174**, 689-694.
165. J.-K. Kim, G. S. Chauhan, J.-H. Ahn and H.-J. Ahn, *Journal of Power Sources*, 2009, **189**, 391-396.
166. A. Yamada, Y. Takei, H. Koizumi, N. Sonoyama, R. Kanno, K. Itoh, M. Yonemura and T. Kamiyama, *Chemistry of Materials*, 2006, **18**, 804-813.
167. K. Zaghib, A. Mauger, F. Gendron, M. Massot and C. Julien, *Ionics*, 2008, **14**, 371-376.
168. M. Kope¢, A. Yamada, G. Kobayashi, S. Nishimura, R. Kanno, A. Mauger, F. Gendron and C. M. Julien, *Journal of Power Sources*, 2009, **189**, 1154-1163.
169. J. Yao, S. Bewlay, K. Konstantionv, V. A. Drozd, R. S. Liu, X. L. Wang, H. K. Liu and G. X. Wang, *Journal of Alloys and Compounds*, 2006, **425**, 362-366.
170. H. Wang, Y. Yang, Y. Liang, L.-F. Cui, H. Sanchez Casalongue, Y. Li, G. Hong, Y. Cui and H. Dai, *Angewandte Chemie*, 2011, **123**, 7502-7506.
171. J. Molenda, W. Ojczyk, K. Świerczek, W. Zając, F. Krok, J. Dygas and R.-S. Liu, *Solid State Ionics*, 2006, **177**, 2617-2624.
172. D.-H. Seo, H. Gwon, S.-W. Kim, J. Kim and K. Kang, *Chemistry of Materials*, 2009, **22**, 518-523.
173. Y.-C. Chen, J.-M. Chen, C.-H. Hsu, J.-J. Lee, T.-C. Lin, J.-W. Yeh and H. C. Shih, *Journal of Power Sources*, 2010, **195**, 6867-6872.
174. G. R. Gardiner and M. S. Islam, *Chemistry of Materials*, 2009, **22**, 1242-1248.
175. V. Ramar and P. Balaya, *Manuscript in preparation*, 2014.
176. G. Chen, J. D. Wilcox and T. J. Richardson, *Electrochemical and Solid-State Letters*, 2008, **11**, A190-A194.
177. J.-W. Lee, M.-S. Park, B. Anass, J.-H. Park, M.-S. Paik and S.-G. Doo, *Electrochimica Acta*, 2010, **55**, 4162-4169.
178. G. Chen, A. K. Shukla, X. Song and T. J. Richardson, *Journal of Materials Chemistry*, 2011, **21**, 10126-10133.
179. R. D. Shannon, *Acta Cryst*, 1976, **A32**, 751-767.
180. J. Kim, Y.-U. Park, D.-H. Seo, J. Kim, S.-W. Kim and K. Kang, *Journal of The Electrochemical Society*, 2011, **158**, A250-A254.
181. H. Yi, C. Hu, H. Fang, B. Yang, Y. Yao, W. Ma and Y. Dai, *Electrochimica Acta*, 2011, **56**, 4052-4057.
182. G. Chen, X. Song and T. J. Richardson, *Electrochemical and Solid-State Letters*, 2006, **9**, A295-A298.

183. G. Yang, H. Ni, H. Liu, P. Gao, H. Ji, S. Roy, J. Pinto and X. Jiang, *Journal of Power Sources*, 2011, **196**, 4747-4755.
184. J. Wolfenstine and J. Allen, *Journal of Power Sources*, 2005, **142**, 389-390.
185. K. Amine, H. Yasuda and M. Yamachi, *Electrochemical and Solid-State Letters*, 2000, **3**, 178-179.
186. M. E. Arroyo-de Dompablo, M. Armand, J. M. Tarascon and U. Amador, *Electrochemistry Communications*, 2006, **8**, 1292-1298.
187. Y. Zhou, J. Wang, Y. Hu, R. O'Hayre and Z. Shao, *Chemical Communications*, 2010, **46**, 7151-7153.
188. J. Yang and J. J. Xu, *Journal of the Electrochemical Society*, 2006, **153**, A716-A723.
189. F. Zhou, M. Cococcioni, K. Kang and G. Ceder, *Electrochemistry Communications*, 2004, **6**, 1144-1148.
190. J. M. Lloris, C. Pérez Vicente and J. L. Tirado, *Electrochemical and Solid-State Letters*, 2002, **5**, A234-A237.
191. A. Eftekhari, *Journal of The Electrochemical Society*, 2004, **151**, A1456-A1460.
192. J. Wolfenstine and J. Allen, *Journal of Power Sources*, 2004, **136**, 150-153.
193. J. Yang and J. J. Xu, *Journal of The Electrochemical Society*, 2006, **153**, A716-A723.
194. B. Jin, H.-B. Gu and K.-W. Kim, *Journal of Solid State Electrochemistry*, 2008, **12**, 105-111.
195. M. E. Rabanal, M. C. Gutierrez, F. Garcia-Alvarado, E. C. Gonzalo and M. E. Arroyo-de Dompablo, *Journal of Power Sources*, 2006, **160**, 523-528.
196. D.-W. Han, Y.-M. Kang, R.-Z. Yin, M.-S. Song and H.-S. Kwon, *Electrochemistry Communications*, 2009, **11**, 137-140.
197. N. N. Bramnik, K. Nikolowski, C. Baehtz, K. G. Bramnik and H. Ehrenberg, *Chemistry of Materials*, 2007, **19**, 908-915.
198. E. Markevich, R. Sharabi, H. Gottlieb, V. Borgel, K. Fridman, G. Salitra, D. Aurbach, G. Semrau, M. A. Schmidt, N. Schall and C. Bruenig, *Electrochemistry Communications*, 2012, **15**, 22-25.
199. L. Dimesso, S. Jacke, C. Spanheimer and W. Jaegermann, *Journal of Solid State Electrochemistry*, 2012, **16**, 911-919.
200. R. Dominko, D. E. Conte, D. Hanzel, M. Gaberscek and J. Jamnik, *Journal of Power Sources*, 2008, **178**, 842-847.
201. A. Nytén, A. Abouimrane, M. Armand, T. Gustafsson and J. O. Thomas, *Electrochemistry Communications*, 2005, **7**, 156-160.
202. M. Armand, C. Michot, N. Ravet, M. Simoneau and P. Hovington, *European patent*, EP 1134 2001, **826**, A1.
203. R. Dominko, M. Bele, M. Gaberšček, A. Meden, M. Remškar and J. Jamnik, *Electrochemistry Communications*, 2006, **8**, 217-222.
204. M. S. Islam, R. Dominko, C. Masquelier, C. Sirisopanaporn, A. R. Armstrong and P. G. Bruce, *Journal of Materials Chemistry*, 2011, **21**, 9811-9818.
205. C. Lyness, B. Delobel, A. R. Armstrong and P. G. Bruce, *Chemical Communications*, 2007, 4890-4892.

206. G. Mali, C. Sirisopanaporn, C. Masquelier, D. Hanzel and R. Dominko, *Chemistry of Materials*, 2011, **23**, 2735-2744.
207. K. Zaghib, A. Ait Salah, N. Ravet, A. Mauger, F. Gendron and C. M. Julien, *Journal of Power Sources*, 2006, **160**, 1381-1386.
208. D. Ensling, M. Stjerndahl, A. Nyten, T. Gustafsson and J. O. Thomas, *Journal of Materials Chemistry*, 2009, **19**, 82-88.
209. A. Kokalj, R. Dominko, G. Mali, A. Meden, M. Gaberscek and J. Jamnik, *Chemistry of Materials*, 2007, **19**, 3633-3640.
210. S.-i. Nishimura, S. Hayase, R. Kanno, M. Yashima, N. Nakayama and A. Yamada, *Journal of the American Chemical Society*, 2008, **130**, 13212-13213.
211. M. E. Arroyo-deDompablo, R. Dominko, J. M. Gallardo-Amores, L. Dupont, G. Mali, H. Ehrenberg, J. Jamnik and E. Morán, *Chemistry of Materials*, 2008, **20**, 5574-5584.
212. V. V. Politaev, A. A. Petrenko, V. B. Nalbandyan, B. S. Medvedev and E. S. Shvetsova, *Journal of Solid State Chemistry*, 2007, **180**, 1045-1050.
213. A. Nyten, M. Stjerndahl, H. Rensmo, H. Siegbahn, M. Armand, T. Gustafsson, K. Edstrom and J. O. Thomas, *Journal of Materials Chemistry*, 2006, **16**, 3483-3488.
214. A. Nyten, S. Kamali, L. Haggstrom, T. Gustafsson and J. O. Thomas, *Journal of Materials Chemistry*, 2006, **16**, 2266-2272.
215. R. Dominko, *Journal of Power Sources*, 2008, **184**, 462-468.
216. C. Sirisopanaporn, C. Masquelier, P. G. Bruce, A. R. Armstrong and R. Dominko, *Journal of the American Chemical Society*, 2010, **133**, 1263-1265.
217. C. Sirisopanaporn, A. Boulineau, D. Hanzel, R. Dominko, B. Budic, A. R. Armstrong, P. G. Bruce and C. Masquelier, *Inorganic Chemistry*, 2010, **49**, 7446-7451.
218. S. Zhang, C. Deng and S. Yang, *Electrochemical and Solid-State Letters*, 2009, **12**, A136-A139.
219. A. Boulineau, C. Sirisopanaporn, R. Dominko, A. R. Armstrong, P. G. Bruce and C. Masquelier, *Dalton Transactions*, 2010, **39**, 6310-6316.
220. Z. L. Gong, Y. X. Li, G. N. He, J. Li and Y. Yang, *Electrochemical and Solid-State Letters*, 2008, **11**, A60-A63.
221. L.-m. Li, H.-j. Guo, X.-h. Li, Z.-x. Wang, W.-j. Peng, K.-x. Xiang and X. Cao, *Journal of Power Sources*, 2009, **189**, 45-50.
222. N. Yabuuchi, Y. Yamakawa, K. Yoshii and S. Komaba, *Electrochemistry*, 2010, **78**, 363-366.
223. C. Sirisopanaporn, R. Dominko, C. Masquelier, A. R. Armstrong, G. Mali and P. G. Bruce, *Journal of Materials Chemistry*, 2011, **21**, 17823-17831.
224. N. Yabuuchi, Y. Yamakawa, K. Yoshii and S. Komaba, *Dalton Transactions*, 2011, **40**, 1846-1848.
225. A. R. Armstrong, N. Kuganathan, M. S. Islam and P. G. Bruce, *Journal of the American Chemical Society*, 2011, **133**, 13031-13035.
226. Z. L. Gong, Y. X. Li and Y. Yang, *Electrochemical and Solid-State Letters*, 2006, **9**, A542-A544.

227. R. Dominko, C. Sirisopanaporn, C. Masquelier, D. Hanzel, I. Arcon and M. Gaberscek, *Journal of The Electrochemical Society*, 2010, **157**, A1309-A1316.
228. Z. L. Gong, Y. X. Li and Y. Yang, *Journal of Power Sources*, 2007, **174**, 524-527.
229. T. Muraliganth, K. R. Stroukoff and A. Manthiram, *Chemistry of Materials*, 2010, **22**, 5754-5761.
230. D. Lv, W. Wen, X. Huang, J. Bai, J. Mi, S. Wu and Y. Yang, *Journal of Materials Chemistry*, 2011, **21**, 9506-9512.
231. Z. Chen, S. Qiu, Y. Cao, J. Qian, X. Ai, K. Xie, X. Hong and H. Yang, *Journal of Materials Chemistry A*, 2013, **1**, 4988-4992.
232. M. Nadherna, R. Dominko, D. Hanzel, J. Reiter and M. Gaberscek, *Journal of The Electrochemical Society*, 2009, **156**, A619-A626.
233. M. Armand and M. E. Arroyo y de Dompablo, *Journal of Materials Chemistry*, 2011, **21**, 10026-10034.
234. V. Aravindan, K. Karthikeyan, K. S. Kang, W. S. Yoon, W. S. Kim and Y. S. Lee, *Journal of Materials Chemistry*, 2011, **21**, 2470-2475.
235. R. Dominko, *Journal of Power Sources*, 2008, **184**, 462-468.
236. Y.-X. Li, Z.-L. Gong and Y. Yang, *Journal of Power Sources*, 2007, **174**, 528-532.
237. G. Mali, A. Meden and R. Dominko, *Chemical Communications*, 2010, **46**, 3306-3308.
238. M. E. Arroyo y de Dompablo, U. Amador, J. M. Gallardo-Amores, E. Morán, H. Ehrenberg, L. Dupont and R. Dominko, *Journal of Power Sources*, 2009, **189**, 638-642.
239. S. Devaraj, M. Kuezma, C. T. Ng and P. Balaya, *Electrochimica Acta*, 2013, **102**, 290-298.
240. M. Kuezma, S. Devaraj and P. Balaya, *Journal of Materials Chemistry*, 2012, **22**, 21279-21284.
241. H. Duncan, A. Kondamreddy, P. H. J. Mercier, Y. Le Page, Y. Abu-Lebdeh, M. Couillard, P. S. Whitfield and I. J. Davidson, *Chemistry of Materials*, 2011.
242. C. A. J. Fisher, N. Kuganathan and M. S. Islam, *Journal of Materials Chemistry A*, 2013, **1**, 4207-4214.
243. I. Belharouak, A. Abouimrane and K. Amine, *The Journal of Physical Chemistry C*, 2009, **113**, 20733-20737.
244. D. M. Kempaiah, D. Rangappa and I. Honma, *Chemical Communications*, 2012, **48**, 2698-2700.
245. D. Rangappa, K. D. Murukanahally, T. Tomai, A. Unemoto and I. Honma, *Nano Letters*, 2012, **12**, 1146-1151.
246. N. Kuganathan and M. S. Islam, *Chemistry of Materials*, 2009, **21**, 5196-5202.
247. P. Barpanda, T. Ye, S.-C. Chung, Y. Yamada, S.-i. Nishimura and A. Yamada, *Journal of Materials Chemistry*, 2012, **22**, 13455-13459.
248. P. Barpanda, G. Rousse, T. Ye, C. D. Ling, Z. Mohamed, Y. Klein and A. Yamada, *Inorganic Chemistry*, 2013, **52**, 3334-3341.
249. S. Lee and S. S. Park, *Chemistry of Materials*, 2012, **24**, 3550-3557.
250. S.-i. Nishimura, M. Nakamura, R. Natsui and A. Yamada, *Journal of the American Chemical Society*, 2010, **132**, 13596-13597.

251. C. V. Ramana, A. Ait-Salah, S. Utsunomiya, A. Mauger, F. Gendron and C. M. Julien, *Chemistry of Materials*, 2007, **19**, 5319-5324.
252. H. Zhou, S. Upreti, N. A. Chernova, G. Hautier, G. Ceder and M. S. Whittingham, *Chemistry of Materials*, 2010, **23**, 293-300.
253. N. Furuta, S.-i. Nishimura, P. Barpanda and A. Yamada, *Chemistry of Materials*, 2012, **24**, 1055-1061.
254. T. Ye, P. Barpanda, S.-i. Nishimura, N. Furuta, S.-C. Chung and A. Yamada, *Chemistry of Materials*, 2013, **25**, 3623-3629.
255. M. Saito, S. Yano, T. Maekawa, A. Tasaka and M. Inaba, *ECS Transactions*, 2013, **50**, 251-259.
256. S.-i. Nishimura, R. Natsui and A. Yamada, *Dalton Transactions*, 2013.
257. V. Legagneur, Y. An, A. Mosbah, R. Portal, A. Le Gal La Salle, A. Verbaere, D. Guyomard and Y. Piffard, *Solid State Ionics*, 2001, **139**, 37-46.
258. A. Yamada, N. Iwane, Y. Harada, S.-i. Nishimura, Y. Koyama and I. Tanaka, *Advanced Materials*, 2010, **22**, 3583-3587.
259. Y. Janssen, D. S. Middlemiss, S.-H. Bo, C. P. Grey and P. G. Khalifah, *Journal of the American Chemical Society*, 2012, **134**, 12516-12527.
260. J. C. Kim, C. J. Moore, B. Kang, G. Hautier, A. Jain and G. Ceder, *Journal of the Electrochemical Society*, 2011, **158**, A309-A315.
261. S. Afyon, D. Kundu, F. Krumeich and R. Nesper, *Journal of Power Sources*, 2013, **224**, 145-151.
262. A. Yamada, N. Iwane, S.-i. Nishimura, Y. Koyama and I. Tanaka, *Journal of Materials Chemistry*, 2011, **21**, 10690-10696.
263. N. A. Kaskhedikar and J. Maier, *Advanced Materials*, 2009, **21**, 2664-2680.
264. J. O. Besenhard and H. P. Fritz, *Angewandte Chemie International Edition in English*, 1983, **22**, 950-975.
265. J. M. Tarascon and D. Guyomard, *Electrochimica Acta*, 1993, **38**, 1221-1231.
266. S. Flandrois and B. Simon, *Carbon*, 1999, **37**, 165-180.
267. S. Komaba, N. Kumagai and Y. Kataoka, *Electrochimica Acta*, 2002, **47**, 1229-1239.
268. E. Frackowiak and F. Béguin, *Carbon*, 2001, **39**, 937-950.
269. G. Che, B. B. Lakshmi, E. R. Fisher and C. R. Martin, *Nature*, 1998, **393**, 346-349.
270. J. Chen, Y. Liu, A. I. Minett, C. Lynam, J. Wang and G. G. Wallace, *Chemistry of Materials*, 2007, **19**, 3595-3597.
271. S. Iijima and T. Ichihashi, *Nature*, 1993, **363**, 603-605.
272. K. Nishidate and M. Hasegawa, *Physical Review B*, 2005, **71**, 245418.
273. L. Zou, L. Gan, F. Kang, M. Wang, W. Shen and Z. Huang, *Journal of Power Sources*, 2010, **195**, 1216-1220.
274. S. Yang, H. Song, X. Chen, A. V. Okotrub and L. G. Bulusheva, *Electrochimica Acta*, 2007, **52**, 5286-5293.
275. G. T. Wu, C. S. Wang, X. B. Zhang, H. S. Yang, Z. F. Qi, P. M. He and W. Z. Li, *Journal of The Electrochemical Society*, 1999, **146**, 1696-1701.
276. W. X. Chen, J. Y. Lee and Z. Liu, *Carbon*, 2003, **41**, 959-966.

277. K. S. Novoselov, A. K. Geim, S. V. Morozov, D. Jiang, Y. Zhang, S. V. Dubonos, I. V. Grigorieva and A. A. Firsov, *Science*, 2004, **306**, 666-669.
278. V. Singh, D. Joung, L. Zhai, S. Das, S. I. Khondaker and S. Seal, *Progress in Materials Science*, 2011, **56**, 1178-1271.
279. M. Liang and L. Zhi, *Journal of Materials Chemistry*, 2009, **19**, 5871-5878.
280. P. Guo, H. Song and X. Chen, *Electrochemistry Communications*, 2009, **11**, 1320-1324.
281. D. Pan, S. Wang, B. Zhao, M. Wu, H. Zhang, Y. Wang and Z. Jiao, *Chemistry of Materials*, 2009, **21**, 3136-3142.
282. E. Yoo, J. Kim, E. Hosono, H.-s. Zhou, T. Kudo and I. Honma, *Nano Letters*, 2008, **8**, 2277-2282.
283. G. Wang, X. Shen, J. Yao and J. Park, *Carbon*, 2009, **47**, 2049-2053.
284. M. Deschamps and R. Yazami, *Journal of Power Sources*, 1997, **68**, 236-238.
285. A. Gerouki, M. A. Goldner, R. B. Goldner, T. E. Haas, T. Y. Liu and S. Slaven, *Journal of The Electrochemical Society*, 1996, **143**, L262-L263.
286. P. Lian, X. Zhu, S. Liang, Z. Li, W. Yang and H. Wang, *Electrochimica Acta*, 2010, **55**, 3909-3914.
287. T. Ohzuku, A. Ueda and N. Yamamoto, *Journal of the Electrochemical Society*, 1995, **142**, 1431-1435.
288. K. M. Colbow, J. R. Dahn and R. R. Haering, *Journal of Power Sources*, 1989, **26**, 397-402.
289. E. Ferg, R. J. Gummow, A. d. Kock and M. M. Thackeray, *Journal of the Electrochemical Society*, 1994, **141**, L147-L150.
290. K. M. Colbow, J. R. Dahn and R. R. Haering, *Journal of Power Sources*, 1989, **26**, 397-402.
291. A. Deschanvres, B. Raveau and Z. Sekkal, *Materials Research Bulletin*, 1971, **6**, 699-704.
292. S. Scharner, W. Weppner and P. Schmid-Beurmann, *Journal of The Electrochemical Society*, 1999, **146**, 857-861.
293. S. Takai, M. Kamata, S. Fujine, K. Yoneda, K. Kanda and T. Esaka, *Solid State Ionics*, 1999, **123**, 165-172.
294. C. Y. Ouyang, Z. Y. Zhong and M. S. Lei, *Electrochemistry Communications*, 2007, **9**, 1107-1112.
295. T.-F. Yi, L.-J. Jiang, J. Shu, C.-B. Yue, R.-S. Zhu and H.-B. Qiao, *Journal of Physics and Chemistry of Solids*, 2010, **71**, 1236-1242.
296. W. J. H. Borghols, M. Wagemaker, U. Lafont, E. M. Kelder and F. M. Mulder, *Journal of the American Chemical Society*, 2009, **131**, 17786-17792.
297. J. M. Feckl, K. Fominykh, M. Döblinger, D. Fattakhova-Rohlfing and T. Bein, *Angewandte Chemie International Edition*, 2012, **51**, 7459-7463.
298. S. Hariharan and P. Balaya, *Manuscript in preparation*, 2014.
299. A. S. Prakash, P. Manikandan, K. Ramesha, M. Sathiya, J. M. Tarascon and A. K. Shukla, *Chemistry of Materials*, 2010, **22**, 2857-2863.

300. N. Takami, H. Inagaki, Y. Tatebayashi, H. Saruwatari, K. Honda and S. Egusa, *Journal of Power Sources*, 2013, **244**, 469-475.
301. K. Ariyoshi, R. Yamato and T. Ohzuku, *Electrochimica Acta*, 2005, **51**, 1125-1129.
302. X. Hu, Z. Deng, J. Suo and Z. Pan, *Journal of Power Sources*, 2009, **187**, 635-639.
303. K. Ariyoshi, S. Yamamoto and T. Ohzuku, *Journal of Power Sources*, 2003, **119–121**, 959-963.
304. P. Reale, A. Fernicola and B. Scrosati, *Journal of Power Sources*, 2009, **194**, 182-189.
305. D. Deng, M. G. Kim, J. Y. Lee and J. Cho, *Energy & Environmental Science*, 2009, **2**, 818-837.
306. Z. Yang, D. Choi, S. Kerisit, K. M. Rosso, D. Wang, J. Zhang, G. Graff and J. Liu, *Journal of Power Sources*, 2009, **192**, 588-598.
307. L. Kavan, M. Grätzel, S. E. Gilbert, C. Klemenz and H. J. Scheel, *Journal of the American Chemical Society*, 1996, **118**, 6716-6723.
308. C. L. Olson, J. Nelson and M. S. Islam, *The Journal of Physical Chemistry B*, 2006, **110**, 9995-10001.
309. K. Saravanan, K. Ananthanarayanan and P. Balaya, *Energy and Environmental Science*, 2010, **3**, 939-948.
310. D. Wang, D. Choi, Z. Yang, V. V. Viswanathan, Z. Nie, C. Wang, Y. Song, J.-G. Zhang and J. Liu, *Chemistry of Materials*, 2008, **20**, 3435-3442.
311. G. Armstrong, A. R. Armstrong, P. G. Bruce, P. Reale and B. Scrosati, *Advanced Materials*, 2006, **18**, 2597-2600.
312. C. W. Mason, I. Yeo, S. Kuppan and P. Balaya, *RSC Advances*, 2012.
313. K. Saravanan, K. Ananthanarayanan and P. Balaya, *Energy & Environmental Science*, 2010, **3**, 939-948.
314. P. Poizot, S. Laruelle, S. Grugeon, L. Dupont and J. M. Tarascon, *Nature*, 2000, **407**, 496-499.
315. H. Li, P. Balaya and J. Maier, *Journal of The Electrochemical Society*, 2004, **151**, A1878-A1885.
316. J. Cabana, L. Monconduit, D. Larcher and M. R. Palacín, *Advanced Materials*, 2010, **22**, E170-E192.
317. P. G. Bruce, B. Scrosati and J.-M. Tarascon, *Angewandte Chemie International Edition*, 2008, **47**, 2930-2946.
318. J. Li, H. M. Dahn, L. J. Krause, D.-B. Le and J. R. Dahn, *Journal of The Electrochemical Society*, 2008, **155**, A812-A816.
319. S. Hariharan, K. Saravanan, V. Ramar and P. Balaya, *Physical Chemistry Chemical Physics*, 2013, **15**, 2945-2953.
320. F. Jiao, J. L. Bao and P. G. Bruce, *Electrochem. Solid State Lett.*, 2007, **10**, A264-A266.
321. D. Larcher, C. Masquelier, D. Bonnin, Y. Chabre, V. Masson, J.-B. Leriche and J.-M. Tarascon, *Journal of The Electrochemical Society*, 2003, **150**, A133-A139.
322. S. Hariharan, K. Saravanan and P. Balaya, *Electrochemical and Solid-State Letters*, 2010, **13**, A132-A134.
323. S. Komaba, T. Mikumo and A. Ogata, *Electrochemistry Communications*, 2008, **10**, 1276-1279.

324. S. Hariharan, V. Ramar, S. P. Joshi and P. Balaya, *RSC Advances*, 2013, **3**, 6386-6394.
325. C. Ban, Z. Wu, D. T. Gillaspie, L. Chen, Y. Yan, J. L. Blackburn and A. C. Dillon, *Advanced Materials*, 2010, **22**, E145-E149.
326. S. Komaba, T. Mikumo, N. Yabuuchi, A. Ogata, H. Yoshida and Y. Yamada, *Journal of The Electrochemical Society*, 2010, **157**, A60-A65.
327. X. J. Liu, H. Yasuda and M. Yamachi, *Journal of Power Sources*, 2005, **146**, 510-515.
328. Q. Fan and M. S. Whittingham, *Electrochem. Solid State Lett.*, 2007, **10**, A48-A51.
329. P. Poizot, S. Laruelle, S. Grugeon and J. M. Tarascon, *Journal of the Electrochemical Society*, 2002, **149**, A1212-A1217.
330. M. S. Wu, P. C. J. Chiang, J. T. Lee and J. C. Lin, *Journal of Physical Chemistry B*, 2005, **109**, 23279-23284.
331. J. Z. Zhao, Z. L. Tao, J. Liang and J. Chen, *Cryst. Growth Des.*, 2008, **8**, 2799-2805.
332. M. M. Thackeray, *Prog. Solid State Chem.*, 1997, **25**, 1-71.
333. P. Lavela, J. L. Tirado and C. Vidal-Abarca, *Electrochimica Acta*, 2007, **52**, 7986-7995.
334. D. Pasero, N. Reeves and A. R. West, *Journal of Power Sources*, 2005, **141**, 156-158.
335. M. J. Aragon, C. Perez-Vicente and J. L. Tirado, *Electrochemistry Communications*, 2007, **9**, 1744-1748.
336. M. N. Obrovac, R. A. Dunlap, R. J. Sanderson and J. R. Dahn, *Journal of the Electrochemical Society*, 2001, **148**, A576-A588.
337. R. Dedryvere, S. Laruelle, S. Grugeon, P. Poizot, D. Gonbeau and J. M. Tarascon, *Chemistry of Materials*, 2004, **16**, 1056-1061.
338. S. Yang, G. Cui, S. Pang, Q. Cao, U. Kolb, X. Feng, J. Maier and K. Müllen, *ChemSusChem*, 2010, **3**, 236-239.
339. L. Zhi, Y.-S. Hu, B. E. Hamaoui, X. Wang, I. Lieberwirth, U. Kolb, J. Maier and K. Müllen, *Advanced Materials*, 2008, **20**, 1727-1731.
340. J. S. Do and C. H. Weng, *Journal of Power Sources*, 2005, **146**, 482-486.
341. L. J. Zhi, Y. S. Hu, B. El Hamaoui, X. Wang, I. Lieberwirth, U. Kolb, J. Maier and K. Mullen, *Advanced Materials*, 2008, **20**, 1727-+.
342. X. W. Lou, D. Deng, J. Y. Lee and L. A. Archer, *Journal of Materials Chemistry*, 2008, **18**, 4397-4401.
343. K. M. Shaju, F. Jiao, A. Debart and P. G. Bruce, *Physical chemistry chemical physics*, 2007, **9**, 1837-1842.
344. A. N. Dey, *Journal of the Electrochemical Society*, 1971, **118**, 1547-1549.
345. J. Yang, M. Winter and J. O. Besenhard, *Solid State Ionics*, 1996, **90**, 281-287.
346. C. K. Chan, H. Peng, G. Liu, K. McIlwrath, X. F. Zhang, R. A. Huggins and Y. Cui, *Nat Nano*, 2008, **3**, 31-35.
347. J. Graetz, C. C. Ahn, R. Yazami and B. Fultz, *Electrochem. Solid State Lett.*, 2003, **6**, A194-A197.

348. L. F. Cui, R. Ruffo, C. K. Chan, H. L. Peng and Y. Cui, *Nano Letters*, 2009, **9**, 491-495.
349. M. Winter and J. O. Besenhard, *Electrochimica Acta*, 1999, **45**, 31-50.
350. S. Naille, C. M. Ionica-Bousquet, F. Robert, F. Morato, P. E. Lippens and J. Olivier-Fourcade, *Journal of Power Sources*, 2007, **174**, 1091-1094.
351. M. T. McDowell, S. Woo Lee, C. Wang and Y. Cui, *Nano Energy*, 2012, **1**, 401-410.
352. P. Ridgway, H. Zheng, G. Liu, X. Song, A. Guerfi, P. Charest, K. Zaghib and V. Battaglia, *ECS Transactions*, 2008, **13**, 1-12.
353. Y. Yao, N. Liu, M. T. McDowell, M. Pasta and Y. Cui, *Energy & Environmental Science*, 2012, **5**, 7927-7930.
354. K. Xu, *Chemical Reviews*, 2004, **104**, 4303-4418.
355. G. E. Blomgren, *Journal of Power Sources*, 2003, **119–121**, 326-329.
356. W. A. V. Schalkwijk and B. Scrosati, *Advances in Lithium-Ion Batteries, Kluwer Academic/Plenum Publishers, NY, Boston, London*, 2002, 251.
357. S. F. Lux, I. T. Lucas, E. Pollak, S. Passerini, M. Winter and R. Kostecki, *Electrochemistry Communications*, 2012, **14**, 47-50.
358. S. E. Sloop, J. K. Pugh, S. Wang, J. B. Kerr and K. Kinoshita, *Electrochemical and Solid-State Letters*, 2001, **4**, A42-A44.
359. S. S. Zhang, *Journal of Power Sources*, 2006, **162**, 1379-1394.
360. F. Cheng, Z. Tao, J. Liang and J. Chen, *Chemistry of Materials*, 2007, **20**, 667-681.
361. L. V. Azaroff and M. J. Buerger, *The powder method in X-ray crystallography*, McGraw Hill, New York, 1958.
362. B. D. Cullity and S. R. Stock, *Elements of X-ray diffraction*, Prentice Hall, New York, 2001.
363. H. Lipson and H. Steeple, *Interpretation of X-ray powder diffraction patterns*, Macmillan-London, St Martin's Press-New York, 1970.
364. A. J. C. Wilson., *Elements of X-ray crystallography* Addison-Wesley Pub. Co, Reading, Mass., 1970.
365. J. I. Goldstein, D. E. Newbury, P. Echlin, D. C. Joy, C. E. Lyman, E. Lifshin, L. Sawyer and J. R. Michael, *Scanning electron microscopy and X-Ray microanalysis*, Kluwer Academic, New York, 1994.
366. P. J. Goodhew, J. Humphreys and R. Beanland, *Electron microscopy and analysis*, Taylor and Francis, London, 2001.
367. M. H. Loretto., *Electron beam analysis of materials* Chapman & Hall London, New York 1994.
368. G. Mobus, *High resolution imaging and spectrometry of materials*, Springer-Verlag, Berlin, 2003.
369. K. S. W. Sing, D. H. Everett, R. A. W. Haul, L. Moscou, R. A. Pierotti, J. Rouquerol and T. Siemieniewska, *Pure & Appl. Chem.*, 1985, **57**, 603-619.
370. C. K. Lee, A. S. T. Chiang and C. S. Tsay, Trans Tech Publications, 1995, pp. 21-44.
371. B. C. Lippens and J. H. de Boer, *Journal of Catalysis*, 1965, **4**, 319-323.

372. J. Nolte, *ICP emission spectrometry: a practical guide, Wiley-VCH, Weinheim*, 2003.
373. T.R. Dulski, *Trace elemental analysis of metals: methode and techniques, Marcel Dekker, New york*, 1999.
374. J. F. Moulder, W. F. Stickle, P. E. Sobol and K. D. Bomben, *Handbook of X-ray Photoelectron spectroscopy, Perkin-Elmer Corp,Eden Prarie, USA*, 1992.
375. B. H. Stuart., *Infrared spectroscopy : fundamentals and applications*, Chichester, England ; Hoboken, NJ : J. Wiley, , 2004. .
376. D. K. Gosser, *Cyclic voltammetry: simulation and analysis of reaction mechanism*, Wiley-VCH, NY, 1993.
377. J. Koryta, J. Dvorák and V. Boháčková, *Electrochemistry* Halsted Press, New York, 1973.
378. A. Yamada and S.-C. Chung, *Journal of The Electrochemical Society*, 2001, **148**, A960-A967.
379. R. Amin, J. Maier, P. Balaya, D. P. Chen and C. T. Lin, *Solid State Ionics*, 2008, **179**, 1683-1687.
380. C. Suryanarayana, *Progress in Materials Science*, 2001, **46**, 1-184.
381. N. Yabuuchi, M. Sugano, Y. Yamakawa, I. Nakai, K. Sakamoto, H. Muramatsu and S. Komaba, *Journal of Materials Chemistry*, 2011.
382. J. H. de Boer, B. G. Linsen, T. van der Plas and G. J. Zondervan, *Journal of Catalysis*, 1965, **4**, 649-653.
383. L. Li, X. Tang, H. Liu, Y. Qu and Z. Lu, *Electrochimica Acta*, 2010, **56**, 995-999.
384. H. Fang, H. Yi, C. Hu, B. Yang, Y. Yao, W. Ma and Y. Dai, *Electrochimica Acta*, 2012, **71**, 266-269.
385. N.-H. Kwon, T. Drezen, I. Exnar, I. Teerlinck, M. Isono and M. Graetzel, *Electrochemical and Solid-State Letters*, 2006, **9**, A277-A280.
386. Z. Bakenov and I. Taniguchi, *Journal of Power Sources*, 2010, **195**, 7445-7451.
387. C. Delacourt, P. Poizot, M. Morcrette, J. M. Tarascon and C. Masquelier, *Chemistry of Materials*, 2004, **16**, 93-99.
388. S.-M. Oh, S.-T. Myung, Y. S. Choi, K. H. Oh and Y.-K. Sun, *Journal of Materials Chemistry*, 2011, **21**, 19368-19374.
389. S.-M. Oh, S.-T. Myung, J. B. Park, B. Scrosati, K. Amine and Y.-K. Sun, *Angewandte Chemie International Edition*, 2012, **51**, 1853-1856.
390. C. Hu, H. Yi, H. Fang, B. Yang, Y. Yao, W. Ma and Y. Dai, *Electrochemistry Communications*, 2010, **12**, 1784-1787.
391. H. Wang, Y. Yang, Y. Liang, L.-F. Cui, H. Sanchez Casalongue, Y. Li, G. Hong, Y. Cui and H. Dai, *Angewandte Chemie International Edition*, 2011, **50**, 7364-7368.
392. M. M. Doeff, J. Chen, T. E. Conry, R. Wang, J. Wilcox and A. Aumentado, *Journal of Materials Research*, 2010, **25**, 1460-1468.
393. R. D. Shannon and C. T. Prewitt, *Acta Crystallographica Section B*, 1970, **26**, 1046-1048.
394. S. Geller and J. L. Durand, *Acta Crystallographica*, 1960, **13**, 325-331.

395. J. Xiao, N. A. Chernova, S. Upreti, X. Chen, Z. Li, Z. Deng, D. Choi, W. Xu, Z. Nie, G. L. Graff, J. Liu, M. S. Whittingham and J.-G. Zhang, *Physical Chemistry Chemical Physics*, 2011, **13**, 18099-18106.
396. V. P. Zakaznova-Herzog, H. W. Nesbitt, G. M. Bancroft and J. S. Tse, *Surface Science*, 2006, **600**, 3175-3186.
397. V. P. Zakaznova-Herzog, H. W. Nesbitt, G. M. Bancroft and J. S. Tse, *Geochimica et Cosmochimica Acta*, 2008, **72**, 69-86.
398. M. Kurth, P. C. J. Graat and E. J. Mittemeijer, *Applied Surface Science*, 2003, **220**, 60-78.
399. H. Yang, X.-L. Wu, M.-H. Cao and Y.-G. Guo, *The Journal of Physical Chemistry C*, 2009, **113**, 3345-3351.
400. Y.-H. Rho, L. F. Nazar, L. Perry and D. Ryan, *Journal of The Electrochemical Society*, 2007, **154**, A283-A289.
401. K.-S. Park, A. Benayad, M.-S. Park, A. Yamada and S.-G. Doo, *Chemical Communications*, 2010, **46**, 2572-2574.
402. D. Choi, J. Xiao, Y. J. Choi, J. S. Hardy, M. Vijayakumar, M. S. Bhuvaneswari, J. Liu, W. Xu, W. Wang, Z. Yang, G. L. Graff and J.-G. Zhang, *Energy & Environmental Science*, 2011, **4**, 4560-4566.
403. K. Tang, X. Yu, J. Sun, H. Li and X. Huang, *Electrochimica Acta*, 2011, **56**, 4869-4875.
404. M. R. Roberts, G. Vitins, G. Denuault and J. R. Owen, *Journal of The Electrochemical Society*, 2010, **157**, A381-A386.
405. T. Aoshima, K. Okahara, C. Kiyohara and K. Shizuka, *Journal of Power Sources*, 2001, **97–98**, 377-380.
406. W. H. Woodford, Y.-M. Chiang and W. C. Carter, *Journal of The Electrochemical Society*, 2010, **157**, A1052-A1059.
407. W. H. Woodford, W. C. Carter and Y.-M. Chiang, *Energy & Environmental Science*, 2012, **5**, 8014-8024.
408. C. M. Burba and R. Frech, *Journal of The Electrochemical Society*, 2004, **151**, A1032-A1038.
409. M. T. Paques-Ledent and P. Tarte, *Spectrochimica Acta Part A: Molecular Spectroscopy*, 1973, **29**, 1007-1016.
410. M. T. Paques-Ledent and P. Tarte, *Spectrochimica Acta Part A: Molecular Spectroscopy*, 1974, **30**, 673-689.
411. N. S. Norberg and R. Kostecki, *Electrochimica Acta*, 2011, **56**, 9168-9171.
412. C. M. Burba and R. Frech, *Journal of Power Sources*, 2007, **172**, 870-876.
413. P. Tarte, A. Rulmont, M. Liégeois-Duyckaerts, R. Cahay and J. M. Winand, *Solid State Ionics*, 1990, **42**, 177-196.
414. C. M. Burba and R. Frech, *Spectrochimica Acta Part A: Molecular and Biomolecular Spectroscopy*, 2006, **65**, 44-50.
415. W. Paraguassu, P. T. C. Freire, V. Lemos, S. M. Lala, L. A. Montoro and J. M. Rosolen, *Journal of Raman Spectroscopy*, 2005, **36**, 213-220.
416. A. A. Salah, P. Jozwiak, J. Garbarczyk, K. Benkhouja, K. Zaghib, F. Gendron and C. M. Julien, *Journal of Power Sources*, 2005, **140**, 370-375.

417. L. Popović, D. de Waal and J. C. A. Boeyens, *Journal of Raman Spectroscopy*, 2005, **36**, 2-11.
418. Z. X. Nie, C. Y. Ouyang, J. Z. Chen, Z. Y. Zhong, Y. L. Du, D. S. Liu, S. Q. Shi and M. S. Lei, *Solid State Communications*, 2010, **150**, 40-44.
419. R. Malik, A. Abdellahi and G. Ceder, *Journal of The Electrochemical Society*, 2013, **160**, A3179-A3197.
420. V. Srinivasan and J. Newman, *Electrochemical and Solid-State Letters*, 2006, **9**, A110-A114.
421. K. Weichert, W. Sigle, P. A. van Aken, J. Jamnik, C. Zhu, R. Amin, T. Acartürk, U. Starke and J. Maier, *Journal of the American Chemical Society*, 2011, **134**, 2988-2992.
422. D. Jang, K. Palanisamy, J. Yoon, Y. Kim and W.-S. Yoon, *Journal of Power Sources*, 2013, **244**, 581-585.
423. B. Wang, B. H. Xu, T. Liu, P. Liu, C. Guo, S. Wang, Q. Wang, D. Wang and G. Zhao, *Nanoscale*, 2013.
424. M. R. Roberts, G. Vitins and J. R. Owen, *Journal of Power Sources*, 2008, **179**, 754-762.
425. M. Armand and J. M. Tarascon, *Nature*, 2008, **451**, 652-657.
426. J. Hassoun, S. Panero, P. Reale and B. Scrosati, *Advanced Materials*, 2009, **21**, 4807-4810.
427. O. K. Park, Y. Cho, S. Lee, H.-C. Yoo, H.-K. Song and J. Cho, *Energy & Environmental Science*, 2011, **4**, 1621-1633.
428. Z. Gong and Y. Yang, *Energy & Environmental Science*, 2011, **4**, 3223-3242.
429. K. Zaghib, A. Salah, N. Ravet, A. Mauger, F. Gendron and C. M. Julien, *J. Power Sources*, 2006, **160**, 1381.
430. G. Zhong, Y. Li, P. Yan, Z. Liu, M. Xie and H. Lin, *The Journal of Physical Chemistry C*, 2010, **114**, 3693-3700.
431. J. Moskon, R. Dominko, R. Cerc-Korosec, M. Gaberscek and J. Jamnik, *Journal of Power Sources*, 2007, **174**, 683-688.
432. S. Liu, J. Xu, D. Li, Y. Hu, X. Liu and K. Xie, *Journal of Power Sources*, 2013, **232**, 258-263.
433. V. Aravindan, S. Ravi, W. S. Kim, S. Y. Lee and Y. S. Lee, *Journal of Colloid and Interface Science*, 2011, **355**, 472-477.
434. V. Aravindan, K. Karthikeyan, S. Ravi, S. Amaresh, W. S. Kim and Y. S. Lee, *Journal of Materials Chemistry*, 2010, **20**, 7340-7343.